A NUMERICAL STUDY OF SWIRLING FLOW AND OXYGEN TRANSPORT IN A MICRO-BIOREACTOR

YU PENG

NATIONAL UNIVERSITY OF SINGAPORE

2006

A NUMERICAL STUDY OF SWIRLING FLOW AND OXYGEN TRANSPORT IN A MICRO-BIOREACTOR

YU PENG

(B.Eng., M.Eng., Xi'an Jiaotong University, China)

A THESIS SUBMITTED

FOR THE DEGREE OF DOCTOR OF PHILOSOPHY

DEPARTMENT OF MECHANICAL ENGINEERING

NATIONAL UNIVERSITY OF SINGAPORE

2006

ACKNOWLEDGEMENTS

I wish to express my deepest gratitude to my Supervisors, Associate Professor Low Hong Tong and Associate Professor Lee Thong See, for their invaluable guidance, supervision, patience and support throughout this study. Their suggestions have been invaluable for the project and for the results analysis.

I would like to express my gratitude to the National University of Singapore (NUS) for providing me a Research Scholarship and an opportunity to do my Ph.D study at the Department of Mechanical Engineering.

I wish to thank all the staff members and students in the Fluid Mechanics Laboratory and Biofluids Laboratory, Department of Mechanical Engineering, NUS for their valuable assistance. I also wish to thank the staff members in the Computer Centre for their assistance on supercomputing.

I am very grateful to my wife Zeng Yan, for her love, support, patience and continued encouragement during the Ph.D period. I am also very grateful to my parents and sister for their selfless love and support.

Finally, I wish to thank all my friends and teachers who have helped me in different ways during my whole period of study in NUS.

Table of Contents

SUMMARY

A micro-bioreactor, with working volume of a few millilitres, is useful for the study of cell culture during the initial experimentation stage before large scale production. One design was based on a chamber stirred by a rotating rod at the bottom. The objective of this work was to investigate the swirling flow and oxygen transport in a stirred micro-bioreactor.

A numerical model was developed to investigate the flow field and mass transport in a micro-bioreactor in which medium mixing was generated by a magnetic stirrer-rod rotating on the bottom. The oxygen transfer coefficient in the micro-bioreactor is around 10^{-3} s^{-1} which is two orders smaller than that of a 10-litre fermentor; hence the oxygen transfer rate is insufficient for bacteria culture. However, it is shown that for certain animal cell cultures, the oxygen concentration level in the micro-bioreactor can become adequate, provided that the magnetic rod is rotated at a high speed (rod Reynolds number of 716). At such high rotation-speed, the micro-bioreactor exhibits a peak shear stress below 0.5 N m^{-2} which is acceptable for animal cell culture.

A numerical model was developed to investigate the axisymmetric flow in a micro-bioreactor with a rotating disk whose radius was smaller than that of the chamber. The partially rotating disk simulates effect of the rotating magnetic-rod at the bottom of the micro-bioreactor. The cylinder-to-disk ratio, up to 1.6, is found to have noticeable effect on vortex breakdown. The contours of streamline, angular momentum, azimuthal vorticity, centrifugal force, radial pressure gradient and the resultant of the tow force are presented and compared with those of whole end-wall rotation, to show the mechanism of vortex breakdown. The shear stress and oxygen

concentration fields show that within the center of the vortex breakdown bubble, the shear stress is substantially low but the oxygen concentration is relatively high.

In order to study the effect of a porous scaffold in the micro-bioreactor, a numerical method was developed to investigate the flow and mass transport with porous media. The momentum jump condition, which includes both viscous and inertial jump parameters, was imposed at the porous-fluid interface. By using multi-block grids, together with body-fitted grids, the present method is more suitable for handling the coupled transport phenomena in homogenous fluid and porous medium regions with complex geometries.

The flow environment in the micro-bioreactor with a tissue engineering scaffold was numerically modeled. The numerical results show that the Reynolds number has noticeable effects on the flow both outside and inside the scaffold. The Darcy number mainly affects the porous flow within the scaffold. The concentration contours are influenced by the flow field and oxygen consumption rate. For a higher Reynolds number or Darcy number, the oxygen concentration within the scaffold is higher and the concentration difference between the top and bottom surfaces is lower as more oxygen is convected into the scaffold. However, for a higher Damkohler number, the concentration within the scaffold is lower due to the higher oxygen consumption rate.

NOMENCLATURE

a	Thermal diffusivity
A_L, A_R	Coefficients of contributions from interface cell faces
A_P^{φ}, A_E^{φ}, A_W^{φ}, A_N^{φ}	Coefficients of the resultant algebraic equations
C	Concentration
C_0	Reference Concentration
C_{avg}	Average oxygen concentration
C_F	Forchheimer coefficient
d	Diameter of the stirrer-rod
D	Diameter of the micro-bioreactor
Da	Damkohler number $= \gamma V_m L^2 \big/ \left(C_0 D_f \right)$
Dar	Darcy number $= K \big/ L^2$
D_c	Diffusivity of oxygen in animal cell phase
D_{eff}	Effective diffusivity of oxygen in porous medium
D_f	Binary diffusivity
D_i	Radius of the impeller
D_T	Diameter of the bioreactor
F	Forchheimer number $= C_F \rho G H_1^{\,4} \big/ \left(K^{1/2} \mu^2 \right)$
F_e, F_w, F_n, F_s	Overall fluxes (including both convection and diffusion)
$F_e^c, F_w^c, F_n^c, F_s^c$	Convective flux
$F_e^d, F_w^d, F_n^d, F_s^d$	Diffusive flux

Fr	Froude number $=\Omega^2 R^2 / gH$
i, j	Index
g	gravitational constant (= 9.81 m/s^2)
H	Height
H/R	Aspect ratio
ISF	Integrated shear factor
$k_L a$	Volumetric oxygen transfer coefficient
k_m	Half-saturation parameter
k_s	Impeller constant
K	Permeability
K_{eq}	Partition coefficient
K_1	Constant for maximum time averaged shear rate
K_τ	Consistency index
L	Length
m_e	Mass flux cross the surface e
n	Flow behavior index
$\vec{n}$	Unit vector normal to the interface
N	Rotational speed of the impeller
N_{Qc}	Flow number
OTR	Volumetric oxygen transfer rate
p	Pressure
Pr	Prandtl number $=\nu/a$
Q_c	Flow rate
Q_φ	Volume integral of the source term

r, z, θ	Cylindrical coordinates
$\vec{r}$	Position vector
r_d	Radius of a rotating disk
R	Radius
Ra	Rayleigh number = $\rho^2 g \beta_T L^3 \Delta T / \mu^2$
Re	Reynolds number
R_m	Source term for oxygen consumption
R/r_d	Cylinder-to-disk ratio
Sc	Schmidt number = ν / D_f
S_e	Surface area of face e
S_M	Mean shear stress
S_N	Mean normal stress
$S_{rr}, S_{zz}, S_{\theta\theta}$	Normal stress components in cylindrical coordinates
$S_{rz}, S_{z\theta}, S_{r\theta}$	Shear stress components in cylindrical coordinates
S_r, S_z, S_θ	Source terms in cylindrical coordinates
S^x, S^y	Surface vector components
S_x, S_y	Source terms in Cartesian coordinates
T	Temperature
u, v	Velocity/Darcy velocity components
u_t	Velocity component parallel to the interface
u_n	Velocity component normal to the interface
U, V	Dimensionless Velocity
$\vec{v}_{\text{interface}}$	Interface velocity vector

v_z, v_r, v_θ	Velocity components in cylindrical coordinates
V_t	Tip speed of the impeller
V_m	Maximum oxygen uptake rate per cell
W	Width of the impeller blade
x, y, z	Cartesian coordinates
Y_{av}	Time-averaged mean shear rate
Y_m	Maximum time averaged shear rate

Greek Symbols

β , β_1	Adjustable parameters for stress jump condition
β_T	Expansion coefficient
γ	Cell density
$\dot{\gamma}$	Shear rate
Γ	Angular momentum
Γ_φ	Diffusivity for quantity φ
ε	Porosity
ε_c	Volume fractions occupied by animal cells
ε_s	Volume fractions occupied by the scaffold
κ	Coefficient = $K_{eq} D_c / D_f$
λ_e	Interpolation factor
μ	Dynamic viscosity
ν	Kinematic viscosity
ρ	Density of the fluid

τ	Shear stress
φ	General scalar quantity
φ_e	Value of φ at the center of the cell face e
Φ	Energy dissipation rate
Ψ	Stream function
ω	Azimuthal vorticity
Ω	Angular velocity

Superscripts

*	Intrinsic average

Subscripts

e, w, n, s	Faces of the control volume

List of Figures

List of Tables

Chapter 1

Introduction

Animal cell culture has wide applications in many areas and numerous types of bioreactors have been designed to grow cells *in vitro*. It is known that animal cells are sensitive to the fluid environment provided by bioreactors. Various experimental and numerical methods have been proposed to investigate fluid environment and its effects on animal cell culture in bioreactors.

1.1 Background

1.1.1 Animal Cell Culture

The first attempt of animal cell culture was achieved at the beginning of the last century (Harrison, 1907). After a century of development, animal cell culture has become a powerful tool used in life science and biotechnology industry today. The investigations and applications of animal cell culture may be divided into four aspects, that is, physiological and toxicological studies (Li et al., 1983), biological productions (Racher et al., 1990), tissue engineering (Toshia et al., 1996), and extracorporeal devices (Legallais et al., 2001).

Animal cells exhibit a wide range of behaviours when they are grown *in vitro*. Animal cells that can only grow when attached to a suitable substrate are called anchorage-dependent cells while animal cells that can grow either attached to a substrate or floating free in suspension are called anchorage-independent cells. Most

animal cells, such as cells derived from normal tissues, are considered to be anchorage-dependent. Some animal cells, such as cells found in blood, which always grow in suspension, are anchorage-independent.

1.1.2 Bioreactors

Bioreactors are vessels for growing cells *in vitro*. There are two basic culture systems used for growing cells *in vitro*, which are based primarily on the ability of cells to either attach to a substrate (adherent culture system) or float free in suspension (suspension culture systems). Generally, the main bioreactors used for adherent culture in the laboratory are tissue culture dishes, T-flasks or multi-well plates; and the bioreactors used for suspension culture are spinner flasks or shaken flasks. Besides these simple bioreactors, other types of bioreactors have been designed. For the adherent culture, a typical one is the hollow fiber bioreactor, which consists of bundles of semi-permeable fibers, offering a matrix environment for cell growth. For the suspension culture system, a common one is the stirred bioreactor, which consists of a cylindrical vessel and a stirrer.

1.1.3 Cell Scaffold

For adherent cell culture, it is better to grow cells in an appropriate three-dimensional (3D) matrix that closely simulates the *in vivo* environment. A variety of scaffolds has been designed to serve as a 3D physical support for *in vitro* cell culture (Freed et al., 1994a; Radisic et al., 2006) as well as *in vivo* tissue

regeneration (Vacanti et al., 1991; Freed et al., 1994b). Generally, scaffold should be biocompatible for cell adhesion and growth and its biodegradation rate should be close to that of the tissue assembly. Also the scaffold structure should have a high porosity (void space) for cell-scaffold interaction, cell proliferation and extracellular matrix regeneration. Moreover, the scaffold should have a high permeability for the purpose of transporting nutrients and metabolites to and from the cells.

1.1.4 Flow Environment in Bioreactor

Although there are many different types of bioreactors, their objectives are the same, that is, the chemical solution and mechanical apparatus surrounding the cells *in vitro* are to recreate the physical, nutritional, hormonal environment of the cells *in vivo* (Butler, 1996). These include controlling the temperature, pH, gaseous environment; providing a suitable substrate and supplying nutrients; protecting cells from physical, chemical and mechanical stresses. From the point of view of fluid dynamics, two requirements are considered here: first, the cells should be able to absorb enough nutrients from the culture medium; secondly, the cells should not be exposed to the flow with high hydrodynamic stresses.

1.2 Literature Review

1.2.1 Flow Field in Stirred Bioreactors

It is essential to obtain the flow field in the stirred bioreactor since it indicates the mixing extent in bioreactor quantitatively. The distributions of velocity components

are also needed to calculate the hydrodynamic stress and to predict nutrients transport in the stirred bioreactor.

Over recent years computational fluid dynamics (CFD) has gained success in the investigation of bioreactor performance (Harris et al., 1996). There have been many computational studies on flow field in industrial stirred-tank bioreactors (Bakker et al., 1997; Armenante et al., 1997; Ranade, 1997; Harvey et al., 1997; Sahu et al., 1999; Lamberto et al., 1999; Jaworski et al., 2000; Montante et al., 2001; Serra et al., 2001; Zalc et al., 2001; Bujalski et al., 2002; Rice et al., 2006; Waters et al., 2006).

Kuncewicz (1992) developed a 3D model for the flow in a tank stirred by paddle impellers or flat-blade turbines operating in a laminar condition. By solving three dimensional Navier-Stokes Equations numerically, the three velocity components were obtained; and the numerical solution was verified by comparing local shear stress calculated from the velocity components and those measured from experiment respectively.

Harvey et al. (1997) investigated the laminar flow in a cylindrical tank with a stack of four 45° pitched blade impellers, four rectangular side-wall baffles and an ellipsoidal shaped bottom. Incompressible, 3D Navier-Stokes equations were solved by pseudo-compressibility technique of coupling the velocity and pressure fields. To simplify the flow, the relative motion between impeller and baffles was neglected and the governing equations were solved in a frame of reference attached to the rotating impeller. Coriolis and centrifugal force terms were added to the momentum equations to account for the rotating frame. The numerical results agree well with experimental

LDV data. Their results showed that the flow patterns within the tank were strongly dependent on the impeller size and spacing.

Bakker et al. (1997) simulated the flow pattern generated by a blade turbine in a stirred reactor. By using FLUENT associated with sliding mesh method, the laminar flow fields for various Reynolds number (*Re*) ranging from 40 to 1200 were successfully predicted. And the numerical results were validated by the experimental data. However, the unsteady simulation is time consuming and the calculation time is about an order of magnitude longer than steady calculations.

Rice et al. (2006) investigated the fluid dynamic characteristics of low *Re* laminar flows in mixing vessels with a Rushton impeller for *Re* = 1, 10 and 28. An in-house code based on an unstructured mesh was used to simulate the flow field. A sliding and deforming mesh technique was employed in order to account for the rotation of the impeller relative to the baffles. The numerical results showed that, at *Re* of 28, the flow exhibited the familiar outward pumping action associated with radial impellers under turbulent flow conditions. The net radial flow during one impeller revolution dropped with *Re* decreasing.

Lamberto et al. (1999) simulated the flow field in an unbaffled tank stirred by a Ruston impeller at *Re* ranging from 8.64 to 69.12. The commercial software FLUENT was used to determine the three-dimensional flow field in the tank. The flow is steady in a rotating frame of reference as there are no baffles. The computational results were verified by PIV measurements. It was found that there were torus-shaped segregated regions above and below the impeller. The sizes and centers of the segregated regions

depended on both *Re* and the position of the impeller blade. It was also found that the regions moved towards the impeller in the radial direction and away from the impeller in the axial direction as a blade approached.

Zalc et al. (2001) studied Newtonian laminar flow fields in a stirred tank equipped with three Rushton turbines. The software ORCA was applied to simulate the flow fields for *Re* in the range of 20 to 200. The velocity field computed by the software agrees well with the planar velocity vectors obtained by PIV. It was found that the dimensional maximum velocity magnitude (divided by the tip velocity) in a vertical plane aligned with one of the impeller blades increased with an increasing of *Re*. The results showed that at a lower *Re*, the recirulating motion of the flow was weak and the flow was azimuthally dominant. At a higher *Re*, the relative strength of the recirculating motion became greater due to the inertial effects.

1.2.2 Hydrodynamic Stress in Stirred Bioreactors

As the stirrer rotates, the local velocity in a stirred bioreactor varies with time and position, hence the hydrodynamic stress varies. The magnitudes of the hydrodynamic stresses and their fluctuations depend on the specific location in the stirred bioreactor, the type of impeller, the stirring speed, and the properties of the culture medium. Therefore, it is important to propose some effective parameters to evaluate the hydrodynamic stress level in the stirred bioreactor.

The impeller speed or the tip velocity has been often qualitatively associated with the cell damage. Different cells have different ranges of tolerated shear stress. For

example, human melanoma cells were affected in the shear environment induced by 1.5 m s^{-1} stirrer tip speed, whereas CHO cells were affected at1.0 m s^{-1} stirrer tip speed (Leist et al., 1990). Abu-Reesh and Kargi (1991) investigated the effects of long-term hydrodynamic shear on mouse-mouse hybridoma cells HDP-1 in a 250-ml spinner flask with three baffled. Cells grown at steady state were subjected to step changes in agitation rates. It was found that high agitation rates caused a steady drop in cell viability and total cell concentration. Smith and Greenfield (1992) investigated shear stress effect on the murine hybridoma cell line JC.l in 2 L bioreactor agitated with a six-bladed, Rushton turbine impeller (50 mm diameter). An increase of glycolysis and a decline of cell viability at 600 rev min^{-1} were found compared with those at 100 rev min^{-1}.

Although the impeller speed has been often used, it is very difficult to use this parameter to evaluate the actual stress levels to animal cells that are exposed in different bioreactor configurations with different impeller geometries. Thus, several different characteristic shear rate values have been proposed to evaluate the stress level, including the time-averaged mean shear rate, the maximum shear rate at the impeller, and the shear rate in the region swept by the impeller blades.

According to Nagata (1975), the maximum time averaged shear rate is proportional to the tip speed of the impeller. A correlation to calculate the maximum time averaged shear rate Y_m was given by:

$$Y_m = K_1 V_t \tag{1.1}$$

$$V_t = \pi N D_i \tag{1.2}$$

where K_1 is a constant; V_t is the tip speed of the impeller; N is the rotational speed of the impeller; and D_i is the radius of the impeller.

Bowen (1986) investigated the hydrodynamic environment in a baffled vessel agitated by a six-bladed Rushton turbine. Correlations on the time-averaged mean shear rate and the time-averaged maximum shear rate were obtained as follows:

$$Y_{av} = 4.2N\left(D_i/D_T\right)^{0.3}\left(D_i/W\right) \tag{1.3}$$

$$Y_m = 2.3Y_{av} \tag{1.4}$$

where Y_{av} is the time-averaged mean shear rate; D_T is the diameter of the bioreactor; and W is the width of the impeller blade.

Sinskey et al. (1981) investigated the effects of agitation on microcarrier cultures in small stirred vessels. They proposed that cell growth can be correlated with an integrated shear factor (ISF), which was expressed as:

$$ISF = 2\pi ND_i/\left(D_T - D_i\right) \tag{1.5}$$

If the distributions of all velocity components in stirred bioreactors have been obtained, the detailed shear stress distribution in the bioreactors can be calculated from the first derivatives of the velocity components. With the development of advanced CFD and experimental technique, the aim can be achieved more easily. An example of such flow field and shear stress computation was given by Begley and Kleis (2000) for the NASA rotating wall perfused-vessel bioreactor. Other studies can be found elsewhere (Williams et al., 2002; Lappa, 2003).

It has been proposed that the damaging hydrodynamic forces on cells arise from the velocity gradients. Hence, besides shear stress, normal stress and the energy

dissipation rate, which also include velocity gradient components, may be used to evaluate the hydrodynamic environment. Joshi et al. (2001) investigated the flow pattern in a stirred bioreactor numerically and experimentally. It was observed that the turbulent normal stress was 2 and 10 times larger than the turbulent shear stress for various impellers. It was also found that the extent of de-activation of enzymes could be co-related with volume averaged normal stress.

Al-Rubeai et al. (1994) examined the death mechanism of Murine hybridoma cells TB/C3 in stirred bioreactors. The cell death was co-related with the energy dissipation rate. It was found that there was no apparent cell damage at an energy dissipation rate of 1.5 W m^{-3}. Cell viability declined at an energy dissipation rate of 320 W m^{-3}. When cells were subjected to the intensive energy dissipation rate of 1870 W m^{-3}, the cell number dropped by 50% within 2 h. Other relative study on the cell response to the energy dissipation rate can be found in many literatures such as Aloi and Cherry (1996) and Gregoriades et al. (1999).

1.2.3 Mass Transport in Stirred Bioreactors

Mass transport is a fundamental issue in animal cell culture. First, maintaining a homogenous environment is of importance and may be the limiting factor for high-quality or high-value products from cell culture. On the other hand, effectively delivering nutrients into or removing waste from culture medium is also essential and crucial for success or failure of cell cultivation.

1.2.3.1 Mixing

Mixing time is an important mixing parameter as it is the time scale associated with mixing the contents of a stirred bioreactor. Jaworski et al. (2000) and Bujalski et al. (2002) applied a FLUENT CFD code to simulate flow and tracer concentration fields in a tank with dual Rushton turbines. The mixing time in the turbulent flow regime was determined and compared with experimental data.

Flow number (see Equation 4.9 for definition) is another important mixing parameter to measure the pumping capacity of an impeller (Costes and Couderc, 1988; Kuncewicz, 1992; Dong et al., 1994). Costes and Couderc (1988) experimentally investigated the flow in a stirred tank, in which the mixing is generated by a six-blade Rushton turbine. They found that the flow number was independent of the stirrer rotational speed. The mean value of the flow number was about 3.4. Dong et al. (1994) measured the flow induced by a flat-paddle impeller with eight blades in an unbaffled tank. They also found that the flow number was approximately independent of the impeller rotational speed and was equal to about 2.0.

1.2.3.2 Oxygen Transfer

Oxygen is a key substrate in aerobic cell culture bioprocesses. However, the solubility of oxygen in most cell culture media is low. The supply of oxygen may not match the requirements of a given cell population, leading to cell hypoxia or even loss of cell viability. Therefore, oxygen transfer in small-scale bioreactors has attracted much attention (Duetz et al., 2000; Hristov et al., 2001; Kostov et al., 2001; Williams

et al., 2002; Lamping et al., 2003; Kensy et al., 2005; Puskeiler et al., 2005; Weuster-Botz et al., 2005; Zhang et al., 2005).

Puskeiler et al. (2005) developed a novel millilitre-scale bioreactor equipped with a gas-inducing impeller. Oxygen transfer coefficients higher than 0.2 s^{-1} can be maintained over a range of 8 to 12-ml working volume with a stirrer speed of 2300rpm. Kostov et al. (2001) designed a novel micro-bioreactor of 2-mL working volume, which could form the basis of a multiple-bioreactor system for high throughput bioprocessing. In their novel design, a small magnetic bar was placed at the base of a 1-cm square cuvette. The bar was magnetically rotated at 300 rpm to provide agitation. Oxygen availability was ensured with bubble aeration. Suspended *Escherichia coli* cells were cultured in this micro-bioreactor. An optical sensing system was developed to measure the variation with time of pH value, dissolved oxygen and optical density and these profiles were satisfactory as compared with those in a 1-L bioreactor.

Numerical methods have also been employed to investigate fluid flow and mass transfer in bioreactors. A 3-D networks-of-zones model was applied to analyse two-phase mixing accompanied by bioreaction in a gas-liquid stirred vessel (Hristov et al., 2001). The simulation indicated severe non-uniformity of gas hold-up distribution and consequently spatially non-homogeneous oxygen transfer in the bioreactor. The mixing in the bioreactor was not uniform and microorganisms would experience large variations in oxygen and nutrient concentrations.

Zhang et al. (2005) employed a CFX CFD model to estimate the volumetric mass

transfer coefficients. Over a range of shaking frequencies between 100 and 300 rpm, shaking diameters between 20 and 60 mm, and working volumes between 25 and 100mL, volumetric mass coefficient was predicted to be in a range of 0.003-0.028 s^{-1}. The results indicated that the oxygen transport may not be sufficient for fermentation but is acceptable for growth of animal cells.

Lamping et al. (2003) investigated the flow environment in a new miniature bioreactor with a set of three impellers mechanically driven via a microfabricated electric motor for fermentation. The diameter of the bioreactor was equal to that of a single well of a 24-well plate. Volumetric mass transfer coefficients in the miniature bioreactor were predicted in the range 100-400 h^{-1}, which were comparable to the typical values reported for large-scale fermentation.

Weuster-Botz et al. (2005) simulated the flow in the gas-inducing millilitre-scale bioreactor by a CFX CFD model. Based on the CFD simulations, it was found that the maximum of local energy dissipation in the culture medium was up to 50 W L^{-1} at 2,800 rpm. Local energy dissipation and total power input were well comparable to standard stirred bioreactors.

1.2.4 Swirling Flow and Vortex Breakdown in Micro-Bioreactors

Vortex breakdown is a sudden structural change of vortex flows near their rotation axis, which is characterized by the formation of a free stagnation point upstream of a region with reversed axial flow on the core of a confined columnar vortex. Vortex breakdown is very important in the field of aeronautics as its

occurrence over delta wing may cause the loss of aircraft control (Hall, 1972).

Interestingly, vortex breakdown phenomena have also been found in bioreactors for animal cell or tissue culture (Dusting et al., 2004; 2006). Vortex breakdown changes the flow structure, shear stress, and concentration distribution in bioreactors. It may have some effects on the function and viability of animal cells. Thus, it is of importance to investigate vortex breakdown and its effect on flow dynamics and mass transport in bioreactors. For tissue engineering, it has been suggested that the appropriate location of the scaffold is at the center of the recirculation zone or the vortex breakdown bubble, where the flow is laminar and shear stress is low (Mununga et al., 2004).

Swirling flow in a cylindrical chamber, of a radius R and a height H, with a bottom-wall rotating at an angular velocity Ω, is particularly suitable for the detailed investigation of the vortex breakdown phenomena because the flow problem has a relatively simple configuration and well defined boundary conditions. Only two dimensionless parameters are needed to characterize the flow structure: the aspect ratio H/R and the Reynolds number $Re = \Omega R^2/\nu$, where ν is the kinematic viscosity.

A detailed and systematical experimental investigation for vortex breakdown has been done by Escudier (1984). The stability boundaries with one, two or even three successive vortex breakdown bubbles, as well as a transition towards unsteady flows, were mapped in a plot of the Reynolds number and the aspect ratio. These experimental visualizations have been confirmed by the numerical model of Lopez (1990), who solved the unsteady, axisymmetric Navier-Stokes equations. Brown and

Lopez (1990) explained that the physical mechanism of vortex breakdown is due to negative azimuthal vorticity induced by an excess centrifugal force near the stationary top end-wall.

Recently, some variants of the above flow problem have also been investigated. Spohn et al. (1993) considered the case in which the stationary end-wall at the top was replaced by a free surface. The experimental results show that the vortex breakdown bubbles may attach to the free surface at certain *Re*. They also found that the mechanism of the attached vortex breakdown bubbles is the same as those that occurred in the interior of the flow domain. The numerical works of Valentine and Jahnke (1994) and Lopez (1995) indicate that the free surface effect may be approximately modeled by having a mid-plane in a cylinder of twice the height, in which both end-walls rotate at the same speed.

Spohn et al. (1998) compared the flow inside two different chamber geometries, one with a rigid cover and the other with a free surface. It was observed that the vortex breakdown bubble inside the chamber is in many ways similar to those in vortex tubes. Their results suggested that along the chamber wall, friction and dissipation decrease the angular momentum of the fluid, which is imparted into the fluid by the Ekman layer on the rotation bottom wall. Higher aspect ratio *H/R* means more angular momentum is lost along the wall. Therefore, vortex breakdown in the chamber is affected by both the aspect ratio *H/R* and the Reynolds number *Re*. They also pointed out that an adverse axial pressure gradient along the rotation axis is essential to cause vortex breakdown.

Another variant is the effect of introducing a rotating central rod, which has been reported by Mullin et al. (2000) and Husain et al. (2003). Mullin et al. (2000) investigated the effect of a sloped inner cylinder on the vortex breakdown. The sloped inner cylinder can either suppress or intensify vortex breakdown, depending on the direction of the slope. This effect is due to the variation of the adverse pressure gradient caused by the sloped cylinder.

Husain et al. (2003) introduced an additional co- or counter-rotation near the axis, which was achieved by a rotating central rod, to control vortex breakdown. It was found that co-rotation is adequate to totally suppress vortex breakdown, whereas counter-rotation increases the size and number of the vortex breakdown bubbles and even makes the flow unsteady. This is because the rod co-rotation decreases the adverse pressure gradient along the axis and thus suppresses vortex breakdown while the rod counter-rotation increases the adverse pressure gradient and thus intensifies vortex breakdown. In another study Mununga et al. (2004) showed the effect a small rotating disk on the onset of vortex breakdown. It was found that the co-rotation of the small disk with the lid can increase the bubble size while the counter-rotation of the small disk can reduce the bubble size, or completely suppress it.

Another interesting configuration is that of a partially rotating end-wall, in which the central part consists of a rotating disk of a smaller radius r_d. Such a configuration was considered by Piva and Meiburg (2005) who numerically studied the case with a free surface. The stationary end-wall at the bottom significantly alters the flow structure. The side wall does not have a significant effect on the flow structure near

the disk if it is far away, as in cases of the cylinder-to-disk ratio above 2.3. Most of their results are for the cylinder-to-disk ratio above 2 although there are streamline patterns for lower ratios down to 1.

The cylindrical chamber with the bottom wall rotating has been used as a cell culture bioreactor because of its capability of producing swirling flows much steadier than those produced by standard bioreactor impellers and magnetic stirrers (Dusting et al., 2004; 2006). By investigating the flow environment in this bioreactor configuration, it was found that the shear stress is lower in the vortex breakdown region than that in the main recirculating flow region.

1.2.5 Flow and Mass Transport in Bioreactors with Scaffolds

Scaffolds have been extensively used in tissue engineering for regeneration of tissues (Vunjak-Novakovic et al., 1998; Goldstein et al., 2001; Koh and Atala, 2004; Cooper et al., 2005). The scaffold provides a three-dimensional structure for cell attachment and tissue organization (Freed et al., 1994a). When the scaffolds with attached cells are cultured in stirred bioreactors, they should provide suitable hydrodynamic and biochemical factors in the cell environment, which include efficient oxygen and nutrient delivery and mechanical stimulation.

1.2.5.1 Coupled Flow in Homogeneous Fluid and Porous Medium Regions

Generally, the scaffold could be considered as a porous medium. Thus, the flow in stirred bioreactors with scaffold could be defined as systems which compose of a

porous medium and a homogenous fluid. This type of flows also occurs in a wide range of the industrial and environmental applications, such as drying process, electronic cooling, ceramic processing, overland flow during rainfall, ground-water pollution etc.. Two different approaches, the single-domain approach (Mercier et al., 2002) and the two-domain approach (Costa et al., 2004), are usually used to solve this type of problems.

In the single-domain approach, the composite region is considered as a continuum and one set of general governing equations is applied for the whole domain. The explicit formulation of boundary conditions is avoided at the interface and the transitions of the properties between the fluid and porous medium are achieved by certain artifacts (Goyeau et al., 2003). Although this method is relatively easier to implement, the flow behaviour at the interface may not be simulated properly, depending on how the code is structured (Nield, 1997).

In the two-domain approach, two sets of governing equations are applied to describe the flow in the two regions and additional boundary conditions are applied at the interface to close the two sets of equations. This method is more reliable since it tries to simulate the flow behaviour at the interface. Hence, in the present study, the two-domain approach, and the implementation of the interface boundary conditions, will be considered. A list of proposed boundary conditions at the porous-fluid interface is summarized in Table 1.1.

One of the several early studies on the interface boundary conditions is that by Beavers and Joseph (1967). In their approach, the flows in a homogenous fluid and a

porous medium are governed by the Navier-Stokes and Darcy equations respectively. A semi-empirical slip boundary condition was proposed at the interface, because the flows in the different regions are governed by the corresponding partial differential equations of different orders. To make the governing equations of the same order, Neale and Nader (1974) introduced a Brinkman term in the Darcy equation for the porous medium; and thus, proposed continuous boundary conditions in both stress and velocity. By matching both velocity and stress, Vafai and Kim (1990) provided an exact solution for the flow at the interface, which includes the inertial and boundary effects. In an alternative model (Kim and Choi, 1996), the effective viscosity was used in the formulation of the continuous stress condition at the interface.

A stress jump condition at the interface was deduced by Ochoa-Tapia and Whitaker (1995a and 1995b) based on the non-local form of the volume averaged method. Based on the Forchheimer equation with the Brinkman correction and the Navier-Stokes Equation, Ochoa-Tapia and Whitaker (1998) developed another stress jump condition which includes the inertial effects. Two coefficients appear in this jump condition: one is associated with an excess viscous stress and the other is related to an excess inertial stress.

Numerical solutions for the coupled viscous and porous flows have been attempted by many researchers (Gartling, 1996; Silva and de Lemos, 2003; Jue, 2004; Costa et al., 2004; Betchen et al., 2006). Jue (2004) simulated vortex shedding behind a porous square cylinder by finite element method. In his study, a general non-Darcy porous media model was applied to describe the flows both inside and outside the

cylinder. A harmonic mean was used to treat the sudden change between the fluid and porous medium. Costa et al. (2004) proposed a control-volume finite element method to simulate the coupled viscous and porous flows. A continuity of both velocity and stress at the interface was assumed and no special or additional procedure was needed to impose the interfacial boundary conditions. Betchen et al. (2006) developed a finite volume model, also based on continuity of both velocity and stress, but special attention was given to the pressure-velocity coupling at the interface.

Different types of interfacial conditions between a porous medium and a homogenous fluid have been proposed; and found to have a pronounced effect on the velocity field as shown by Alazmi and Vafai (2001). Although the one-domain approach, or a continuity of both velocity and stress, is easier to implement, the stress jump conditions have been adopted by researchers.

The implementation of the numerical methodology on the stress jump condition based on Ochoa-Tapia and Whitaker (1995a and 1995b) can be found in the work of Silva and de Lemos (2003). Although they proposed that their treatment could be used in a complex geometry, their results were based on finite volume method in an orthogonal Cartesian coordinate system and for the case of fully developed flow. In their study, only the jump in shear stress was included and no special treatment on velocity derivatives was mentioned. However, for flow in general, it is needed to consider how to formulate the velocity derivatives at the interface. Also, for the 2D problem, the normal stress condition is needed to close the sets of equations.

1.2.5.2 Numerical Simulation on Flow around/through Scaffold

Analysis of the flow and mass transport in stirred bioreactors with scaffolds is very important to understand how to achieve the best possible condition for cell culture or tissue growth. It is very difficult to directly measure the velocity or concentration at the position in the scaffold due to its complex micro-structure. Thus, it is essential to develop numerical models to predict the transport phenomena in stirred bioreactor with scaffold. However, there are only a few numerical studies related to this topic.

Williams et al. (2002) developed a FLUENT CFD model to calculate flow fields, shear stresses and oxygen profiles around tissue-engineered cartilage constructs in a concentric cylinder bioreactor. The oxygen distribution in the bioreactor showed that fluid-phase oxygen transport to the cartilage constructs was uniform. However, in their study, the cartilage constructs were considered as solid structures and the flow and oxygen concentration in the constructs were unknown.

Sucosky et al. (2004) experimentally and numerically investigated the flow and shear stress around tissue-engineered cartilage constructs in a spinner-flask bioreactor agitated by a magnetic stir bar. The commercial software FLUENT was used to simulate the flow field by assuming the cartilage constructs as solid structures. Once the flow and the forces on the assumed-solid construct surface were determined, a porous flow model based on Darcy's law was applied to predict the volume-flow rate of culture medium through the porous construct by using the previous solid-construct results as initial conditions.

Porter et al. (2005) applied the Lattice-Boltzmann method to simulate the cell culture media flowing though scaffolds in a bioreactor. Microcomputed tomography imaging was used to define the microarchitecture of the scaffold for the simulations. The local shear stress distribution was estimated from velocity derivatives at various media flow rates. Boschetti et al. (2006) developed a CFD model of the flow though a 3D scaffold of homogeneous geometry. The scaffold was idealized as made of many sub-units which obtained by subtracting a solid sphere form a concentric solid cub. Although the two methods have been successfully applied to simulate the porous flows in the scaffolds, they are time and memory consuming as a large number of elements are needed to describe the micro-structure of the scaffolds.

1.3 Objectives of the Study

1.3.1 Motivations

A micro-bioreactor of 2-mL working volume was designed by Kostov et al. (2001), which was stirred by a magnetic rod at the base. It was shown to be successful in culturing Escherichia coli cells but has not been tested with other cells, especially animal cells, which are more sensitive to the flow environment. The rotating rod in the stirred micro-bioreactor generates a swirling flow and vortex breakdown phenomena may occur in under certain conditions. Although there are many fundamental studies on vortex breakdown, there are few works on vortex breakdown in bioreactors. Also, there are limited works on investigating coupled flow and mass transport in and around a scaffold in bioreactors.

1.3.2 Objectives

The objectives of this thesis were:

a. To develop a numerical model of the flow field and oxygen transport in a micro-bioreactor which is stirred by a small magnetic rod at the bottom.

b. To examine vortex breakdown in the stirred bioreactor by an axisymmetric model, in which the rotating rod is simulated by a partially rotating bottom-wall.

c. To develop a numerical method for coupled transport problems with fluid and porous media.

d. To investigate the flow and oxygen transport in the axisymmetric bioreactor model which has a tissue-engineering scaffold.

1.3.3 Scope

The flow study for the prototype micro-bioreactor was based on a three-dimensional model using a finite volume method. The flow study for vortex breakdown in a micro-bioreactor and swirling flow around a porous scaffold were based on an axisymmetric model using a finite volume code developed in the present study. The culture medium (with and without suspended cells) was assumed to be Newtonian fluid. The Reynolds number based on the radius of the rotating part was limited to a maximum of 2000, in which range the swirling flow is laminar. The microstructure of the porous medium was not considered. The porous medium was assumed homogeneous with a permeability range between 10^{-11} to 10^{-9} m^2,

corresponding to the Darcy number from 10^{-7} to 10^{-5}.

1.4 Organization of the Thesis

In Chapter 2, a finite volume method based on non-orthogonal body-fitted and multi-block structure grids is developed to simulate the coupled flow and mass transport problems with homogenous flow and porous medium regions.

In Chapter 3, a variety of numerical experiments are performed to test the validation of the present code.

In Chapter 4, the flow environment in a novel micro-bioreactor, of working volume below 5 ml, in which the medium is mixed by a magnetic stirrer rod at the base, is investigated by a finite volume method.

In Chapter 5, the flow in a micro-bioreactor, which consists of an enclosed cylinder with a partially rotating bottom-wall, is simulated by using the numerical method developed in Chapter 2. The effects of vortex breakdown on shear stress and oxygen transport in the bioreactor are also studied.

In Chapter 6, the flow and oxygen transport in the micro-bioreactor with a scaffold is investigated by the numerical method developed in Chapter 2.

In Chapter 7, a summary of the most important conclusions is presented. The recommendations for future research work are also proposed.

Chapter 2

A Numerical Method for Coupled Flow in Porous and Homogenous Fluid Regions*

In the present chapter, a finite volume code based on nonorthogonal body-fitted and multi-block grids will be developed to simulate the coupled flow and mass transport problems in the homogenous flow and porous medium regions. For such problems, commercial software such as FLUENT only provides a rather simple model for porous flow and a simple interfacial boundary condition to couple the flows in the homogenous flow and porous medium regions. The present code provides a flexible platform to implement complex interfacial boundary conditions and new porous models. The finite volume method is chosen because it has been well developed and has relatively high computational efficiency. The use of multi-block technique is for convenience because the structured grid is applied.

In the remainder of this chapter, the mathematical equations governing the fluid flow and mass transport in the homogenous flow and porous medium regions for Cartesian coordinates are described, followed by the discretization procedures of the governing equations. The SIMPLEC algorithm is used to couple the velocity and pressure. Special attention is given to the treatment of the interface between the homogenous flow and porous medium regions. The strongly implicit procedure (SIP) is applied to solve the resultant algebraic equation system. Finally, the present code will be extended to simulate the axisymmetric flows in cylindrical coordinates.

*Parts of this chapter have been published in Int. J. Numer. Methods Fluids (Yu et al., 2007a)

2.1 Governing Equations in Cartesian Coordinate

2.1.1 Homogenous Fluid Region

For the two-dimensional, incompressible, steady, and viscous flow, the governing equations with primitive variables are:

$$\frac{\partial u}{\partial x}+\frac{\partial v}{\partial y}=0 \tag{2.1}$$

$$\rho u\frac{\partial u}{\partial x}+\rho v\frac{\partial u}{\partial y}=-\frac{\partial p}{\partial x}+\mu\nabla^2 u+\rho S_x \tag{2.2}$$

$$\rho u\frac{\partial v}{\partial x}+\rho v\frac{\partial v}{\partial y}=-\frac{\partial p}{\partial y}+\mu\nabla^2 v+\rho S_y \tag{2.3}$$

where u and v are velocity components in x and y direction respectively; p the pressure; ρ the fluid density; μ the fluid dynamic viscosity; S_x and S_y are the source terms in x and y direction respectively.

The equation describing conservation of a scalar quantity, φ, is analogous to the Navier-Stokes equations and can be written as:

$$\rho u\frac{\partial \varphi}{\partial x}+\rho v\frac{\partial \varphi}{\partial y}=\Gamma_\varphi\nabla^2\varphi+\rho S_\varphi \tag{2.4}$$

where Γ_φ is the diffusivity for the quantity φ; S_φ the source term for the quantity φ. The examples of the scalar equation are the energy equation and species concentration equations. Equation (2.4) can be regarded as a general form of the governing equations. In the discretization section, the analysis will be carried out from the general conservation equation (Equation 2.4).

2.1.2 Porous Medium Region

The porous medium is considered to be rigid, homogeneous and isotropic; and saturated with the same single-phase fluid as that in the homogenous fluid region. In order to include all the non-Darcy effects, the governing equations for porous region based on a generalized model including both Brinkman and Forchheimer terms as well as the non-linear advection term (Hsu and Cheng, 1990; Gartling et al., 1996; Nithiarasu et al., 2002) can be written as:

$$\frac{\partial u}{\partial x}+\frac{\partial v}{\partial y}=0 \tag{2.5}$$

$$\frac{\rho u}{\varepsilon}\frac{\partial u}{\partial x}+\frac{\rho v}{\varepsilon}\frac{\partial u}{\partial y}=-\frac{\partial\left(\varepsilon p^{*}\right)}{\partial x}+\mu\nabla^{2}u-\frac{\mu\varepsilon}{K}u-\frac{\rho\varepsilon C_{F}\sqrt{u^{2}+v^{2}}}{\sqrt{K}}u \tag{2.6}$$

$$\frac{\rho u}{\varepsilon}\frac{\partial v}{\partial x}+\frac{\rho v}{\varepsilon}\frac{\partial v}{\partial y}=-\frac{\partial\left(\varepsilon p^{*}\right)}{\partial y}+\mu\nabla^{2}v-\frac{\mu\varepsilon}{K}v-\frac{\rho\varepsilon C_{F}\sqrt{u^{2}+v^{2}}}{\sqrt{K}}v \tag{2.7}$$

where u and v are the local average velocity components (Darcy velocity components) in x and y direction respectively; p^{*} the intrinsic average pressure; μ the fluid viscosity; ε the porosity; K the permeability; and C_F the Forchheimer coefficient. The superscript "*" denotes the intrinsic average. The local average and intrinsic average can be linked by the Dupuit-Forchheimer relationship, for example, $u=\varepsilon u^{*}$.

The equation describing conservation of a scalar quantity, φ, in the porous medium also can be written as:

$$\rho u\frac{\partial\varphi}{\partial x}+\rho v\frac{\partial\varphi}{\partial y}=\Gamma_{p}\nabla^{2}\varphi+\rho S_{\varphi_{p}} \tag{2.8}$$

where Γ_p and S_{φ_p} are the diffusivity and the source term for the quantity φ in the porous medium respectively.

2.1.3 Interface Conditions

At the interface between homogeneous fluid and porous medium, additional boundary conditions must be applied to couple the flows in the two regions. In the present study, the stress jump condition (Ochoa-Tapia and Whitaker, 1998) is applied:

$$\frac{\mu}{\varepsilon}\frac{\partial u_t}{\partial n}\bigg|_{\text{porous}} - \mu\frac{\partial u_t}{\partial n}\bigg|_{\text{fluid}} = \beta\frac{\mu}{\sqrt{K}}u_t\bigg|_{\text{interface}} + \beta_1\rho u_t^2 \tag{2.9}$$

where in the porous medium region, u_t is the Darcy velocity component parallel to the interface aligned with the direction t and normal to the direction n while in the homogenous fluid region u_t is the fluid velocity component parallel to the interface; β and β_1 are adjustable parameters which account for the stress jump at the interface.

Ochoa-Tapia and Whitaker (1998) derived analytical expressions for parameters β and β_1 which indicate their dependence on permeability and porosity. They concluded that these two parameters are both of order one. Ochoa-Tapia and Whitaker (1995b) experimentally determined that β varies from +0.7 to -1.0 for different materials with permeability varying from 15×10^{-6} to 127×10^{-6} in^2 and average pore size from 0.016 to 0.045 in. There is presently no experimental data for β_1. It is not known how much the two parameters may change from one type of interface to another; and it is assumed in this study that the changes should be in the same range as those for different types of materials. Thus, for the purpose of demonstrating the implementation of the present formulation, both β and β_1 are varied in the range -0.7 to +0.7 in the present study.

In addition to Equation (2.9), the continuities of velocity and normal-stress prevailing at the interface are given by:

$$u\big|_{\text{fluid}} = u\big|_{\text{porous}} = u_{\text{interface}} \tag{2.10}$$

$$v\big|_{\text{fluid}} = v\big|_{\text{porous}} = v_{\text{interface}} \tag{2.11}$$

$$\frac{\mu}{\varepsilon}\frac{\partial u_n}{\partial n}\bigg|_{\text{porous}} - \mu\frac{\partial u_n}{\partial n}\bigg|_{\text{fluid}} = 0 \tag{2.12}$$

where in the porous medium region, u_n is the Darcy velocity component normal to the interface; and in the homogenous fluid region, u_n is the fluid velocity component normal to the interface. By combining with the other appropriate conditions at the boundary of the composite region, the governing equations associated the Equations (2.9) to (2.12) can be used to simulate the flow in a system composed of a porous medium and a homogenous fluid.

2.2 Discretization Procedures

2.2.1 Homogenous Fluid Region

A typical control volume is shown in Figure 2.1. For a general dependent variable φ, a final discrete-form over the control volume can be written as:

$$F_e + F_w + F_n + F_s = Q_\varphi \tag{2.13}$$

where F_e, F_w, F_n and F_s are the overall fluxes (including both convection and diffusion) of φ at faces *e*, *w*, *n*, *s*, which denote *east*, *west*, *north*, and *south* of the control volume, and Q_φ the volume integral of the source term. The detailed numerical methodology for obtaining the convective flux (F_e^c, F_w^c, F_n^c, and F_s^c), diffusive flux (F_e^d, F_w^d, F_n^d, and F_s^d), and Q_φ can be found elsewhere (Ferziger and Perić, 1999).

With the midpoint rule (mean theorem) approximation, the convective flux at face *east* can be calculated as:

$$F_e^c = \int_{S_e} \rho\varphi\vec{u}\cdot\vec{n}dS \approx m_e\varphi_e \tag{2.14}$$

where m_e is the mass flux cross the surface e; S_e is the surface area of face e; and φ_e is the value of φ at the center of the cell face. m_e and S_e can be calculated as:

$$m_e = \rho_e\left(S^x u + S^y v\right)_e \tag{2.15}$$

$$S_e = \sqrt{\left(S_e^x\right)^2 + \left(S_e^y\right)^2} \tag{2.16}$$

Where u and v are the velocity components in the x and y directions; S^x and S^y are the surface vector components.

To avoid the non-orthogonal effect, the midpoint rule with the deferred correction term (Muzaferija, 1994) applied to the integrated diffusive flux is given by:

$$F_e^d = \mu_e\left(\frac{\partial\varphi}{\partial \mathrm{n}}\right)_e S_e = \mu_e S_e\left(\frac{\partial\varphi}{\partial\xi}\right)_e + \mu_e S_e\left[\overline{\left(\frac{\partial\varphi}{\partial \mathrm{n}}\right)_e} - \overline{\left(\frac{\partial\varphi}{\partial\xi}\right)_e}\right]^{old} \tag{2.17}$$

An implicit flux approximation of the term $\left(\frac{\partial\varphi}{\partial\xi}\right)_e$ is applied:

$$\left(\frac{\partial\varphi}{\partial\xi}\right)_e = \frac{\varphi_E - \varphi_P}{L_{PE}} \tag{2.18}$$

where L_{PE} stands for the distance between P and E. The deferred correction terms can be obtained as:

$$\overline{\left(\frac{\partial\varphi}{\partial \mathrm{n}}\right)_e} = \overline{\left(grad\varphi\right)_e}\cdot\vec{n};\quad \overline{\left(\frac{\partial\varphi}{\partial\xi}\right)_e} = \overline{\left(grad\varphi\right)_e}\cdot\vec{i}_\xi \tag{2.19}$$

where $\vec{i}_\xi$ is the unit vector in the ξ-direction. The final expression of Equation (2.17) then becomes:

$$F_e^d = \mu_e S_e\left(\varphi_E - \varphi_P\right)/L_{PE} + \mu_e S_e\overline{\left(grad\varphi\right)_e}^{old}\cdot\left(\vec{n} - \vec{i}_\xi\right) \tag{2.20}$$

The different methods to approximate the value of φ and its derivative at the cell face result in different interpolation schemes. In the present study, the central

difference scheme (CDS) is used. Then the cell-face values of the variables are approximated as:

$$\varphi_e \approx \varphi_{e'} = \lambda_e \varphi_E + (1-\lambda_e)\varphi_P \quad \text{for face } e \tag{2.21}$$

where the interpolation factor λ_e is defined as:

$$\lambda_e = \frac{|\vec{r}_e - \vec{r}_P|}{|\vec{r}_e - \vec{r}_P| + |\vec{r}_E - \vec{r}_e|} \tag{2.22}$$

and $\vec{r}_e$ is the position vector.

Equation (2.21) is a second order approximation at the location e' on the straight line connecting nodes P and E. If the cell-face center e does not coincide with the location e', a correction term must be added in Equation (2.21) to restore the second-order accuracy, which can be expressed as follows:

$$\varphi_e \approx \varphi_{e'} + (grad\varphi)_{e'} \cdot (\vec{r}_e - \vec{r}_{e'}) \tag{2.23}$$

To obtain the deferred derivatives at the cell face, they are calculated first at the control volume centers and then interpolated to the cell faces. By using the Gauss' theorem, the derivative at the CV centers can be approximated by the average value over the cell:

$$\left(\frac{\partial\varphi}{\partial x_i}\right)_P \approx \frac{\int_\Omega \frac{\partial\varphi}{\partial x_i} d\Omega}{\Delta\Omega} = \int_S \varphi \vec{i}_i \cdot \vec{n} dS \approx \sum_c \varphi_c S_c^i, \quad c = e, n, w, s \tag{2.24}$$

Then the cell-center derivatives can also be interpolated to the cell-face centers using the same interpolation as that described by Equations (2.21) to (2.23). It is noted that the derivative at the cell-face center can be directly evaluated by using Gauss theorem if a new control volume whose center is located at the original cell-face center is defined.

For the volume integral of the source term, it can be obtain from the product of the CV center value of the integrand and the CV volume:

$$Q_\varphi = \int_\Omega S_\varphi d\Omega \approx S_\varphi \Delta\Omega \tag{2.25}$$

where Ω is the cell volume.

Finally, in a typical control volume, the discretized generic conservation equations have the following form:

$$A_P^\varphi \varphi_P + \sum_l A_l^\varphi \varphi_l = Q_{\varphi,P} \tag{2.26}$$

where *P* is the index of an arbitrary node; the index *l* denotes the four neighbor points *E*, *W*, *S*, *N*; and the coefficients A_P^φ, A_E^φ, A_W^φ, A_N^φ, A_S^φ are those of the resultant algebraic equations.

The momentum equations contain a contribution from the pressure. The volume integral of the pressure gradient term in *u*-momentum equation can be obtained by:

$$Q_{u,P}^p = \int_\Omega -\left(\frac{\partial p}{\partial x}\right)_P d\Omega \approx -\left(\frac{\delta p}{\delta x}\right)_P \Delta\Omega \tag{2.27}$$

The final discretized form of the *u*-momentum equation is:

$$A_P^u u_P + \sum_l A_l^u u_l = Q_{u,P}^* - \left(\frac{\delta p}{\delta x}\right)_P \Delta\Omega \tag{2.28}$$

where $Q_{u,P}^*$ is the integral of the source term contributed by other forces. By using the Gauss' theorem, the mean pressure gradient over the control volume is:

$$\left(\frac{\delta p}{\delta x}\right)_P \approx \frac{\int_\Omega \frac{\partial p}{\partial x} d\Omega}{\Delta\Omega} = \int_S p\vec{i}_i \cdot \vec{n} dS \approx \sum_c p_c S_c^i, \quad c = e,n,w,s \tag{2.29}$$

In the present study, SIMPLEC method (van Doormal and Raithby, 1984) is applied to couple the velocity and pressure. To avoid oscillations in the pressure or

velocity, the interpolation proposed by Rhie and Chow (1983) is adopted:

$$u_e^m = \overline{\left(u^m\right)}_e - \Delta\Omega_e \overline{\left(\frac{1}{A_P^u + \sum_l A_l^u}\right)}_e \left[\left(\frac{\delta p}{\delta x}\right)_e - \overline{\left(\frac{\delta p}{\delta x}\right)}_e\right]^{m-1} \tag{2.30}$$

2.2.2 Porous Medium Region

Equations (2.6) and (2.7) recover the standard Navier-Stokes equations when the porosity approaches unity. Thus, the discretizing procedure for porous medium is similar to that for the homogenous fluid as the two sets of governing equations are similar in form. The discretized diffusion flux is similar in form to Equation (2.17). The convective flux at a cell face is similar in form to Equation (2.14) except for a small change:

$$F_e^c = \int_{S_e} \frac{\rho u}{\varepsilon} \vec{u} \cdot \vec{n} dS \approx \frac{m_e}{\varepsilon_e} u_e \tag{2.31}$$

The volume integral of the pressure gradient term (similar in form to Equation 2.27) is:

$$Q_{u,P}^{p*} = \int_\Omega -\left(\frac{\partial\left(\varepsilon p^*\right)}{\partial x}\right)_P d\Omega \approx -\left(\varepsilon \frac{\delta p}{\delta x}\right)_P \Delta\Omega \tag{2.32}$$

For the Darcy term in Equation (2.6), the volume integral gives:

$$Q_D^u = \int_\Omega -\left(\frac{\mu\varepsilon}{K} u\right)_p d\Omega = -\left(\frac{\mu\varepsilon}{K}\right)_p \Delta\Omega \cdot u_p \tag{2.33}$$

For the Forchheimer term, the volume integral is given by:

$$Q_F^u = \int_\Omega -\left(\frac{\rho\varepsilon C_F \sqrt{u^2+v^2}}{\sqrt{K}} u\right)_p d\Omega = -\left(\frac{\rho\varepsilon C_F \sqrt{u^2+v^2}}{\sqrt{K}}\right)_p \Delta\Omega \cdot u_p \tag{2.34}$$

It is convenient to treat the Darcy and Forchheimer terms as source terms.

However, Equations (2.33) and (2.34) indicate that, after integrating, both terms become a product of Darcy velocity component and a coefficient. The two coefficients can be added into the coefficients of the algebraic equation A_p^u, which will accelerate the convergence rate.

The procedure to obtain the pressure correction equation is also similar to that for homogenous fluid (Equation 2.30), except for a small change:

$$u_e^m = \overline{\left(u^m\right)}_e - \Delta\Omega_e \overline{\left(\frac{1}{A_P^u + \sum_l A_l^u}\right)}_e \left[\left(\frac{\delta\left(\varepsilon p^*\right)}{\delta x}\right)_e - \overline{\left(\frac{\delta\left(\varepsilon p^*\right)}{\delta x}\right)}_e\right]^{m-1} \tag{2.35}$$

2.2.3 Interface Treatment

In some cases, structured grids are difficult, even impossible, to construct for complex geometries. Therefore, in the present study, multi-block grids method is applied to provide a compromise between the simplicity and wide variety of solvers available for structured grids and ability to handle complex geometries that unstructured grids allow.

Figure 2.2 shows details of the interface between two different blocks. Two neighboring control volumes, lying in Block A and Block B respectively, share the interface. The grids in two neighboring blocks match at the interface. Generally, there are three types of interfaces when the block-structured grids method is employed to calculate the flow in the composite region: fluid - fluid interface, porous medium - porous medium interface, and fluid - porous medium interface.

2.2.3.1 Interface between the Same Medium

In this case, both blocks A and B (Figure 2.2) represent the same medium, either fluid or porous. The method proposed by Lilek et al. (1997) is applied to treat the block interface. A special data structure is designed to save the information at the interface, which consists of: the indices of the left (*L*) and right (*R*) neighboring cells, the surface vector (pointing from *L* to *R*) and the coordinates of cell-surface center (Figure 2.2). The interface cell surface shared by two CVs is treated as a cell surface in the interior of the block. Thus, the convective and diffusive terms at the block interface can be calculated in the same way as that for the cell faces in the interior of the block (Section 2.2.1). Then the contributions from the interface cell faces, namely A_L and A_R, can be obtained.

Each interface cell face contributes to the source terms for the neighboring CVs. Thus, if the east side of a CV is a block interface, the coefficient A_E (Equation 2.28) is set to zero. However, the algebraic equation at node L receives the contribution $A_R\varphi_R$, while at node R, the contribution is $A_L\varphi_L$.

2.2.3.2 Interface between Fluid and Porous Media

In this case, blocks A and B (Figure 2.2) represent fluid and porous medium respectively. The velocity vector at the interface is given by $\vec{v}_{\text{interface}}$. It can be written in either the *x*-*y* or *n*-*t* coordinate systems as:

$$\vec{v}_{\text{interface}} = u\vec{e}_x + v\vec{e}_y = u_n\vec{n} + u_t\vec{t} \tag{2.36}$$

where u and v are the components of $\vec{v}_{\text{interface}}$ in the x and y directions while

u_n and u_t are the $\vec{v}_{\text{interface}}$ components along *n* and *t* directions respectively. And the component u_t then can be written as:

$$u_t = u\vec{e}_x \cdot \vec{t} + v\vec{e}_y \cdot \vec{t} \tag{2.37}$$

By combining Equations (2.9), (2.12) and (2.36):

$$\frac{\mu}{\varepsilon}\frac{\partial \vec{v}_{\text{interface}}}{\partial n}\bigg|_{\text{porous}} - \mu\frac{\partial \vec{v}_{\text{interface}}}{\partial n}\bigg|_{\text{fluid}} = \beta\frac{\mu}{\sqrt{K}}u_t\vec{t} + \beta_1\rho u_t^2\vec{t} \tag{2.38}$$

The unit vector ($\vec{t}$) parallel to the interface (Figure 2.2) is calculated from:

$$\vec{t} = \frac{\left(x_{ne}-x_{se}\right)\vec{e}_x + \left(y_{ne}-y_{se}\right)\vec{e}_y}{\sqrt{\left(x_{ne}-x_{se}\right)^2 + \left(y_{ne}-y_{se}\right)^2}} = \frac{\Delta x_e\vec{e}_x + \Delta y_e\vec{e}_y}{l_e} \tag{2.39}$$

By substituting the components of $\vec{v}_{\text{interface}}$ in the *x* and *y* directions, the Equation (2.38) becomes:

$$\frac{\mu}{\varepsilon}\frac{\partial u}{\partial n}\bigg|_{\text{porous}} - \mu\frac{\partial u}{\partial n}\bigg|_{\text{fluid}} = \beta\frac{\mu}{\sqrt{K}}\frac{u\Delta x_e\Delta x_e + v\Delta y_e\Delta x_e}{l_e^2} + \beta_1\rho\frac{\Delta x_e\left(u\Delta x_e + v\Delta y_e\right)^2}{l_e^3} \tag{2.40}$$

$$\frac{\mu}{\varepsilon}\frac{\partial v}{\partial n}\bigg|_{\text{porous}} - \mu\frac{\partial v}{\partial n}\bigg|_{\text{fluid}} = \beta\frac{\mu}{\sqrt{K}}\frac{u\Delta x_e\Delta y_e + v\Delta y_e\Delta y_e}{l_e^2} + \beta_1\rho\frac{\Delta y_e\left(u\Delta x_e + v\Delta y_e\right)^2}{l_e^3} \tag{2.41}$$

The derivatives at the interface are calculated from the values at auxiliary nodes L' and R'; these nodes lie at the intersection of the cell face normal *n* and straight lines connecting nodes *L* and *N* or *R* and *NR*, respectively, as shown in Figure 2.2. The normal gradients at the interface are calculated as:

$$\frac{\partial u}{\partial n}\bigg|_{\text{porous}} = \frac{u|_{R'} - u|_e}{L_{eR'}},\quad \frac{\partial v}{\partial n}\bigg|_{\text{porous}} = \frac{v|_{R'} - v|_e}{L_{eR'}} \tag{2.42}$$

$$\frac{\partial v}{\partial n}\bigg|_{\text{fluid}} = \frac{v|_e - v|_{L'}}{L_{L'e}},\quad \frac{\partial v}{\partial n}\bigg|_{\text{fluid}} = \frac{v|_e - v|_{L'}}{L_{L'e}} \tag{2.43}$$

The Cartesian velocity components at L' and R' can be calculated by using bilinear interpolation or by using the gradient at the control volume center:

$$u\big|_{L'} = u\big|_{L} + \left(gradu\right)_{L} \cdot \overrightarrow{L'L} \tag{2.44}$$

To obtain higher order approximation of the derivatives, the velocity components at more auxiliary nodes may be needed. Alternatively, the shape functions may be used, which produces a kind of combined Finite Element/Finite Volume method for calculating the higher order approximations.

By using Equations (2.40) to (2.44) and explicitly calculating the terms at the right hand sides of Equations (2.40) and (2.41), the Cartesian velocity components u and v at the interface are obtained. Then the convective fluxes at the interface can be calculated. The diffusive fluxes are calculated from Equations (2.42) to (2.43). Then the coefficients A_L and A_R can be obtained.

To close the algebra equation system, the pressure at the interface must be determined. However, the pressure gradient at the interface may not be continuous due to the rather large Darcy and Forchheimer terms (Equations 2.6 and 2.7), which may result in a rapid pressure drop at the porous side (Betchen et al., 2006). This discontinuity of the pressure gradient becomes more severe at higher *Re* and lower *Dar*. Thus it requires special treatment to estimate the interface pressure from that of the vicinity at either side. A simplistic pressure estimation may give unrealistic, oscillatory velocity profile. The coupling issue of pressure-velocity at the interface was described in a recent paper by Betchen et al. (2006) who proposed a solution that enables stable calculations. The pressure is extrapolated in the fluid side to a location at a small distance near the interface. From this location, a momentum balance is then used to estimate the interface pressure. This estimate is then averaged with the

pressure extrapolated from the porous side to obtain the interface pressure. In the present study, a less complex treatment was adopted. Extrapolations from the fluid and porous sides give two different estimates of the interface pressure. The average of the two estimates is used as the interface pressure.

2.3 Solution Algorithm

The SIMPLEC algorithm based on Multi-block grids and a SIP solver is described as follows:

1. Estimate the initial flow and pressure fields in each block.
2. Assemble the elements of matrix A and the source term Q in each block, ignoring the contributions of the block interfaces.
3. Loop over the list of interface cell faces, updating A_P and Q_P at nodes L and R, and calculate the matrix elements stored at the cell face, A_L and A_R.
4. Assemble and solve the momentum equations to obtain u^{m*} and v^{m*}; then assemble and solve the pressure-correction equation to obtain p': Calculate the residuals in each block using the regular part of the matrix A. Loop over the list of interface cell faces and update the residuals at nodes L and R by adding the products of $A_R\varphi_R$ and $A_L\varphi_L$, where φ denotes u, v or p'.
5. Correct the velocities and pressure to obtain the velocities u^m and v^m, which satisfy the continuity equation, and the new pressure p^m in each blocks.
6. Return to step 2 and repeat, using u^m, v^m and p^m as improved estimates for the next iteration, until all corrections are negligibly small.

2.4 Extension to Axisymmetric flows

Axisymmetric flows are three-dimensional with respect to Cartesian coordinates but they are only two-dimensional in a cylindrical coordinate system since all derivatives with respect to the azimuthal direction are zero and all three velocity components are functions of only the axial and radial coordinates.

2.4.1 Governing Equations

For the incompressible, steady, viscous, and axisymmetric flow, the governing equations in a cylindrical coordinate system can be written as:

$$\frac{1}{r}\frac{\partial\left(rv_r\right)}{\partial r}+\frac{\partial v_z}{\partial z}=0 \tag{2.45}$$

$$\frac{1}{r}\frac{\partial\left(rv_rv_z\right)}{\partial r}+\frac{\partial\left(v_zv_z\right)}{\partial z}=-\frac{1}{\rho}\frac{\partial p}{\partial z}+\nu\left[\frac{1}{r}\frac{\partial}{\partial r}\left(r\frac{\partial v_z}{\partial r}\right)+\frac{\partial^2 v_z}{\partial z^2}\right]+S_z \tag{2.46}$$

$$\frac{1}{r}\frac{\partial\left(rv_rv_r\right)}{\partial r}+\frac{\partial\left(v_zv_r\right)}{\partial z}=-\frac{1}{\rho}\frac{\partial p}{\partial r}+\nu\left[\frac{\partial}{\partial r}\left(\frac{1}{r}\frac{\partial}{\partial r}\left(rv_r\right)\right)+\frac{\partial^2 v_r}{\partial z^2}\right]+\frac{v_\theta^2}{r}+S_r \tag{2.47}$$

$$\frac{1}{r}\frac{\partial\left(rv_rv_\theta\right)}{\partial r}+\frac{\partial\left(v_zv_\theta\right)}{\partial z}=\nu\left[\frac{\partial}{\partial r}\left(\frac{1}{r}\frac{\partial}{\partial r}\left(rv_\theta\right)\right)+\frac{\partial^2 v_\theta}{\partial z^2}\right]-\frac{v_rv_\theta}{r}+S_\theta \tag{2.48}$$

where v_z, v_r, and v_θ are the velocity components in z, r, and θ directions respectively and S_z, S_r, and S_θ are the source terms in z, r, and θ directions respectively.

For the porous medium region:

$$\frac{1}{r}\frac{\partial\left(rv_r\right)}{\partial r}+\frac{\partial v_z}{\partial z}=0 \tag{2.49}$$

$$\frac{1}{r}\frac{\partial}{\partial r}\left(\frac{rv_rv_z}{\varepsilon}\right)+\frac{\partial}{\partial z}\left(\frac{v_zv_z}{\varepsilon}\right)=-\frac{1}{\rho}\frac{\partial\left(\varepsilon p^*\right)}{\partial z}+\nu\left[\frac{1}{r}\frac{\partial}{\partial r}\left(r\frac{\partial v_z}{\partial r}\right)+\frac{\partial^2 v_z}{\partial z^2}\right]$$

$$-\frac{\nu\varepsilon}{K}v_z-\frac{\varepsilon C_F\sqrt{v_z^{\,2}+v_r^{\,2}+v_\theta^{\,2}}}{\sqrt{K}}v_z \tag{2.50}$$

$$\frac{1}{r}\frac{\partial}{\partial r}\left(\frac{rv_rv_r}{\varepsilon}\right)+\frac{\partial}{\partial z}\left(\frac{v_zv_r}{\varepsilon}\right)=-\frac{1}{\rho}\frac{\partial\left(\varepsilon p^*\right)}{\partial r}+\nu\left[\frac{\partial}{\partial r}\left(\frac{1}{r}\frac{\partial}{\partial r}\left(rv_r\right)\right)+\frac{\partial^2 v_r}{\partial z^2}\right]+\frac{\varepsilon v_\theta^2}{r}$$

$$-\frac{\nu\varepsilon}{K}v_r-\frac{\varepsilon C_F\sqrt{v_z^{\,2}+v_r^{\,2}+v_\theta^{\,2}}}{\sqrt{K}}v_r \tag{2.51}$$

$$\frac{1}{r}\frac{\partial}{\partial r}\left(\frac{rv_rv_\theta}{\varepsilon}\right)+\frac{\partial}{\partial z}\left(\frac{v_zv_\theta}{\varepsilon}\right)=\nu\left[\frac{\partial}{\partial r}\left(\frac{1}{r}\frac{\partial}{\partial r}\left(rv_\theta\right)\right)+\frac{\partial^2 v_\theta}{\partial z^2}\right]-\frac{\varepsilon v_rv_\theta}{r}$$

$$-\frac{\nu\varepsilon}{K}v_\theta-\frac{\varepsilon C_F\sqrt{v_z^{\,2}+v_r^{\,2}+v_\theta^{\,2}}}{\sqrt{K}}v_\theta \tag{2.52}$$

where v_z, v_r, and v_θ are the Darcy velocity components in z, r, and θ directions respectively; p^* the intrinsic average pressure; and ν the fluid kinematic viscosity.

Equations (2.45) to (2.47) and Equations (2.49) to (2.51) are similar in form to those in Cartesian coordinates except for the addition force terms, v_θ^2/r and $\varepsilon v_\theta^2/r$ in the v_r-equations (Equations 2.47 and 2.51), which represent the apparent centrifugal forces. Equations (2.48) and (2.52) are similar to the generic conservation equations (Equations 2.4 and 2.8) except for the addition force terms, v_rv_θ/r and $\varepsilon v_rv_\theta/r$, which represent the apparent Coriolis forces. These force terms arise from the coordinate transformation. If the swirl velocity v_θ is zero, the apparent forces are zero and the Equations (2.48) and (2.52) become redundant.

It is noted that for the axisymmetric flow problems, the governing equations at $r = 0$ are singular. Thus, suitable boundary conditions are needed at $r = 0$. In the present study, the first derivatives of the three velocity components are set to zero there.

2.4.2 Interface Condition

The interface conditions are the same as those in Cartesian coordinate. The continuities of velocity components at the interface are given by:

$$v_r\big|_{\text{fluid}} = v_r\big|_{\text{porous}} = v_r\big|_{\text{interface}} \tag{2.53}$$

$$v_z\big|_{\text{fluid}} = v_z\big|_{\text{porous}} = v_z\big|_{\text{interface}} \tag{2.54}$$

$$v_\theta\big|_{\text{fluid}} = v_\theta\big|_{\text{porous}} = v_\theta\big|_{\text{interface}} \tag{2.55}$$

The shear-jump condition can be expressed as:

$$\frac{\mu}{\varepsilon}\frac{\partial v_t}{\partial n}\bigg|_{\text{porous}} - \mu\frac{\partial v_t}{\partial n}\bigg|_{\text{fluid}} = \beta\frac{\mu}{\sqrt{K}}v_t\bigg|_{\text{interface}} + \beta_1\rho v_t^2\big|_{\text{interface}} \tag{2.56}$$

where n is the unit vector normal to the interface, v_t is the velocity component parallel to the interface. The continuity of the normal stress can be written as:

$$\frac{\mu}{\varepsilon}\frac{\partial v_n}{\partial n}\bigg|_{\text{porous}} - \mu\frac{\partial v_n}{\partial n}\bigg|_{\text{fluid}} = 0 \tag{2.57}$$

where v_n is the velocity component perpendicular to the interface. And the velocity vector at the interface can be written as:

$$\vec{v}_{\text{interface}} = v_r\vec{e}_r + v_z\vec{e}_z + v_\theta\vec{e}_\theta = v_n\vec{n} + v_t\vec{t} \tag{2.58}$$

The component v_t then can be written as:

$$v_t = \left(v_r\vec{e}_r + v_z\vec{e}_z + v_\theta\vec{e}_\theta\right)\cdot\vec{t} \tag{2.59}$$

By combining Equations (2.56) to (2.58):

$$\frac{\mu}{\varepsilon}\frac{\partial\vec{v}_{\text{interface}}}{\partial n}\bigg|_{\text{porous}} - \mu\frac{\partial\vec{v}_{\text{interface}}}{\partial n}\bigg|_{\text{fluid}} = \beta\frac{\mu}{\sqrt{K}}v_t\vec{t} + \beta_1\rho v_t^2\vec{t} \tag{2.60}$$

As the flow is axisymmetric, the unit vector ($\vec{t}$) parallel to the interface is calculated from:

$$\vec{t} = \frac{\left(\frac{v_r \Delta r + v_z \Delta z}{l}\right)\left(\frac{\Delta r \vec{e}_r + \Delta z \vec{e}_z}{l}\right) + v_\theta \vec{e}_\theta}{\sqrt{\left(\frac{v_r \Delta r + v_z \Delta z}{l}\right)^2 + v_\theta^2}} \tag{2.61}$$

By substituting the components of $\vec{v}_{\text{interface}}$ in z, r, and θ directions, Equation (2.60) can be rewritten as:

$$\frac{\mu}{\varepsilon}\frac{\partial v_z}{\partial n}\bigg|_{\text{porous}} - \mu\frac{\partial v_z}{\partial n}\bigg|_{\text{fluid}} = \beta\frac{\mu}{\sqrt{K}}\frac{v_z \Delta z \Delta z + v_r \Delta r \Delta z}{l^2} + \beta_1 \rho \frac{v_z \Delta z \Delta z + v_r \Delta r \Delta z}{l^2}\sqrt{\left(\frac{v_r \Delta r + v_z \Delta z}{l}\right)^2 + v_\theta^2} \tag{2.62}$$

$$\frac{\mu}{\varepsilon}\frac{\partial v_r}{\partial n}\bigg|_{\text{porous}} - \mu\frac{\partial v_r}{\partial n}\bigg|_{\text{fluid}} = \beta\frac{\mu}{\sqrt{K}}\frac{v_z \Delta z \Delta r + v_r \Delta r \Delta r}{l^2} + \beta_1 \rho \frac{v_z \Delta z \Delta r + v_r \Delta r \Delta r}{l^2}\sqrt{\left(\frac{v_r \Delta r + v_z \Delta z}{l}\right)^2 + v_\theta^2} \tag{2.63}$$

$$\frac{\mu}{\varepsilon}\frac{\partial v_\theta}{\partial n}\bigg|_{\text{porous}} - \mu\frac{\partial v_\theta}{\partial n}\bigg|_{\text{fluid}} = \beta\frac{\mu}{\sqrt{K}} v_\theta + \beta_1 \rho v_\theta \sqrt{\left(\frac{v_r \Delta r + v_z \Delta z}{l}\right)^2 + v_\theta^2} \tag{2.64}$$

The discretization procedures of the velocity components v_z and v_r at the interface are the same as those in Cartesian coordinate. The derivatives of v_θ at the interface is also calculated from the values at auxiliary nodes L' and R'; these nodes lie at the intersection of the cell face normal n and straight lines connecting nodes *L* and *N* or *R* and *NR*, respectively. The normal gradients of v_θ at the interface can be calculated by using the first order difference approximation:

$$\frac{\partial v_\theta}{\partial n}\bigg|_{\text{porous}} = \frac{v_\theta|_{R'} - v_\theta|_e}{L_{eR'}} \quad \text{and} \quad \frac{\partial v_\theta}{\partial n}\bigg|_{\text{fluid}} = \frac{v_\theta|_e - v_\theta|_{L'}}{L_{L'e}} \tag{2.65}$$

The values of v_θ at L' and R' can be calculated by using bilinear interpolation or by using the gradient at the control volume center:

$$v_\theta|_{P'} = v_{\theta p} + \left(grad v_\theta\right)_P \cdot \overrightarrow{L'L} \tag{2.66}$$

By making use of Equations (2.64) to (2.66), the values of v_θ at the interface are obtained. Then the convective fluxes at the interface can be calculated. The diffusive fluxes are calculated from Equations (2.65) and (2.66). Once the overall fluxes at interface are obtained, the equations for v_θ can be solved.

2.4.3 Solution Procedures

Besides the additional force terms, the difference compared to flow problems in Cartesian coordinates is the calculation of cell face areas and volumes. The areas of cell faces *n*, *e*, *w* and *s* must multiply a factor of r_c (where *c* denotes the cell face center) compared to those in Cartesian coordinates. The formulation for the volume calculation becomes:

$$\Delta\Omega = \frac{1}{6}\sum_{i=1}^{4}\left(z_{i-1} - z_i\right)\left(r_{i-1}^2 + r_i^2 + r_i r_{i-1}\right) \tag{2.67}$$

where *i* denotes the number of vertices of the control volume, counterclockwise, with $i = 0$ corresponding to $i = 4$.

The discretization (CDS) and solution (SIMPLEC) procedures for the axisymmetric coupled flow problems in both the fluid and porous medium regions are similar to those in Cartesian coordinates. If the swirl velocity v_θ is zero, then the procedure is the same as that in Cartesian Coordinates. Otherwise, an addition step, which is applied to calculate v_θ, must be added in solution procedures, after the corrected velocities and pressure are obtained.

Chapter 3

Validation of Numerical Method*

In this chapter, the present numerical method is applied to some well-studied cases. First, the flow problems on the homogeneous fluid are investigated, which include: 1) lid driven flow in a square cavity; 2) flow around a circular cylinder; 3) natural convection in a square cavity; 4) fully developed flow in a circular pipe; and 5) swirling flow in an enclosed chamber. Secondly, the flow problems in the porous medium are considered, which include: 1) flow in a fluid-saturated porous-medium channel; and 2) natural convection in a fluid saturated porous-medium cavity. Finally, the coupled flows in porous and homogenous domains are studied, which include: 1) fully developed flow in a channel partially filled with a layer of a porous medium; 2) flow thorough a channel with a porous plug; and 3) flow around a porous square cylinder. The computed results are compared with published experimental or computational data in order to validate the accuracy of the present numerical method.

3.1 Flow in Homogeneous Fluid Region

3.1.1 Lid Driven Flow

The flow geometry is shown in Figure 3.1. The Reynolds number is defined as:

$$\mathrm{Re} = \frac{\rho U_{lid} L}{\mu} \tag{3.1}$$

Here the cavity problem is solved for *Re* = 400 and 1000. The numerical results obtained here are based on the mesh of 62 × 62 nodes. Figure 3.2 shows the

*Parts of this chapter have been published in Int. J. Numer. Methods Fluids (Yu et al., 2007a)

streamlines for *Re* = 400. The detailed comparisons of the present results and the numerical results presented by Ghia et al. (1982) are shown in Figure 3.3. The horizontal *U* velocity component on the vertical centerline of the cavity and the vertical *V* velocity component along the horizontal centerline of the cavity show very good agreement with the bench mark solution of Ghia et al. (1982).

3.1.2 Flow Around a Circular Cylinder

For this case, the Reynolds number is based on the free stream velocity U_∞ and the diameter of the cylinder *D*:

$$\mathrm{Re} = \frac{\rho U_\infty D}{\mu} \tag{3.2}$$

Figure 3.4 shows that the streamlines of flow past cylinder for *Re* = 20 and 40. The numerical results obtained here are based on the mesh of 162 × 162 nodes. At *Re* = 20, the flow separates from the rear of the cylinder and a pair of attached eddies are formed. As *Re* increases to 40, the eddies become elongated. The main closed-wake geometrical parameters, wake length and separation angle, have been calculated. The quantitative comparisons of the present geometrical parameters with the experimental data (Coutanceau and Bouard, 1977) are shown in Table 3.1. The wake length is expressed in units of *D*/2. From the table, it is seen that the results obtained by the present code agree well with experimental data, which indicate the present code is valid for the simulation of external flow problems.

3.1.3 Natural Convection in a Square Cavity

To validate whether the present code could solve the heat and mass transfer problems, the natural convection of air in a square cavity is simulated. The geometry and boundary conditions for the flow problem are shown in Figure 3.5. The fluid is considered as a Boussinesq fluid. The dimensionless governing equations are:

$$\frac{\partial u}{\partial x}+\frac{\partial v}{\partial y}=0 \tag{3.3}$$

$$\frac{\partial (uu)}{\partial x}+\frac{\partial (vu)}{\partial y}=-\frac{\partial p}{\partial x}+\mathrm{Pr}\nabla^2 u \tag{3.4}$$

$$\frac{\partial (uv)}{\partial x}+\frac{\partial (vv)}{\partial y}=-\frac{\partial p}{\partial y}+\mathrm{Pr}\nabla^2 v+\mathrm{Pr}\cdot Ra\cdot T \tag{3.5}$$

$$\frac{\partial (uT)}{\partial x}+\frac{\partial (vT)}{\partial y}=\nabla^2 T \tag{3.6}$$

where T is the dimensionless temperature, which is defined as:

$$T=(T'-T_L)/(T_H-T_L)=(T'-T_L)/\Delta T \tag{3.7}$$

where T' is the local temperature; T_H and T_L are the temperature of the hot wall and the cool wall respectively. The velocity components are non-dimensionalized by the velocity scale a/L, where a is the thermal diffusivity and L is the cavity width (or height). The pressure is non-dimensionalized by $\rho a^2/L^2$. Pr and Ra are the Prandtl number and the Rayleigh number respectively, which are defined as:

$$\mathrm{Pr}=\nu/a \tag{3.8}$$

$$Ra=\rho^2 g\beta_T L^3\Delta T/\mu^2 \tag{3.9}$$

where ν is the kinematic viscosity, g is the gravity constant, β_T is the expansion coefficient and other parameters have their usual meanings.

Three cases are tested at $Ra = 10^3$, 10^4 and 10^5 while Pr is kept constant at 0.71. The numerical results obtained here are based on the mesh of 122 × 122 nodes. The contours of the streamlines and temperature for different Ra are shown in Figure 3.6. The detailed comparisons of the present maximum U velocity component in the vertical central line and maximum V velocity component in the horizontal central line with the bench mark solutions (de Vahl Davis, 1983) are shown in Table 3.2.

The detailed comparisons of the average, maximum and minimum Nusselt numbers along the vertical lines are shown in Table 3.3. For the case of $Ra = 10^3$, the maximum U velocity components along vertical central line is 3.648 at $y = 0.813$, while the bench mark solution is 3.649 at $y = 0.813$. The average Nusselt number is 1.117, the maximum Nusselt number is 1.503 at $y = 0.092$, and the minimum Nusselt number is 0.691 at $y = 1.0$ along the vertical central line while the bench mark solutions give the average one of 1.117, the maximum one of 1.505 at $y = 0.092$, and the minimum one of 0.692 at $y = 1.0$. The good agreements with the bench mark solutions indicate that the present code is valid for the heat transfer problems.

3.1.4 Fully Developed Flow in a Circular Pipe

The geometry and boundary conditions for the flow problem are shown in Figure 3.7. As the flow is fully developed, Navier-Stokes equations can be simplified as:

$$\frac{1}{r}\frac{d}{dr}\left(r\frac{dv_z}{dr}\right)=\frac{1}{\mu}\frac{dp}{dz} \tag{3.10}$$

The velocity profile along the radial direction then can be solved as:

$$v_z = -\frac{1}{4\mu}\frac{dp}{dz}\left(r_0^2 - r^2\right) \tag{3.11}$$

If the velocity is non-dimensionalized by the center-line velocity

$$v_{zc} = -\frac{1}{4\mu}\frac{dp}{dz}r_0^2 \tag{3.12}$$

which yields the well known parabolic velocity profile:

$$U_z = 1 - \left(r/r_0\right)^2 \tag{3.13}$$

For the numerical simulation, the inlet velocity is set to a constant value. The numerical results obtained here are based on the mesh of 62 × 32 nodes. The comparisons of the present numerical solution and the analytical solution are shown in Figure 3.8, which shows the good agreement of the velocity profiles along the radial direction.

3.1.5 Swirling Flow in an Enclosed Chamber

To consider the effect of the swirling velocity, the flow in an enclosed chamber with a rotating bottom-wall is simulated. The geometry and boundary conditions for the flow problem are shown in Figure 3.9. The governing equations are the same as Equations (2.45) to (2.48) except all the source terms S_r, S_z, and S_θ are zero. The problem has been studied by many authors, experimentally (Escudier, 1984) and numerically (Lopez, 1990). It has been found that only two dimensionless parameters are needed to characterize the flow structure: the aspect ratio H/R and the Reynolds number $Re = \Omega R^2/\nu$, where H is the height of the chamber, R is the radius of the chamber, and Ω is the rotating velocity of the bottom-wall.

In the present study, the case with the aspect ratio of $H/R = 2$ is simulated. The numerical results obtained here are based on the mesh of 102 × 202 nodes. The contours of streamline for the two different *Re*, 1200 and 1500, are shown in Figure 3.10. For *Re* = 1200, there is no vortex breakdown bubble (Figure 3.10a). For *Re* = 1500 there is a vortex breakdown bubble (Figure 3.10b) along the rotation axis. The appearance and disappearance of vortex breakdown at different *Re* are consistent with the experimental visualization (Escudier, 1984). And the location, size and shape of the bubble also agree well with the experimental flow visualization reported by Escudier (1984).

3.2 Flow in Porous Medium Region

3.2.1 Flow in a Fluid Saturated Porous Medium Channel

The geometry and boundary conditions for the flow in a fluid saturated porous medium channel are shown in Figure 3.11. For the fully developed flow, in the non-dimensional form, the governing equation is simplified as:

$$\frac{1}{\varepsilon}\frac{d^2U}{dY^2}-\frac{U}{Dar}-FU^2+1=0 \tag{3.14}$$

where $Dar = K/H^2$, $F = c_F \rho G H^4 / \left(K^{1/2}\mu^2\right)$, $Y = y/H$, $U = \mu u / \left(GH^2\right)$; and *Dar* is the Darcy number; *F* is the Forchheimer number; *G* is a constant applied gradient $G = -dp^*/dx$; μ is the viscosity of the fluid. The analytical solution of (3.14) has been obtained by Nield et al. (1996), which gives:

$$\left(\frac{2F\varepsilon}{3}\right)^{1/2} = \int_0^{b_2}\left[P(t)\right]^{-1/2}dt \tag{3.15}$$

$$\left(\frac{2F\varepsilon}{3}\right)^{1/2} Y = \int_U^{b_2} \left[P(t)\right]^{-1/2} dt \tag{3.16}$$

where $P(U) = (U - b_1)(U - b_2)(U - b_3)$, $b_2 = U(0)$, $b_1 < b_2 < b_3$

$$(b_1, b_3) = \frac{1}{4F}\left\{-\frac{3}{Dar} - 2Fb_2 \mp \left[\frac{9}{Dar^2} + 48F - \frac{12Fb_2}{Dar} - 12F^2 b_2^2\right]^{1/2}\right\}$$

The Equations (3.15) and (3.16) can be solved by numerical quadrature.

If $F = 0$, Equation (3.14) becomes Brinkman equation and the dimensionless analytical solution is:

$$U = Dar\left\{1 - \cosh\left(Y\sqrt{1/(\varepsilon Dar)}\right) \Big/ \cosh\left(\sqrt{1/(\varepsilon Dar)}\right)\right\} \tag{3.17}$$

For the numerical simulation, the inlet velocity is set to a constant value. The numerical results obtained here are based on the mesh of 82 × 32 nodes. The comparisons of analytical solution and numerical solution for the Brinkman model and the generalized model are presented in Figure 3.12. The good agreement between the analytical and numerical solutions indicates that the present code is valid for the porous flow.

3.2.2 Natural Convection in a Fluid Saturated Porous Medium Cavity

The geometry and boundary conditions for the natural convection in a fluid saturated porous medium cavity are shown in Figure 3.13. The fluid is considered as a Boussinesq fluid. The dimensionless governing equations are expressed as:

$$\frac{\partial U}{\partial X} + \frac{\partial V}{\partial Y} = 0 \tag{3.18}$$

$$\frac{U}{\varepsilon}\frac{\partial}{\partial X}\left(\frac{U}{\varepsilon}\right) + \frac{V}{\varepsilon}\frac{\partial}{\partial Y}\left(\frac{U}{\varepsilon}\right) = -\frac{1}{\varepsilon}\frac{\partial(\varepsilon P)}{\partial X}$$

$$+\frac{\Pr}{\varepsilon}\left(\frac{\partial^2 U}{\partial X^2}+\frac{\partial^2 U}{\partial Y^2}\right)-\frac{\Pr}{Dar}U-\frac{F}{\sqrt{Dar}}\left|\vec{U}\right|U \tag{3.19}$$

$$\frac{U}{\varepsilon}\frac{\partial}{\partial X}\left(\frac{V}{\varepsilon}\right)+\frac{V}{\varepsilon}\frac{\partial}{\partial Y}\left(\frac{V}{\varepsilon}\right)=-\frac{1}{\varepsilon}\frac{\partial(\varepsilon P)}{\partial Y}+Ra\,\Pr\theta$$

$$+\frac{\Pr}{\varepsilon}\left(\frac{\partial^2 V}{\partial X^2}+\frac{\partial^2 V}{\partial Y^2}\right)-\frac{\Pr}{Dar}V-\frac{F}{\sqrt{Dar}}\left|\vec{U}\right|V \tag{3.20}$$

$$U\frac{\partial T}{\partial X}+V\frac{\partial T}{\partial Y}=\frac{\partial^2 T}{\partial X^2}+\frac{\partial^2 T}{\partial Y^2} \tag{3.21}$$

where $X=\frac{x}{L}$, $Y=\frac{y}{L}$, $U=\frac{u}{a/L}$, $V=\frac{v}{a/L}$, $P=\frac{p^*}{\rho a^2/L^2}$, $T=\frac{T'-T_L}{T_H-T_L}$, $Ra=\frac{\rho g\beta_T\Delta T L^3}{\mu^2}$, $\Pr=\frac{\mu}{\rho a}$, $Dar=\frac{K}{L^2}$; and a is the thermal diffusivity; L is the cavity width (or height); g is the gravity constant; β_T is the expansion coefficient; other parameters have their usual meanings.

In this case, the thermal properties of the solid matrix and the fluid have been taken to be identical and the effective viscosity of the porous medium is assumed to be equal to the viscosity of the homogenous fluid. The cases are tested at $Dar = 10^{-2}$, 10^{-4}, and 10^{-6}, porosity ε = 0.4 and 0.9, and Ra between 10^3 and 10^9, while Pr is kept constant at 1. The numerical results obtained here are based on the mesh of 122 × 122 nodes. The contours of streamline and temperature for $Dar = 10^{-4}$ and $Ra = 10^5$ are shown in Figure 3.14. It is seen that the contours are similar to those of natural convection of the air in an empty cavity as shown in Figure 3.6. The comparisons of Nusselt numbers along the hot wall between the present results and Nithiarasu et al.'s results (1997) are listed in Table 3.4. The good agreements indicate that the present code is valid to simulate heat and mass transfer problems in porous medium.

3.3 Coupled Flow in Porous and Homogenous Domains

3.3.1 Fully Developed Flow in a Channel Partially Filled With a Layer of a Porous Medium

The physical domain is shown schematically in Figure 3.15. It consists of a planar channel which is horizontally divided into a homogenous fluid region of height H_1 above and a fluid-saturated porous region of height H_2 below. The case of height ratio $H_2 / H_1 = 1$ is considered.

The flow is assumed laminar and fully developed. The governing equations are simplified as follows:

$$\frac{d^2u}{dy^2} = \frac{1}{\mu}\frac{dp}{dx} \qquad \text{for homogenous fluid} \qquad (3.22)$$

$$\frac{d}{dy}\left(\frac{\mu}{\varepsilon}\frac{du}{dy}\right) = \frac{1}{\varepsilon}\frac{d\left(\varepsilon p^*\right)}{dx} + \frac{\mu}{K}u + \frac{\rho C_F}{\sqrt{K}}u^2 \qquad \text{for porous medium} \qquad (3.23)$$

Introducing the dimensionless variables:

$U = \mu u \big/ \left(GH_1^{\,2}\right)$ and $Y = y/H_1$, where $G = -dp^*/dx$

Equations (3.22) and (3.23) can be rewritten as:

$$\frac{d^2U}{dY^2} = -1 \qquad \text{for homogenous fluid} \qquad (3.24)$$

$$\frac{1}{\varepsilon}\frac{d^2U}{dY^2} = -1 + \frac{1}{Dar}U + FU^2 \qquad \text{for porous medium} \qquad (3.25)$$

where the Darcy number $Dar = K/H_1^{\,2}$ and the Forchheimer number $F = C_F \rho G H_1^{\,4} \big/ \left(K^{1/2}\mu^2\right)$. The boundary conditions are:

$$U = 0 \quad \text{at} \quad Y = 1 \quad \text{and} \quad U = 0 \;\; Y = -H_2 / H_1 \qquad (3.26)$$

$$\frac{1}{\varepsilon}\frac{dU}{dY}\bigg|_{\text{porous medium}} - \frac{dU}{dY}\bigg|_{\text{homogenous fluid}} = \frac{\beta}{\sqrt{Dar}}U_{\text{interface}} \quad \text{at} \quad Y = 0 \qquad (3.27)$$

Following the proposal of Nield et al. (1996), Integrating Equation (3.25) gives:

$$\frac{1}{\varepsilon}\left(\frac{dU}{dY}\right)^2 = \frac{2}{3}FU^3 + \frac{U^2}{Dar} - 2U + C \tag{3.28}$$

Using Equations (3.26) and (3.27), the constant C can be expressed as:

$$C = \varepsilon\left[\frac{\beta_1}{\sqrt{Dar}}U_i + \left(\frac{1}{2} - U_i\right)\right]^2 - \left(\frac{2}{3}FU_i^3 + \frac{U_i^2}{Dar} - 2U_i\right) \tag{3.29}$$

Since $\frac{dU}{dY}$ should be real and negative in this region, it is expressed as:

$$\frac{dU}{dY} = -\sqrt{\varepsilon\left(\frac{2}{3}FU^3 + \frac{U^2}{Dar} - 2U + C\right)} \tag{3.30}$$

Integrated Equation (3.30), we can obtain:

$$\int_0^{U_{\text{interface}}} Q\left(\langle U\rangle\right) d\langle U\rangle = -H_2/H_1 \tag{3.31}$$

where $Q\left(\langle U\rangle\right) = -\left[\varepsilon\left(\frac{2}{3}F\langle U\rangle^3 + \frac{\langle U\rangle^2}{Dar} - 2\langle U\rangle + C\right)\right]^{-1/2}$

Similarly:

$$\int_{\langle U\rangle}^{U_{\text{interface}}} Q\left(\langle U\rangle\right) d\langle U\rangle = Y \tag{3.32}$$

Given the values of *Dar*, *F* and ε, the value of $U_{\text{interface}}$ is given in an inverse manner from Equation (3.31). Pairs of values (*Y*, *U*) determining the velocity profile can then be obtained from Equation (3.32). The integrals in Equations (3.31) and (3.32) can be solved using Romberg's numerical integration method.

To ensure grid-independent solution and accurate resolution, a sufficiently fine mesh should be used. For the fully developed flow, a mesh of 60 grids in the *x* direction is found to be sufficient. In *y* direction, it is found that at least 40 grids are needed to obtain grid-independent solution (Figure 3.16), which is consistent with the

results of Silva and de Lemos (2003) and Costa et al. (2004). The interface velocities obtained with different grids are summarized in Table 3.5. It confirms that above 40 grids in y direction there is little change in the results. Also, the interface velocity agrees with the analytical solution (of the present study) to an accuracy of about 5%.

Figure 3.17 shows the variation of the residual as a function of the number of the iterations. The rate of convergence is fast and the residual drops to 10^{-6} within 600 iteration steps when a mesh of 60 × 60 CVs is used.

The comparisons of the numerical and analytical solutions are presented for further validation of the present numerical implementation. Figure 3.18 shows the u velocity profile under different flow conditions. It is seen that the numerical and analytical results are in good agreement. The effect of *Dar* on the u velocity profile is presented in Figure 3.18a in which the Darcy number varies from 10^{-3} to 5×10^{-2} while the other parameters are kept constant. Although in practical applications, the Darcy number may not go up to 10^{-2} (Large, 1992), nevertheless this range is also presented to show *Dar* effect more clearly. From Figure 3.18a, it is seen that the u velocity decreases with the increase of *Dar*. When the Darcy number is less than 10^{-3}, the u velocity in the porous medium is almost zero except the region near the interface. The effect of the porosity (ε) on the u profile is shown in Figure 3.18b. The u velocity should decrease as the porosity decreases and the numerical results seem to show the trend. However, in the porous medium region around $-0.33 < Y < -0.62$, the u velocity is slightly larger when the porosity is smaller. This may be because the β chosen here is kept constant even though it should vary with the variation of ε . The

Forchheimer number (*F*) does not have much effect on the velocity distribution. The velocity decreases slightly when *F* increases from 1 to 100 as shown in Figure 3.18c. The effect of jump parameter (β) on the flow is shown in Figure 3.18d, which shows that the u velocity increases noticeably as β increases.

3.3.2 Flow through a Channel With a Porous Plug

The physical domain of the second problem is shown schematically in Figure 3.19, which is the same as that by Gartling et al. (1996), Costa et al. (2004) and Betchen et al. (2006). In this problem the flow passes through a planar channel with a porous plug under an imposed overall pressure gradient. Different from the first problem, the governing dimensionless parameters are: the Reynolds number based on the mean velocity, $Re = \rho UH / \mu$, the Darcy number $Dar = K/H^2$, the porosity ε, the Forchheimer coefficient C_F and the jump parameters β and β_1. For this case, Forchheimer coefficient C_F is evaluated as $C_F = 1.75/\sqrt{150\varepsilon^5}$ (Costa et al., 2004; Betchen et al., 2006).

The numerical results for the case of $Da = 10^{-2}$ and 10^{-3} are shown in Figure 3.20, where the centerline *u* velocity and pressure along *x* direction are presented. The other parameters for the flows illustrated in Figure 3.20 are *Re* = 1, $\varepsilon = 0.7$, $\beta = 0$ and $\beta_1 = 0$. The lengths are set to $\Delta x_1 = \Delta x_3 = 3H$ and $\Delta x_2 = 2H$.

The numerical studies by Costa et al. (2004) and Betchen et al. (2006) have shown that a mesh of (20 + 20 + 20) × 20 CVs is fine enough to obtain accurate results; the node density in *x* direction is increasing towards the interfaces, and the

node distribution in *y* direction is uniform. In the present study, the same mesh was used and the preliminary numerical tests confirmed that the solutions are grid-independent.

Figure 3.20 shows that the velocity drops rapidly in the porous plug, across which there is a large pressure drop, especially for the case with the low *Dar*. The flow field is predominantly axial over most of the homogenous fluid and porous medium regions, but it is two-dimensional in the region near the interface between the homogenous fluid and the porous medium. The present results are in good agreement with those of Gartling et al. (1996) and Betchen et al. (2006). The trends of the present results are in general agreement with that of Costa et al. (2004) except for slight differences in the velocity magnitude in the porous medium.

The effect of the shear jump parameters β and β_1 on the centerline velocity distribution is shown in Figure 3.21. It is seen that the two parameters have very small effect as the dominant flow direction is perpendicular to the interface.

Another case similar to Betchen et al. (2006) is investigated in which the Darcy number is set to $Dar = 10^{-2}$ and the channel segment lengths (Figure 3.19) are: $\Delta x_1 = \Delta x_2 = 5H$ and $\Delta x_3 = 50H$. In this case (Figure 3.22), the shear jump coefficient also has a negligible effect on the velocity distribution along the centerline. The centerline velocity profile shows that the velocity remains free of oscillation in the region near the two interfaces; this indicates that the present method is capable of dealing with discontinuous pressure gradient at the interface.

Note that the present Reynolds number is limited to *Re* = 200 because above this

value, velocity oscillation was observed. For a higher *Re*, the Forchheimer term becomes dominantly large, which may cause severe pressure drop in the porous side. Thus a severe discontinuity in pressure gradient arises at the interface, and the difficulty in estimating the interface pressure may cause velocity oscillation there. The present method to estimate the interface pressure has been explained in Chapter 2. The more complex method to estimate the interface pressure proposed by Betchen et al. (2006) is more robust for higher *Re* up to 1000.

3.3.3 Flow around a Porous Square Cylinder

The above two problems concern internal flows with regions of homogenous fluid and porous medium. To illustrate an external flow problem, the flow around a porous square cylinder is considered. The computational domain and mesh are shown schematically in Figures 3.23 and 3.24 respectively. The governing dimensionless parameters are the same as that of the porous plug problem above: the Reynolds number based on the mean velocity and the height of the cylinder, $Re = \rho UH / \mu$, the Darcy number $Dar = K/H^2$, porosity ε, Forchheimer coefficient C_F and jump parameter β and β_1.

The flow streamline for the flow around a porous square cylinder at different *Dar* are presented in Figure 3.25. In this case, the Reynolds number is chosen as *Re* = 20 to ensure the steady and laminar flow. Three different Darcy numbers, $Dar = 10^{-2}$, 10^{-3} and 10^{-4}, are chosen and other parameters are kept constant namely, $\varepsilon = 0.4$, $C_F = 1$, $\beta = 0.7$ and $\beta_1 = 0$. The preliminary numerical test (data not shown) confirmed that a

mesh of 40 × 40 CVs for the cylinder and a mesh of 160 × 100 CVs for the external region can provide grid-independent solutions. At a smaller *Dar* (= 10^{-4} in Figure 3.25a), that is the cylinder permeability is small, very little fluid flows through the cylinder. Hence the flow field resembles that around a solid cylinder. When the Darcy number increases to 10^{-3} (Figure 3.25b), the vortex in the wake is reduced as there is more bleed fluid. At a higher *Dar* (= 10^{-2} in Figure 3.25c), the large bleed flow has prevented vortex formation.

Figure 3.26 shows the variation of recirculation length with *Dar*, for *Re* = 20. The recirculation length is defined as the streamwise distance, along the wake centerline, from the cylinder rear to the re-attachment point. The recirculation length becomes longer with the decrease of *Dar*. However the recirculation length approaches to a constant value at a low *Dar* as the porous cylinder tends to a solid one. The recirculation length at *Dar* = 10^{-7} is about 1.32 (Figure 3.26), which is rather close to the value of around 1.34 for the solid cylinder (Sharma and Eswaran, 2004).

Figure 3.27 shows the effects of the jump coefficients on the tangential velocity component at the porous-fluid interface. There is not much effect for the rear interface as the tangential velocity there is small. Elsewhere, the first coefficient β has a noticeable effect whereas the second coefficient β_1 has very small effect. From the shear-jump equation, the viscous term $\beta\mu u_t/\sqrt{K}$ is large if the permeability *K* is small, that is the Darcy number is small. The inertial term $\beta_1\rho u_t^2$ may be important at a high *Re*; however, the external flow would become unsteady, which is out of the scope of the present shear-jump modeling based on steady flow.

3.4 Concluding Remarks

A finite volume code has been developed to predict the flow and mass transport in homogenous fluid region, in porous region and in conjugate fluid and porous regions. The present code was based on nonorthogonal, body fitted, and multi-block structured grids, which are effective for dealing with the problems in complex domain. The SIMPLEC algorithm was used to couple the velocity and pressure. The strongly implicit procedure (SIP) was applied to solve the resultant algebraic equation system.

For the pure fluid problems, the block interface was treated as the interior cell faces rather than boundaries, which were proposed by Lilek et al. (1997). A variety of numerical experiments are performed to test the validation of the present code. The agreements between the present numerical results and the bench mark results indicate that the present code can be used to predict the 2D, incompressible, steady, laminar flow and mass transfer problems in both Cartesian and cylindrical coordinates.

For the porous flow problems, the governing equations were based on a generalized model including Brinkman and Forchheimer terms as well as non-linear advection term (Hsu and Cheng, 1990; Gartling et al., 1996; Nithiarasu et al., 2002), which recovers the NS equations when the porosity approaches unity. The block interface was also treated as the interior cell faces. Several computed results on the flow and heat transfer in porous media are presented to validate the present method. Comparisons between the present numerical results and analytical solutions, or computational results provided by other researchers confirm that the present code is a reliable and efficient tool for the steady, laminar flow problems in porous media.

For the flow problems with the homogenous fluid and porous medium interface, the main novelty of this study is a numerical method for the theory developed by Ochoa-Tapia and Whitaker (1998) to model the momentum jump condition at the interface, which includes both viscous and inertial jump parameters β and β_1. A distinctive feature of the present method is the use of multi-block grids which, together with body-fitted grids, makes it more suitable for handling complex geometries. The shear stress jump condition affects both the convective and diffusive fluxes. The normal stress condition, assumed continuous at the interface, is also needed in order to close the two sets of equations.

The numerical results obtained by the present code were consistent with the results reported from the literatures, which indicate that the present method can solve such problems effectively and accurately. The numerical simulation of flow over a porous layer extends the work of Silva and de Lemos (2003) by using multi-block grid and including the diffusive flux term; the results compares well with the analytical solution proposed by Nield et al. (1996). The numerical results for flow through a porous plug exhibit slight difference in velocity in the porous medium, as compared with the studies of Costa et al. (2004); however there is good agreement with Gartling et al. (1996) and Betchen et al. (2006). The centerline velocity profile is free of oscillation in the region near the two interfaces, which confirms that the present method is capable of dealing with discontinuous pressure gradient there. The numerical simulation of flow past a porous square cylinder demonstrates the use of multi-block grid for coupled fluid-porous flows involving complex geometries.

Chapter 4
Fluid Dynamics of a Micro-Bioreactor for Tissue Engineering*

The advantages of cost reduction, parallelization and automatization have made cell culture in small volumes more useful. Besides microtiter plates with shaking systems (Duetz et al., 2000; Girard et al., 2001; Kensy et al., 2005), several novel micro-bioreactors with various agitation systems for high throughput bioprocessing have been designed (Kostov et al., 2001; Puskeiler et al., 2005; Lamping et al., 2003). One novel design was based on a chamber stirred by a rotating rod at the bottom (Kostov et al., 2001). However, to date this novel micro-bioreactor has not been tested with other types of cells (other than suspended Escherichia coli cells) like animal cells which are less robust to fluid shear stress and more sensitive to medium mixing conditions. Furthermore, it is not known whether the oxygen transfer would be adequate if the bioreactor was operated in a simpler way without the bubble aeration system. These basic fluid-dynamic and oxygen-transfer issues represent the motivation of the present study devoted to develop a computational fluid dynamics model of the flow field and mass transport in the micro-bioreactor.

The present micro-bioreactor consists of a culture well in which a small magnetic rod is placed on the bottom to enhance the medium mixing. The flow and oxygen concentration fields are simulated by FLUENT, a commercial software based on finite volume method. The results of velocity components, circulation coefficients,

*Parts of this chapter have been published in Fluid Dyn. Mater. Proc. (Yu et al., 2005b)

hydrodynamic stresses, oxygen concentration and volumetric oxygen transfer coefficients are presented in non-dimensional form for general applications.

4.1 Computational Methods

4.1.1 Mathematical Model

The magnetic rod is located on the bottom and rotates about the axis of the chamber as shown in Figure 4.1 (Yu et al., 2005a; 2005d). The chamber is filled with the medium, and does not have any microcarriers. The chamber of the present micro-bioreactor has diameter D of 22 mm and height H of 12 mm. The stirrer-rod diameter d is 1 mm and its length L is 12 mm. In a typical application, the medium volume is about 4 ml. In contrast, industrial bioreactors of the stirred-tank type may be of several thousand litres in volume (Leist et al., 1990).

As the magnetic rod is driven by a magnetic stirrer, the presence of the magnetic field may affect both the animal cells and the culture medium motion. It was reported that the magnetic field of the stirrer affects certain cell metabolism (Kula, 1996). However, bioreactor magnetic fields do not affect growth and antibody productivity of hybridomas (Cherry and Robinson, 1989). Generally, the electrical conductivity of the culture medium is in the order of 1 S m^{-1} (Mazzoleni et al., 1986) and its magnetic permeability is in the order of 10^{-6} N A^{-2}. The magnetic Reynolds number in the present micro-bioreactor is about 10^{-9}. Thus, the effect of magnetic field on the flow can be neglected.

The moving reference frame method is used to model the flow. In the original inertial frame, the flow is unsteady because the rod sweeps the flow domain periodically. By transferring the coordinates system from the original frame to the rotating frame of the stirrer rod, the flow is steady relative to the rotating frame. The velocities in the two reference frames are related by the following equation:

$$\vec{u}_r = \vec{u} - \left(\vec{\Omega} \times \vec{r}\right) \tag{4.1}$$

where $\vec{u}$ is the absolute velocity; $\vec{u}_r$ is the relative velocity; $\vec{\Omega}$ is the angular velocity vector of the rotating frame; and $\vec{r}$ is the position vector in the rotating frame.

It was assumed that animal cells were suspended in the micro-bioreactor uniformly. Animal cell suspensions usually exhibit Newtonian fluid characteristics as the cell density is relatively low and the culture medium contains low concentrations of solutes (Bliem and Katinger, 1988; van der Pol and Tramper, 1998). Thus, it was assumed the presence of the cells did not affect the flow fields. The substrate numerically modeled here is oxygen. Insufficient oxygen supply is one of the limiting factors in the scaling up of animal cell culture processes (Leist et al., 1990). It is envisaged that the present scaling-down process may likewise be limited by insufficient oxygen supply, especially if there is no bubble aeration. The governing equations for the flow and oxygen transport can be written as:

$$\nabla \cdot \vec{u} = 0 \tag{4.2}$$

$$\left(\rho \vec{u} \nabla\right) \cdot \vec{u} = -\nabla p + \mu \nabla^2 \vec{u} \tag{4.3}$$

$$\vec{u} \cdot \nabla C = D_f \nabla^2 C - R_m \tag{4.4}$$

where ρ is the culture medium density; p is the static pressure; μ is the dynamic viscosity of the culture medium; C is the molar concentration of oxygen (mol m^{-3}); D_f is binary diffusivity (m^2 s^{-1}); R_m is the term that represents oxygen consumption by animal cells. Usually, the density ρ is around 10^3 kg m^{-3}, which is similar to that of the water, and the viscosity μ is in the range of 0.5 to 2.0 x 10^{-3} Pa s.

In the present study, the oxygen consumption by the animal cells was assumed to base on Michaelis-Menten equation and the consumption term R_m could be written as:

$$R_m = \frac{\gamma V_m C}{C + k_m} \tag{4.5}$$

where γ is the cell density in the micro-bioreactor; V_m is the maximum oxygen uptake rate (OUR) per cell and k_m is the half-saturation parameter. The cell density is in the range of 1×10^{12} - 5×10^{12} cells m^{-3}.

For fluid flow, the no-slip conditions were applied at the all solid wall. For the top surface of the culture medium, our experiment shows that the free surface deformation is negligible at a low *Re* (of less than 800). Hence, the zero shear-stress condition is imposed at the top surface to simplify the free surface condition. For oxygen transport, the zero flux conditions were applied at the solid walls. The oxygen concentration at the top surface is assumed constant and equal to the saturation concentration in the culture media as determined from Henry's law.

The Reynolds number based on the length of the magnetic bar is defined as:

$$\mathrm{Re} = \frac{\rho N L^2}{\mu} \tag{4.6}$$

where N (rev s^{-1}) is the rotating speed of the bar. Flow with different Re in the range of 100 to 720, corresponding to the rotation speeds from 0.7 to 5 rev s^{-1} respectively, was simulated. The lift on the stirrer at Re = 432 is about 2.08×10^{-5} N and the external torque needed is about 1.62×10^{-7} N m. Since the maximum Reynolds number is less than the critical value of 1,000 (Nagata, 1975), the assumption of laminar flow is reasonable.

The non-dimensional parameter Damkohler number, which quantitatively describes the nutrients consumption, is defined as:

$$Da = \frac{\gamma V_m L^2}{C_0 D_f} \tag{4.7}$$

where C_0 is the reference concentration, chosen as the gas-phase equilibrium oxygen concentration of 0.27 mol m^{-3} in the present study. As an example, a typical value of the Damkohler number can be calculated for a typical CHO cell culture from the data of Deshpande and Heinzle (2004). If the cell density $\gamma = 1\times10^{12}$ cells m^{-3}, oxygen uptake rate $V_m = 8\times10^{-17}$ mol $cell^{-1}$ s^{-1}, the Damkohler number is 19. 57.

4.1.2 Numerical Method

The commercial software FLUENT was used for the numerical solution of the flow and oxygen concentration fields. Commercial software such as this have been used to simulate the flow field in bioreactors by many researchers (For examples, Jaworski et al., 2000; Unger et al., 2000; Bujalski et al., 2002; Williams et al., 2002). FLUENT uses a control-volume approach to integrate the governing equations over each cell in the mesh. The resulting set of algebraic equations are linearized and

solved numerically. The second order upwind scheme was applied for discretization and the SIMPLEC method was used to coupled velocity and pressure.

It was found that in the numerical model, a small gap has to be imposed between the rod and the base of the bioreactor. Without this artifact, the commercial mesh generator code GAMBIT could not generate an accurate mesh for the whole flow domain. The minimum size of the gap between the stirrer and bottom for numerical convergence depends on the mesh size. In the present study, the gap is 0.1 mm. If a fine mesh is used, the gap could be smaller.

4.1.3 Validation

For rotation flow problem, the mesh should be sufficiently refined to resolve large gradients in pressure and rotation speed. To check grid independence, a study has been performed with three sets of mesh at a higher *Re* of 576. The cells numbers of the three sets of mesh are 245,188, 326,533 and 444,973. Dimensionless velocity components curves (the reference velocity is πNL) for the different sets of meshes are shown in Figure 4.2. To ensure computational accuracy, the finest mesh with 444,973 cells has been selected for the final computation.

To verify the CFD model, the flow in a tank stirred by a two-blade impeller has been simulated, using the same conditions as those in the experiments of Youcefi's (1993). The comparison of the numerical and experimental results is presented in Figure 4.3. The agreement indicates that the present numerical model gives velocity components with satisfactory accuracy.

4.2 Flow Field

4.2.1 Flow Pattern

Figure 4.4 presents the velocity field in a vertical plane (at angle 0 ° from the magnetic rod) for different *Re* of 288, 432 and 576. It shows that the fluid in the micro-bioreactor does not behave like that of a solid body rotation which has no axial mixing. It is seen that a central recirculating region is formed.

The fluid recoils away from the rotating rod towards the wall, where it flows upward and returns downward near the axis. This creates a recirculation flow above the stirring rod. The recirculation is weak at a low *Re* of 288. At *Re* = 432, the recirculation flow appears stronger. It was found there is an attached vortex breakdown bubble near the axial region, which is similar to that of the swirling flow in a cylindrical container with a free surface (Spohn et al., 1993). In the present flow situation, the critical *Re* for vortex breakdown was found to be about 380. At a higher *Re* of 576 (Figure 4.4c), the vortex breakdown bubbles are clearer. The recirculation flow, though beneficial for enhancing medium mixing, may be detrimental to cell culture as it may have the effect of centrifuging cells towards the micro-bioreactor wall.

4.2.2 Effect of Top Lid

In some situations, the liquid may not be exposed to the surrounding environment directly but covered with a rigid lid (Yu et al., 2002; 2005a). The lid will prevent foam generating at the liquid surface, which may occur at the free surface condition

and damage animal cells. Thus it is relevant to investigate the effect of a rigid wall for the boundary condition at the top surface of the bioreactor.

Figure 4.5 presents the velocity field in a vertical plane (at angle 0 ° from the magnetic rod) for three different *Re* of 288, 432 and 720. At a low *Re*, the flow field is quite similar to those with a free surface (Figure 4.4a) and there is a recirculation flow above the stirring rod (Figure 4.5a). At a higher *Re* of 432, the recirculation flow becomes stronger (Figure 4.5b). However, at this *Re*, there is no vortex breakdown bubble like that which appears in free surface condition (Figure 4.4b). At a high *Re* of 720 (Figure 4.5c), the vortices generated by the rotating rod are different from those at smaller *Re*. There is a well defined vortex breakdown near the axial region, which is similar to that of the swirling flow in a cylindrical container (Escudier, 1984; Lopez, 1990). In this situation, the critical *Re* for vortex breakdown was found to be about 580. The vortex breakdown bubbles in the micro-bioreactor with the rigid lid are different with those with the free surface. The bubbles are embedded in the interior of the flow domain but never attached to the top surface.

Figure 4.6 shows the detailed comparisons of three dimensionless velocity components along a radial line between the rigid lid and free surface conditions. Note that the axis of rotation of the magnetic rod is at $2r/D = 0$. Along the line at the middle of the micro-bioreactor (z = 6 mm), the distributions of three velocity components are quite similar (Figure 4.6a). However, there are some differences between the two axial velocity components near the axial region due to the occurrence of vortex breakdown at the free surface condition. Along the line near the top surface (z = 11

mm), the tangential velocity component of the free surface condition are somewhat higher than that of the rigid lid due to the absence of the friction at the free surface (Figure 4.6b). The distributions of the two axial velocity components are similar except for the region near the axis due to the occurrence of vortex breakdown. The radial velocity component of the free surface condition is slightly lower than that of the rigid lid.

Figure 4.6 indicates that the rigid lid has some effect on flow field near the top region due to its friction. Also, the rigid lid delays the onset of vortex breakdown, which may affect the flow field where it occurs. In the other regions, the rigid lid effect is relatively smaller.

4.3 Mass Transfer

4.3.1 Medium Mixing

From the velocity distribution (Figure 4.4), the flow in the upper part of the chamber is weak. The mixing in this region may be poor because the axial mass transfer is largely dependent on axial velocity components, as generated by the secondary circulation. The axial upward flow rate Q_c can be given as (Costes and Couderc, 1988; Kuncewicz, 1992; Dong et al., 1994):

$$Q_c = \frac{1}{2}\int_s |V_z| dS \tag{4.8}$$

where $|V_z|$ is the modulus of axial velocity component V_z , and dS is incremental area over which V_z acts. Since mass balance shows that the upward flow is equal to the downward flow at any horizontal plane, Q_c is therefore the upward (or downward)

axial-flow rate through a certain horizontal plane. The mass rate as an integral is a rough indication for mixing extent. A larger axial upward flow rate will give better mixing. The circulation capacity along the vertical direction at different *Re* is presented in Figure 4.7. For each *Re*, the circulation capacity Q_c reaches a maximum at height of z = 1.5 mm plane that is just above the rod. Then it decreases gradually with height. At a higher *Re*, the circulation capacity is larger, giving enhanced mixing.

The dimensionless form of the circulation capacity is the flow number:

$$N_{Qc} = \frac{Q_c}{NL^3} \tag{4.9}$$

Figure 4.8 shows the flow number N_{Qc} along the height z at different *Re*. The trends of the flow number N_{Qc} at *Re* are rather similar and so are their magnitudes, indicating an approximate collapse of data. Therefore, the flow number N_{Qc} may be considered a non-dimensional parameter independent of *Re*. The maximum flow number is about 0.19 and occurs at a height z of 1.5 mm.

The flow number N_{Qc} of the present rod is smaller than that of impellers in larger stirred bioreactors; for example the flow number is around 1.0 in a one-litre bioreactor (Dong et al., 1994), which is about 5 time of the present one. One reason for the difference is that their impeller has six blades but the present rod is equivalent to only two blades. Also the diameter of the present rod is small and its profile is not aerodynamically designed. Furthermore, the present stirring rod is located at the bottom of the chamber, which is not effective for flow mixing. The small flow number indicates that fluid mixing is not high in the present micro-bioreactor. Thus it

is necessary to check whether mass transport is adequate, particularly for oxygen transfer without bubble aeration.

4.3.2 Oxygen Transfer Coefficient

The oxygen concentration distributions in the micro-bioreactor at various *Re* and *Da* are presented in Figure 4.9. The oxygen concentration is non-dimensionalized by its saturation concentration in the medium. The oxygen concentration is low in the central region above the stirrer-rod tip (Figure 4.9a) because of the low mass transport in the recirculation region there (Figure 4.4a). The Reynolds number of 288 is too low to provide sufficient mixing, thus the oxygen concentration in the whole micro-bioreactor is not high. At a higher *Re* of 432 (Figure 4.9b), the concentration distribution is more uniform than that at a lower *Re*. The concentration is still low in the region above the stirrer rod tip because of the recirculation region there (Figure 4.4c). The concentration is higher near the axis region due to higher flow-velocities there which convect oxygen from the top surface (Figure 4.4c).

From the oxygen concentration field, its minimum values were determined and are presented in Figure 4.10 at various *Re* and *Da*. The minimum concentration is lower at a smaller *Re* due to poor mixing as expected; and it is also lower at higher *Da* due to higher consumption by the animal cells.

The critical value of the dimensionless oxygen concentration that causes cell hypoxia for CHO is 0.05 (Lin and Miller, 1992). Assuming *Da* of CHO is less than 50, operating the micro-bioreactor at the small rotating speed corresponding to *Re* = 144

(Figure 4.10) would be adequate to achieve sufficient oxygen transfer. The critical oxygen concentration of rat hepatocytes is 0.035 (Roy et al., 2001). However its Damkohler number is above 50, which may require a higher operating speed with *Re* above 144. When operating at *Re* = 432, the micro-bioreactor can support animal cell culture up to *Da* of 140 (Figure 4.10), assuming a critical value of 0.05 for the dimensionless oxygen concentration.

From the oxygen concentration field, the volumetric oxygen transfer coefficient is determined from:

$$OTR = k_L a\left(C_0 - C_{avg}\right) \tag{4.10}$$

where *OTR* is the volumetric oxygen-transfer rate; k_La is the volumetric oxygen transfer coefficient; C_0 is the oxygen saturation concentration in the medium; and C_{avg} is the average oxygen concentration. The average oxygen concentration C_{avg} may be determined from the concentration field. At steady state, the oxygen transferred into the micro-bioreactor is in equilibrium with the oxygen consumed by the cells. Thus the volumetric oxygen transfer rate *OTR* may be calculated from volumetric integration of Equation (4.5) using the oxygen concentration field.

$$OTR = \frac{1}{V}\int_V \gamma V_m \frac{C}{C + k_m} dV \tag{4.11}$$

The oxygen-transfer coefficient is an important parameter in the performance of bioreactors. The transfer coefficient is useful for determining the oxygen transfer in a bioreactor, for laboratory-scale use or when scaling up to a larger process. The coefficient has been used to measure the oxygen-uptake rate of cells, which is an

important experimental parameter to monitor and control cell culture experiments (Ruffieux et al., 1998; Oliveira et al., 2005).

Figure 4.11 presents the relationship between *OTR* and concentration difference (C_0 - C_{avg}) at various *Re*. Since C_0 is a constant value, different *Da* results in different C_{avg} and subsequently different (C_0 - C_{avg}). From Figure 4.11, it is seen that at the same *Re*, the data points at different *Da* are in the same straight line. The volumetric oxygen transfer coefficient at different *Re* is equal to the slope of the corresponding straight line.

The result is not affected by *Da*, within a reasonable range, because the oxygen transfer coefficient is a characteristic of the stirring system and does not depend on the cell consumption rate. The oxygen transfer coefficient k_La of the micro-bioreactor operating at various *Re* is presented in Figure 4.12. When the Reynolds number is small (less than 380), k_La increases fast with *Re*, but the change is less at a higher *Re*.

In the present micro-bioreactor, k_La is in the order of 10^{-3} s^{-1}. However, in the shaking microtiter plates for fermentation, k_La may be in order of 10^{-2} s^{-1} (Duetz et al., 2000). And in a gas-inducing millilitre-scale bioreactor, k_La of higher than 0.2 s^{-1} could be maintained over a range of 8 to 12-ml working volume with a stirrer speed of 2300 rpm (Puskeiler et al., 2005). In the case of bacteria culture, an oxygen transfer coefficient k_La of up to 0.2 s^{-2} has been achieved in a 10-litre fermentor with aeration (Badino et al., 2001). Hence, the present micro-bioreactor would be unable to generate sufficient oxygen transfer for bacteria and plant culture. And the main reasons for the low k_La value are the low agitation speed and the low efficient surface

aeration. Clearly for bacteria culture, aeration is needed to achieve adequate oxygen transfer as was used by Kostov et al. (2001).

However, for animal cell cultures which have a lower oxygen uptake rate, the critical oxygen concentration level in the present micro-bioreactor, as shown earlier for CHO cells and hepatocytes, is adequate without using aeration bubbles which may cause cell trauma (Wang et al., 1994). Also compared with k_La of 1.77×10^{-3} s^{-1} in the 250ml flask with stirrer speed of 100rpm (Zhong et al., 2002) and k_La of $O(10^{-3}$ $s^{-1})$ in a shake-flask (Zhang et al., 2005), k_La in the present micro-bioreactor is acceptable for animal cell culture.

4.4 Hydrodynamic Stress

Animal cells are sensitive to hydrodynamic stress (Chisti, 2001; Joshi et al., 1996) and its effects have been studied (see for example Schmid-Schönbein, 1987; Barakat, 1999; Zhang et al., 1995). In this section, results of shear stress, normal stress and energy dissipation rate will be presented.

4.4.1 Shear Stress

Three shear stress components in cylindrical coordinates are (Currie, 2002):

$$S_{r\theta} = \mu\left[r\frac{\partial}{\partial r}\left(\frac{V_\theta}{r}\right) + \frac{1}{r}\frac{\partial V_r}{\partial \theta}\right] \tag{4.12}$$

$$S_{\theta z} = \mu\left[\frac{\partial V_\theta}{\partial z} + \frac{1}{r}\frac{\partial V_z}{\partial \theta}\right] \tag{4.13}$$

$$S_{rz} = \mu\left[\frac{\partial V_z}{\partial r} + \frac{\partial V_r}{\partial z}\right] \tag{4.14}$$

The mean shear-stress level is defined as (Begley and Kleis, 2000):

$$S_M = \frac{1}{3}(S_{r\theta}^2 + S_{\theta z}^2 + S_{rz}^2)^{\frac{1}{2}} \tag{4.15}$$

Figure 4.13 shows shear stress field in a horizontal plane at z/H = 0.01 and Re of 432. The shear stress values are relatively low inside throughout the micro-bioreactor. The maxima of mean shear stresses are found around the rod and its wake region; and the peak value is near the tip of the rod.

The peak shear stresses at different Re are presented in Figure 4.14 (that also shows the normal stress to be discussed later). The peak shear-stress is below 0.5 N m^{-2}, which is not large. The present shear-stress is comparable to the experimental value of 0.26 N m^{-2} for the shear stress in a stirred bioreactor obtained by Joshi et al. (1996). Furthermore, the peak shear values only occur over a small region, near the tip of the rod. It has been computed that for all Re, the mean shear stresses are less than 0.01 N m^{-2} in more than 98% total volume; and mean shear-stresses greater than 0.1 N m^{-2} occupies less than 0.02% of total volume.

Mammalian cells are sensitive to shear stress which may affect their viability and functions, and may even damage them. For hybridoma cell line, Born et al. (1992) reported that laminar shear stress up to 208 N m^{-2}, acting for 20 minutes, in unaerated flow led to substantial loss in cell count and viability. However, for shear sensitive hybridoma cells CRL-8018, Petersen et al. (1988) reported that a laminar shear stress of 5 N m^{-2} may result in high levels of cellular damage and death within 10 minutes. For white blood cells, Dewitz (1977) reported that a shear stress of 60 N m^{-2} may cause one-fourth of cells lyses over 10 minutes. Thus the peak shear-stress of below

0.5 N m^{-2} suggests that shear-stress level in the present micro-bioreactor is acceptable for animal cell culture.

4.4.2 Normal Stress

Besides the shear stress, also of detriment to cells are the normal stress as found by Joshi et al. (2001), and Garcia-Briones and Chalmers (1994). In a stirred tank bioreactor, the normal stress would be of the same order of magnitude as the shear stress. Three normal stress components in cylindrical coordinates are (Currie, 2002):

$$S_{rr} = 2\mu \frac{\partial V_r}{\partial r} \tag{4.16}$$

$$S_{\theta\theta} = 2\mu \left[\frac{V_r}{r} + \frac{1}{r} \frac{\partial V_\theta}{\partial \theta} \right] \tag{4.17}$$

$$S_{zz} = 2\mu \frac{\partial V_z}{\partial z} \tag{4.18}$$

The mean normal stress can be defined as:

$$S_N = \frac{1}{3} (S_{rr}^2 + S_{\theta\theta}^2 + S_{zz}^2)^{\frac{1}{2}} \tag{4.19}$$

The normal stress has a rather similar distribution and magnitude as the shear stress. The values of mean normal stress are relatively low throughout the micro-bioreactor, with high values near the rod and its wake region. The peak normal stresses at various *Re* are presented in Figure 4.14. At the same *Re*, the peak normal stress is about twice the peak shear stress, which is consistent with that reported by Joshi et al. (2001).

4.4.3 Energy Dissipation Rate

It has been proposed that the damaging hydrodynamic forces on cells arise from the velocity gradients. Hence, the energy dissipation rate, that includes all velocity gradient components, may be used to evaluate the hydrodynamic environment. The energy dissipation levels in bioreactors have been related to cell damage (Garcia-Briones and Chalmers, 1994; Gregoriade et al., 2000; Ma et al., 2002). The energy dissipation rate is expressed as:

$$\Phi = \mu\left[\left(\nabla\vec{u} + \nabla\vec{u}^{T}\right) : \nabla\vec{u}\right] \tag{4.20}$$

Figure 4.15 shows the distribution of local energy dissipation rate in a horizontal plane at z/H = 0.01 and Re of 432. The maximum value lies near the tip of the rod. In the annulus region between the rod tip and the side-wall, the energy dissipation rate is low. The maximum and volume averaged values of energy dissipation rate at different Re are presented in Figure 4.16. The maximum local energy dissipation rate is below 14,000 W m^{-3}. In comparison a value of 90,000 W m^{-3} was determined in a 10 litre vessel equipped with one Rushton impeller (Zhou and Kresta, 1996). The maximum energy dissipation rate in the present micro-bioreactor is acceptable as it is much smaller than the damaging value for CHO cell line, which is in the range of 10^4 kW m^{-3} (Gregoriade et al., 2000).

It is noted that the ratio of maximum to mean values of the energy dissipation rate is in the order of four (Figure 4.16). It is reported that the ratio is of the order of two in other bioreactors (Zhou and Kresta, 1996; Ma et al., 2002). The present high-ratio is attributed to the magnetic rod being located at the bottom of the micro-bioreactor,

which generates higher velocity gradients and hence higher energy dissipation rate there.

4.5 Concluding Remarks

A numerical model was developed for a micro-bioreactor, of working volume below 5 ml, in which the medium was mixed by a magnetic stirrer rod at the base. The fluid mixing, oxygen concentration and hydrodynamic stresses in the micro-bioreactor were evaluated with a view to applications in animal cell culture.

The computed flow field shows that a recirculation region arises above the rotating stirrer-rod, which provides the medium mixing in the axial direction. The medium mixing is characterized by a circulation coefficient of about 0.2, which is about 5 times smaller than that in a one-litre bioreactor with six impellers. Thus a high rotational speed is needed to ensure adequate mixing, as indicated by the results of the concentration-level and transfer-coefficient of oxygen.

At the highest rotation speed studied, rod Reynolds number of 720, the volumetric oxygen-transfer coefficient of the micro-bioreactor is around 2.1×10^{-3} s^{-1} that is small compared with the value of 0.2 s^{-1} achieved in a 10-litre bacteria culture bioreactor with aeration. Thus for bacteria culture, it is necessary to enhance oxygen transfer by bubble aeration as was used by Kostov et al. (2001). However, the oxygen concentration level in the present micro-bioreactor is adequate for certain animal cell cultures without using bubble aeration. Assuming a critical value of 0.05 for the

dimensionless oxygen concentration, animal cell with *Da* up to 140 may be grown in the micro-bioreactor if operated at a high *Re* of 432.

The peak shear stress, at the highest *Re* of 720, is about 0.5 N m^{-2} which is around two times that in a large scale stirred-tank bioreactor but, nevertheless, still below the level acceptable for animal cell culture. The maximum energy dissipation rate (that characterizes the detrimental velocity gradients) is 14 kWm^{-3}; that is around 6 times lower than that in a 10 litre stirred-tank bioreactor fitted with a Rushton impeller. Hence the hydrodynamic stress environment would be acceptable for animal cell culture when the micro-bioreactor is operated at the highest *Re* of 720.

It is found that the attached vortex breakdown bubble may occur in the micro-bioreactor when the Reynolds number is beyond certain critical value. If the free surface is replaced by a rigid lid, the swirling flow near the top region will be reduced, which affects the occurrence of vortex breakdown.

Chapter 5

Swirling Flow and Mass Transfer in a Micro-Bioreactor with a Partially Rotating Bottom-Wall*

Vortex breakdown is important in the field of aeronautics as it occurs over delta-winged aircraft (Hall, 1972). Interestingly, vortex breakdown also occur in the stirred micro-bioreactor as shown in Chapter 4. It is well known that animal cells are sensitive to shear stress and nutrient concentration. When vortex breakdown occurs in bioreactors, the flow pattern undergoes a sudden change, which may affect shear stress and nutrient concentration distribution as a consequence. Thus vortex breakdown may also influence the function and viability of cells. In order to achieve desirable conditions for animal cell culture, it is important to investigate the vortex breakdown phenomena in bioreactors.

In this chapter, the swirling flow and vortex breakdown in a micro-bioreactor, which consists of a cylindrical vessel and the rotating disk embedded in the bottom-wall to generate medium mixing, will be investigated. One of the main motivations is to simulate the flow pattern in a micro-bioreactor stirred by a rotating magnetic-rod at the bottom. As vortex breakdown in an open chamber with a partial bottom-wall rotating has been investigated by Piva and Meiburg (2005), only the enclosed chamber will be examined.

Furthermore, the effect of vortex breakdown on the shear stress and oxygen transfer in the micro-bioreactor are studied. For this purpose, the micro-bioreactor

*Parts of this chapter have been published in Mod. Phys. Lett. B (Yu et al., 2005c) and Phys. Fluids (Yu et al. 2007b)

with the free surface is considered because the vortex breakdown bubbles exhibit various configurations in the chamber.

5.1 Numerical Methods

Figure 5.1 schematically shows the flow model in the micro-bioreactor, which is a cylindrical chamber of radius *R* filled with fluid and driven by a disk of radius r_d rotating at angular velocity Ω (Yu et al., 2006). For a typical application, the radius of the bioreactor is 10 mm. Both steady (Mullin et al., 1998; Mullin et al., 2000) and unsteady (Lopez, 1990; Piva and Meiburg, 2005) flow equations have been used for numerical modeling of the onset of vortex breakdown phenomena in earlier works. The present study is based on the primitive-variable formulation of the steady, axisymmetric Navier-Stokes equations, expressed as follows:

$$\frac{1}{r}\frac{\partial(rv_r)}{\partial r}+\frac{\partial v_z}{\partial z}=0 \tag{5.1}$$

$$\frac{1}{r}\frac{\partial(rv_r v_r)}{\partial r}+\frac{\partial(v_z v_r)}{\partial z}=-\frac{1}{\rho}\frac{\partial p}{\partial r}+\nu\left[\frac{\partial}{\partial r}\left(\frac{1}{r}\frac{\partial}{\partial r}(rv_r)\right)+\frac{\partial^2 v_r}{\partial z^2}\right]+\frac{v_\theta^2}{r} \tag{5.2}$$

$$\frac{1}{r}\frac{\partial(rv_r v_z)}{\partial r}+\frac{\partial(v_z v_z)}{\partial z}=-\frac{1}{\rho}\frac{\partial p}{\partial z}+\nu\left[\frac{1}{r}\frac{\partial}{\partial r}\left(r\frac{\partial v_z}{\partial r}\right)+\frac{\partial^2 v_z}{\partial z^2}\right] \tag{5.3}$$

$$\frac{1}{r}\frac{\partial(rv_r v_\theta)}{\partial r}+\frac{\partial(v_z v_\theta)}{\partial z}=\nu\left[\frac{\partial}{\partial r}\left(\frac{1}{r}\frac{\partial}{\partial r}(rv_\theta)\right)+\frac{\partial^2 v_\theta}{\partial z^2}\right]-\frac{v_r v_\theta}{r} \tag{5.4}$$

where v_r, v_z and v_θ are the radial, axial and azimuthal velocities respectively; *r* and *z* are the radial and axial coordinates respectively.

The boundary conditions can be expressed as:

$$\begin{cases} v_r = 0 \\ v_z = 0 \\ v_\theta = 0 \end{cases} \quad \text{on stationary wall} \tag{5.5}$$

$$\begin{cases} v_r = 0 \\ v_z = 0 \\ v_\theta = \Omega r \end{cases} \quad \text{on rotational wall} \tag{5.6}$$

In the present study, the cylinder-to-disk ratio R/r_d is varied up to 1.6, a range typical of the ratio of bioreactor diameter to rod length. The Reynolds number is varied up to 2000 and the aspect ratio is between 0.8 to 2.8.

To ensure grid-independent solution and accurate resolution in space, a sufficiently fine grid should be used. For *Re* less than 2000, a grid size of 1/60 was found to be sufficient for the flow in a cylindrical enclosure with the rotating bottom-wall (Lopez, 1990). Valentine and Jahnke (1994) also reported that there were no significant differences between the results using grid sizes of 1/60 and 1/120 for *Re* up to 3000 for the flow in a cylinder with both end-walls rotating. The above studies indicate that for *Re* less than 2000, a uniform grid size of 1/60 associated with second-order difference scheme is fine enough for these types of flow problems. However, to precisely capture the first onset of the vortex breakdown bubble, which is small, a uniform grid size of 1/200 was used to perform the present simulations. It was found that the errors in detecting *Re* at which the bubble appeared and disappeared are within 0.5% if the uniform grid sizes are varied between 1/100 and 1/200 for *Re* less than 2000.

Note that there is a discontinuity in the boundary conditions at the outer edge of the rotating disk. In the present study, as the grid size was chosen as 1/100 or 1/200,

there is a grid line located just at the outer edge of the rotating disk. Thus, the singularity problem was avoided as properties were evaluated at the control volume center. The comparison of the testing simulations between the grid sizes 1/100 and 1/200 also confirmed that the solutions are not affected by the discontinuity.

For further validation, the present code was used to capture the vortex breakdown phenomena in the enclosed chamber with the whole bottom-wall rotation. The occurrence of the vortex breakdown bubble is a continuous process with the increase of *Re*. The procedure of Mullin et al. (2000) was used to distinguish between parameter regions where the vortex breakdown bubble appears and disappears. Keeping the aspect ratio fixed and gradually increasing *Re* in steps of 10, the streamline was calculated and vortex breakdown was deemed to occur when a region was first visibly noted to be enclosed by the zero streamline.

The onsets of vortex breakdown are estimated in a wide range of parameter space as shown in Figure 5.2 and compared with Escudier's experimental results (Escudier, 1984). There are two boundaries for the curve of first vortex breakdown (solid line): as the Reynolds number increases, the right boundary shows the onset of vortex breakdown and the left boundary shows its disappearance. There is also an upper curve (dash line) which shows boundary between one and two vortex breakdown bubbles as the Reynolds number increases. The good agreement with Escudier's experimental results (Escudier, 1984) indicates that the present code is satisfactory for detecting the appearance and disappearance of the vortex breakdown bubbles.

5.2 Vortex Breakdown in a Micro-Bioreactor with a Partially Rotating Bottom-Wall

5.2.1 Boundary Curves for Vortex Breakdown

The boundaries for the onset of vortex breakdown are mapped in a plot of the Reynolds number and the aspect ratio (see Figures 5.3a to d), with different curves for different R/r_d. However there are two possible definitions for Re $\left(\Omega R^2/\nu,\ \Omega r_d^2/\nu\right)$ and the aspect ratio $\left(H/R,\ H/r_d\right)$, as either the cylinder radius R or the disk radius r_d may be chosen as the length scale. Thus four plots are presented to cover the combinations of dimensionless parameters.

First, consider the Reynolds number comprised by the cylinder radius, that is $Re = \Omega R^2/\nu$. The breakdown boundaries are presented in terms of H/r_d in Figure 5.3a and H/R in Figure 5.3b. In both plots, the effect of a smaller cylinder-disk ratio $R/r_d \leq 1.1$ is not significant. However at a larger cylinder-disk ratio $R/r_d \geq 1.3$ there seems to be a larger effect as the breakdown curves are further apart.

The Reynolds number characterizes the effect of angular momentum generated by the rotating bottom-wall. With the whole bottom-wall rotating it is appropriate to use the cylinder radius R as the length scale and the Reynolds number has been so defined by all previous studies with the whole bottom-wall rotating, for example by Lopez (1990). However with a partial bottom-wall rotating, using this definition may not be meaningful. It will show that a larger Reynolds number $Re = \Omega R^2/\nu$ is needed to cause vortex breakdown, especially with a smaller rotating disk or large R/r_d (see Figures 5.3a and b, in which the boundary curves are shifted higher for larger R/r_d). It

would seem that a smaller rotating disk is less effective in causing vortex breakdown. But this effect had arisen from defining *Re* based on a radius larger than that which is actually rotating; it does not mean that a smaller rotating disk needs a larger input of angular momentum, as characterized by Ωr_d^2, to cause vortex breakdown. Thus, using $Re = \Omega R^2/\nu$ may be somewhat misleading for a partially rotating bottom-wall as regards the influence of the angular momentum.

Next, consider the Reynolds number comprised by the rotating disk radius, that is $Re = \Omega r_d^2/\nu$. The breakdown boundaries are presented in terms of H/r_d in Figure 5.3c and H/R in Figure 5.3d. In both plots there is some effect of *Re*; but it is not as large as that in Figures 5.3a and b, which has been explained above to be misleading.

It is interesting that Figure 5.3c seems to indicate vortex breakdown will occur at a smaller *Re* if R/r_d is larger, for the same H/r_d, since the boundary curves are shifted downwards. In other words, a smaller rotating disk seems to be more effective in causing vortex breakdown, but this effect had arisen because H/R had become smaller. Thus using H/r_d may be misleading as it does not show the effect of R/r_d at a constant aspect ratio H/R; that is the real influence of R/r_d has not been isolated .

In a previous study on a partially rotating bottom-wall by Piva and Meiburg (2005) the results are presented in terms of parameters $\Omega r_d^2/\nu$ and H/r_d. However their main results are for larger R/r_d from 2.3 to 3.3. Their results show that for $R/r_d \geq 2.3$ the influence of the side-wall becomes insignificant. This is different from the present study with the cylinder-to-disk ratio $R/r_d \leq 1.6$ in which case the side-wall has more influence and the aspect ratio H/R is important. Thus it is more meaningful to

use the aspect ratio *H/R* if the side-wall is not distant. Only by considering a constant aspect ratio *H/R* can the effect of a varying R/r_d be isolated

In Figure 5.3d, the boundary curves for vortex breakdown are presented in terms of the Reynolds number $\Omega r_d^2/\nu$, the aspect ratio *H/R* and the cylinder-to-disk ratio R/r_d. The curves of different R/r_d are now closer to that of the whole bottom-wall rotation ($R/r_d = 1$). It shows the real effect of the partial rotation, unlike Figures 5.3a, b and c which may be misleading as explained earlier.

The critical aspect ratio to have vortex breakdown is reduced to $H/R \approx 1.0$ as compared to the whole bottom-wall rotation in which the critical aspect ratio is 1.2. The minimum *Re* for vortex breakdown is reduced to 850 as compared to 1000 for the whole bottom-wall rotation.

The shape of the boundary curves is rather similar to that of the whole bottom-wall rotation. With the increase of *Re*, the right boundary-curve shows transition from no bubble to single bubble; and the left boundary-curve, from single bubble to no bubble. The right boundary curve does not seem to show any consistent trend with R/r_d; *Re* for the onset of vortex breakdown reduces when R/r_d increases from 1.0 to 1.1, after which the onset *Re* increases with R/r_d. As for the left boundary curve, there is no much effect for R/r_d from 1.0 to 1.1, after which the Reynolds number increases with R/r_d.

5.2.2 Description of Flow Behaviour

A typical flow field in the meridional plane is shown by the streamline plot

labeled by Ψ in Figures 5.4a (i) and (ii) which are for $R/r_d = 1$, the case of the whole bottom-wall rotation. The flow pattern (left diagram labeled by Ψ) indicates an Ekman boundary layer at the bottom-wall generated by the rotation. The Ekman boundary layer imparts angular momentum ($\Gamma = rv_\theta$) to the fluid and centrifuges it towards the side-wall. The fluid then spirals up the side-wall followed by the top wall, forming boundary layers at these two walls. The angular momentum is nearly conserved (Spohn et al., 1998) during the radial inward flow near the upper region. Finally, the fluid on the top wall spirals down along the center axis to be sucked back into the Ekman layer.

In Figure 5.4a (i) $Re = 1200$, $H/R = 2$, there is no vortex breakdown bubble because this corresponds to the no-breakdown region (Figure 5.3d) of the boundary plot. However, for the condition of $Re = 1500$ and $H/R = 2$, the boundary plot indicates one vortex breakdown bubble (Figure 5.3d); and it is consistent that the flow pattern in Figure 5.4a (ii) shows a vortex breakdown bubble. The location, size and shape of the bubble agree well with the experimental flow visualization reported by Escudier (1984).

In Figures 5.4a (i) and (ii) are also shown diagrams of the angular momentum labeled by Γ and azimuthal vorticity labeled by ω. It is noted that the vortex breakdown bubble is located near the regions where the angular momentum is wavy (see Figure 5.4a (ii) under label Γ) and where the azimuthal vorticity is positive (see Figure 5.4a (ii) under label ω). This is consistent with the observation of Lopez (1990) (negative in Brown and Lopez (1990)).

5.2.3 Mechanism of Vortex Breakdown

As pointed out by Brown and Lopez (1990), vortex breakdown can be explained from a balance between the radial pressure gradient and the centrifugal force. In Figure 5.4 and 5.5 are also presented the contours of the centrifugal force, the radial pressure gradient force and the resultant of the two forces.

Ideally, to show the sequence of events leading to vortex breakdown the force and pressure-gradient contours should be presented before the onset of vortex breakdown. This sequence of events has been explained by Lopez (1990) in terms of angular momentum. In the present study, the force and pressure gradient contours have been computed for cases before and after vortex breakdown. However, illustrations are presented for cases before and just after vortex breakdown occurred which shows more clearly the differences in the contours. In most cases, the vortex breakdown bubbles are small and thus have less effect on the force and pressure gradient contours.

Generally, the resultant force has a positive region near the top axial region (See Figure 5.4 under the label "Resultant Force"), which makes the angular momentum contours and streamlines deviate away from the axis there (See Figure 5.4 under the label Γ). The flow divergence and its subsequent turning towards the axis have been explained by Brown and Lopez (1990). On the diverging stream surface the centrifugal force v^2/r is decreased due to conservation of angular momentum. Also the axial and azimuthal velocity components are reduced due to the divergence, leading to an increase in pressure and reduction in radial pressure gradient. However

the centrifugal force reduces more than the radial pressure gradient. So the flow has turning towards the axis. This explains the waviness in the stream surface. When the amplitude of the wave increased and the wavelength decreased, the associated axial deceleration causes the flow to stagnate below the crest of the wave. A near spherical region of recirculating fluid is formed, termed a vortex breakdown bubble.

5.2.4 Effect of Reynolds Number

The effect of *Re* on the boundary of vortex breakdown is summarized in Figure 5.3d. At an aspect ratio greater than 1.2, there is no vortex breakdown bubble at a low *Re* lower than 1000 (for whole bottom-wall rotation). As the Reynolds number increases, there is transition to vortex breakdown bubble (at the right boundary curve). The vortex breakdown bubble grows larger with *Re*. As the Reynolds number increases further, the vortex breakdown bubble grew smaller and then disappears (at the left boundary curves).

The contours of streamlines, angular momentum and vorticity are shown in Figures 5.4a (i) Re = 1200 and (ii) Re = 1500 for the case of the whole bottom-wall rotation, R/r_d = 1. It shows the change to vortex breakdown as *Re* is increased to 1500, in accordance with the vortex boundary plot of Figure 5.3d, for aspect ratio 2.

At higher *Re*, a greater proportion of the fluid's angular momentum is advected to the upper core region (near the top wall at the axial region), as may be seen by comparing Figure 5.4a (ii) with 5.4a (i); this gives a higher centrifugal force. The imbalance of centrifugal force and radial pressure gradient (see resultant force in

Figure 5.4a i and ii) generates a weak centrifugal wave on the fluid as it moves downwards away from the top wall near the axial region. Thus the contours of angular momentum near the upper axial region show waviness, as seen in Figure 5.4a (ii), which is a mechanism for vortex breakdown as explained by Lopez (1990). This mechanism explains the transition to vortex breakdown and the growth in bubble size.

However, at a smaller aspect ratio of 1.3, the opposite trend occurs; with the increase of *Re* from 1200 to 1500, vortex breakdown disappears (Figures 5.5a i and ii). Although this phenomenon is known, there has been little explanation for it. At a higher *Re*, similar to the case of the high aspect ratio of 2, a greater proportion of the fluid's angular momentum is advected to the upper core region (near the top wall at the axial region). The higher angular momentum gives steeper gradient in its contours near the top surface, due to the small aspect ratio. Thus there is greater loss of angular momentum, due to viscous losses at the top surface; and hence smaller centrifugal force near the upper core region. The resultant force is thus less at a higher *Re*. The centrifugal wave is not strong enough to generate vortex breakdown.

The region of positive azimuthal vorticity near the axial region, coinciding roughly with the wavy streamlines, is extended noticeably at the higher *Re*, as seen by comparing ω plots of Figures 5.4a (i) and (ii). The development of a recirculation bubble is a result of the positive azimuthal vorticity, as explained by Brown and Lopez (1990) (negative vorticity in their paper) through the stretching and tilting of vortex lines.

5.2.5 Effect of Aspect Ratio

The effect of the aspect ratio on the boundary of vortex breakdown is shown in Figure 5.3d. For higher aspect ratio, the vortex breakdown bubble disappears as the aspect ratio increases beyond the right boundary curve; for example there is no vortex breakdown bubble at H/R = 2 for a Re of 1200. To examine the aspect ratio effects, the streamlines, angular momentum and azimuthal vorticity are shown in Figure 5.5a (i) and Figure 5.4a (i) for H/R = 1.3 and H/R = 2 respectively, at Re of 1200. The streamline contours show that there is a change to no vortex breakdown as the aspect ratio is increased from H/R = 1.3 to 2.0. At H/R = 2, the angular momentum is lower at the upper core region (near the top wall at the axial region).

The angular momentum of the fluid is decreased by viscous dissipation along the cylinder side wall (Spohn et al., 1998). Hence, for a chamber with a bigger aspect ratio, the angular momentum near the top axial region is less than that for a smaller aspect ratio. Thus, the centrifugal force is smaller which leads to the resultant force being smaller and the centrifugal wave is not big enough to generate vortex breakdown (Compare Figures 5.4a i and 5.5a i).

However for lower aspect ratio, the vortex breakdown bubble disappears as the aspect ratio decreases to values before the left boundary curve; for example there is no vortex breakdown bubble at H/R = 1.3 for a Re of 1500. The effects of the aspect ratio on the streamlines, angular momentum and azimuthal vorticity are shown in Figure 5.5a (ii) and Figure 5.4a (ii) for H/R = 1.3 and H/R = 2 respectively, at a Re of 1500. The streamline contours show that there is a change to no vortex breakdown as the

aspect ratio is reduced to 1.3, as seen in Figure 5.4a (ii). At *H*/R = 1.3, the angular momentum is lower at the upper core region (near the top wall at the axial region).

At a smaller aspect ratio, there is high viscous loss near the top lid region, as the angular momentum gradients are steeper due to the chamber being more confined. Reducing the aspect ratio further will increase the viscous effect of the top lid which leads to decrease of the angular momentum; and hence decrease the centrifugal force and resultant force. Thus, vortex breakdown disappear with the reduction of the aspect ratio (Compare Figures 5.4a ii and 5.5a ii).

To summarize there are two main mechanisms which explain the effect of aspect ratio. When the aspect ratio is high, the losses are mainly from the side wall and increasing the aspect ratio leads to vortex breakdown disappearance. However, when the aspect ratio is small the losses are mainly from the top lid and reducing the aspect ratio will lead to vortex breakdown disappearance.

5.2.6 Effect of Cylinder-to-Disk Ratio

In Figures 5.4b to d and Figures 5.5b to d are shown diagrams of streamline Ψ, angular momentum Γ and azimuthal vorticiy ω for the case of the partial bottom-wall rotation. The arrow below the bottom-wall indicates the radius of the rotating wall. As compared with the whole bottom-wall rotation, the partial bottom-wall rotation has some effect on the onset and size of the vortex breakdown bubble, which are consistent with that of the boundary curves of Figure 5.3d.

The contours of streamlines show that the corner vortex becomes obvious for the

smaller rotating disk (see Figure 5.4d and Figure 5.5d) as the fluid is unable to turn a sharp corner. In a previous study by Piva and Meiburg (2005) the corner vortex extends to the top surface at a large R/r_d greater than 2.3.

The distribution of the angular momentum is of particular interest in the present study. The fluid obtains its angular momentum in the Ekman layer on the rotating disk and loses it as it moves along the stationary bottom- and side- walls. The momentum contours clearly show that it is being dissipated when the fluid leaves the rotating disk (see Figure 5.4d below label Γ) and moves along the stationary bottom-wall.

The azimuthal vorticity contours show some differences as compared with those of the whole bottom-wall rotation. The positive azimuthal vorticity near the side-wall starts from the edge of the rotating disk (Figure 5.4d for partial bottom-wall rotation) instead of from the corner (Figure 5.4a for whole bottom-wall rotation), which is consistent with the development of an additional boundary layer along the stationary bottom-wall.

It is noted that when there is a vortex breakdown bubble the angular momentum shows waviness (for example compare Γ plots of Figures 5.4b (i) and (ii)). Also the positive azimuthal vorticity has a larger region (compare ω plots of Figures 5.4b (i) and (ii)). These two features are consistent with the results of Lopez (1990).

For the right boundary curve of Figure 5.3d, it is shifted rightwards when R/r_d is increased from 1.0 to 1.1. Then it is shifted leftwards when R/r_d is further increased from 1.1 to 1.5. There seems to be two opposing influences of R/r_d; and thus its resultant effect depends on which one is more dominant.

The opposing influences of R/r_d may be interpreted by using the physical mechanism of vortex breakdown for swirling flow as explained by Brown and Lopez (1990). The central core flow diverges if the centrifugal force exceeds the radial pressure gradient. The initial increase of R/r_d 1.0 to 1.1 has the effect of increasing the centrifugal force near the upper core region, because the fluid is rotated through a smaller rotating wall which gives more swirling motion away from the side wall where there is viscous loss of angular momentum. The increased centrifugal force causes an imbalance with the pressure gradient, which leads to bigger vortex breakdown bubble. Thus the physical aspect ratio has to be larger for vortex breakdown to cease; that is the effective aspect ratio has become smaller.

The increase of R/r_d from 1.1 to 1.5 has the effect of causing loss of angular momentum because the stationary part of the bottom-wall is bigger. The centrifugal force at the axial region near the top wall is reduced which leads to cessation of vortex breakdown. As compared to the whole bottom-wall rotation, R/r_d of 1.5 has no vortex breakdown at a smaller aspect ratio. That is, the effective aspect ratio seems to be larger; thus the physical aspect ratio can be smaller for vortex breakdown to cease.

Figure 5.3d (left boundary curve) shows that with a smaller rotating disk, the boundary curve is shifted rightwards when the cylinder-to-disk ratio is increased from 1.0 to 1.1. Then it is shifted leftwards when the cylinder-to-disk ratio is further increased from 1.1 to 1.5. Again, there seems to be two opposing influences of R/r_d; and thus its resultant effect depends on which one is more dominant.

The initial increase of R/r_d 1.0 to 1.1 has the effect of reducing the centrifugal

force at axial core region near the top, because the fluid is rotated through a smaller rotating wall which gives more swirling motion at the top region. The viscous loss of angular momentum there is more due to the steeper gradient. The reduced centrifugal force leads to no vortex breakdown bubble.

The increase of R/r_d from 1.1 to 1.5 has the effect of reducing viscous loss of angular momentum from the top surface as the main swirling motion is nearer to the axis. The centrifugal force at the axial region near the top wall is higher which leads to vortex breakdown. As compared to the whole bottom-wall rotation, the cylinder-to-disk ratio R/r_d of 1.5 has no vortex breakdown at a smaller aspect ratio.

There is an aspect ratio H/R above which vortex breakdown first occurs (see left boundary curves of Figure 5.3d). It is seen that this critical aspect ratio is less than that of the whole bottom-wall rotation; the critical value is 0.97 for R/r_d = 1.5. The critical value is summarized in Figure 5.6, which decreases approximately linearly with the increase of R/r_d. The additional stationary bottom-wall acts like a side-wall, which seems to have the effect increasing the aspect ratio; thus vortex breakdown may occur at a smaller aspect ratio.

5.3 Effects of Vortex Breakdown in Bioreactor

In this section, shear stress and oxygen concentration distributions in the micro-bioreactor with free surface will be investigated to show the effect of vortex breakdown on animal cell culture. The cylinder-to-disk ratio is constant at R/r_d = 1, i.e. only the micro-bioreactor with the whole bottom-wall rotating will be considered.

5.3.1 Computational Model

Figure 5.7 schematically shows the flow model in the micro-bioreactor. The governing equations for the fluid flow have been introduced in Section 5.1. It should be noted that the deformation of the free surface due to the rotation of the fluid is proportional to the Froude number, which is defined as:

$$Fr = \Omega^2 R^2 / gH \tag{5.7}$$

where g is the gravitational constant. In the present study, as the Reynolds number is less than 2000, the Froude number Fr is negligibly small (in the order of 10^{-3}) and the free surface is assumed as a flat stress-free surface.

Thus, the free surface is modeled by having a mid-plane in a cylinder of twice the height, in which both end-walls rotate at the same speed. This assumption has been applied by several authors to investigate the swirling flow in the chamber with the free surface (Valentine and Jahnke, 1994; Lopez, 1995; Piva and Meiburg, 2005).

The oxygen transport in the bioreactor is considered as oxygen is a key substrate in aerobic cell culture bioprocesses. Oxygen consumption by animal cells is assumed to be based on Michaelis-Menten equation. The governing equation can be written as:

$$\frac{1}{r}\frac{\partial\left(rv_r C\right)}{\partial r}+\frac{\partial\left(v_z C\right)}{\partial z}=D_f\left[\frac{1}{r}\frac{\partial}{\partial r}\left(r\frac{\partial C}{\partial r}\right)+\frac{\partial^2 C}{\partial z^2}\right]-\frac{\gamma V_m C}{C+k_m} \tag{5.8}$$

The zero flux conditions are imposed for both side-wall and bottom-wall. The oxygen concentration at the top surface is assumed constant and equal to the saturation concentration C_0 in the culture medium as determined from Henry's law.

For oxygen transport, the important non-dimensional parameters are the Damkohler number $Da = \gamma V_m R^2 \big/ \left(C_0 D_f\right)$ and the Schmidt number $Sc = \nu / D_f$. In

the present study, only the effect of the Damkohler number is considered and varied from 5 to 70. The Schmidt number *Sc* is fixed at 500. The oxygen concentration *C* and the half-saturation parameter k_m in this chapter have been non-dimensionalized by the top surface concentration C_0.

In the present study, the bioreactor has a radius *R* of 10 mm. The density of the culture medium is 10^3 kg m^{-3} and the viscosity μ is 10^{-3} Pa s. The top surface concentration C_0 is equal to 0.27 mol m^{-3}. For a typical CHO cell culture (Deshpande and Heinzle, 2004), the maximum oxygen uptake rate V_m is 8×10^{-17} mol $cell^{-1}$ s^{-1}.

5.3.2 Oxygen Transport

Figure 5.8 shows the flows in the bioreactor with the free surface for the aspect ratio *H/R* = 1 at different *Re*. When the Reynolds number is less than 450, there is no breakdown bubble (Figure 5.8a). However, when the Reynolds number is between 450 and 475, a detached bubble is observed (Figure 5.8b). If the Reynolds number is above 475, the upper stagnation point of the bubble approaches the surface, forming an attached bubble (Figure 5.8c). Interestingly, when the Reynolds number is beyond 1125, the bubble is not at the axis and forms a closed recirculation torus (Figure 5.8d).

The flow patterns obtained by our computational method agree well with the experimental data observed by Spohn et al. (1993). However, the critical *Re* for the onsets of the non-attached and attached bubbles are slightly lower (by about 5%) than those reported by the experiments. This may be due to the assumption of a flat stress-free surface.

Figure 5.9 shows the corresponding oxygen concentration distributions for the above flow at a fixed *Da* = 40. Generally, the concentration is lower in the recirculation region and higher near the axis region. In the recirculation center, the concentration is the lowest. The concentration level in the bioreactor increases with the increase of *Re*.

When vortex breakdown occurs, the higher concentration region near the axis extends with the bubble. The concentration in the center of the vortex breakdown bubble is higher than that in the main recirculation center (Figures 5.9b to f). The bubble occurs near the top axis region where oxygen concentration is higher and its size is smaller compared with the main recirculation region. Thus, oxygen can be easily transported into the bubble center, resulting in a higher concentration there.

Figure 5.10 summarizes the minimum concentrations in the vortex breakdown center and the main recirculation center for different *Re* and *Da* in the bioreactors with different *H/R*. The minimum concentrations in both regions decrease with the increase of *Da* due to higher oxygen consumption rate. The concentration in the vortex breakdown center is much higher than that in the main recirculation center at the same *Da*.

The minimum concentration in the main recirculation center increases with the increase of *Re* as the flow becomes stronger (Figures 5.10a, c and e). However, the minimum concentration in the vortex breakdown center first decreases with the increase of *Re* (Figures 5.10b, d and f) as the vortex breakdown region extends (Figures 5.8b to d). When the Reynolds number increases furthermore, the

concentration increases as the vortex breakdown region becomes smaller (see Figures 5.8d and e) and the flow around the bubble becomes stronger.

From Figure 5.10a, it is seen that *Re* of 1000 can support cell culture with *Da* up to 50 (assume a critical dimensionless oxygen concentration of 0.05 for the cell hypoxia), corresponding to the maximum cell density about 3×10^{12} cells m^{-3}. The result is comparable with the typical value of 1.8×10^{12} cells m^{-3} reported for cell culture in mechanically stirred bioreactor (Frahm et al., 2002).

After the oxygen concentration field has been obtained, the volumetric oxygen transfer coefficient k_La can be determined as mentioned in Chapter 4. Figure 5.11 shows the variation of k_La at different *Re* and *H/R*. It is seen that k_La increases with the increase of *Re* and decreases with the increase of *H/R*. For the bioreactor at *H/R* = 1, the value of k_La is about 1.3×10^{-3} s^{-1} at *Re* = 1800. The results are comparable with k_La of O(10^{-3} s^{-1}) in a shake-flask (Zhang et al., 2005) and in the micro-bioreactor of Yu et al. (2005b). Thus, k_La in the present micro-bioreactor with a bottom-wall rotating is acceptable for animal cell culture.

5.3.3 Shear Stress

All derivatives with respect to the circumferential direction in the shear-stress formulations are zero due to the axisymmetric assumption. The three shear-stress components, $\overline{S_{r\theta}}$, $\overline{S_{\theta z}}$ and $\overline{S_{rz}}$, are non-dimensionalized by $\mu\Omega$ (Dusting et al., 2006). Similar to Equation (4.15), the mean shear stress is defined as:

$$\overline{S_M} = \frac{1}{3}(\overline{S_{r\theta}}^2 + \overline{S_{\theta z}}^2 + \overline{S_{rz}}^2)^{\frac{1}{2}} \tag{5.9}$$

Figure 5.12 shows the mean shear-stress and the three shear-stress-component fields in the meridional plane for H/R = 1 for Re = 1000. The mean shear stress and the three components are extremely high at the bottom corner where the velocity gradient is very deep due to the conjunction of the rotating bottom-wall and the stationary side-wall there. Along the side- and bottom- wall, the shear stresses are higher due to the boundary layer shearing. Another region with higher stresses locates at the right boundary of the vortex breakdown bubble. In other regions, especially near the axis region, the stresses are low. The results agree well with the experimental observation of Dusting et al. (2006).

Figure 5.13 shows the mean shear-stress distributions in the top and central region where vortex breakdown appears for the case H/R =1 with different Re, which demonstrates the effect of vortex breakdown on mean shear-stress distributions. When vortex breakdown occurs, a region with higher shear stress is formed at the right boundary of the vortex breakdown bubble. However, within the vortex breakdown bubble, the shear stress is low. With increasing Re, the high shear-stress region moves rightwards and upwards, corresponding to the movement of the bubble. The magnitude of shear stress in this region increases with the increase of Re. These results are also consistent with Dusting et al.'s findings (2006).

Although the vortex breakdown bubble causes a non-uniform stress distribution in the top and central region of the bioreactor, it does not affect the maximum mean shear stress which occurs at the bottom corner.

5.4 Concluding Remarks

The flow in an enclosed cylinder with a partially rotating bottom-wall may be of interest to a cell-culture bioreactor stirred by a magnetic rotating-rod at the bottom, in which the mixing parameter and shear stress may be influenced by the vortex breakdown phenomena. This study presents non-dimensional results of the boundary curves for the first onset of vortex breakdown. Various ways to define the non-dimensional parameters were investigated. It is concluded that the Reynolds number should be based on the disk radius, whereas the aspect ratio should be based on cylinder radius. An additional parameter is the cylinder-to-disk ratio. It is shown that correlating the results in terms of these parameters, so defined, is more meaningful to avoid ambiguous interpretation of the effects of the partial rotation. The present definition of *Re* is different from that in previous studies with whole bottom-wall rotating; but similar to that of Piva and Meiburg (2005), whose flow chamber also has a partially rotating bottom-wall but with a free surface. However their aspect ratio is differently defined as H/r_d because their cylinder-to-disk ratio R/r_d is varied to a value much larger than that of the present study.

The critical aspect ratio to have vortex breakdown is found to be reduced to about 1, as compared to the whole bottom-wall rotation in which the critical aspect ratio is 1.2. The minimum *Re* for vortex breakdown is reduced to 850 as compared to 1000 for the whole bottom-wall rotation. At the same *Re*, R/r_d influences the vortex breakdown boundary curve by either increasing or reducing the effective aspect-ratio. Thus the physical aspect-ratio for onset or cessation of vortex breakdown is changed

as compared with that of whole bottom-wall rotation. The influence may be interpreted from the balance between radial pressure gradient and centrifugal force, a physical mechanism of vortex breakdown as explained by Brown and Lopez (1990). Results are presented of the contours of the streamlines, angular momentum and azimuthal vorticity; these detailed contours are consistent with the findings of Lopez (1990) that vortex breakdown occurs when, near the axial region, the angular momentum contours is wavy and the extent of positive azimuthal vorticity is larger.

It is well known that animal cells are sensitive to shear stress and nutrient concentration. When vortex breakdown occurs in bioreactors, the flow pattern undergoes a sudden change, which may affect shear stress (Dusting et al., 2006) and nutrient concentration distribution as a consequence. Thus, vortex breakdown may also influence the function and viability of cells.

The effects of vortex breakdown on shear stress and oxygen concentration fields in the present micro-bioreactor are evaluated. It is found that within the center of the vortex breakdown bubble, the shear stress is substantially low but the oxygen concentration is relatively high. Within the center of the main recirculation, the concentration is the lowest and the cell may experience hypoxia there at a low *Re* or high *Da*. At the edge of the main recirculation, the cells are subjected to very high stress when they travel through the bottom corner region, which may cause cell lysis. Thus, the appropriate location of the scaffold is at the center of the vortex breakdown bubble, where shear stress is low (Mununga et al., 2004; Dusting et al., 2006) and the oxygen concentration is higher.

Chapter 6
Swirling Flow and Mass Transfer in a Micro-Bioreactor with a Scaffold

The porous scaffold is widely used for animal cell culture as it provides a three-dimensional structure for cell attachment and tissue organization (Freed et al., 1994a). However, there are very few works on investigating flow and mass transport both around and within a scaffold in bioreactors. In Chapter 2, a numerical method has been developed to simulate the coupled transport problem in both homogenous fluid and porous medium regions. In the present chapter, this method is applied to predict the flow and mass transport in a micro-bioreactor with a cell scaffold. Based on the numerical results, the effect of the presence of the scaffold on the flow and oxygen concentration fields in the bioreactor is studied. The effects of the important parameters, such as *Re* and *Dar*, on flow and oxygen concentration fields inside and outside the scaffold are investigated.

6.1 Computational Methods

6.1.1 Mathematical Model

The micro-bioreactor with a cell scaffold is shown schematically in Figure 6.1a. The micro-bioreactor consists of a cylinder chamber filled with culture medium. The medium mixing is generated by the rotating bottom-wall. The scaffold with a concentric hole is coaxially mounted in the bioreactor. All animal cells are assumed to

uniformly attach to the scaffold and no animal cells suspend in the culture medium. The substrate considered here is oxygen as insufficient oxygen supply is one of the limiting factors for cell culture in scaffold.

The computational domain for the bioreactor with the scaffold is shown in Figure 6.1b. As the scaffold and the bioreactor can be regarded as two concentric cylinders, the geometry is axisymmetric. For a typical application, the height of the bioreactor is 10 mm and the diameter is 20 mm. The thickness of the scaffold is 2 mm and the diameter is 12 mm. The diameter of the hole is 3 mm. The scaffold is fixed at the 60% height of the bioreactor.

The porous medium is assumed to consist of the scaffold structure and animal cells attached on the scaffold. ε_s and ε_c are the volume fractions occupied by the scaffold and animal cells respectively. The porosity of the porous medium ε can be calculated as:

$$\varepsilon = 1 - \left(\varepsilon_s + \varepsilon_c \right) \tag{6.1}$$

Generally, for the scaffold without animal cell, the porosity may vary from 0.6 to 0.95 (Cooper et al., 2005; Gugala and Gogolewski, 2005). The permeability of the scaffold is in the range of 10^{-12} to 10^{-9} m^2 (Wang and Tarbell, 2000; Li et al., 2003). However, when animal cells attach to the scaffold, the porosity and permeability may change with the cell proliferation.

Considering the culture medium as a Newtonian fluid and oxygen consumption by the animal cells to be based on Michaelis-Menten equation, the governing equations for the flow and oxygen transport (Lasseux et al., 2004; Wood et al., 2002;

Galban and Locke, 1999) can be written as:

For homogenous fluid region:

$$\frac{1}{r}\frac{\partial\left(rv_r\right)}{\partial r}+\frac{\partial v_z}{\partial z}=0 \tag{6.2}$$

$$\frac{1}{r}\frac{\partial\left(rv_rv_z\right)}{\partial r}+\frac{\partial\left(v_zv_z\right)}{\partial z}=-\frac{1}{\rho}\frac{\partial p}{\partial z}+\nu\left[\frac{1}{r}\frac{\partial}{\partial r}\left(r\frac{\partial v_z}{\partial r}\right)+\frac{\partial^2 v_z}{\partial z^2}\right] \tag{6.3}$$

$$\frac{1}{r}\frac{\partial\left(rv_rv_r\right)}{\partial r}+\frac{\partial\left(v_zv_r\right)}{\partial z}=-\frac{1}{\rho}\frac{\partial p}{\partial r}+\nu\left[\frac{\partial}{\partial r}\left(\frac{1}{r}\frac{\partial}{\partial r}\left(rv_r\right)\right)+\frac{\partial^2 v_r}{\partial z^2}\right]+\frac{v_\theta^2}{r} \tag{6.4}$$

$$\frac{1}{r}\frac{\partial\left(rv_rv_\theta\right)}{\partial r}+\frac{\partial\left(v_zv_\theta\right)}{\partial z}=\nu\left[\frac{\partial}{\partial r}\left(\frac{1}{r}\frac{\partial}{\partial r}\left(rv_\theta\right)\right)+\frac{\partial^2 v_\theta}{\partial z^2}\right]-\frac{v_rv_\theta}{r} \tag{6.5}$$

$$\frac{1}{r}\frac{\partial\left(rv_rC^*\right)}{\partial r}+\frac{\partial\left(v_zC^*\right)}{\partial z}=D_f\nabla^2C^* \tag{6.6}$$

For porous medium region:

$$\frac{1}{r}\frac{\partial\left(rv_r\right)}{\partial r}+\frac{\partial v_z}{\partial z}=0 \tag{6.7}$$

$$\frac{1}{r}\frac{\partial}{\partial r}\left(\frac{rv_rv_z}{\varepsilon}\right)+\frac{\partial}{\partial z}\left(\frac{v_zv_z}{\varepsilon}\right)=-\frac{1}{\rho}\frac{\partial\left(\varepsilon p^*\right)}{\partial z}+\nu\left[\frac{1}{r}\frac{\partial}{\partial r}\left(r\frac{\partial v_z}{\partial r}\right)+\frac{\partial^2 v_z}{\partial z^2}\right]-\frac{\varepsilon v_rv_z}{r}$$
$$-\frac{\nu\varepsilon}{K}v_z-\frac{\varepsilon C_F\sqrt{v_z^{\,2}+v_r^{\,2}+v_\theta^{\,2}}}{\sqrt{K}}v_z \tag{6.8}$$

$$\frac{1}{r}\frac{\partial}{\partial r}\left(\frac{rv_rv_r}{\varepsilon}\right)+\frac{\partial}{\partial z}\left(\frac{v_zv_r}{\varepsilon}\right)=-\frac{1}{\rho}\frac{\partial\left(\varepsilon p^*\right)}{\partial r}+\nu\left[\frac{\partial}{\partial r}\left(\frac{1}{r}\frac{\partial}{\partial r}\left(rv_r\right)\right)+\frac{\partial^2 v_r}{\partial z^2}\right]+\frac{\varepsilon v_\theta^2}{r}$$
$$-\frac{\nu\varepsilon}{K}v_r-\frac{\varepsilon C_F\sqrt{v_z^{\,2}+v_r^{\,2}+v_\theta^{\,2}}}{\sqrt{K}}v_r \tag{6.9}$$

$$\frac{1}{r}\frac{\partial}{\partial r}\left(\frac{rv_rv_\theta}{\varepsilon}\right)+\frac{\partial}{\partial z}\left(\frac{v_zv_\theta}{\varepsilon}\right)=\nu\left[\frac{\partial}{\partial r}\left(\frac{1}{r}\frac{\partial}{\partial r}\left(rv_\theta\right)\right)+\frac{\partial^2 v_\theta}{\partial z^2}\right]-\frac{\varepsilon v_rv_\theta}{r}$$
$$-\frac{\nu\varepsilon}{K}v_\theta-\frac{\varepsilon C_F\sqrt{v_z^{\,2}+v_r^{\,2}+v_\theta^{\,2}}}{\sqrt{K}}v_\theta \tag{6.10}$$

$$\frac{1}{r}\frac{\partial\left(rv_rC^*\right)}{\partial r}+\frac{\partial\left(\rho v_zC^*\right)}{\partial z}=D_{eff}\nabla^2C^*-\gamma V_m\frac{K_{eq}C^*}{K_{eq}C^*+k_m} \tag{6.11}$$

where C^* is the intrinsic average concentration in both homogenous fluid region and porous medium region; K_{eq} is the partition coefficient; and D_{eff} is the effective diffusivity of oxygen in the porous medium.

It is noted that Equation (6.11) starts from a boundary value problem of diffusion-convection and reaction in cell culture systems. The diffusion-convection equation is applied to describe nutrient transport in culture medium. The scaffold is considered as a rigid impermeable phase while animal cells is considered as a continuum and the physical model used in this phase to describe reaction and mass transport is a single diffusion-reaction equation. The set of microscopic equations governing transport phenomena in the culture systems are averaged in a representative elementary volume, which is much larger than the pore scale considerately smaller than the macroscopic flow domain, to form a macroscopic, one-equation model to describe the nutrient transport by diffusion and convection. A complete derivation of Equation (6.11) has been addressed in details in the work by Lasseux et al. (2004).

To solve Equation (6.11), the effective diffusivity for oxygen has to be determined first. It is difficult to calculate the effective diffusivity as it depends on both the geometrical structure and on the hydrodynamic in the fluid with in the porous medium. In the present study, the effective diffusivity is estimated by the Maxwell's equation (Wood and Whitaker, 2000; Wood et al., 2002):

$$\frac{D_{eff}}{D_f} = \frac{3\kappa - 2\varepsilon(\kappa - 1)}{3 + \varepsilon(\kappa - 1)} \tag{6.12}$$

where $\kappa = K_{eq} D_c / D_f$ and D_c is the diffusivity of oxygen in animal cell phase. And in the present study, K_{eq} and κ are set at 1 and 0.25 respectively (Wood and Whitaker,

2000). By substituting Equation (6.12), Equation (6.11) becomes:

$$\frac{1}{r}\frac{\partial\left(rv_r C^*\right)}{\partial r}+\frac{\partial\left(\rho v_z C^*\right)}{\partial z}=\frac{3\kappa-2\varepsilon\left(\kappa-1\right)}{3+\varepsilon\left(\kappa-1\right)}D_f\nabla^2 C^*-\gamma V_m\frac{K_{eq}C^*}{K_{eq}C^*+k_m} \tag{6.13}$$

Equation (6.12) neglects the resistance for mass transfer across the cell membrane. If this resistance has to be considered, the effective diffusivity can be approximated by the Chang's unit cell model (Chang, 1983; Wood and Whitaker, 2000).

As the flow is generated by the rotating bottom-wall, the Reynolds number is still defined as $Re = \Omega R^2/\nu$. Re is kept within 2000 to ensure steady flow condition. The Darcy number is defined as $Dar = K/R^2$ and the range of Dar varies from 10^{-7} to 10^{-5}. The important non-dimensional parameters for oxygen transport are the Damkohler number $Da=\gamma V_m R^2/\left(C_0 D_f\right)$ and the Schmidt number $Sc=\nu/D_f$. The aspect ratio is fixed at H/R = 1.0.

In fact, the effective Reynolds number for the flow around the porous scaffold is small although the present Reynolds number based on the rotating bottom-wall is up to 2000. The effective reference length scale for the scaffold is about half of the bioreactor radius. From the numerical results in Chapter 4, it is found that the velocity components in r-z plane at the upper region of the bioreactor without the scaffold are less than 1/20 of the swirling velocity ΩR. Therefore, the effective Reynolds number for the flow around the porous scaffold is less than 40 even the Reynolds number based on the rotating bottom-wall is up to 2000. Based on this estimation, the assumption of the steady flow in the bioreactor with the scaffold is still valid.

6.1.2 Boundary Conditions

6.1.2.1 Interface Conditions

To solve Equations (6.2) to (6.11), the appropriate boundary conditions have to be imposed at the interface between the homogenous fluid and porous medium regions. The continuities of velocity components at the interface are given by:

$$v_r\big|_{\text{fluid}} = v_r\big|_{\text{porous}} = v_r\big|_{\text{interface}} \tag{6.14}$$

$$v_z\big|_{\text{fluid}} = v_z\big|_{\text{porous}} = v_z\big|_{\text{interface}} \tag{6.15}$$

$$v_\theta\big|_{\text{fluid}} = v_\theta\big|_{\text{porous}} = v_\theta\big|_{\text{interface}} \tag{6.16}$$

The shear-jump condition can be expressed as:

$$\frac{\mu}{\varepsilon}\frac{\partial v_t}{\partial n}\bigg|_{\text{porous}} - \mu\frac{\partial v_t}{\partial n}\bigg|_{\text{fluid}} = \beta\frac{\mu}{\sqrt{K}}v_t\bigg|_{\text{interface}} + \beta_1\rho v_t^2\big|_{\text{interface}} \tag{6.17}$$

where n is the unit vector normal to the interface, v_t is the velocity component parallel to the interface. In the present chapter, β and β_1 are set to 0.7 and 0 respectively.

The continuity of the normal stress can be written as:

$$\frac{\mu}{\varepsilon}\frac{\partial v_n}{\partial n}\bigg|_{\text{porous}} - \mu\frac{\partial v_n}{\partial n}\bigg|_{\text{fluid}} = 0 \tag{6.18}$$

where v_n is the velocity component perpendicular to the interface.

As for the oxygen transport equation, the interface boundary conditions can be given as (Valencia-López et al., 2003):

$$\varepsilon D_{eff}\frac{\partial C^*}{\partial n}\bigg|_{\text{porous}} - D_f\frac{\partial C^*}{\partial n}\bigg|_{\text{fluid}} = 0 \tag{6.19}$$

$$C^*\big|_{\text{fluid}} = C^*\big|_{\text{porous}} = C^*\big|_{\text{interface}} \tag{6.20}$$

6.1.2.2 Other Boundary Conditions

For the velocity, the non-slip boundary condition is imposed on the solid wall. As mentioned in Chapter 5, the deformation of the free surface due to the rotation of the fluid is proportional to the Froude number *Fr*. As the Reynolds number is less than 2000, *Fr* is negligibly small (in the order of 10^{-3}). Thus, the free surface can be simplified as a flat stress-free surface. For the oxygen transfer, the zero flux conditions are imposed for both side-wall and bottom-wall. The oxygen concentration at the free surface is assumed constant and equal to the saturation concentration C_0 in the culture media as determined from Henry's law.

6.1.3 Numerical Method

The discretization procedures for the velocity components at the interface have been introduced in Chapter 2. In the present chapter, the emphases are on the treatment of C^* at the interface.

The derivatives of C^* at the interface is also calculated from the values at auxiliary nodes L' and R'; these nodes lie at the intersection of the cell face normal n and straight lines connecting nodes *L* and *N* or *R* and *NR*, respectively. The normal gradients of C^* at the interface can be calculated by using the first order difference approximation:

$$\left.\frac{\partial C^*}{\partial n}\right|_{\text{porous}} = \frac{C^*\big|_{E'} - C^*\big|_e}{L_{eE'}} \quad \text{and} \quad \left.\frac{\partial C^*}{\partial n}\right|_{\text{fluid}} = \frac{C^*\big|_e - C^*\big|_{P'}}{L_{P'e}} \tag{6.21}$$

The values of C^* at L' and R' can be calculated by using bilinear interpolation or by using the gradient at the control volume center:

$$C^*\big|_{P'} = C^*\big|_p + \left(gradC^*\right)_P \cdot \overrightarrow{L'L} \tag{6.22}$$

By making use of Equations (6.19) to (6.22), the values of C^* at the interface are obtained. Then the convective fluxes at the interface are calculated. The diffusive fluxes are calculated from Equations (6.21) to (6.22). Once the overall fluxes at interface are obtained, the equations for C^* can be solved.

6.2 Flow Field

6.2.1 Flow Pattern

Figure 6.2 presents the typical flow field and streamlines in the bioreactor with the scaffold. The rotating bottom-wall imparts angular momentum to the fluid just above it and centrifuges the fluid towards the side-wall. The fluid then spirals up along the side-wall. Near the free surface, the fluid converges towards the center. A vortex breakdown bubble is attached to the free surface (Figure 6.2b). There is a recirculation region at the right hand side, which is compressed by the presence of the scaffold (as compare with Figure 5.8 without a scaffold). The scaffold diverts some of the fluid to the axial region. Another effect of the scaffold is to confine the vortex breakdown bubble to a region above the scaffold. Partly diverted by the vortex breakdown bubble, the fluid approaches the scaffold almost normally. There is some porous flow through the scaffold. Below the scaffold, it is interesting that there is no wake or recirculation region.

The presence of the scaffold will obstruct the recirculating flow generated by the rotating bottom-wall. If the obstruction is large, regions of flow separation and wake

may be formed. Such unfavorable flow patterns were found for a scaffold configuration without the axial hole (see Figure 6.3), in which the axial returning flow was prevented. Only a very small proportion of the fluid passes through the scaffold (Figure 6.3a). A large vortex breakdown bubble is formed above the scaffold (Figure 6.3b). The vortex breakdown bubble hampers flow mixing above the scaffold. Thus it is important that a scaffold configuration does not cause large recirculation bubbles.

6.2.2 Effect of Reynolds Number

The flow field shown above (Figure 6.2) is for *Re* of 1500. Two other Reynolds numbers, 500 and 1000, are considered in Figure 6.4. The streamline results (Figures 6.2 and 6.4) show that the recirculation region elongates towards the free surface with the increase of *Re*. This means that more fluid is convected to the upper region; and the velocity around the top surface of the scaffold becomes higher.

An interesting phenomenon associated with the change of *Re* is that the flow approaches the scaffold differently. At a low *Re* (Figure 6.4a), the flow approaches the scaffold more obliquely than that at a high *Re* (Figure 6.2). At a low *Re*, the approaching flow divides at the top right hand corner of the scaffold (Figure 6.4a). However at a high *Re* the dividing point has moved to the top surface (Figure 6.2). These changes of the approaching flow with *Re* are attributed to the formation of a vortex breakdown bubble near the top surface.

It is seen that there is a vortex breakdown bubble at *Re* = 1500 (Figure 6.2). However, the results for other *Re* (not shown) indicate that the onset of vortex

breakdown is between *Re* = 1000 and 1200. This critical *Re* for the onset is higher than that in the bioreactor without the scaffold (Figure 5.8). The size of the vortex breakdown bubble is also smaller. The presence of the scaffold seems to hamper the formation of a vortex breakdown bubble.

The porous flow within the scaffold is shown enlarged in Figure 6.5 at different *Re*. Generally, the flow enters the scaffold from the top and right surfaces, which are the two surfaces that the external flow approaches. The porous flow exits from the bottom and left surfaces, which are the two surfaces that the external flow moves away from. The porous flow pattern is related to the external flow pattern.

Although the porous flow is dominant in the axial direction (from top to bottom), there are noticeable radial velocity components at the corner regions, mainly due to the external corner flow. At the corner, the external flow changes direction and has a higher radial component, which causes noticeable porous flow in the radial direction.

By comparing Figures 6.5a, b and c, it is noted that there is more porous flow at higher *Re*. However the increase is not as much at *Re* = 1500. The porous flow at the left and right corners are higher at *Re* = 1000 due to the external flow approaching the scaffold less obliquely than that at *Re* = 500. However at *Re* = 1500, only the porous flow at the right corner increases noticeable compared with that at *Re* = 1000; this is attributed to the formation of the vortex breakdown bubble which has diverted some of the external flow to the right side. The porous flow at this high *Re* = 1500 also has a relatively larger radial velocity component towards the left hand side; this is attributed to the larger interface velocity at the top surface (Figure 6.2a) arising from

the presence of the nearby vortex breakdown bubble.

Figure 6.6 shows the pressure distributions along the scaffold surface for different *Re*. The pressures are presented with respect to that at the top of the axis. Generally, the pressure is high along the top surface and drops abruptly along the two side surfaces. The pressure is low along the bottom surface. At the dividing point (on top surface), the pressure is higher. Since only a small proportion of fluid can pass through scaffold, the velocity at the dividing point decreases to a very small value, causing an increase in pressure according to Bernoulli equation. Thus, the peak pressure is located at the top surface where the flow divides.

It is seen that the pressure distribution changes much with the variation of *Re*. At a higher *Re*, the pressure at the top surface is higher and more non-uniform because the flow approaches the scaffold less obliquely (compare Figures 6.2 and 6.4). At *Re* = 500, the flow obliquely approaches the left upper corner, and then becomes almost parallel to the top surface; thus the pressure there is rather uniform. At *R*e = 1000, the normal flow has a dividing point, where the pressure is higher; thus there is non-uniformity of pressure as it drops to the corner. At *Re* = 1500, the vortex breakdown bubble constrains the flow above the scaffold, which increases the approach velocity; thus an even higher pressure at the dividing point is generated.

With the flow at a more normal angle, the pressure drop between the top and right surfaces is also higher. However the pressure drop between the top and left surfaces is smaller, at higher *Re*, due to the bigger porous flow. The bigger porous flow also explains the higher pressure at the bottom surface at higher at *Re*.

However there are other influences on the pressure distribution which are more complex. The flow pattern will change at different *Re* due to the balance between the centrifugal force and the pressure gradient (Brown and Lopez, 1990). The different flow pattern will give the different pressure variation across streamlines and thus affect the pressure distribution on the scaffold surfaces.

6.2.3 Effect of Porous Properties

Figure 6.7 shows the effect of the permeability, as characterized by *Dar*, on the flow field around the scaffold in the bioreactor. It is seen that the flow fields around the permeable scaffolds (Figures 6.7b and c) do not differ greatly from that of the impermeable scaffold (Figure 6.7a). The flow fields are dominated by the vortex breakdown bubble and recirculation region which appear to be around the same size for the various cases. The swirling flow behaviour, in particular the vortex breakdown phenomenon, seems to be mainly influenced by the chamber aspect-ratio, the Reynolds number, the scaffold configuration and the scaffold location. The effect of the permeability or the porosity is secondary for the present range of parameters.

Figure 6.8 shows the effect of *Dar* on the porous flow within the scaffolds. It is seen that the porous velocity is noticeably higher at a higher *Dar* (see also Figure 6.5c). This is expected because a higher Darcy number means more porous flow for a certain pressure drop.

Figure 6.9 shows the pressure distributions along the scaffold surface for different *Dar*. As before, the pressures are presented with respect to that at the top of the axis.

Generally, the pressure distributions show similar trend for the different permeability. The pressure is high along the top surface, drops abruptly along the two side surfaces, and is low along the bottom surface. There is a peak pressure on the top surface, associated with the dividing point. The reason has been explained in Section 6.2.2. It is seen that the pressure distribution around the permeable scaffold is different from that of the solid one.

Surprisingly, the pressure at the top surface is lower for the solid scaffold than for the permeable scaffold. It is seen that the dividing point of the flow past the solid scaffold is nearer to the right hand corner (compare Figure 6.7c with Figure 6.7a), because the vortex breakdown bubble has hampered flow to the left hand side. Thus the peak pressure point of the solid scaffold is lower as it is near the low pressure region at the corner. However if some of the flow is permitted to go through the scaffold, then less flow need to move to the right hand side; thus the dividing streamline shifts towards the left hand side, that is further from the right hand corner. The pressure drops between the top and side surfaces are slightly smaller for the permeable scaffolds. This is attributed to the porous flow.

However, as discussed before, there are other complex influences on the pressure distribution. The flow pattern may change slightly at different *Dar* because the porous flow within the scaffold is different. The different flow pattern will give different pressure variation across streamlines and thus affect the pressure distribution for scaffolds of different permeability.

The results (Figure 6.9) show that permeability does not significantly change the

pressure drop between the top and bottom surfaces; this pressure drop is the main driving force for the porous flow as it is mainly in the axial direction. From the Darcy's law, if the pressure drop is not changed, the average velocity in the scaffold is approximately proportional to the permeability. Thus it explains why the porous velocity is higher at higher permeability (Figures 6.8 and 6.5c)

Figure 6.10 shows the effect of the porosity on the porous flow within scaffolds of the same permeability. It is seen that the porosity has a very small effect on the flow field within the scaffold (see also Figure 6.5c). The scaffold permeability is the primary factor which determines the porous flow in it, and the porosity is of secondary importance.

6.2.4 Effect of Top Lid

The main results of the present study are based on free surface for the boundary condition at the top, which is the usual condition in a bioreactor. In some cases, to reduce surface foam formation which may be traumatic for the cell, the medium level extends to the top cover. Thus it is relevant to investigate the effect of a rigid wall for the boundary condition at the top surface of the bioreactor.

Figure 6.11 shows the flow field and streamlines in the bioreactor at different *Re*. The flow fields outside the scaffold do not differ much from those for the condition of free surface except at $Re = 1500$. With the top lid, there is no vortex breakdown. This is not surprising because at the aspect ratio of $H/R = 1$, there is no onset of vortex breakdown (Figure 5.2) in a bioreactor without a scaffold.

Figure 6.12 shows the variation of the porous flow with *Re* for the top lid case. It is found that the flow velocity within the scaffold increases with the increase of *Re*. However, the increase of the velocity is more obvious for the lower range of *Re*. At *Re* = 1500, compared with that for the free surface case, the radial velocity components within the scaffold for the rid lid case are smaller. This is because, for the case with the top lid, there is no vortex breakdown bubble (see Figure 6.2) to induce a large radial-flow above the top surface.

Figure 6.13 shows the pressure distributions along the scaffold surface for different *Re*. The pressure distribution at the top surface is rather uniform. The explanation may be seen from the flow pattern (Figure 6.11) which shows that the flow does not approach the surface in a normal direction (compare with Figure 6.2). The top pressures are not much affected by *Re*. The extent to which the streamlines pattern above the scaffold can change seems to be limited by the presence of the top lid. Thus for the pressure gradient above the top surface, there will also be limited extent in its change with *Re*.

At *Re* = 500, there is a small pressure drop from the top to right surfaces. The streamline pattern (Figure 6.11a) shows that the flow approaches at the right corner. It does not turn the right corner which would have generated a big pressure drop there. But the flow has to turn around the left hand corner accounting for the pressure drop there. At *Re* = 1000 and 1500, the flow divides at the top surface and then turns abruptly at both left and right corners. This has generated the high pressure drops at both corners.

The pressure at the bottom surface is higher at a higher *Re*. This is due to the higher porous flow (Figure 6.12) at a higher *Re*. Also the flow pattern below the bottom surface is changed (Figure 6.11) as the recirculation flow seems to be longer.

Figure 6.14 shows the pressure distributions along the scaffold surface for different *Dar*. The effect is not large as the external flow pattern (and pressure gradient) is not greatly affected by the permeability. However the pressure drop at the corners of the solid scaffold is more abrupt than that of the permeable scaffold. The pressure at the bottom surface is slightly higher if the permeability is higher.

The comparison between Figures 6.14 and 6.9 (or Figures 6.13 and 6.6) indicates that the scaffold surface pressure is affected by the boundary condition at the top surface. The top lid reduces the swirling flow above the scaffold, which affects the flow pattern and thus the pressure gradient across them. The top lid also delays vortex breakdown, which affects the flow approaching the scaffold top surface.

6.3 Oxygen Concentration

The oxygen transport in the bioreactor is considered for the case of free surface at the top. The concentrations presented are in the form of the intrinsic average and non-dimensionalized by the saturated concentration C_0 at the free surface.

6.3.1 Oxygen Concentration Field

Figure 6.15 shows the oxygen concentration field in the bioreactor. The oxygen source is above the free surface which is assumed to be at saturated value. Comparing

Figure 6.15 and Figure 6.2b, it is seen that the concentration contours are generally similar to the streamline contours.

Near the axial region, oxygen from the free surface is convected downwards to the bottom. Along the rotating bottom-wall, it moves within a thin boundary layer to the side-wall and then up along the wall to the surface (compare flow pattern in Figure 6.2b). The concentration in the narrow core at the axis and the thin boundary layers along the walls are high because they are not spread over a large region; moreover they are not consumed by any cells. Near the top axial region there is also a high concentration region, where oxygen from the free surface is recirculated within the vortex breakdown bubble.

At the top region near the side-wall, oxygen is transported from the free surface and convected downwards by the recirculating flow. Some of the downward flow convects oxygen to the scaffold. It is noted that the oxygen convection to the scaffold is mainly from this region to the right of the vortex breakdown bubble. The axial region and the vortex breakdown region play a small role in convecting oxygen to the scaffold.

The concentration in the recirculation region is not as high as those at the axis region, about 15% below the saturated concentration. This indicates that the mixing in the bioreactor may be satisfactory. The concentration around the scaffold is satisfactory despite the minimal role of the axial region and the vortex breakdown bubble in oxygen transport.

The concentration in the scaffold is around 40% lower than those of the

surrounding medium. The concentration is higher at the top and right surfaces and lower near the bottom surface. The concentration reduces inside the scaffold due to the consumption by the cells inside. The concentration contours are influenced by the general direction of the porous flow. The medium enters from the top and right surfaces and exit from the left and bottom surfaces (as described in Section 6.2.2), which is consistent with the concentration contours. The concentration falls as the medium passes through the scaffold, because oxygen is being consumed by the cells.

When the low-oxygen medium exits from the bottom surface of the scaffold, it radially converges towards the left bottom edge of the scaffold (Figure 6.15). From that corner, a streak of low-oxygen fluid spirals downwards.

6.3.2 Effect of Reynolds Number

Figure 6.16 shows the oxygen concentration distribution in the bioreactor without any medium circulation (Re = 0). It is seen that with no flow, the oxygen concentration falls rapidly from its saturation value at the surface to around 10% at the scaffold surface and near zero within the scaffold. This indicates that diffusion alone is not adequate to transfer enough oxygen into the scaffold.

Figure 6.17 shows that the oxygen concentration distributions within the scaffold at different medium circulation (Re = 500 and Re = 1500). With recirculating flow generated by the bottom-wall rotation, there is more oxygen convection to the scaffold surface. At a high Re, the concentration within the scaffold is above 80% of saturation but at a small Re it is below 20% (see Figures 6.17a and b).

The surface concentration is important in determining the concentration within the scaffold. Figure 6.18 shows the oxygen concentration distribution along the scaffold surface at different *Re*. Generally, the concentration is higher at the top and right surfaces because the flow comes from that direction. It is lower at the left surface but lowest at the bottom surface where it could fall to as low as 10% of saturation at *Re* = 500. The surface concentrations increase with the increase of *Re*. At a small *Re* of 500, the surface concentration is about 35% of saturation. However, at a *Re* of 1500, the surface concentration is higher, around 80% of saturation.

Besides increasing the surface concentration, a higher Reynolds number reduces the concentration difference across the scaffold surfaces, in particular from top to bottom. There is a concentration difference because of consumption by the cells as the oxygen is convected by the porous flow through the scaffold. The porous flow is low at a small *Re* of 500, which gives a large concentration difference between top and bottom surfaces. However, with the increase of *Re*, the concentration difference becomes smaller because of higher porous flow (Figure 6.5).

The concentration within the scaffold could reach a low value especially at a small *Re* (Figure 6.17a). It is important to make sure that the minimum value does not fall below the critical value to avoid hypoxia. Figure 6.19 summarizes the variation of the minimum oxygen concentrations within the scaffold with *Re*. It is seen that the minimum concentrations increase rapidly with the increase of *Re* (Figure 6.19). At a low *Re* of 500, it is below that the critical value of 5% of saturation for CHO cell culture (Lin and Miller, 1992). Thus, the micro-bioreactor should be operated at *Re*

above 500. However, to have an optimal concentration of 50% of saturation (Meuwly et al., 2006), the Reynolds number should be around 1000.

Figure 6.20 shows the locations of the minimum oxygen concentration in the scaffold at different *Re*. With no medium circulation (*Re* = 0) the location of the minimum concentration is around the central region because of oxygen diffusion from the four surfaces. With porous flow, the location of the minimum oxygen concentration moves downwards to the bottom surface. It is around the middle of the bottom surface at moderate *Re* from 500 to 1000. This is because the porous flow is generally from top to bottom surfaces. At a *Re* from 1000 to 2000, the minimum location moves towards the left edge. This is because there is a bigger component of porous flow in the radial direction as discussed above in Section 6.2.2.

6.3.3 Effect of Porous Properties

Figure 6.21 shows that the oxygen concentration distributions within the scaffold for different *Dar*. It is seen that, for a low *Dar*, the concentration within the scaffold is low (Figure 6.21b). In the central region it is around 50% of its saturation value, and near the bottom it falls to around 25% of saturation. In comparison, the concentration for a high *Dar* of 10^{-5} is above 80% of saturation (Figure 6.21a). The porous flow at a small *Dar* is small (Figure 6.8) and thus less oxygen is convected into scaffold, resulting in lower concentration distribution.

Figure 6.22 shows the oxygen concentration distributions along the scaffold surface at different *Dar*. At a higher *Dar*, the oxygen concentration is higher at the top

and right surfaces because the scaffold is more permeable to the incoming flow. With higher porous flow, the concentration differences between different surfaces are also smaller; thus the concentration at the left and bottom surfaces does not fall to low values. In contrast, at a *Dar* of 5×10^{-7} the concentration at the bottom surface falls to as low as 30% of saturation.

Figure 6.23 shows the minimum oxygen concentrations within the scaffold at different *Dar*. It is seen that the minimum concentration is very low at small *Dar* due to low porous flow. In fact at *Dar* below 5×10^{-7} it is even below the critical concentration of 5%. To ensure that the concentration is optimal everywhere within the scaffold, the Darcy number should be larger than 1×10^{-6}. Note that this condition is for *Re* of 1500. At a lower *Re*, the concentration will be lower.

Figure 6.24 shows the variation of the locations of the minimum oxygen concentrations within the scaffold with *Dar*. At a higher *Dar*, the minimum concentration shifts towards the bottom left corner due to more porous flow. However the shift is not much as compared to that caused by *Re* (Figure 6.20). The shift of minimum location is influenced by porous flow and its direction, on which the Reynolds number has a dominant effect.

Figure 6.25 shows the effect of the porosity on the concentration distribution within the scaffold. There is no much difference between the concentration contours for different porosity. The results indicate that the scaffold permeability has an important effect on oxygen concentration distribution in it, and the porosity is of secondary importance.

6.3.4 Effect of Damkohler Number

Figure 6.26 shows the oxygen concentration distributions within the scaffold for different *Da*. It is seen that, for a high *Da*, the concentration within the scaffold is low (Figure 6.26b). In the central region it is around 40% of its saturation value, and near the bottom it falls to around 10% of saturation. In comparison, the concentration for a low *Da* of 74 is above 90% of saturation (Figure 6.26a). A higher Damkohler number means a higher oxygen consumption rate. Thus, more oxygen is consumed by the cells, resulting in lower concentration distribution.

Figure 6.27 shows the oxygen concentration distributions along the scaffold surface at different *Da*. As expected, at a lower *Da*, the oxygen concentration level is higher at the top and right surfaces because the oxygen concentration in the surrounding is also higher due to less oxygen consumption. With less oxygen consumption, the concentration differences are also smaller; thus the concentration at the left and bottom surfaces do not fall to low values. In contrast, at a *Da* of 740 the concentration at the bottom surface falls to as low as 10% of saturation.

Figure 6.28 shows the minimum oxygen concentrations within the scaffold at different *Da*. It is seen that the minimum concentration is very low at a high *Da* due to high oxygen consumption rate. In fact at *Da* above 800 it is even below the critical concentration (5% of saturation). To ensure that the concentration is optimal (around 50% of saturation) everywhere within the scaffold, the Damkohler number should be less than 500. Note that this condition is for *Re* of 1500 and *Dar* of 5×10^{-6}. At a lower *Re* or *Dar*, the concentration will be lower.

During the cell culture, the cell density may increase much because of the proliferation. The increase of the cell density means the increase of *Da*. Thus, the oxygen concentration within the scaffold drops with the cell proliferation. Moreover, when animal cells are seeded in the scaffold, they occupy the void space and change the micro-structure of the porous medium. Thus, the presence of the cells may decrease the porosity and permeability of the scaffold. As mentioned before, the permeability has an important effect on the porous flow, subsequently the oxygen convection in the scaffold. If the increase of the cell density decreases the permeability of the scaffold, the oxygen concentration will suffer an additional drop with the cell proliferation. However, it is very difficult to quantitatively investigate the effect of the cell density on the permeability as it is very difficult to determine the change of the micro-structure of the scaffold when the cells attach and multiply there.

6.4 Concluding Remarks

Biomaterial scaffolds have been widely used as structural templates for cell attachment and tissue formation, many of which are subjected to fluid flow, either *in vivo* or in bioreactors. In the present study, the flow and oxygen concentration fields in a micro-bioreactor with a cell scaffold were simulated. The medium mixing in the micro-bioreactor was generated by the rotating bottom-wall and the scaffold was considered as a porous medium.

It is seen that there is a recirculation region above the bottom-wall. Beyond certain *Re*, a vortex breakdown bubble attached to the free surface is observed. These

phenomena are similar to those in the micro-bioreactor without scaffold. However, compared with those in the micro-bioreactor without scaffold, the presence of the scaffold compresses the recirculation region, delays the onset of vortex breakdown and confines the vortex breakdown bubble to a region above the scaffold. There is some porous flow through the scaffold. Generally, the porous flow is dominant in the axial direction (from the top to bottom). Interestingly there is no wake or recirculation region below the scaffold.

The Reynolds number has noticeable effects on the flow field both outside and inside the scaffold. At a higher *Re*, the velocity around the top surface of the scaffold becomes higher and the flow approaches the scaffold more perpendicularly. Also, there is more porous flow within the scaffold with the increase of *Re*. The vortex breakdown bubble occurs at *Re* above 1200, which causes a relatively larger radial velocity component towards the left hand side within the scaffold.

The flow field outside the scaffold is not affected much by the variation of the permeability or the porosity. Also the porous flow inside the scaffold is not influenced much by the variation of porosity. However, the porous flow within the scaffold is higher at larger permeability.

If the free surface is replaced by a lid, the swirling flow above the scaffold will be reduced. Thus the flow pattern and the pressure distribution near the top region are affected. The top lid also obstructs the onset of vortex breakdown, which affects the flow approaching the scaffold top surface.

The concentration contours are influenced by the general direction of the porous

flow. For a higher *Re* or *Dar*, the oxygen concentration within the scaffold is higher and the concentration difference between the top and bottom surfaces is lower. The porosity only has a secondary effect on concentration distribution as it does not affect the flow much.

The concentration within the scaffold decreases with the increase of *Da*. During the cell culture, the cell density may increase much because of the proliferation, which means the increase of *Da*. Thus, the oxygen concentration within the scaffold decreases with the cell proliferation. Moreover, the presence of the cells may decrease the permeability, which further decreases the concentration within the scaffold.

Chapter 7

Conclusions and Recommendations

7.1 Conclusions

A numerical model was developed for a stirred micro-bioreactor, of a few millilitres working volume, in which the medium was mixed by a magnetic stirrer rod at the base. The flow pattern in the micro-bioreactor was found to resemble swirling flow with vortex breakdown. To examine the conditions for vortex breakdown, an axisymmetric model was developed for the swirling flow in an enclosed cylinder, in which the rotating rod was simulated by a partially rotating bottom-wall. It was considered that the micro-bioreactor may be used for growing adhesive cells on a porous scaffold. To study the porous flow around and through the scaffold, a numerical method was developed of the general flow-conditions at the interface of a homogeneous fluid and a porous medium. The interface flow-conditions were then included in a numerical model which was developed of the axisymmetric, swirling flow in the micro-bioreactor with the porous scaffold.

7.1.1 Flow Environment in a Stirred Micro-Bioreactor

The computed flow field shows that a recirculation region arises above the rotating stirrer-rod, which provides the medium mixing in the axial direction. The medium mixing is characterized by a circulation coefficient of about 0.2, which is about 5 times smaller than that in a one-litre bioreactor with six impellers. Thus a high

rotational speed is needed to ensure adequate mixing.

At the highest rotation speed studied, rod Reynolds number of 720, the volumetric oxygen-transfer coefficient of the micro-bioreactor is around 2.0×10^{-3} s^{-1} that is small compared with the value of 0.2 s^{-1} achieved in a 10-litre bacteria culture bioreactor with aeration. Thus for bacteria culture, it is necessary to enhance oxygen transfer by bubble aeration as was used by Kostov et al. (2001). However, the oxygen concentration level in the present micro-bioreactor is adequate for certain animal cell cultures without using bubble aeration. Assuming a critical value of 0.05 for the dimensionless oxygen concentration, animal cell with *Da* up to 140 may be grown in the micro-bioreactor if operated at a high *Re* of 432.

The peak shear stress, at the highest *Re* of 720, is about 0.5 N m^{-2} which is around two times that in a large scale stirred-tank bioreactor but, nevertheless, still below the level acceptable for animal cell culture. The maximum energy dissipation rate (that characterizes the detrimental velocity gradients) is 14 kWm^{-3}; that is around 6 times lower than that in a 10 litre stirred-tank bioreactor fitted with a Rushton impeller. Hence the hydrodynamic stress environment would be acceptable for animal cell culture when the micro-bioreactor is operated at the highest *Re* of 720.

It is noted that the oxygen concentration and shear stress distributions are severely non-uniform in the present micro-bioreactor. It is not meaningful to provide a global average index for them. In the present study, the peak value of stresses and the minimum oxygen concentration in the micro-bioreactor at different operating conditions were summarized because a low concentration may cause cell hypoxia and

a high stress may cause cell lysis. An optimized bioreactor should provide adequate (or optimal) oxygen concentration as well as keep suitable stress level for cell growth.

7.1.2 Swirling Flow and Vortex Breakdown in a Micro-Bioreactor

Non-dimensional results of the boundary curves were presented for the first onset of vortex breakdown. Various ways to define the non-dimensional parameters were investigated. It is concluded that the Reynolds number should be based on the rotating-disk radius, whereas the aspect ratio should be based on cylinder radius. An additional parameter is the cylinder-to-disk ratio. It is shown that correlating the results in terms of these parameters, so defined, is more meaningful to avoid ambiguous interpretation of the effects of the partial rotation.

The critical aspect ratio to have vortex breakdown is found to be reduced to about 1, as compared to the whole bottom-wall rotation in which the critical aspect ratio is 1.2. The minimum *Re* for vortex breakdown is reduced to 850 as compared to 1000 for the whole bottom-wall rotation. At the same *Re*, the cylinder-to-disk ratio influences the vortex breakdown boundary curve by either increasing or reducing the effective aspect-ratio. Thus the physical aspect-ratio for the onset or cessation of vortex breakdown is changed as compared with that of whole bottom-wall rotation. The influence may be interpreted from the balance between radial pressure gradient and centrifugal force as may be seen from results of their contour distributions. The imbalance gives rise to waviness in the angular-momentum contours which leads to vortex breakdown.

7.1.3 Numerical Method for Coupled Flow in Porous Medium and Homogeneous Fluid Domains

The present numerical method models the momentum jump condition at the boundary between a porous and fluid media, which includes both viscous and inertial jump parameters. The use of multi-block grids, together with body-fitted grids, makes it more suitable for handling complex geometries. The shear stress jump condition affects both the convective and diffusive fluxes. The normal stress condition, assumed continuous at the interface, is also needed in order to close the two sets of equations. The general method was verified by solving three flow configurations: parallel flow over a porous layer, flow through a porous plug; flow past a porous square cylinder.

7.1.4 Swirling Flow and Mass Transfer in a Bioreactor with a Scaffold

The presence of the scaffold compresses the region of recirculatory flow, delays the onset of vortex breakdown and confines the vortex breakdown bubble to a region above the scaffold. Generally, the porous flow in the scaffold is dominant in the axial direction (from the top to bottom). Interestingly there is no wake or recirculation region below the scaffold.

The Reynolds number has noticeable effects on the flow field both outside and inside the scaffold. At a higher *Re*, the velocity around the top surface of the scaffold becomes higher and the flow approaches the scaffold in a more perpendicular direction. There is more porous flow within the scaffold with the increase of *Re*. The vortex breakdown bubble occurs at *Re* above 1200, which causes the porous flow

within the scaffold to have a relatively larger radial velocity component towards the left hand side.

The flow field outside the scaffold is not affected much by the variation of the permeability or the porosity. However, the porous flow within the scaffold is higher at larger permeability.

The oxygen concentration contours are influenced by the general direction of the porous flow. For a higher *Re* or *Dar*, the oxygen concentration within the scaffold is higher and the concentration difference between the top and bottom surfaces is lower.

7.2 Recommendations

In the present study, animal cell suspensions are assumed to exhibit Newtonian fluid characteristics. However, in certain condition, for example the high cell density, the cell suspensions may become non-Newtonian fluid, which exhibit both viscoelastic and shear thinning characteristics (Curtis and Emery, 1993; Chen et al., 1997). The flow pattern in the stirred bioreactor may change much if non-Newtonian fluid is used, which may be considered to extend the present study.

In the present study, only the steady vortex breakdown is investigated. However, the flow may become time dependent when the Reynolds number is beyond a certain critical value. It would be of interest to understand the instability mechanism behind this transition, and to examine its influence on the mixing efficiency and hydrodynamic stress distribution. From the point of view of animal cell culture, it would also be of interest to investigate methods to control the flow so as to achieve a

desirable environment.

In the present study, the shear jump condition, which includes two jump parameters β and β_1, is imposed at the porous-fluid interface. The two parameters are of order one as predicted by the theory of Ochoa-tapia and Whitaker (1995a; 1995b; 1998). However, values of these parameters for various interface conditions will require further studies. For example, numerical simulations based on the microscopic model could be carried out to investigate the detailed flow behaviour at the interface region. Then the empirical formulations for these parameters might be deduced from the numerical simulation.

Cells occupy the void space and may change the micro-structure of the scaffold. The permeability of the scaffold may be affected by the presence of the cells. It would be of interest to study the effect of the presence of the cells on the permeability, for example, by a microscopic model; then its effect on the flow and mass transport in the scaffold could be determined.

References

Abu-Reesh, I. and Kargi, F., "Biological responses of hybridoma cells to defined hydrodynamic shear stress", J. Biotechnol., 9: 167-178, 1989.

Abu-Reesh, I. and Kargi, F., "Biological responses of hybridoma cells to hydrodynamic shear in an agitated bioreactor", Enzyme Microb. Tech., 13: 913-919, 1991.

Alazmi, B. and Vafai, K., "Analysis of fluid flow and heat transfer interfacial conditions between a porous medium and a fluid layer", Int. J. Heat Mass Transfer, 44: 1735-1749, 2001.

Aloi, L. E. and Cherry, R. S., "Cellular response to agitation characterized by energy dissipation at the impeller tip", Chem. Eng. Sci., 51: 1523-1529, 1996.

Al-Rubeai, M. , Singh, R. P., Goldman, M. H. and Emery, A. N., "Death mechanisms of animal cells in conditions of intensive agitation", Biotechnol. Bioeng., 45: 463-472, 1995.

Armenante, P. M., Luo, C. G., Chou, C. C., Fort, I. and Medek, J., "Velocity profiles in a closed, unbaffled vessel - comparison between experimental LDV data and numerical CFD predictions", Chem. Eng. Sci., 52: 3483-3492, 1997

Augenstein, D. C., Sinskey, A. J. and Wang, D. I. C., "Effect of shear on the death of two strains of mammalian tissue cells", Biotechnol. Bioeng., 13: 409-418, 1971.

Badino Jr, A.C., Facciotti, M. C. R. and Schmidell Neto, W., "Volumetric oxygen transfer coefficients (k_La) in batch cultivations involving non-Newtonian broths", Biochem. Eng. J., 8: 111-119, 2001.

Bakker, A., Laroche, R. D., Wang, M. H. and Calabrese, R. V., “Sliding mesh simulation of laminar flow in stirred reactors”, Chem. Eng. Res. Des., 75: 42-44, 1997.

Bakker, A. D., Soejima1, K., Klein-Nulend, J. and Burger, E. H., “The production of nitric oxide and prostaglandin E2 by primary bone cells is shear stress dependent”, J. Biomech., 34: 671–677, 2001.

Barakat, A. I., “Responsiveness of vascular endothelium to shear stress: potential role of ion channels and cellular cytoskeleton (review)”, Int. J. Mol. Med., 4: 323-332, 1999.

Beavers, G. S. and Joseph, D. D., “Boundary conditions at a natural permeable wall”, J. Fluid Mech., 30: 197-207, 1967.

Begley, C. M. and Kleis, S. J., “The fluid dynamic and shear environment in the NASA/JSC rotating-wall perfused-vessel bioreactor”, Biotechnol. Bioeng., 70: 32-40, 2000.

Betchen, L., Straatman, A. G. and Thompson, B. E., “A nonequilibrium finite-volume model for conjugate fluid/porous/solid domains”, Numer. Heat Transfer A, 49: 543-565, 2006.

Bliem, R. and Katinger, H., “Scale-up engineering in animal cell technology: part II”, Trends Biotechnol., 6: 224-230, 1988.

Born, C., Zhang, Z., Al-Rubeai, M. and Thomas, C. R., “Estimation of disruption of animal cells by laminar shear stress”, Biotechnol. Bioeng., 40: 1004-1010, 1992.

Boschetti, F., Raimondi, M. T., Migliavacca, F. and Dubini, G., “Prediction of the

micro-fluid dynamic environment imposed to three-dimensional engineered cell systems in bioreactors", J. Biomech., 39: 418-425, 2006.

Bowen, R. L., "Unraveling the mysteries of shear-sensitive mixing systems", Chem. Eng., 93: 55-63, 1986.

Brown, G. L. and Lopez, J. M., "Axisymmetric vortex breakdown, part 2. physical mechanisms", J. Fluid Mech., 221: 553-576, 1990.

Bujalski, W., Jaworski, Z. and Nienow, A. W., "CFD study of homogenization with dual Rushton turbines-comparison with experimental results, part II: the multiple reference frame", Chem. Eng. Res. Des., 80: 97-104, 2002.

Butler, M., "Animal cell culture and technology: the basics", Oxford University Press, Oxford, 1996.

Chang, H. C., "Effective diffusion and conduction in two-phase media: a unified approach", AIChE J., 29: 846-853, 1983.

Chen, F., Chen, H. and Gong, X., "Mixotrophic and heterotrophic growth of Haematococcus Lacustris and rheological behaviour of the cell suspensions", Bioresource Technol., 62: 19-24, 1997.

Cherry, R. S. and Robinson, M. A., "Bioreactor magnetic fields do not affect growth and antibody productivity of GAP-A3 hybridomas", Biotechnol. Tech., 3: 385-388, 1989.

Chisti, Y., "Hydrodynamic damage to animal cells", Crit. Rev. Biotechnol., 21: 67-110, 2000.

Cooper, J. A., Lu, H. H., Ko, F. K., Freeman, J. W. and Laurencin, C. T., "Fiber-based

tissue-engineered scaffold for ligament replacement: design considerations and in vitro evaluation", Biomaterials, 26: 1523-1532, 2005.

Costa, V. A. F., Oliveira, L. A., Baliga, B. R. and Sousa, A. C. M., "Simulation of coupled flows in adjacent porous and open domains using a control-volume finite-element method", Numer. Heat Transfer A, 45: 675-697, 2004.

Costes, J. and Couderc, J. P., "Study by laser Doppler anemometry of the turbulent flow induced by a Rushton turbine in a stirred tank: influence of the size of the units-I. mean flow and turbulence", Chem. Eng. Sci., 43: 2751-2764, 1988.

Coutanceau, M. and Bouard, R., "Experimental determination of the main features of the viscous flow in the wake of a circular cylinder in uniform translation, part 1, steady flow", J. Fluid Mech., 79: 231-256, 1977.

Currie, I. G., "Fundamental mechanics of fluids", Marcel Dekker, New York, 2002.

Curtis, W. R. and Emery, A. H., "Plant cell suspension culture rheology", Biotechnol. Bioeng., 42: 520-526, 1993.

de Vahl Davis, G., "Natural convection of air in a square cavity: a bench mark numerical solution", Int. J. Numer. Methods Fluids, 3: 249-264, 1983.

Deshpande, R. R. and Heinzle, E., "On-line oxygen uptake rate and culture viability measurement of animal cell culture using microplates with integrated oxygen sensors", Biotechnol. Lett., 26: 763-767, 2004.

Dewitz, T. S., Hung, T. C., Martin, R. R. and McIntire, L. V., "Mechanical trauma in leukocytes", J. Lab. Clin. Med., 90: 728-736, 1977.

Dong, L., Johansen, S. T. and Engh, T. A., "Flow induced by impeller in an unbaffled

tank - I. experimental", Chem. Eng. Sci., 49: 549-560, 1994.

Duetz, W. A., Rüedi, L., Hermann, R., O'Connor, K., Büchs, J. and Witholt, B., "Methods for intense aeration, growth, storage, and replication of bacterial strains in microtiter plates", Appl. Environ. Microb., 66: 2641-2646, 2000.

Dusting, J., Sheridan, J. and Hourigan, K., "Flows within a cylindrical cell culture bioreactor with a free-surface and a rotating base", 15th Australasian Fluid Mechanics Conference, Sydney, Australia, 2004.

Dusting, J., Sheridan, J. and Hourigan, K., "A fluid dynamic approach to bioreactor design for cell and tissue culture", Biotech. Bioeng., 94: 1197-1208, 2006.

Escudier, M. P., "Observations of the flow produced in a cylindrical container by a rotating endwall", Exp. Fluids, 2: 189-196, 1984.

Ferziger, J. H. and Perić, M., "Computational methods for fluid dynamics", 2nd ed: 222-233, Springer, Berlin, 1999.

Frahm, B., Blank, H., Cornand, P., Oelssner, W., Guth, U., Lane, P., Munack, A., Johannsen, K. and Portner, R., "Determination of dissolved CO(2) concentration and CO(2) production rate of mammalian cell suspension culture based on off-gas measurement", J. biotechnol., 99: 133-148, 2002.

Freed, L. E., Vunjak-Novakovic, G., Biron, R. J., Eagles, D. B., Lesnoy, D. C., Barlow, S. K. and Langer, R., "Biodegradable polymer scaffolds for tissue engineering", Bio/technology, 12: 689-93, 1994a.

Freed, L. E., Marquis, J. C., Vunjak-Novakovic, G., Emmanual, J. and Langer, R., "Composition of cell-polymer cartilage implants", Biotechnol. .Bioeng. 43:

605-614, 1994b

Galban, C. J. and Locke, B. R., “Analysis of cell growth kinetics and substrate diffusion in a polymer scaffold”, Biotechnol. Bioeng. 65: 121-132, 1999.

Garcia-Briones M. A. and Chalmers, J. J., “Flow parameters associated with hydrodynamic cell injury”, Biotechnol. Bioeng., 44: 1089-1098, 1994.

Gartling, D. K., Hickox, C. E. and Givler, R. C., “Simulation of coupled viscous and porous flow problems”, Comp. Fluid Dyn., 7: 23-48, 1996.

Ghia, U., Ghia, K. N. and Shin, C. T., “High-Re solutions for incompressible glow using the Navier-Stokes equations and a mutigrid method”, J. Comp. Phys., 48: 387-411, 1982.

Girard, P., Jordan, M., Tsao, M. and Wurm, F. M., “Small-scale bioreactor system for process development and optimization”, Biochem. Eng. J., 7: 117-119, 2001.

Goldstein, A. S., Juarez, T. M., Helmke, C. D., Gustin, M. C. and Mikos, A. G., “Effect of convection on osteoblastic cell growth and function in biodegradable polymer foam scaffolds”, Biomaterials, 22: 1279-1288, 2001.

Goyeau, B., Lhuillier, D., Gobin, D. and Velarde, M. G., “Momentum transport at a fluid-porous interface”, Int. J. Heat Mass Transfer, 46: 4071-4081, 2003.

Gregoriades, N., Clay, J., Ma, N., Koelling, K. and Chalmers, J. J., “Cell damage of microcarrier cultures as a function of local energy dissipation created by a rapid extensional flow”, Biotechnol. Bioeng., 69: 171-182, 2000.

Gugala, Z. and Gogolewski, S., “The *in vitro* growth and activity of sleep osteoblasts on three-dimensional scaffolds from poly (L/DL-lactide) 80/20%”, J. Biomed.

Mater. Res., 75A: 702-709, 2005.

Hall, M. G., “Vortex breakdown”, Annu. Rev. Fluid Mech., 4: 195-218, 1972.

Harris, C. K., Roekaerts, D., Rosendal, F. J. J., Buitendijk, F. G. J., Daskopoulos, Ph., Vreenegoor, A. J. N. and Wang, H., “Computational fluid dynamics for chemical reactor engineering”, Chem. Eng. Sci., 51: 1569-1594, 1996.

Harrison, R. G., “Observations on the living developing nerve fiber”, Proc. Soc. Exp. Biol. Med., 4: 140–143, 1907.

Harvey, A. D., Wood, S. P. and Leng, D. E., “Experimental and computational study of multiple impeller flows”, Chem. Eng. Sci., 52: 1479-1491, 1997.

Hristov, H., Mann, R., Lossev, V., Vlaev, S. D. and Seichter, P., “A 3-D analysis of gas-liquid mixing, mass transfer and bioreaction in a stirred bio-reactor”, Food Bioprod. Process., 79: 232-241, 2001.

Hsu, C. T. and Cheng, P., “Thermal dispersion in a porous medium”, Int. J. Heat Mass Transfer, 33: 1587-1597, 1990.

Husain, H. S., Shtern, V. and Hussain, F., “Control of vortex breakdown by addition of near-axial swirl”, Phys. Fluids, 15: 271-279, 2003.

Jaworski, Z., Bujalski, W., Otomo, N. and Nienow, A. W., “CFD study of homogenization with dual Rushton turbines-comparison with experimental results, part I: initial studies”, Chem. Eng. Res. Des., 78: 327-333, 2000.

Joshi, J. B., Elias, C. B. and Patole, M. S., “Role of hydrodynamic shear in the cultivation of animal, plant and microbial cells”, Chem. Eng. J., 62: 121-141, 1996.

Joshi, J. B., Sawant, S. B., Patwardhan, A. W., Patil, D. J., Kshatriya, S. S. and Nere, N. K., "Relation between flow pattern and de-activation of enzymes in stirred reactors", Chem. Eng. Sci., 56: 443-452, 2001.

Jue, T. C., "Numerical analysis of vortex shedding behind a porous cylinder", Int. J. Numer. Methods Heat Fluid Flow, 14: 649-663, 2004.

Kensy, F., Zimmermann, H. F., Knabben, I., Anderlei, T., Trauthwein, H., Dingerdissen, U. and Büchs, J., "Oxygen transfer phenomena in 48-well microtiter plates: determination by optical monitoring of sulfite oxidation and verification by real-time measurement during microbial growth", Biotechnol. Bioeng., 89: 698-708, 2005.

Kim, S. J. and Choi, C. Y., "Convection heat transfer in porous and overlying layers heated from below", Int. J. Heat Mass Transfer, 39: 319-329, 1996.

Koh, C. J. and Atala, A., "Tissue engineering, stem cells, and cloning: opportunities for regenerative medicine", J. Am. Soc. Nephrol., 15: 1113-1125, 2004.

Kostov, Y., Harms, P., Randers-Eichhorn, L. and Rao, G., "Low-cost micro-bioreactor for high-throughput bioprocessing", Biotechnol. Bioeng., 72: 346-352, 2001.

Kula, B., "A study of magnetic field effects on fibroblast cultures part 3. The evaluation of the effects of static and extremely low frequency (ELF) magnetic fields on glycosaminoglycan metabolism in fibroblasts, cell coats and culture medium", Bioelectrochem. Bioenerg., 39: 31-37, 1996.

Kuncewicz, C., "Three-dimensional model of laminar liquid flow for paddle impellers and flat-blade turbines", Chem. Eng. Sci., 47: 3959-3967, 1992.

Lamberto, D. J., Alvarez, M. M., Muzzio, F. J., “Experimental and computational investigation of the laminar flow structure in a stirred vessel”, Chem. Eng. Sci., 54: 919–942, 1999.

Lamping, S. R., Zhang, H., Allen, B. and Shamlou, P. A., “Design of a prototype miniature bioreactor for high throughput automated bioprocessing”, Chem. Eng. Sci., 58: 747-758, 2003.

Lappa, M., “Organic tissues in rotating bioreactors: fluid-mechanical aspects, dynamic growth models, and morphological evolution”. Biotech. Bioeng., 84: 518-532, 2003.

Lasseux, D., Ahmadi, A., Cleis, X. and Garnier, J., “A macroscopic model for species transport during in vitro tissue growth obtained by the volume averaging method”, Chem. Eng. Sci., 59: 1949-1964, 2004.

Legallais, C., David, B. and Doré, E., “Bioartificial livers (BAL): Current technological aspects and future developments”, J. Membrane Sci., 181: 81-95, 2001.

Leist, C. H., Meyer, H. P. and Fiechter, A., “Potential and problems of animal cells in suspension culture”, J. Biotechnol., 15: 1-46, 1990.

Li, A. P., Hahn, F. F., Zamora, P. O., Shimizu, R. W., Henderson, R. F., Brooks, A. L. and Richards, R., “Characterization of a lung epithelial cell strain with potential applications in toxicological studies”, Toxicology, 27: 257-272, 1983.

Lilek, Ž., Muzaferija, S., Perić, M. and Seidl, V., “An implicit finite-volume method using nonmatching blocks of structured grid”, Numer. Heat Transfer B, 32:

385-401, 1997.

Li, S. H., De Wijn, J. R., Li, J. P., Layrolle, P. and De Groot, K., "Macroporous biphasic calcium phosphate scaffold with high permeability/porosity ratio", Tissue Eng., 9: 535-548, 2003.

Lin, A. A. and Miller, W. M., "CHO cell responses to low oxygen: regulation of oxygen consumption and sensitization to oxidative stress", Biotechnol. Bioeng., 40: 505-516, 1992.

Lopez, J. M., "Axisymmetric vortex breakdown. part 1. confined swirling flow", J. Fluid Mech., 221: 533-552, 1990.

Lopez, J. M., "Unsteady swirling flow in an enclosed cylinder with reflectional symmetry", Phys. Fluids, 7: 2700-2714, 1995.

Ma, N., Koelling, K. W. and Chalmers, J. J., "Fabrication and use of transient contractional flow device to quantify the sensitivity of mammalian and insect cells to hydrodynamic forces", Biotechnol. Bioeng., 80: 428-437, 2002.

Mazzoleni, A. P., Sisken, B. F., and Kahler, R. L., "Conductivity values of tissue culture medium from 20 ºC to 40 ºC", Bioelectromagnetics, 7: 95-99, 1986.

McQueen, A., Meilhoc, E. and Bailey, J. E., "Flow effects on the viability and lysis of suspended mammalian cells", Biotechnol. Lett., 9: 831-836, 1987.

Mercier, J., Weisman, C., Firdaouss, M. and Quéré, P. L., "Heat transfer associated to natural convection flow in a partly porous cavity", ASME J. Heat Transfer, 124: 130-143, 2002.

Meuwly, F., Loviat, F., Ruffieux, P.-A., Bernard, A. R., Kadouri, A. and von Stockar,

U., “Oxygen supply for CHO cells immobilized on a packed-bed of Fibra-Cel ® disks”, Biotechnol. Bioeng., 93: 791-800, 2006.

Montante, G., Lee, K. C., Brucato, A. and Yianneskis, M., “Numerical simulations of the dependency of flow pattern on impeller clearance in stirred vessels”, Chem. Eng. Sci., 56: 3751-3770, 2001.

Mullin, T., Tavener, S. J. and Cliffe, K. A., “On the creation of stagnation points in a rotating flow”, J. Fluids Eng., 120: 685-689, 1998.

Mullin, T., Kobine, J. J., Tavener, S. J. and Cliffe, K. A., “On the creation of stagnation points near straight and sloped walls”, Phys. Fluids, 12: 425-431, 2000.

Mununga, L., Hourigan, K., Thompson, M. C. and Leweke, T., “Confined flow vortex breakdown control using a small rotating disk”, Phys. Fluids, 16: 4750-4753, 2004.

Muzaferija, S., “Adaptive finite volume method for flow predictions using unstructured meshes and multigrid approach”, PhD Thesis, University of London, 1994.

Nagata, S., “Mixing – principles and application”, Wiley, New York, 1975.

Neale, G. and Nader, W., “Practical significance of brinkman’s extension of Darcy’s law: coupled parallel flows within a channel and a bounding porous medium”, Can. J. Chem. Eng., 52: 475-478, 1974.

Nield, D. A., Junqueira, S. L. M. and Lage, J. L., “Forced convection in a fluid-saturated porous-medium channel with isothermal or isoflux boundaries”, J.

Fluid Mech., 322: 201-214, 1996.

Nield, D. A., “Discussion”, ASME J. Heat Transfer, 119: 193-194, 1997.

Nithiarasu, P., Seetharamu, K. N. and Sundararajan, T., “Natural convective heat transfer in a fluid saturated variable porosity medium”, Int. J. Heat Mass Transfer, 40: 3955-3967, 1997.

Nithiarasu, P., Seetharamu, K. N. and Sundararajan, T., “Finite element modelling of flow, heat and mass transfer in fluid saturated porous media”, Arch. Comput. Meth. Engng., 9: 3-42, 2002.

Ochoa-Tapia J. A. and Whitaker, S., “Momentum transfer at the boundary between a porous medium and a homogeneous fluid I: theoretical development”, Int. J. Heat Mass Transfer, 38: 2635-2646, 1995a.

Ochoa-Tapia J. A. and Whitaker, S., “Momentum transfer at the boundary between a porous medium and a homogeneous fluid II: comparison with experiment”, Int. J. Heat Mass Transfer, 38: 2647-2655, 1995b.

Ochoa-Tapia, J. A. and Whitaker, S., “Momentum jump condition at the boundary between a porous medium and a homogeneous fluid: inertial effect”, J. Porous Media, 1: 201-217, 1998.

Oliveira, R., Clemente, J. J., Cunha, A. E. and Carrondo, M. J. T., “Adaptive dissolved oxygen control through the glycerol feeding in a recombinant Pichia Pastoris cultivation in conditions of oxygen transfer limitation”, J. Biotechnol., 116: 35-50, 2005.

Petersen, J. F., Mclntire, L. V. and Papoutsakis, E. T., “Shear sensitivity of cultured

hybridoma cells (CRL-8018) depends on mode of growth, culture age and metabolite concentration", J. Biotechnol., 7: 229-246, 1988.

Piva, M. and Meiburg, E., "Steady axisymmetric flow in an open cylindrical with a partially rotating bottom wall", Phys. Fluids, 17, 063603, 2005.

Porter, B., Zauel, P., Stockman, H., Guldberg, R. and Fyhrie, D., "3-D computational modeling of media flow through scaffolds in a perfusion bioreactor", J. Biomech., 38: 543-549, 2005.

Puskeiler, R., Kaufmann, K. and Weuster-Botz, D., "Development, parallelization, and automation of a gas-inducing milliliter-scale bioreactor for high-throughput bioprocess design (HTBD)", Biotechnol. Bioeng., 89: 512-523, 2005.

Racher, A. J., Looby, D. and Griffiths, J. B., "Studies on monoclonal antibody production by a hybridoma cell line (C1E3) immobilized in a fixed bed, porosphere culture system", J. Biotechnol., 15: 129-145, 1990.

Radisic, M., Cannizzaro, C. and Vunjak-Novakovic, G., "Scaffolds and fluid flow in cardiac tissue engineering", Fluid Dyn. Mater. Proc., 2: 1-16, 2006.

Ranade, V., "An efficient computational model for simulating flow in stirred vessels: a case of Rushton turbine", Chem. Eng. Sci., 52: 4473–4484, 1997.

Rhie, C. M. and Chow, W. L., "Numerical study of the turbulent flow past an airfoil with trailing edge separation", AAIA J., 21: 1525-1532, 1983.

Rice, M., Hall, J., Papadakis, G. and Yianneskis, M., "Investigation of laminar flow in a stirred vessel at low Reynolds numbers", Chem. Eng. Sci., 61: 2762-2770, 2006.

Roy, P., Baskaran, H., Tilles, A. W., Yarmush, M. L. and Toner, M., "Analysis of oxygen transport to hepatocytes in a flat-bed microchannel bioreactor", Ann. Biomed. Eng., 29: 947-955, 2001

Ruffieux, P. A., von Stockar, U. and Marison, I. W., "Measurement of volumetric (OUR) and determination of specific (qO2) oxygen uptake rates in animal cell cultures", J. Biotechnol., 63: 85-95, 1998.

Sahu, A. K., Kumar, P., Patwardhan, A. W. and Joshi, J. B., "CFD modelling and mixing in stirred tanks", Chem. Eng. Sci., 54: 2285-2293, 1999.

Schmid-Schönbein, G. W., "Rheology of Leukocytes", in: Skalak, R. and Chien, S. (Eds), "Handbook of Bioengineering", McGraw-Hill, New York, 13.1-13.25, 1987.

Serra, A., Campolo, M. and Soldati, A., "Time-dependent finite-volume simulation of the turbulent flow in a free surface CSTR", Chem. Eng. Sci., 56: 2715-2720, 2001.

Sharma, A. and Eswaran, V., "Heat and fluid flow across a square cylinder in the two dimensional laminar flow regime", Numer. Heat Transfer A, 45: 247-269, 2004.

Silva, R. A. and de Lemos, M. J. S., "Numerical analysis of the stress jump interface condition for laminar flow over a porous layer", Numer. Heat Transfer A, 43: 603-617, 2003.

Sinskey, A. J., Fleischaker, R. J., Tyo, M. A., Giard, D. J. and Wang, D. I. C., "Production of cell-derived products: virus and interferon", Ann. N. Y. Acad. Sci., 369: 47-59, 1981.

Smith, C. G., and Greenfield, P. F., “Mechanical Agitation of Hybridoma suspension cultures: metabolic effects of serum, Pluronic F68, and albumin supplements”, Biotechnol. Bioeng., 40: 1045-1055, 1992.

Spohn, A., Mory, M. and Hopfinger, E. J., “Observations of vortex breakdown in an open cylindrical container by a rotating bottom”, Exp. Fluids, 14: 70-77, 1993.

Spohn, A., Mory, M. and Hopfinger, E. J., “Experiments on vortex breakdown in a confined flow generated by a rotating disc”, J. Fluid Mech., 370: 73-99, 1998.

Sucosky, P., Osorio, F. F., Brown, J. B. and Neitzel G. P., “Fluid mechanics of a spinner-flask bioreactor”, Biotechnol. Bioeng., 85: 34-46, 2004.

Toshia, F., Toshinobu, S., Liu, Q. and Yoshito, I., “Effect of Basic Fibroblast growth factor on cartilage regeneration in chondrocyte-seeded collagen sponge scaffold”, Biomaterials, 17: 155-162, 1996.

Unger, D. R., Muzzio, F. J., Auninsm J. G. and Singhvi, R., “Computational and experimental investigation of flow and fluid mixing in the roller bottle bioreactor”, Biotech. Bioeng., 70: 117-130, 2000.

Vacanti, C. A., Langer, R., Schloo, B., Vacanti, J. P., “Synthetic polymers seeded with chondrocytes provide a template for new cartilage formation”, Plast. Reconstr. Surg., 88: 753-759, 1991.

Vafai, K. and Kim, S. J., “Fluid mechanics of the interface region between a porous medium and a fluid layer – an exact solution”, Int. J. Heat Fluid Flow, 11: 254-256, 1990.

Valencia-López, J. J., Espinosa-Paredes, G. and Ochoa-Tapia, J. A., “Mass transfer

jump condition at the boundary between a porous medium and a homogeneous fluid", J. Porous Medium, 6: 33-49, 2003.

Valentine, D. T. and Jahnke, C. C., "Flows induced in a cylinder with both end walls rotating", Phys. Fluids, 6: 2702- 2710, 1994.

van der Pol, L. and Tramper, J., "Shear sensitivity of animal cells from a culture-medium perspective", Trends Biotechnol., 16: 323-328, 1998.

van Doormal, J. P. and Raithby, G. D., "Enhancements of the SIMPLE method for predicting incompressible fluid flows", Numer. Heat Transfer, 7: 147-163, 1984.

Vunjak-Novakovic, G., Obradovic, B., Martin, I., Bursac, P. M., Langer, R. and Freed, L. E., "Dynamic cell seeding of polymer scaffolds for cartilage tissue engineering", Biotechnol. Prog., 14: 193-202, 1998.

Wang, N. S., Yang, J. D., Calabrese, R. V. and Chang, K. C., "Unified modeling framework of cell death due to bubbles in agitated and sparged bioreactors", J. Biotechnol., 33: 107-122, 1994.

Wang, S. and Tarbell, J. M., "Effect of fluid flow on smooth muscle cells in a 3-dimensional collagen gel model", Arterioscler. Thromb. Vasc. boil., 20: 2220-2225, 2000.

Waters, S. L., Cummings, L. J., Shakesheff, K. M. and Rose, F. R. A. J., "Tissue growth in a rotating bioreactor. Part I: mechanical stability", Math. Med. Biol., published online on 2006.

Weuster-Botz, D., Puskeiler, R., Kusterer, A., Kaufmann, K., John, G. T., Arnold, M., "Methods and milliliter scale devices for high-throughput bioprocess design",

Bioproc. Biosyst. Eng., 28: 109-119, 2005.

Williams, K. A., Saini, S. and Wick, T. M., "Computational fluid dynamics modeling of steady-state momentum and mass transport in a bioreactor for cartilage tissue engineering", Biotechnol. Prog., 18: 951-963, 2002.

Wood, B. D., Quintard, M. and Whitaker, S., "Calculation of effective diffusivities for biofilms and tissues", Biotechnol. Bioeng., 77: 495-516, 2002.

Wood, B. D. and Whitaker, S., "Multi-species diffusion and reaction in biofilms and cellular media", Chem. Eng. Sci. , 55: 3397-3418, 2000.

Youcefi, A., "Etude exp´erimentale de 1'ecoulement d'un fluide visco´elastique autour d'un agitateur bipale en cuve agit´ee", Th`ese de Doctorat., INP Toulouse, France, 1993.

Yu, P., Lee, T. S., Zeng, Y. and Low, H. T., "Numerical study of flow in a bioreactor", 11th International Conference on Biomedical Engineering, Singapore, Dec., 2002.

Yu, P., Lee, T. S., Zeng, Y. and Low, H. T., "Fluid flow and mass transport in a low-cost micro-bioreactor for high-throughput bioprocessing", 4th International Conference on Computational Heat and Mass Transfer, Paris, France, May, 2005a.

Yu, P., Lee, T. S., Zeng, Y. and Low, H. T., "Fluid Dynamics of a Micro-Bioreactor for Tissue Engineering", Fluid Dyn. Mater. Proc., 1: 235-246, 2005b.

Yu, P., Lee, T. S., Zeng, Y. and Low, H. T., "Effect of vortex breakdown on mass transfer in a cell culture bioreactor", Mod. Phys. Lett. B, 19: 1543-1547, 2005c.

Yu, P., Lee, T. S., Zeng, Y. and Low, H. T., "Fluid flow and oxygen transfer in a

low-cost micro-bioreactor", 12th International Conference on BioMedical Engineering, Singapore, Dec., 2005d.

Yu, P., Lee, T. S., Zeng, Y. and Low, H. T., "Numerical simulation of vortex breakdown in an enclosed chamber: accelerated computing with PC Grid system", GridAsia 2006, Singapore, May, 2006a.

Yu, P., Lee, T. S., Zeng, Y. and Low, H. T., "A numerical method for flows in porous and open domains coupled at the interface by stress jump", Int. J. Numer. Methods Fluids, 53: 1755-1775, 2007a.

Yu, P., Lee, T. S., Zeng, Y. and Low, H. T., "Characterization of Flow Behavior in an Enclosed Cylinder with a Partially Rotating End-Wall", Phys. Fluids, in press, 2007b.

Zalc, J. M., Alvarez, M. M., Muzzio, F. J. and Arik, B. E., "Extensive validation of computed laminar flow in a stirred tank with three Rushton turbines", AIChE J., 47: 2144-2154, 2001.

Zhang, Z. G., Chisti, Y. and Moo-Young, M. "Effects of the hydrodynamic environment and shear protectants on survival of erythrocytes in suspension", J. Biotechnol., 43: 33-40, 1995.

Zhang, H., Williams-Dalson, W., Keshavarz-Moore, E. and Shamlou, P. A., "Computational-fluid-dynamics (CFD) analysis of mixing and gas-liquid mass transfer in shake flasks", Biotechnol. Appl. Biochem., 41: 1-8, 2005.

Zhong, J. J., Pan, Z. W., Wang, Z. Y., Wu, J. Y., Chen, F., Takaji, M. and Yoshida, T., "Effect of mixing time on taxoid production using suspension cultures of Taxus

chinensis in a centrifugal impeller bioreactor", J. of Biosci. Bioeng., 94: 244-250, 2002.

Zhou, G. and Kresta, S. M., "Impact of tank geometry on the maximum turbulence energy dissipation rate for impellers", AIChE J., 42: 2476-2490, 1996.

Table 1.1 Interface boundary conditions between the porous medium and homogenous fluid domains

Model	Velocity	Velocity Gradient	Reference
1		$\left.\frac{\partial u_x}{\partial y}\right\|_{\text{fluid}} = \frac{\alpha}{\sqrt{K}}\left(u_x\|_{\text{interface}} - u_\infty\right)$	Beavers and Joseph, 1976
2	$u_x\|_{\text{porous}} = u_x\|_{\text{fluid}}$	$\left.\frac{\partial u_x}{\partial y}\right\|_{\text{porous}} = \left.\frac{\partial u_x}{\partial y}\right\|_{\text{fluid}}$	Neale and Nader, 1974
3	$u_x\|_{\text{porous}} = u_x\|_{\text{fluid}}$	$\mu_{eff}\left.\frac{\partial u_x}{\partial y}\right\|_{\text{porous}} = \mu\left.\frac{\partial u_x}{\partial y}\right\|_{\text{fluid}}$	Kim and Choi, 1996; Vafai and Kim, 1990
4	$u_x\|_{\text{porous}} = u_x\|_{\text{fluid}}$	$\frac{\mu}{\varepsilon}\left.\frac{\partial u_x}{\partial y}\right\|_{\text{porous}} - \mu\left.\frac{\partial u_x}{\partial y}\right\|_{\text{fluid}} = \beta\frac{\mu}{\sqrt{K}}u_x\|_{\text{interface}}$	Ochoa-Tapia and Whitaker, 1995a and 1995b
5	$u_x\|_{\text{porous}} = u_x\|_{\text{fluid}}$	$\frac{\mu}{\varepsilon}\left.\frac{\partial u_x}{\partial y}\right\|_{\text{porous}} - \mu\left.\frac{\partial u_x}{\partial y}\right\|_{\text{fluid}} = \beta\frac{\mu}{\sqrt{K}}u_x\|_{\text{interface}} + \beta_1\rho u_x^2\|_{\text{interface}}$	Ochoa-Tapia and Whitaker, 1998

Table 3.1 Comparisons of geometrical parameters

		Present Study	Coutanceau and Bouard
Re=20	Wake Length	1.84	1.86
	Separation angle	44.2°	44.8°
Re=40	Wake Length	4.48	4.26
	Separation angle	53.7°	53.5°

Table 3.2 Comparisons of the maximum horizontal velocity along the vertical central line and the maximum vertical velocity along the horizontal central line, together with their locations

Ra		U_{max}		V_{max}	
		value	location (*y*)	value	location (*x*)
10^3	Present results	3.648	0.813	3.696	0.179
	de Vahl Davis (1983)	3.649	0.813	3.697	0.178
10^4	Present results	16.188	0.824	19.636	0.121
	de Vahl Davis (1983)	16.178	0.823	19.617	0.119
10^5	Present results	34.75	0.857	68.44	0.067
	de Vahl Davis (1983)	34.73	0.855	68.59	0.066

Table 3.3 Comparisons of the average, maximum and minimum Nusselt numbers along the vertical central line together with their locations

Ra		Nu_{avg}	Nu_{max}		Nu_{min}	
			value	location	value	location
10^3	Present results	1.117	1.503	0.092	0.691	1.0
	de Vahl Davis (1983)	1.117	1.505	0.092	0.692	1.0
10^4	Present results	2.242	3.526	0.143	0.582	1.0
	de Vahl Davis (1983)	2.238	3.528	0.143	0.586	1.0
10^5	Present results	4.517	7.738	0.081	0.725	1.0
	de Vahl Davis (1983)	4.509	7.717	0.081	0.729	1.0

Table 3.4 Comparisons of Nusselt number along the hot wall (Pr = 1)

Dar	*Ra*	$\varepsilon = 0.4$		$\varepsilon = 0.9$	
		Present	Reference	Present	Reference
10^{-2}	10^3	1.008	1.01	1.018	1.023
	10^4	1.361	1.408	1.631	1.64
	10^5	2.989	2.983	3.914	3.91
10^{-4}	10^5	1.064	1.067	1.070	1.072
	10^6	2.589	2.55	2.790	2.740
	10^7	7.777	7.81	9.335	9.202
10^{-6}	10^7	1.080	1.079	1.08	1.08
	10^8	3.070	2.97	3.100	3.00
	10^9	12.290	11.46	13.201	12.01

Table 3.5 Interface velocity with different grids in *y* direction

Grids in y direction	Interface velocity
40	0.0444
80	0.0434
160	0.0428
Analytical Solution	0.0423

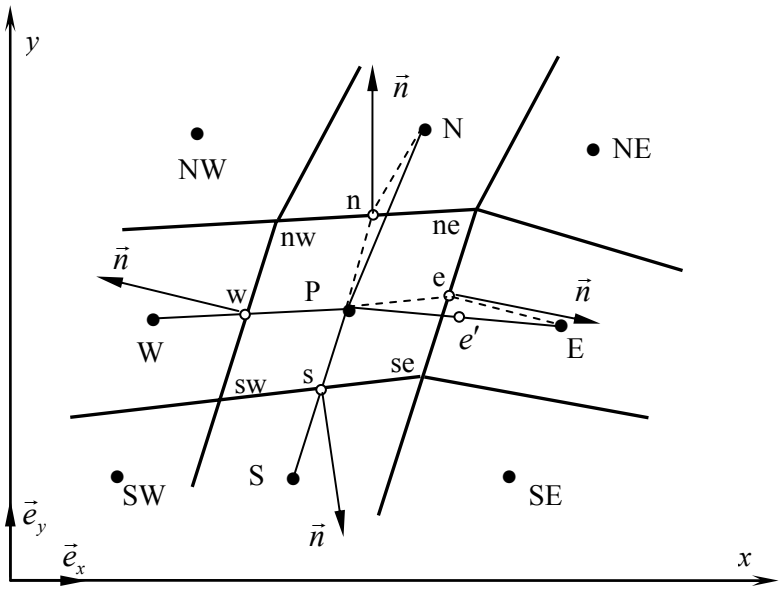

Figure 2.1 A typical 2D control volume

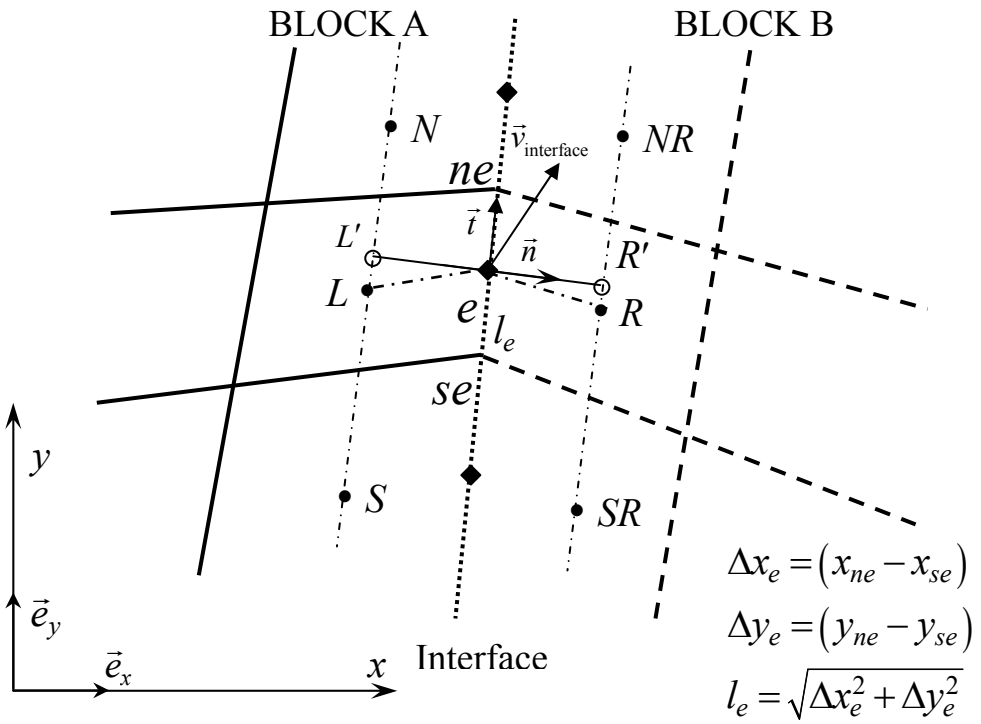

Figure 2.2 Interface between two blocks with matching grids

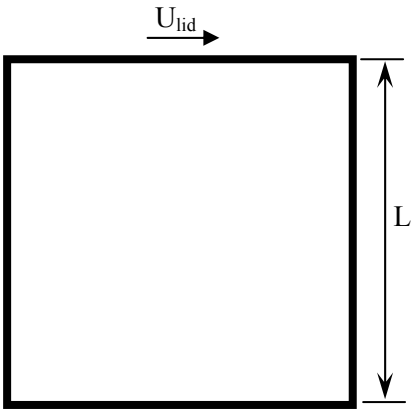

Figure 3.1 Schematic of a lid driven flow in a square cavity.

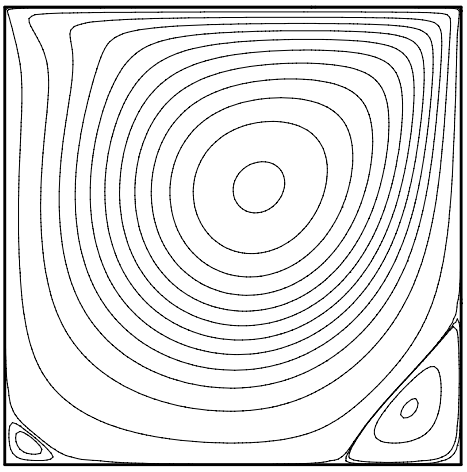

Figure 3.2 Streamline contours of the lid driven flow at *Re* = 400.

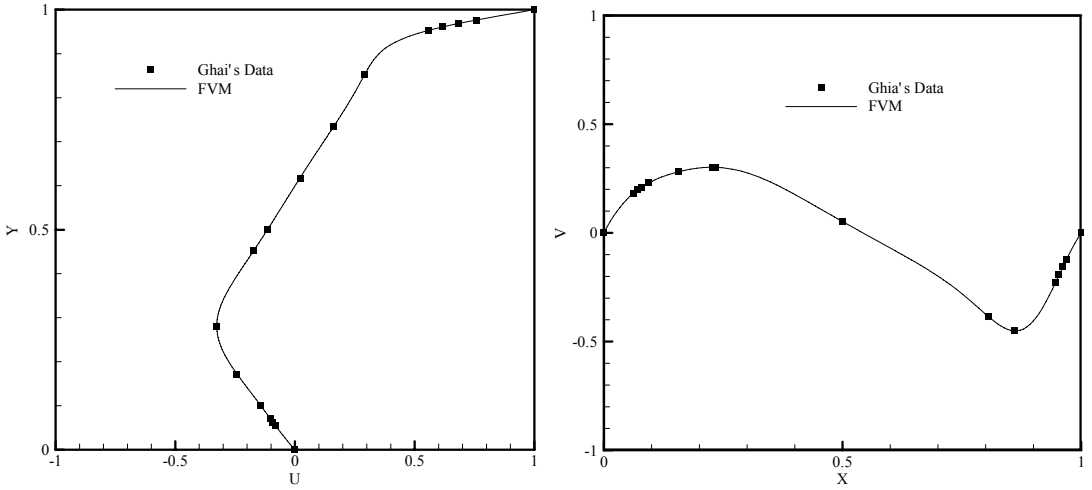

a) *Re* = 400

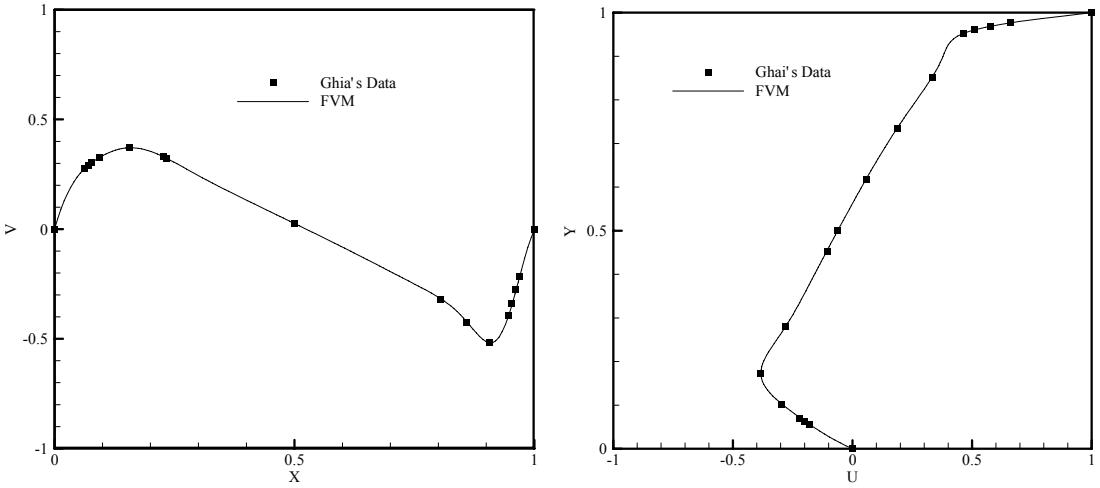

b) *Re* = 1000

Figure 3.3 Distributions of the velocity components along the central lines: a) *Re* = 400; b) *Re* = 1000.

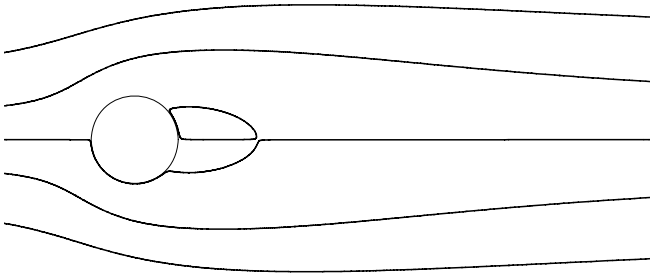

a) *Re* =20

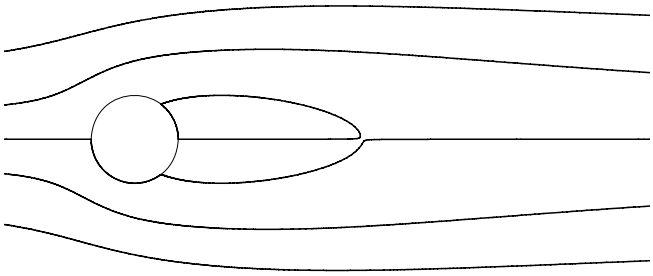

b) *Re* = 40

Figure 3.4 Streamline contours for flow past cylinder at different *Re*.

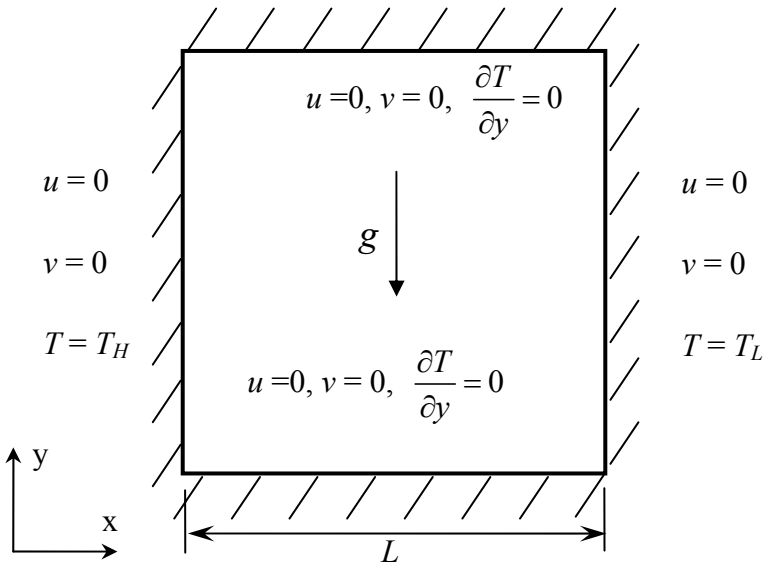

Figure 3.5 Schematic of nature convection in a square cavity.

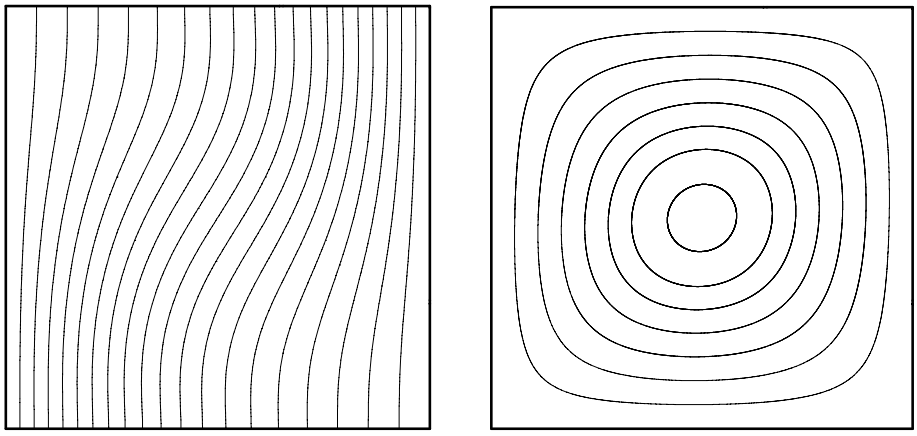

Temperature Streamlines

a) $Ra = 10^3$

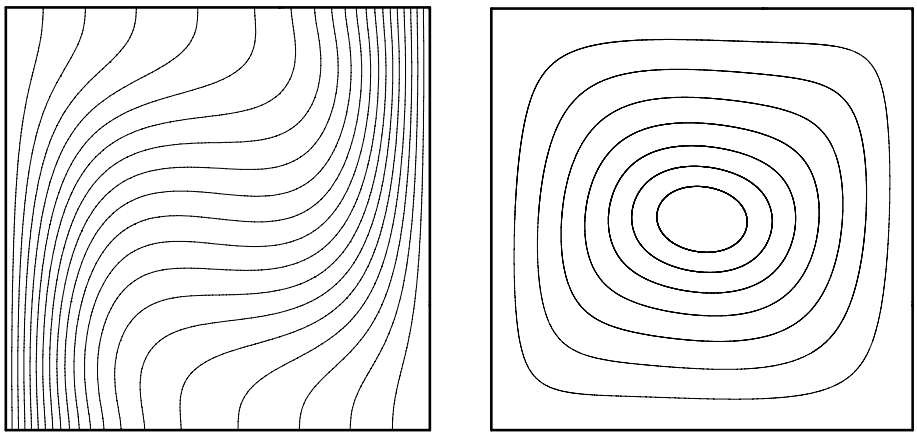

Temperature Streamlines

b) $Ra = 10^4$

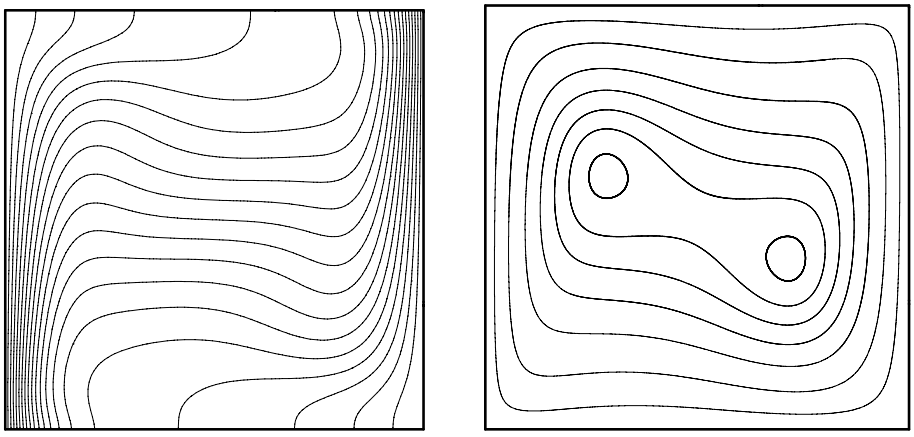

Temperature Streamlines

c) $Ra = 10^5$

Figure 3.6 Temperature and streamline contours for difference *Ra*.

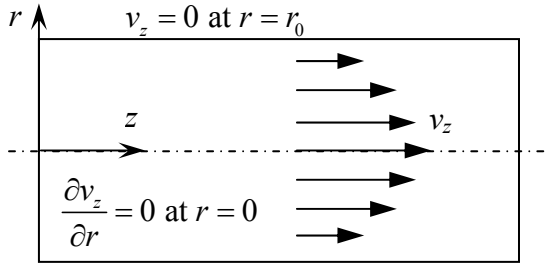

Figure 3.7 Schematic of the flow in a pipe.

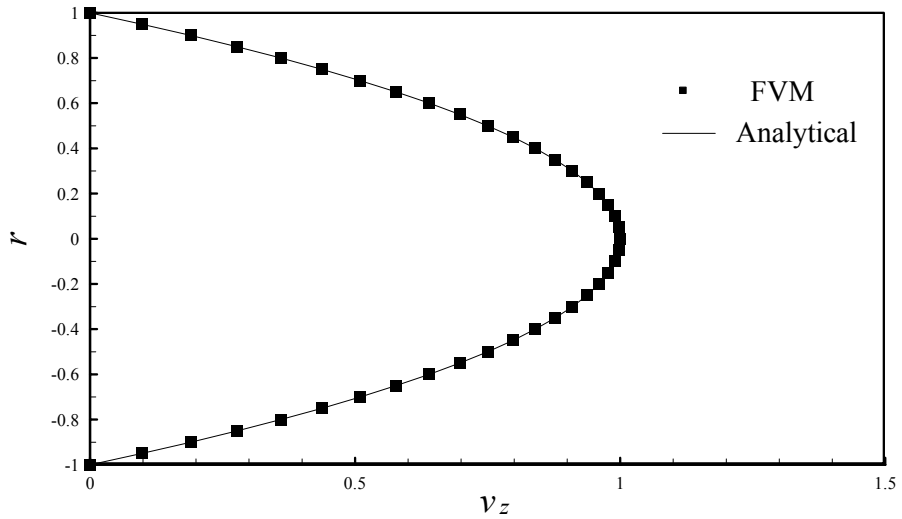

Figure 3.8 Velocity profiles of the pipe flow.

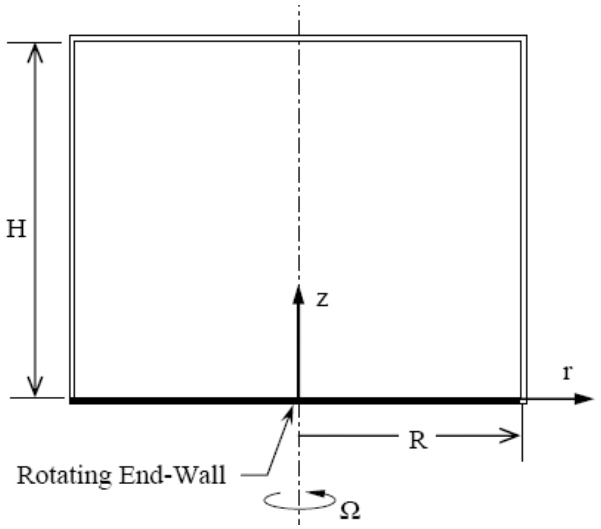

Figure 3.9 Schematic of flow in a chamber with a bottom-wall rotating.

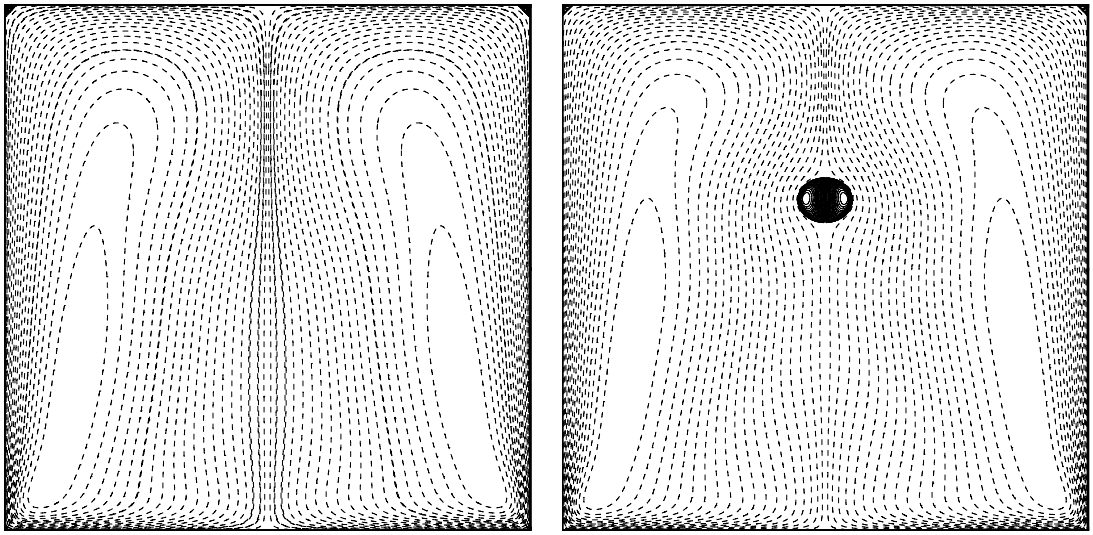

a) *Re* = 1200 *b) Re* = 1500

Figure 3.10 Streamline Contour of in the meridional plane in the cylindrical chamber with a bottom-wall rotating; *H/R* = 2.0 and *Re* as indicated.

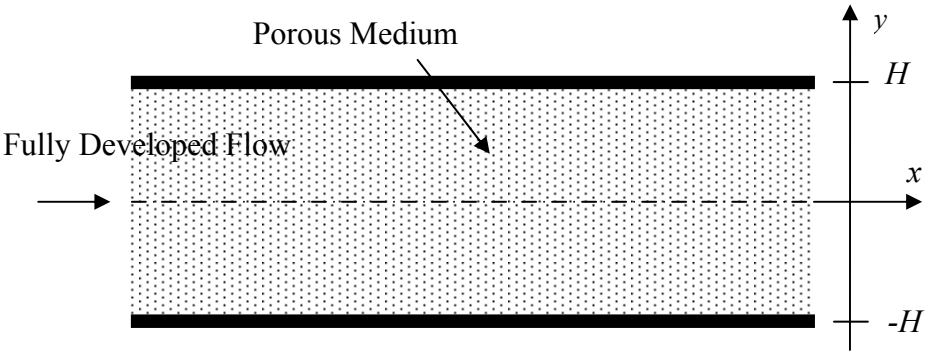

Figure 3.11 Schematic of a flow in a porous square channel

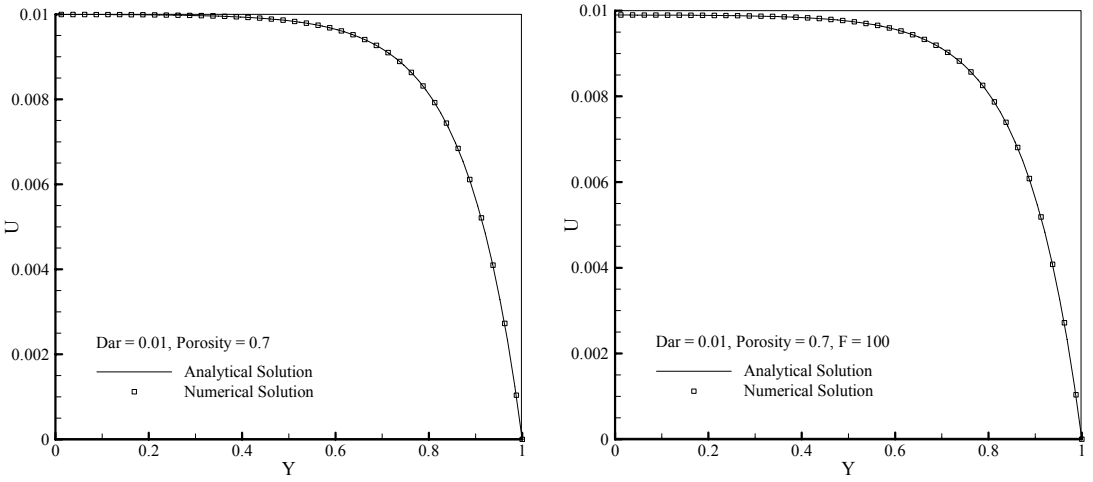

a) Brinkman model b) Darcy-Brinkman-Forchheimer model

Figure 3.12 Comparisons of the velocity profile in the porous channel.

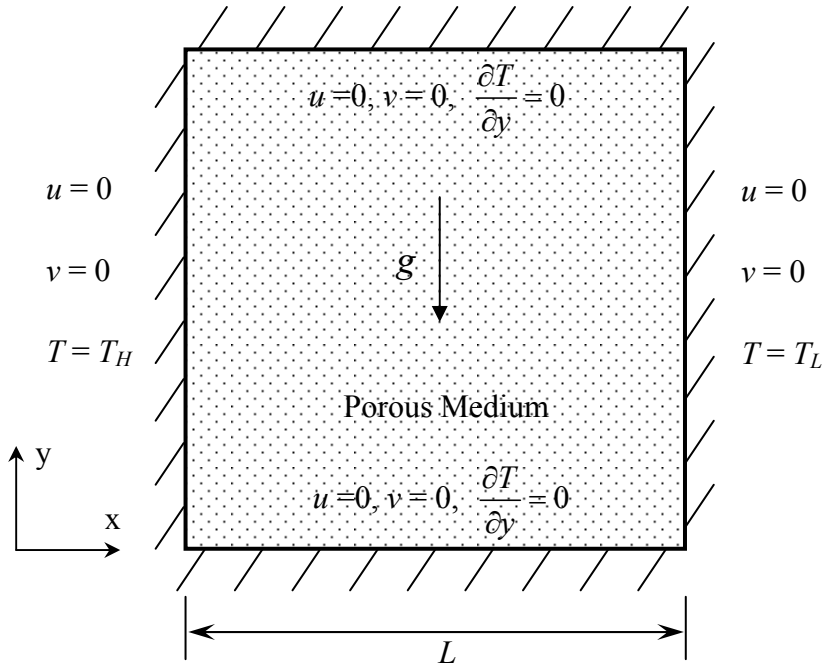

Figure 3.13 Schematic of a natural convection in a porous square cavity.

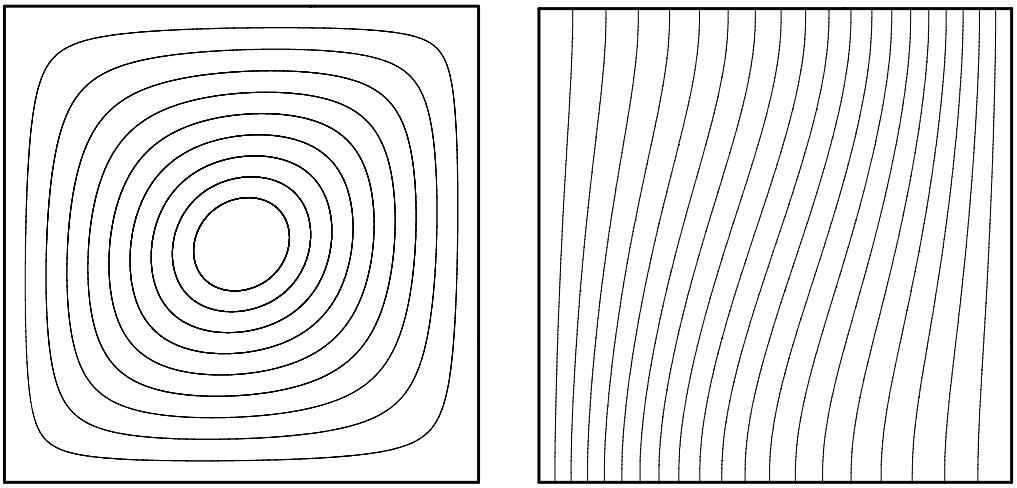

a) Streamline b)Temperature

Figure 3.14 Temperature and streamline contours for $Ra = 10^5$ and $Dar = 10^{-4}$.

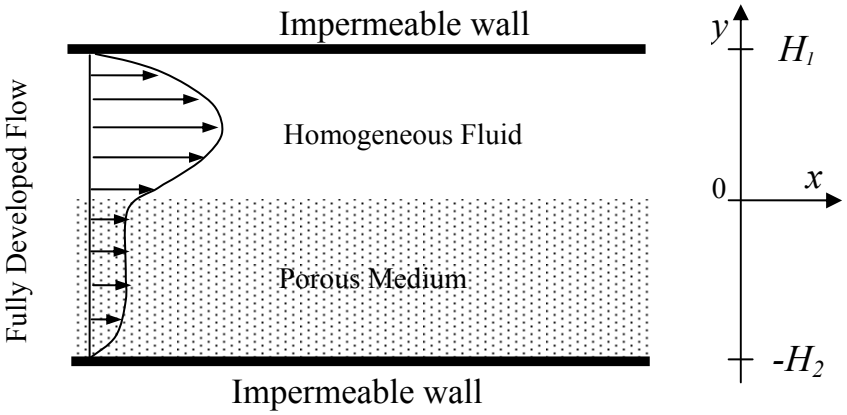

Figure 3.15 Schematic of fully developed flow in a channel partially filled with saturated porous medium.

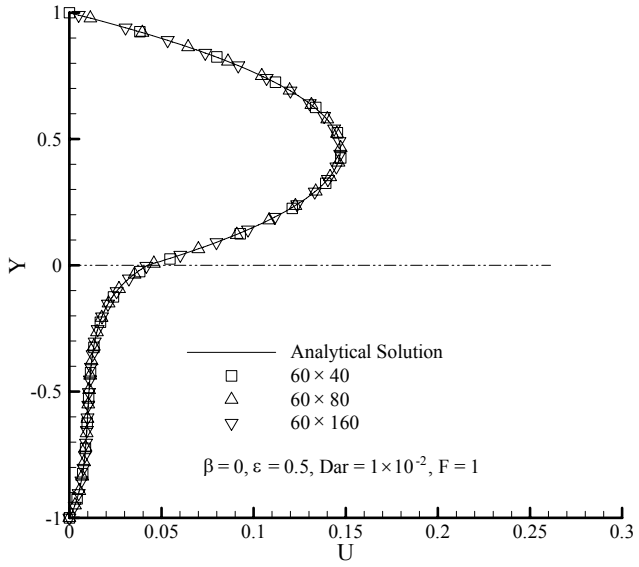

Figure 3.16 Effect of grid size on velocity profile.

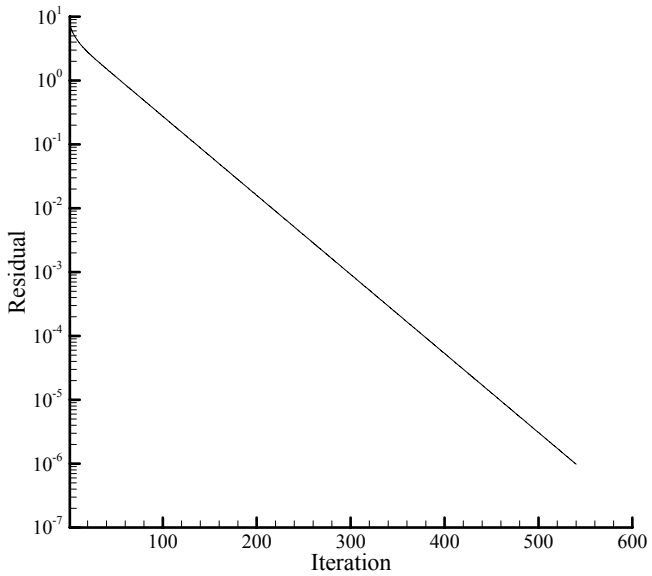

Figure 3.17 Variation of the residual as a function of iterations; 60 × 60 CV grid.

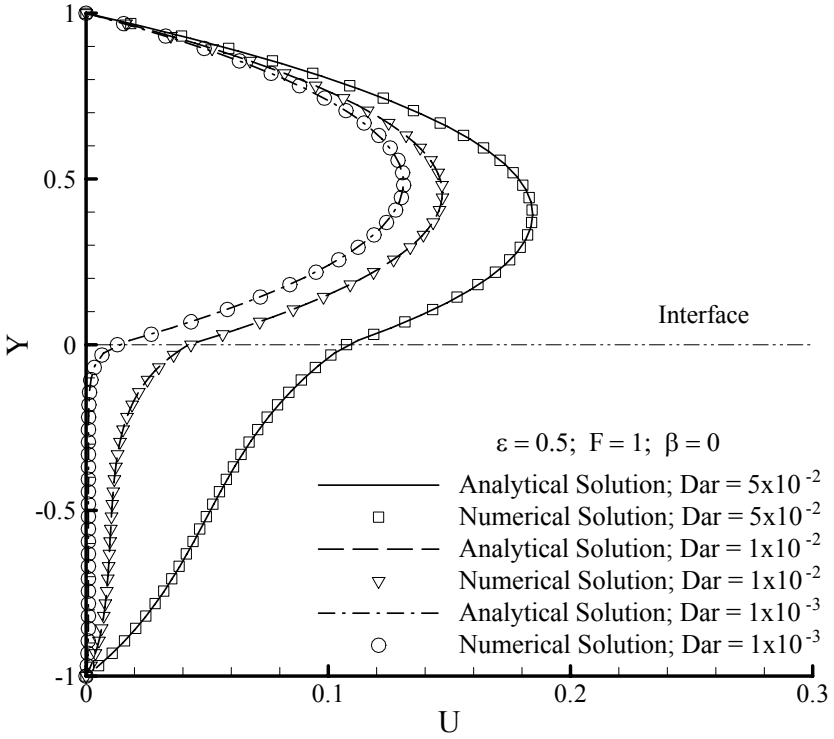

a) Darcy Number Effect

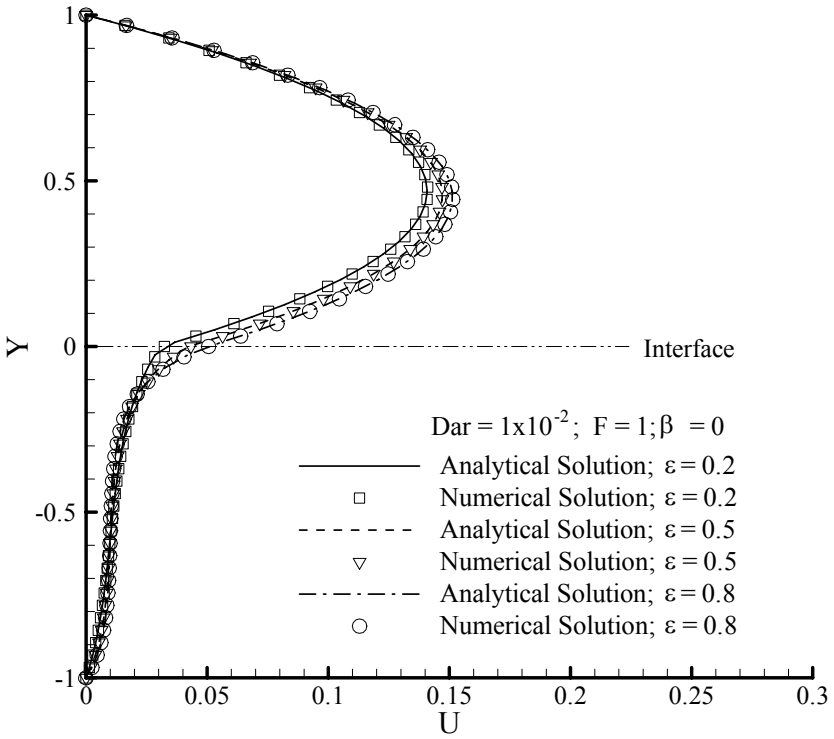

b) Porosity Effect

Figure 3.18 Profile of *u* velocity under different flow conditions; a) Darcy number effect; b) Porosity effect; c) Forchheimer number effect; d) Jump parameter effect.

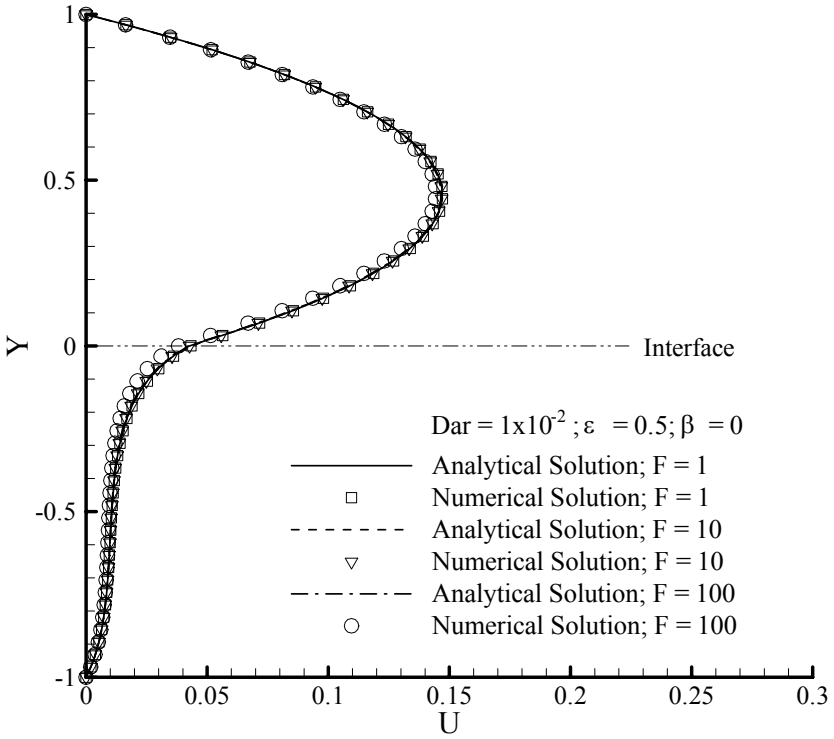

C) Forchheimer number effect

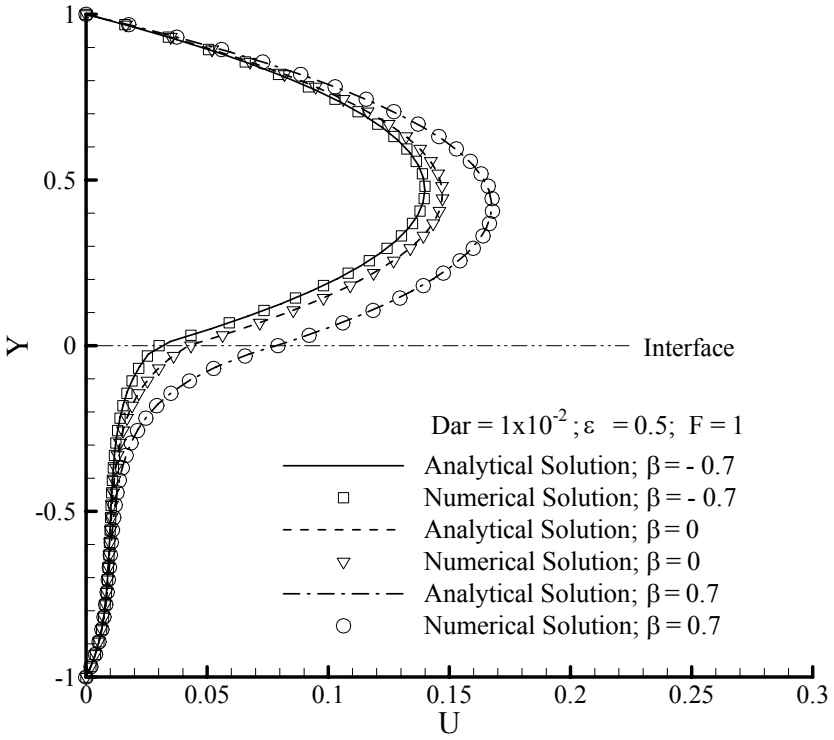

d) Jump parameter effect

Figure 3.18 (continued).

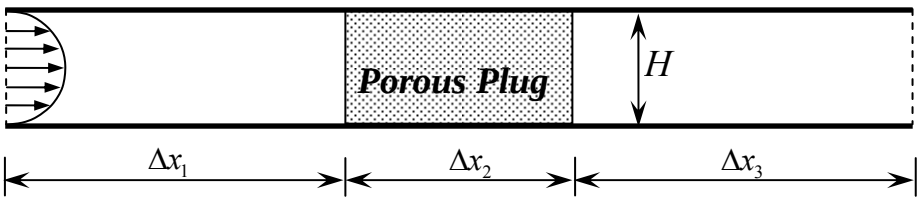

Figure 3.19 Schematic of a flow in a channel with a porous plug.

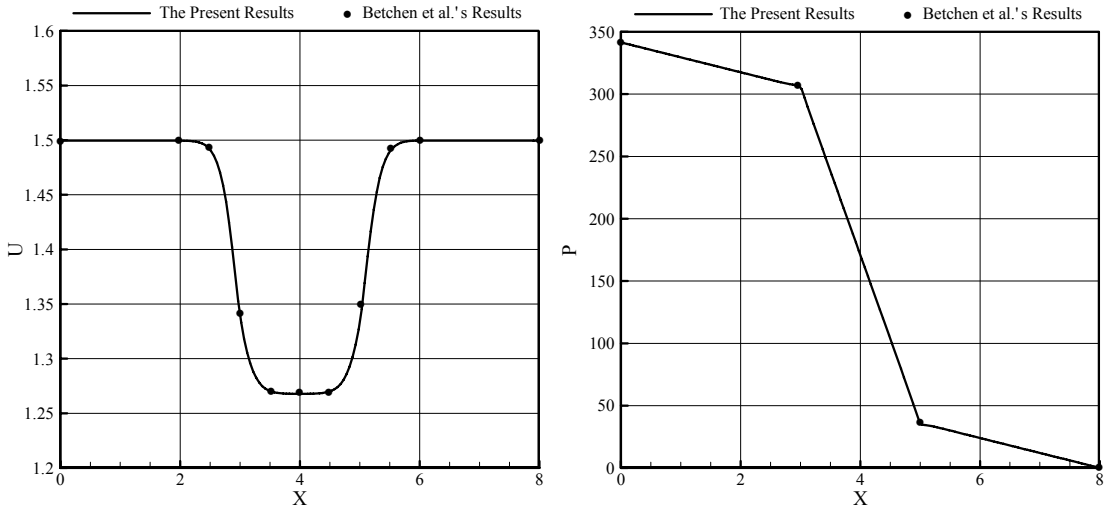

a)

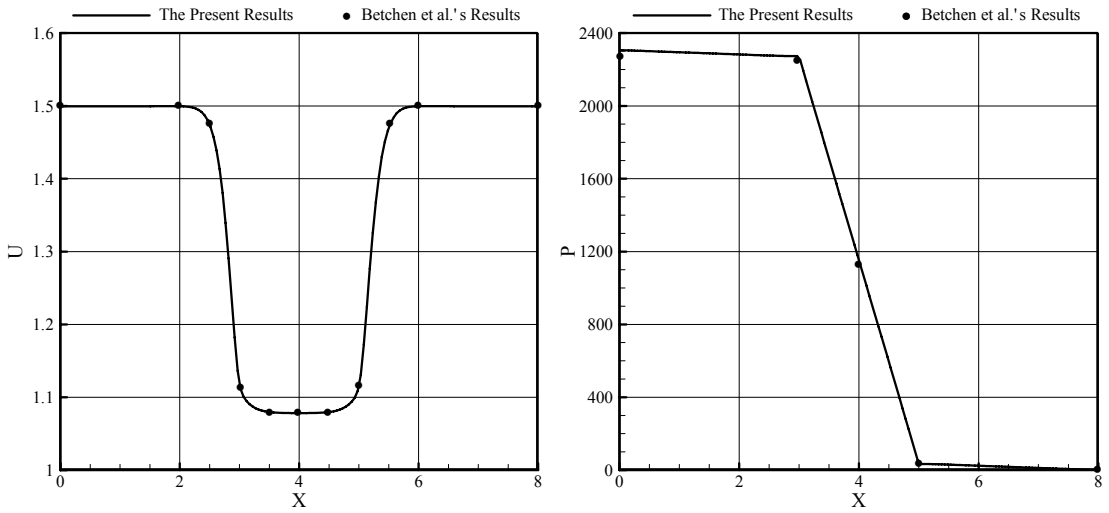

b)

Figure 3.20 Velocity and pressure distributions along the centerline at a) $Dar = 10^{-2}$ and b) $Dar = 10^{-3}$; other parameters are $Re = 1$, $\varepsilon = 0.7$, $\beta = 0$, $\beta_1 = 0$, $\Delta x_1 = \Delta x_3 = 3H$ and $\Delta x_2 = 2H$.

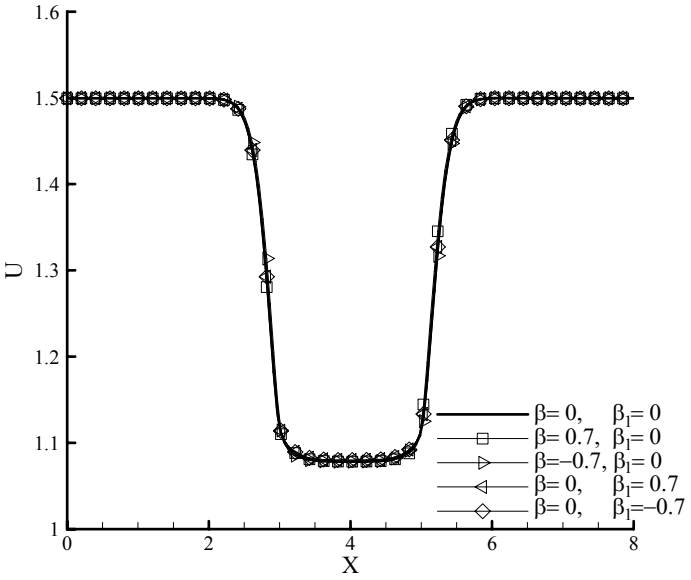

Figure 3.21 Effect of the jump coefficients on the velocity distribution along the centerline at $Dar = 10^{-3}$, $Re = 1$, $\varepsilon = 0.7$, $\Delta x_1 = \Delta x_3 = 3H$ and $\Delta x_2 = 2H$.

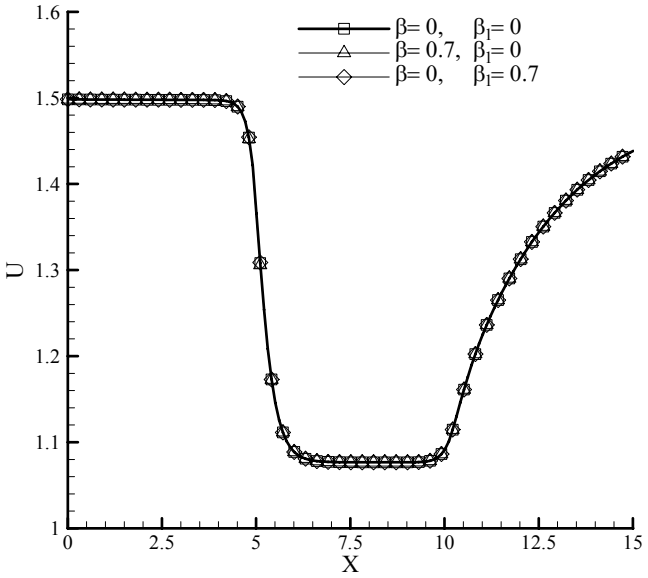

Figure 3.22 Velocity distribution along the centerline at $Dar = 10^{-2}$, $Re = 200$, $\varepsilon = 0.7$, $\Delta x_1 = \Delta x_2 = 5H$ and $\Delta x_3 = 50H$.

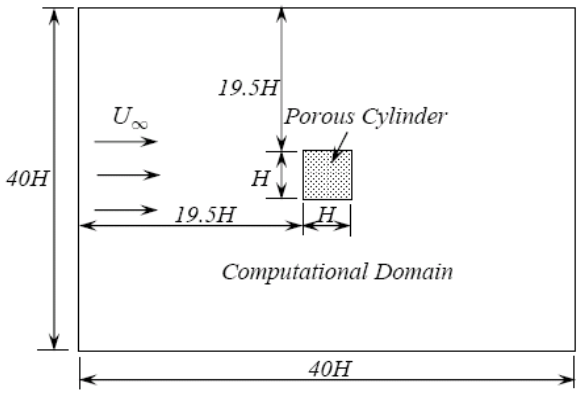

Figure 3.23 Schematic of flow past a porous square cylinder.

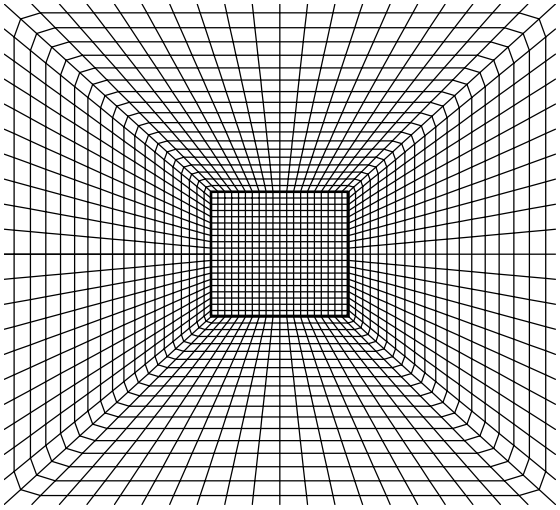

Figure 3.24 Illustration of the computational mesh for flow past a porous cylinder.

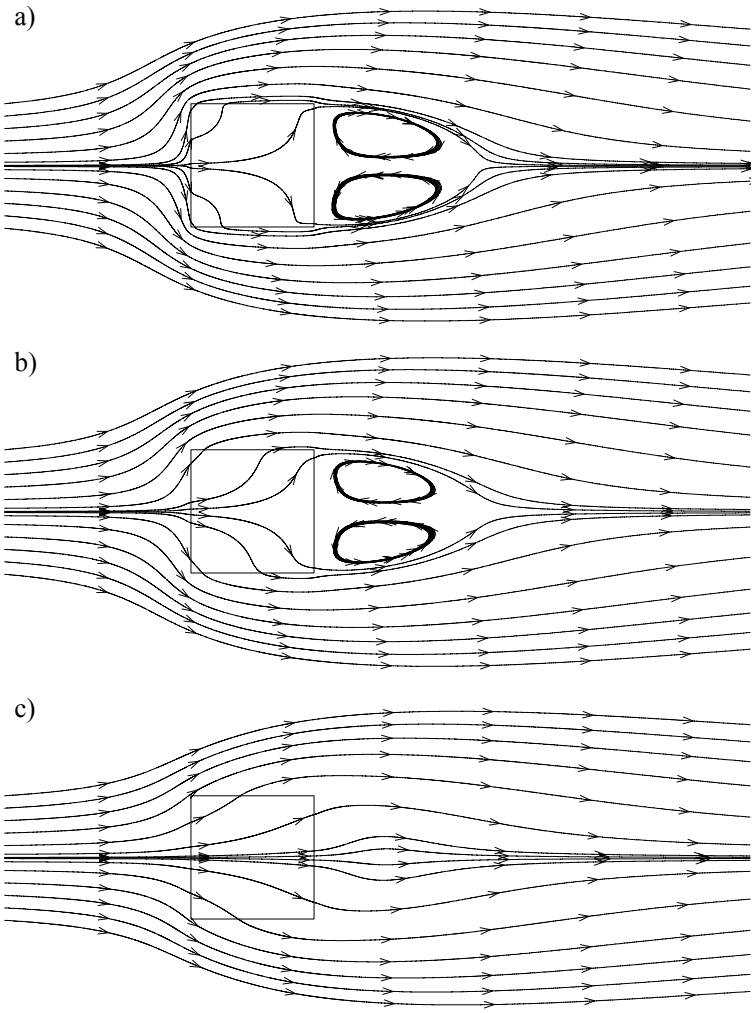

Figure 3.25 Streamline of flow past a porous cylinder at different *Dar*; a) $Dar = 10^{-4}$, b) $Dar = 10^{-3}$, c) $Dar = 10^{-2}$.

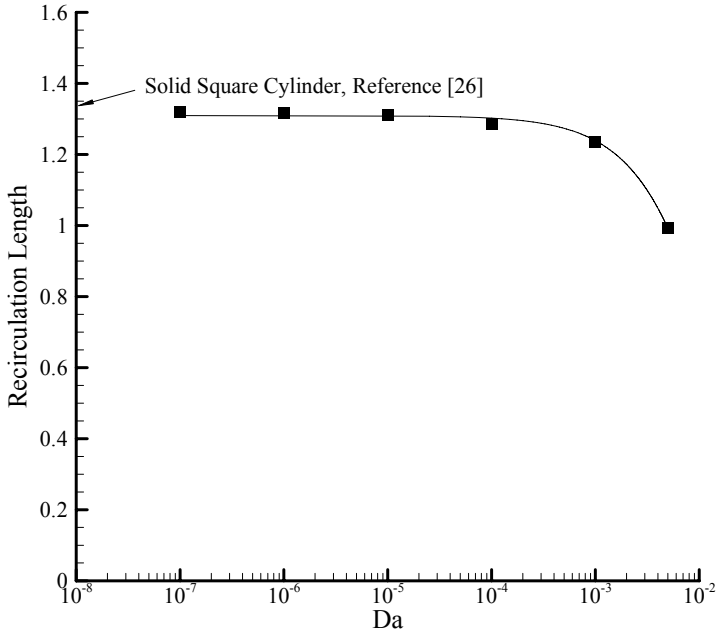

Figure 3.26 Variation of recirculation length with *Dar*.

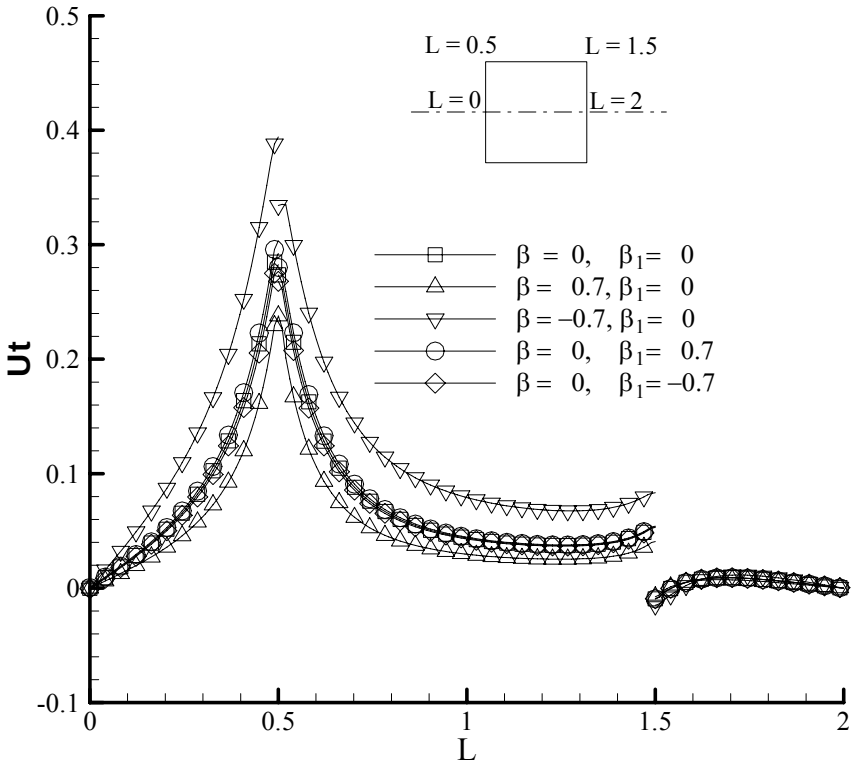

Figure 3.27 Tangential velocity distribution along the interface; $\varepsilon = 0.4$, $C_F = 1$, *Re* = 20 and *Dar* = 10^{-3}.

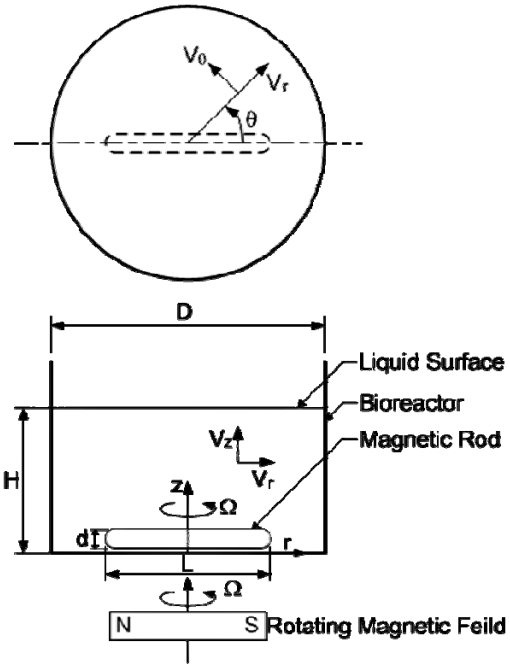

Figure 4.1 Diagram of the micro-bioreactor system.

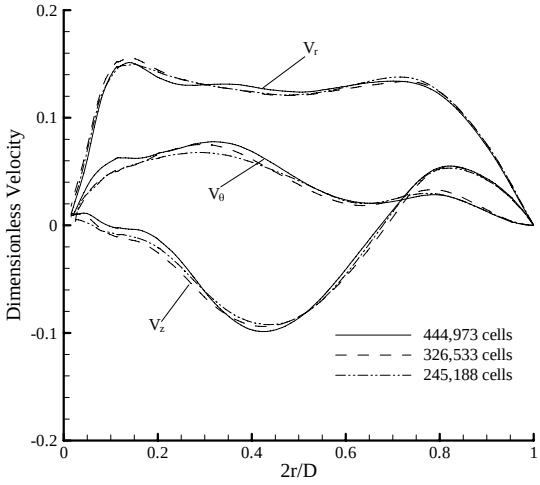

Figure 4.2 Dimensionless velocity components versus radial position at height z/H = 0.25, Re = 576 and angular coordinate from rod θ = 90º.

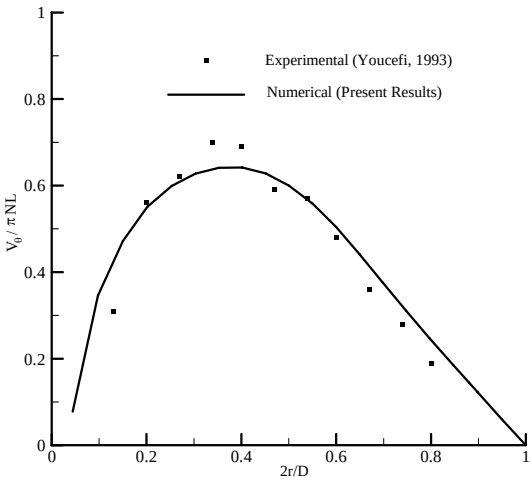

Figure 4.3 Dimensionless tangential velocity versus radial position at height z = 1.1 mm, Re = 38 and angular coordinate from impeller θ = 90º.

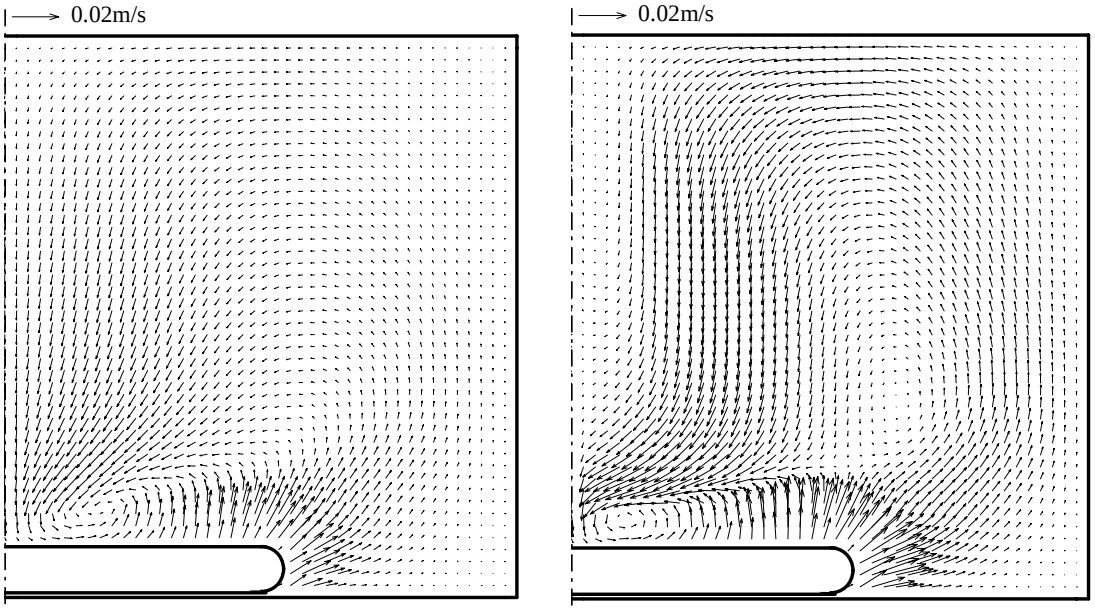

a) *Re* = 288 b) *Re* = 432

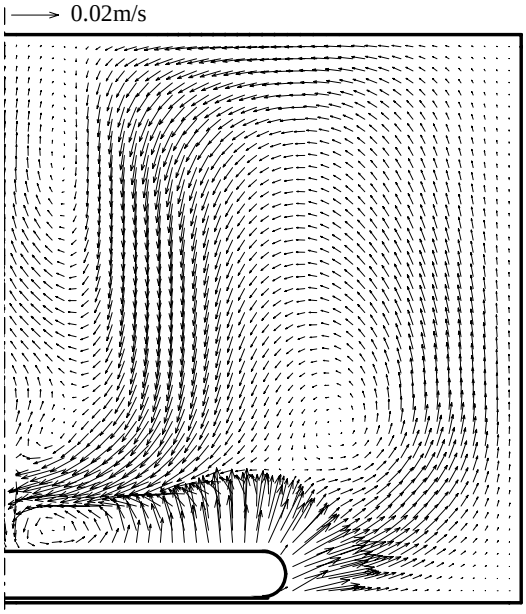

c) *Re* = 576

Figure 4.4 Velocity field in a vertical plane at angular coordinate from rod $\theta = 0^{o}$; a) *Re* = 288, b) *Re* = 432; c) *Re* = 576.

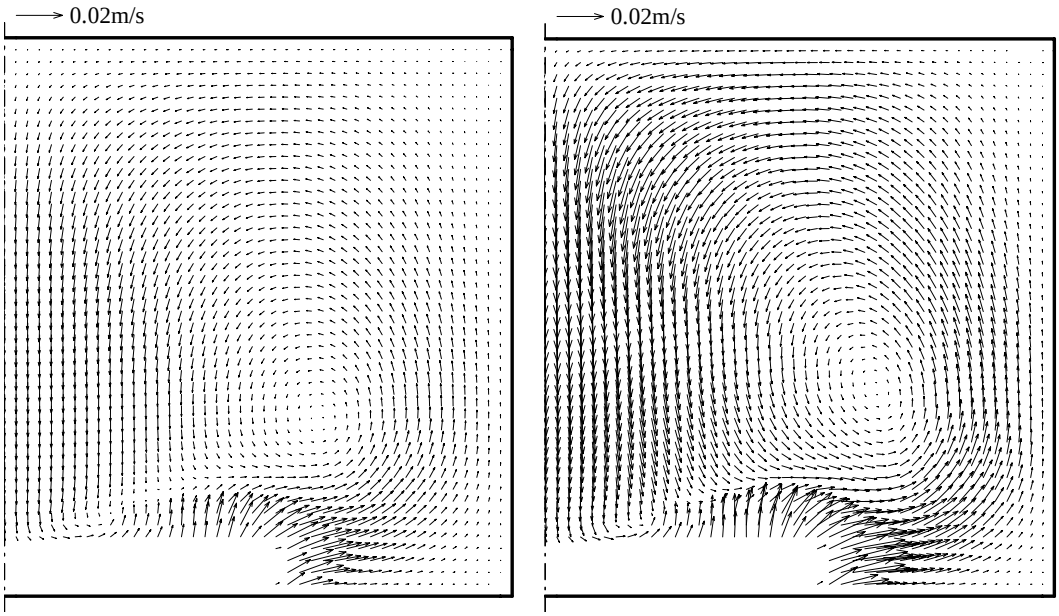

a) *Re* = 288 b) *Re* = 432

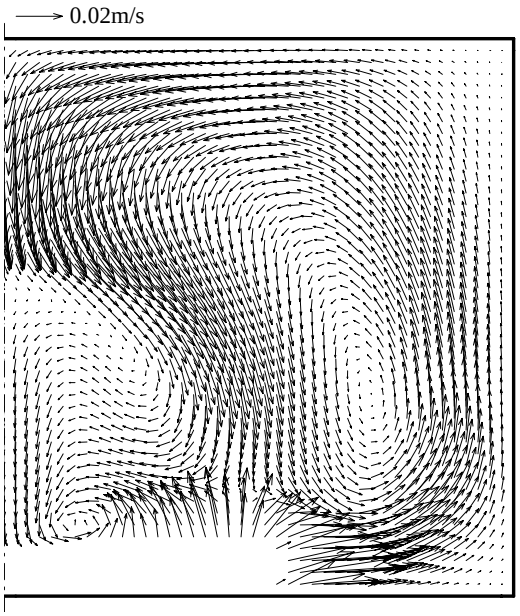

c) *Re* = 720

Figure 4.5 Velocity field in a vertical plane at angular coordinate from rod $\theta = 0^{o}$; a) *Re* = 288; b) *Re* = 432; c) *Re*= 720.

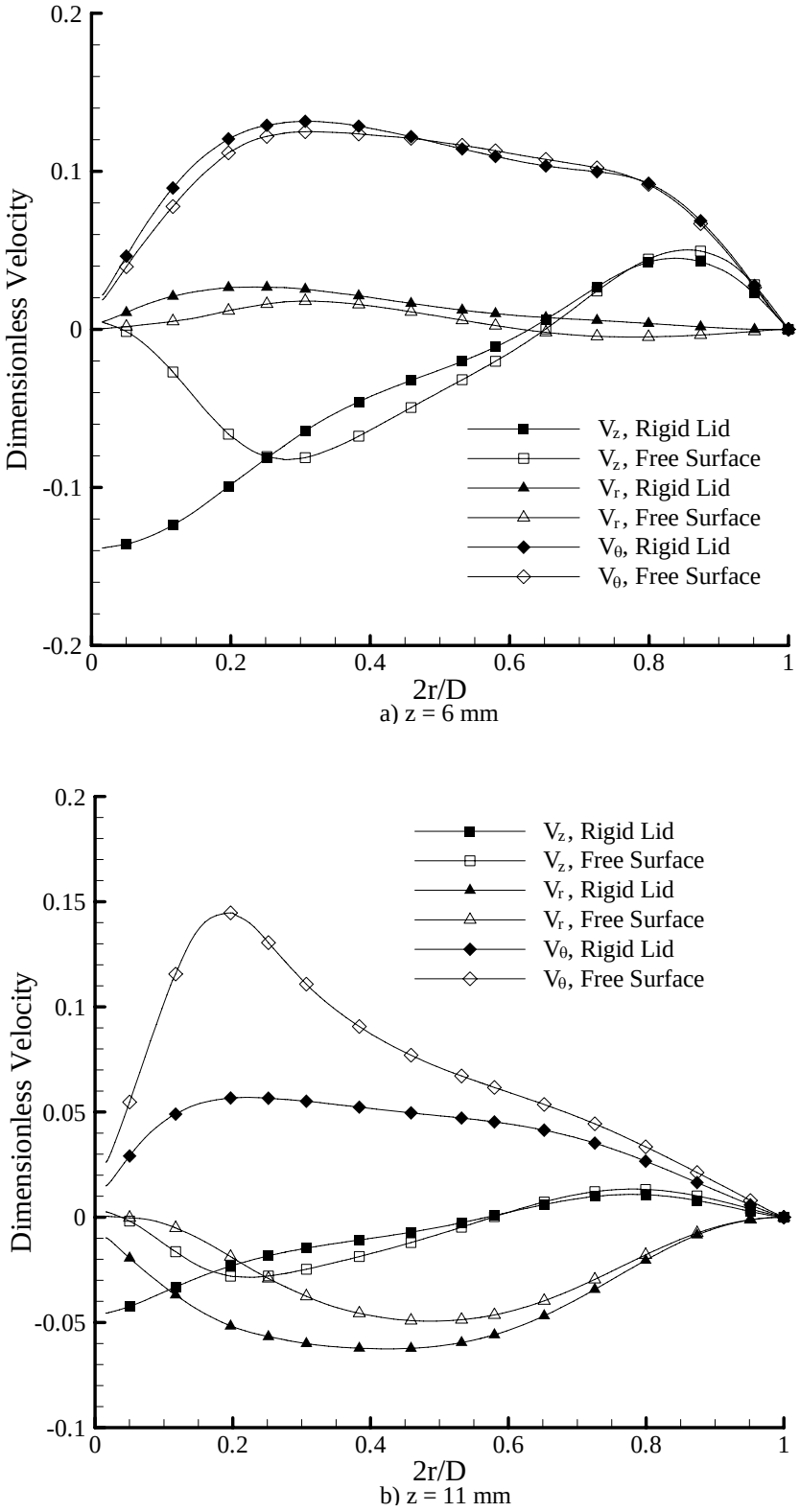

Figure 4.6 Comparison of dimensionless velocity components along a radial line at *Re* = 432 and angular coordinate from rod $\theta = 0^{o}$; a) z = 6 mm; b) z = 11 mm.

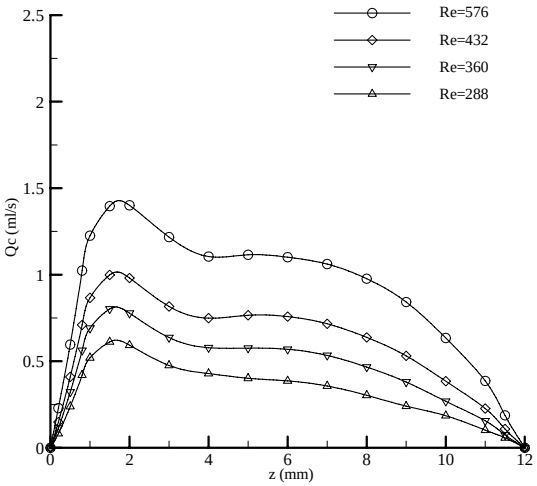

Figure 4.7 Variation of circulation capacity with height at various *Re*.

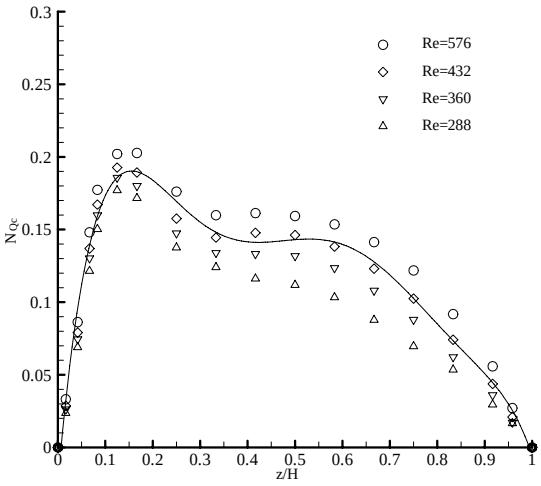

Figure 4.8 Variation of flow number with height at various *Re*.

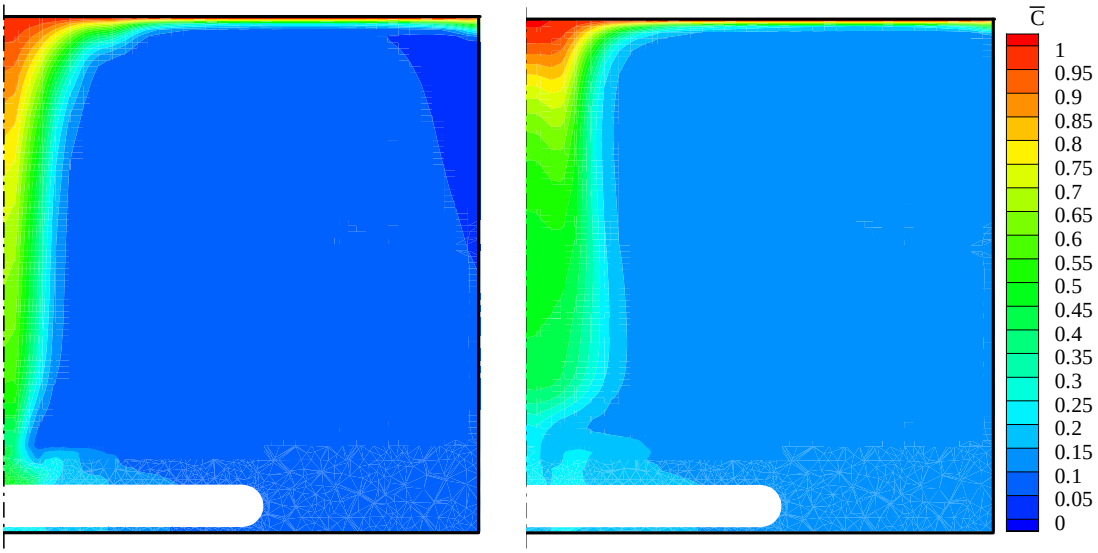

a) *Re* = 288 b) *Re* = 432

Figure 4.9 Oxygen concentration field in a vertical plane at angular coordinate from rod θ = 0°, *Da* = 122.3; a) *Re* = 288; b) *Re* = 432.

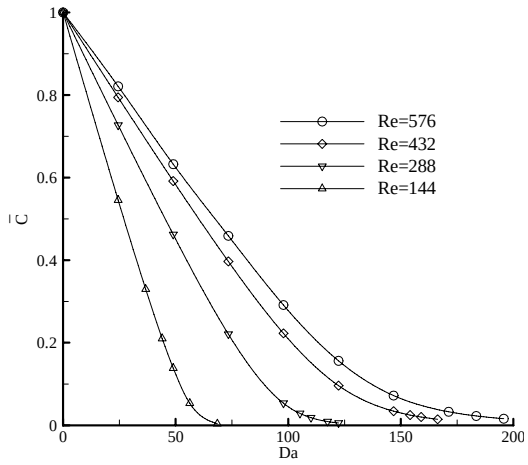

Figure 4.10 Minimum oxygen concentration against *Da* at various *Re*.

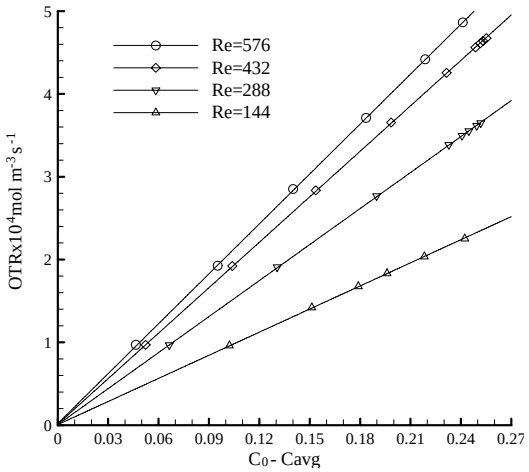

Figure 4.11 Relationship between *OTR* and concentration difference C_0 - C_{avg}.

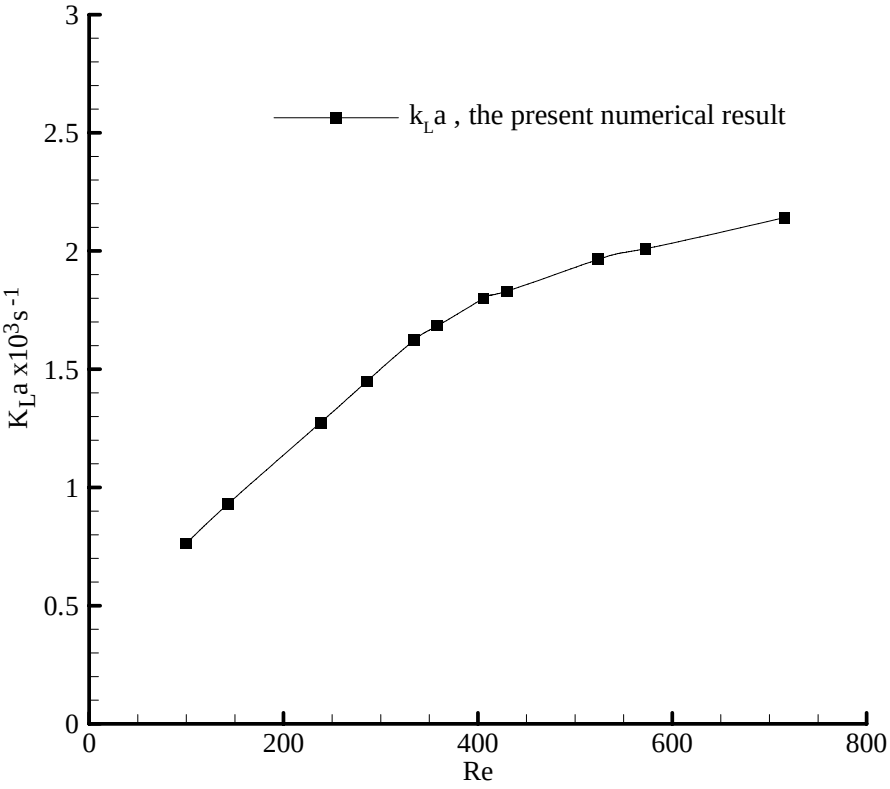

Figure 4.12 Variation of volumetric oxygen transfer coefficient with *Re*.

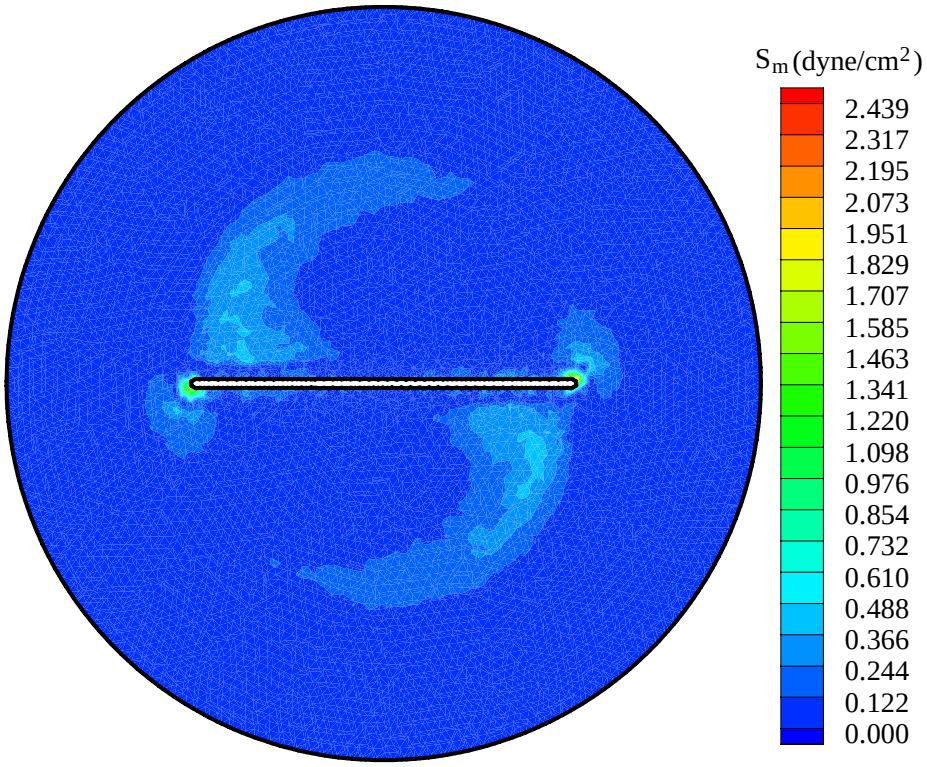

Figure 4.13 Shear stress field in a horizontal plane at z/H = 0.01 and Re = 432.

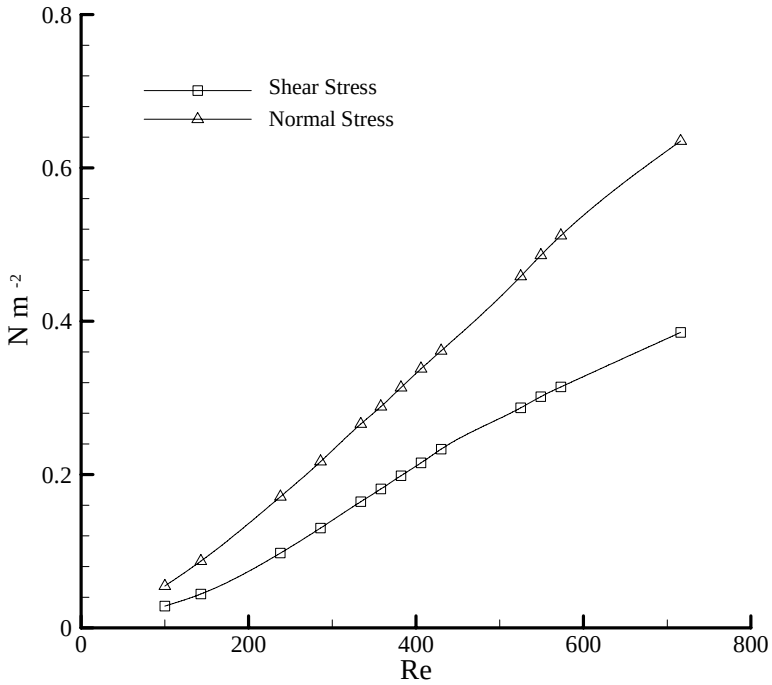

Figure 4.14 Peak values of shear and normal stresses against Re.

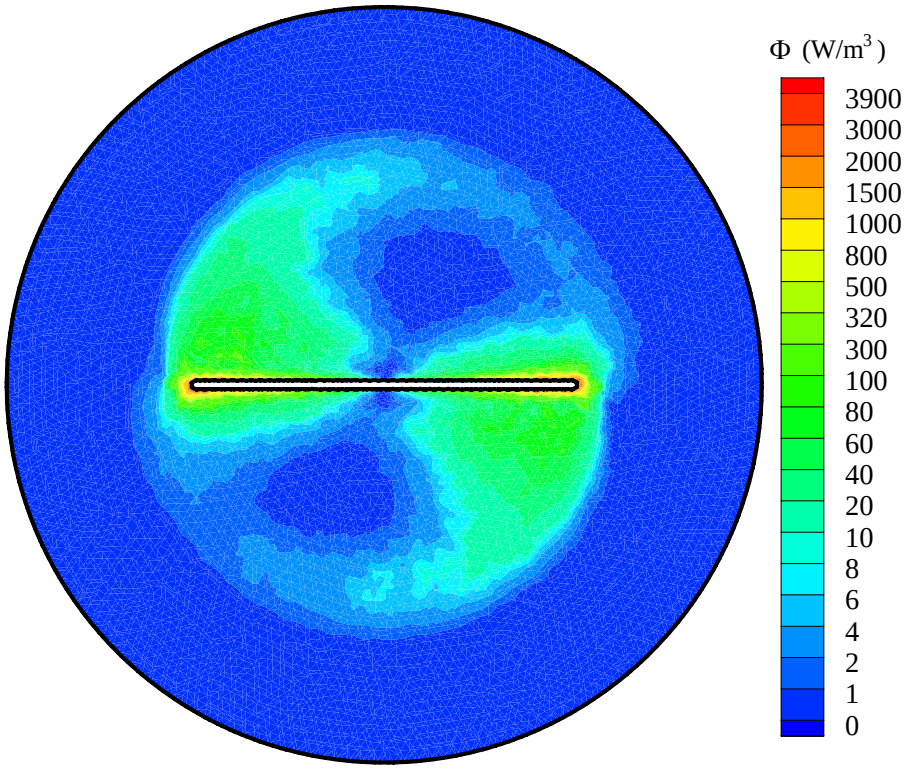

Figure 4.15 Distribution of local energy dissipation rate in a horizontal plane z/H = 0.01 and Re = 432.

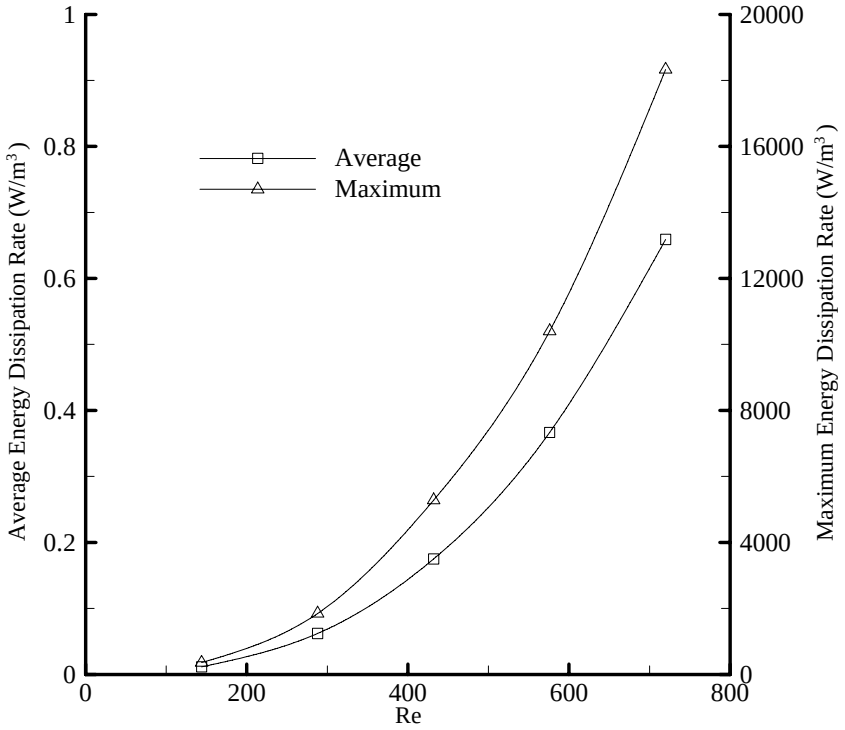

Figure 4.16 Average and maximum energy dissipation rates at various Re.

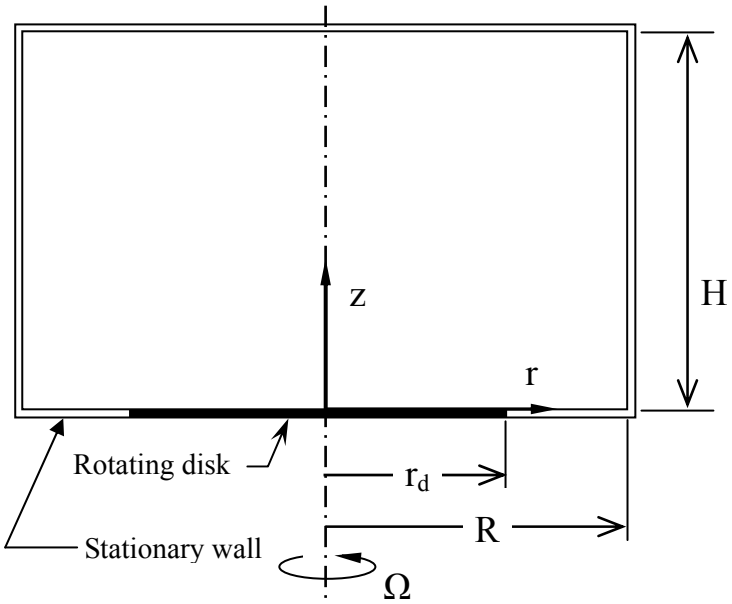

Figure 5.1 Micro-Bioreactor with a partially rotating bottom-wall.

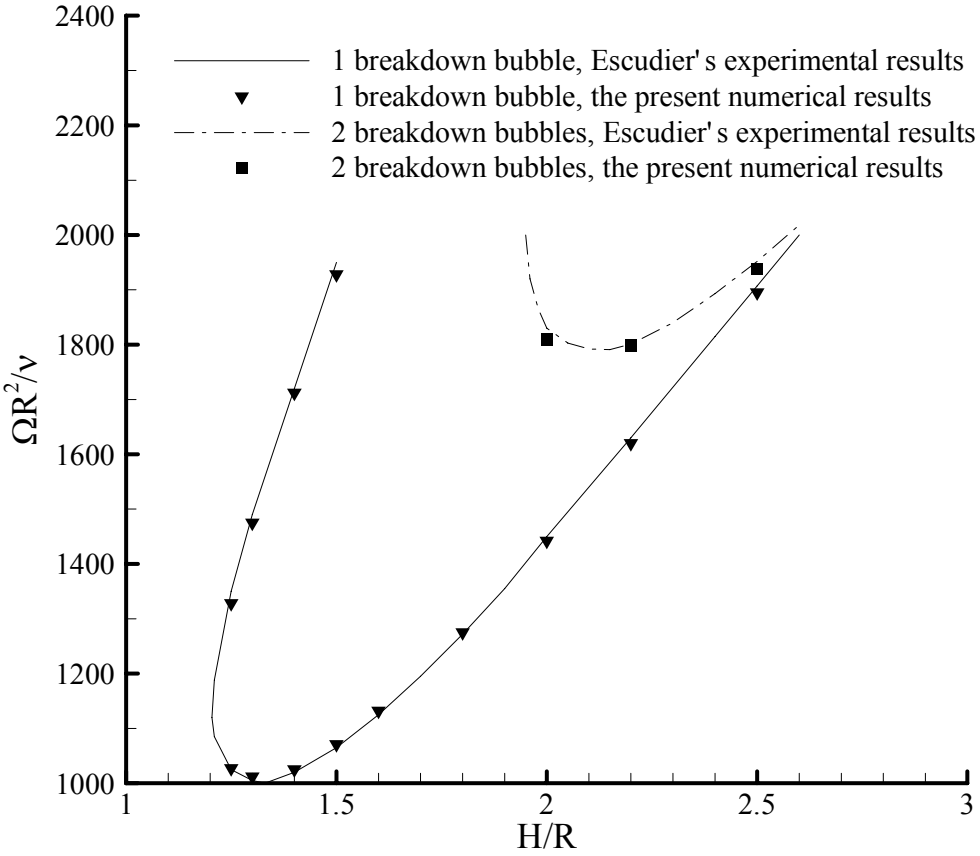

Figure 5.2 Boundary curves for the onset of vortex breakdown; $R/r_d = 1.0$.

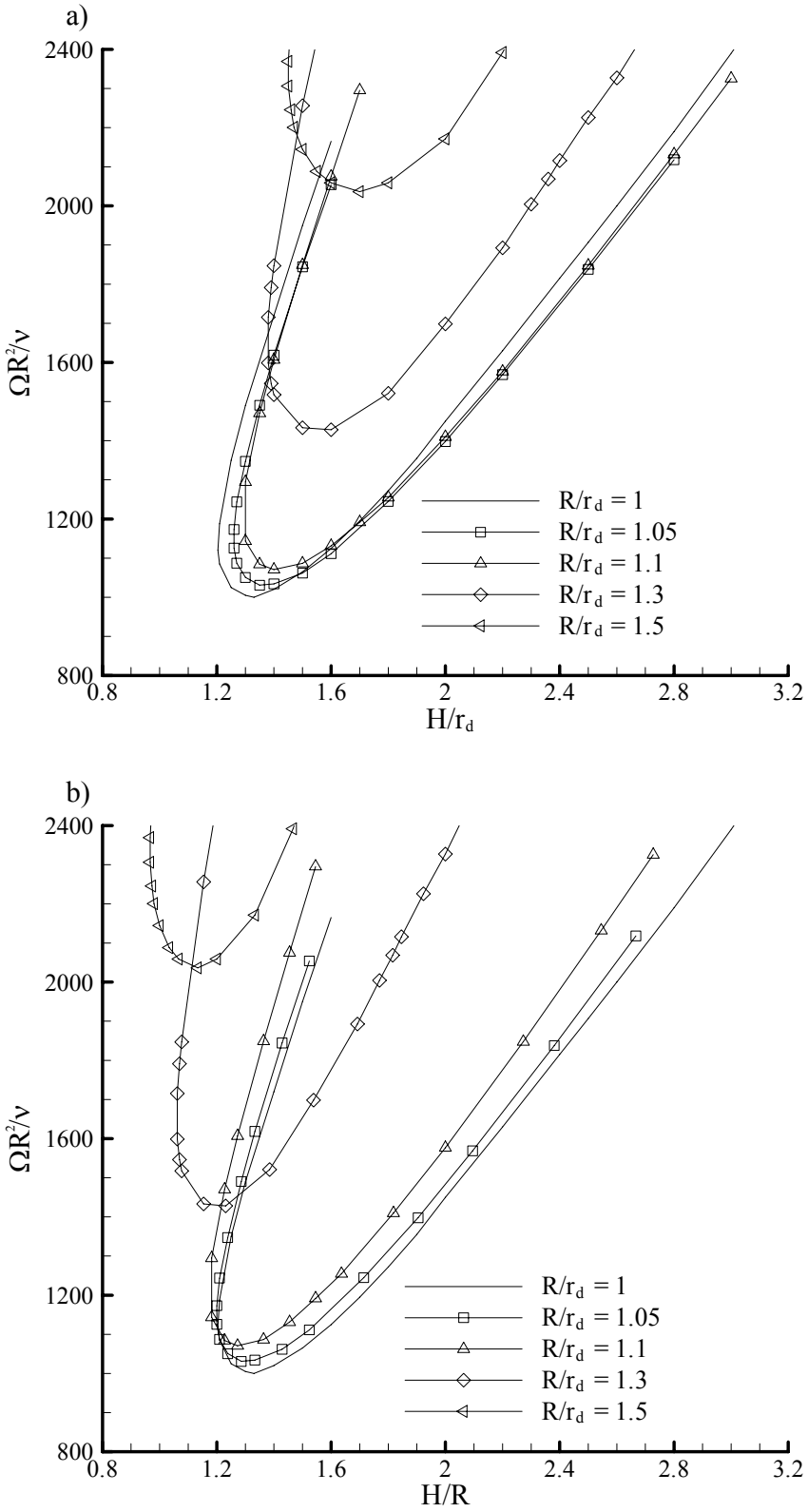

Figure 5.3 Boundary curves for the onset of vortex breakdown for a partially rotating bottom-wall; different parameters effect: a) ($\Omega R^2/\nu$, H/r_d), b) ($\Omega R^2/\nu$, H/R), c) ($\Omega r_d{}^2/\nu$, H/r_d), d) ($\Omega r_d{}^2/\nu$, H/R).

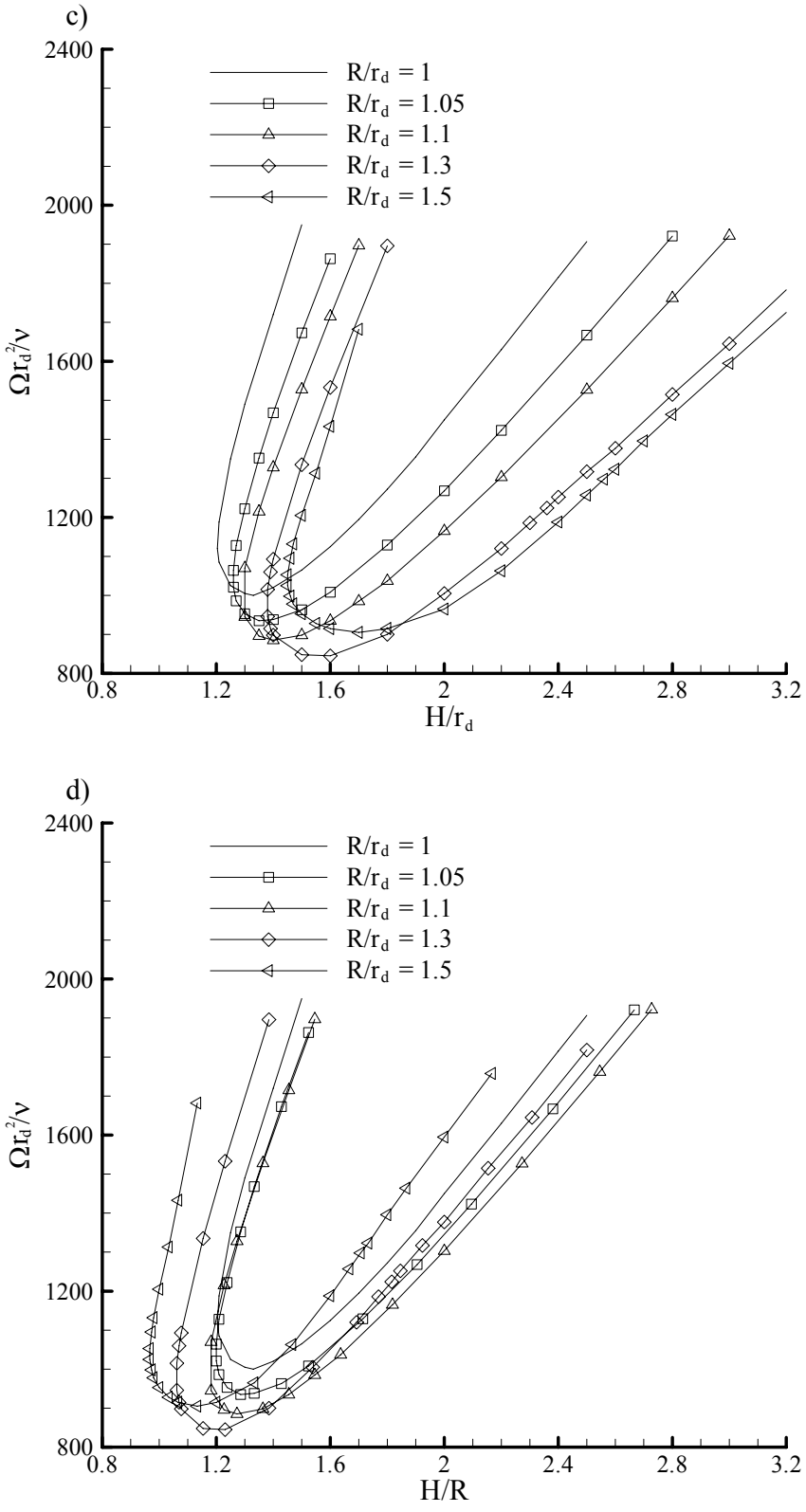

Figure 5.3 (continued).

i) *Re*=1200

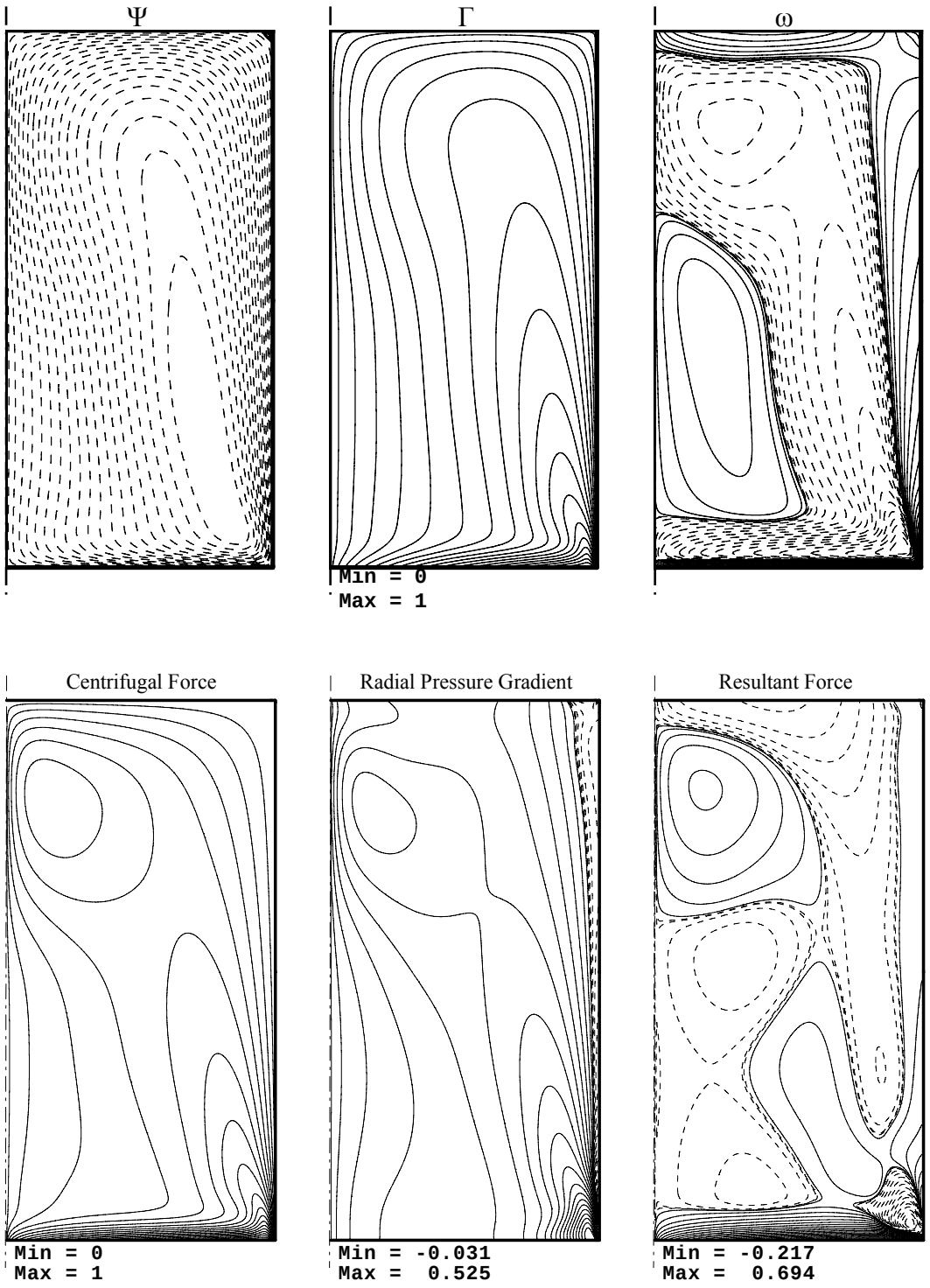

Figure 5.4 Contours of streamline Ψ, angular momentum Γ, azimuthal vorticity ω, centrifugal force v/r^2, radial pressure gradient $(1/\rho)(\partial p/\partial r)$, and resultant force v/r^2 - $(1/\rho)(\partial p/\partial r)$ in the meridional plane for the aspect ratio H/R = 2; i) Re = 1200 and ii) Re =1500; a) R/r_d = 1.0, b) R/r_d = 1.1, c) R/r_d = 1.3, d) R/r_d = 1.5; Contour levels C_i are non-uniformly spaced, with 20 positive levels C_i = Max(variable) × $(i/20)^3$ and 20 negative levels C_i = Min(variable) × $(i/20)^3$.

ii) Re = 1500

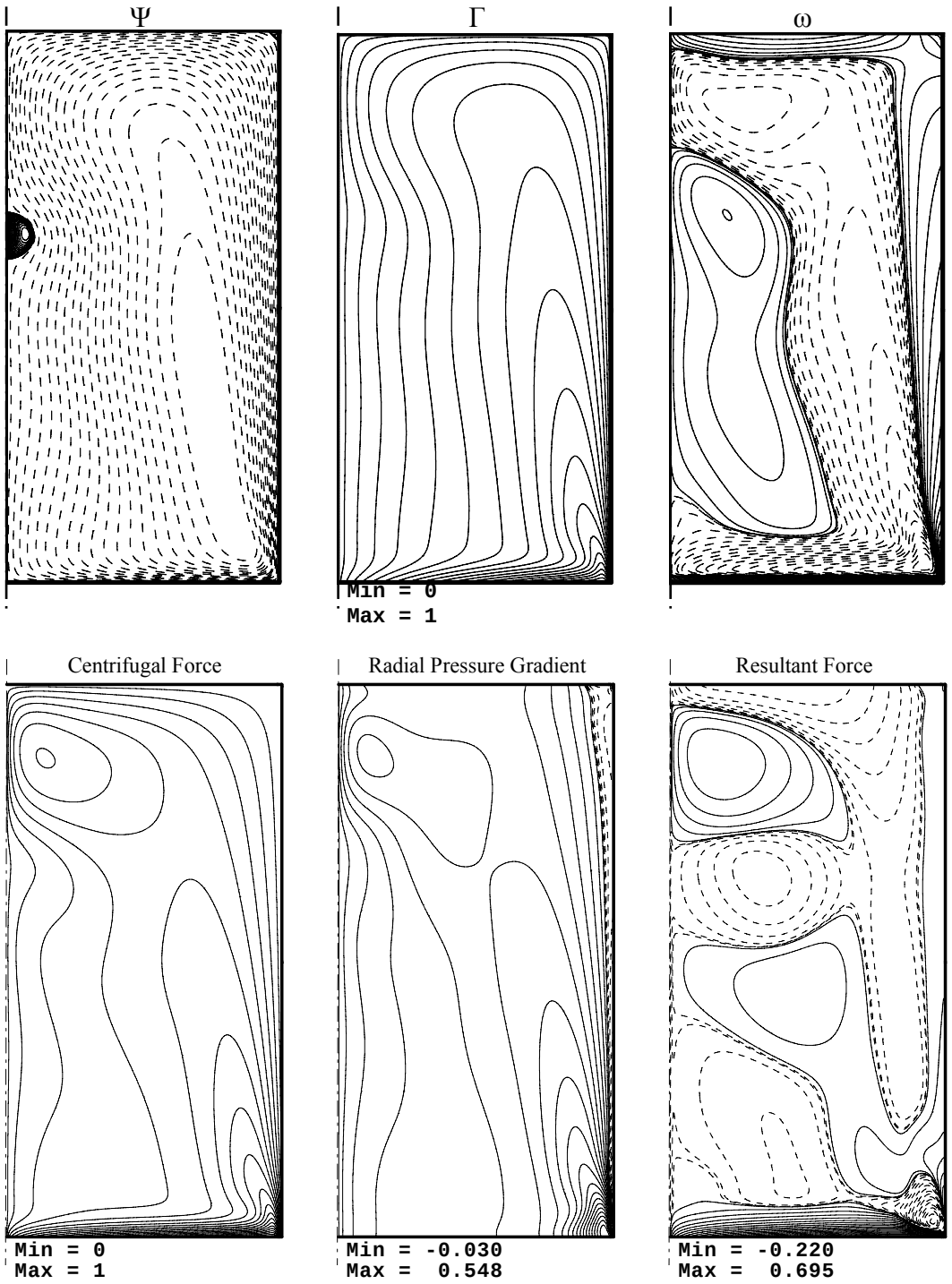

a) R/r_d = 1

Figure 5.4 (continued).

i) *Re*=1200

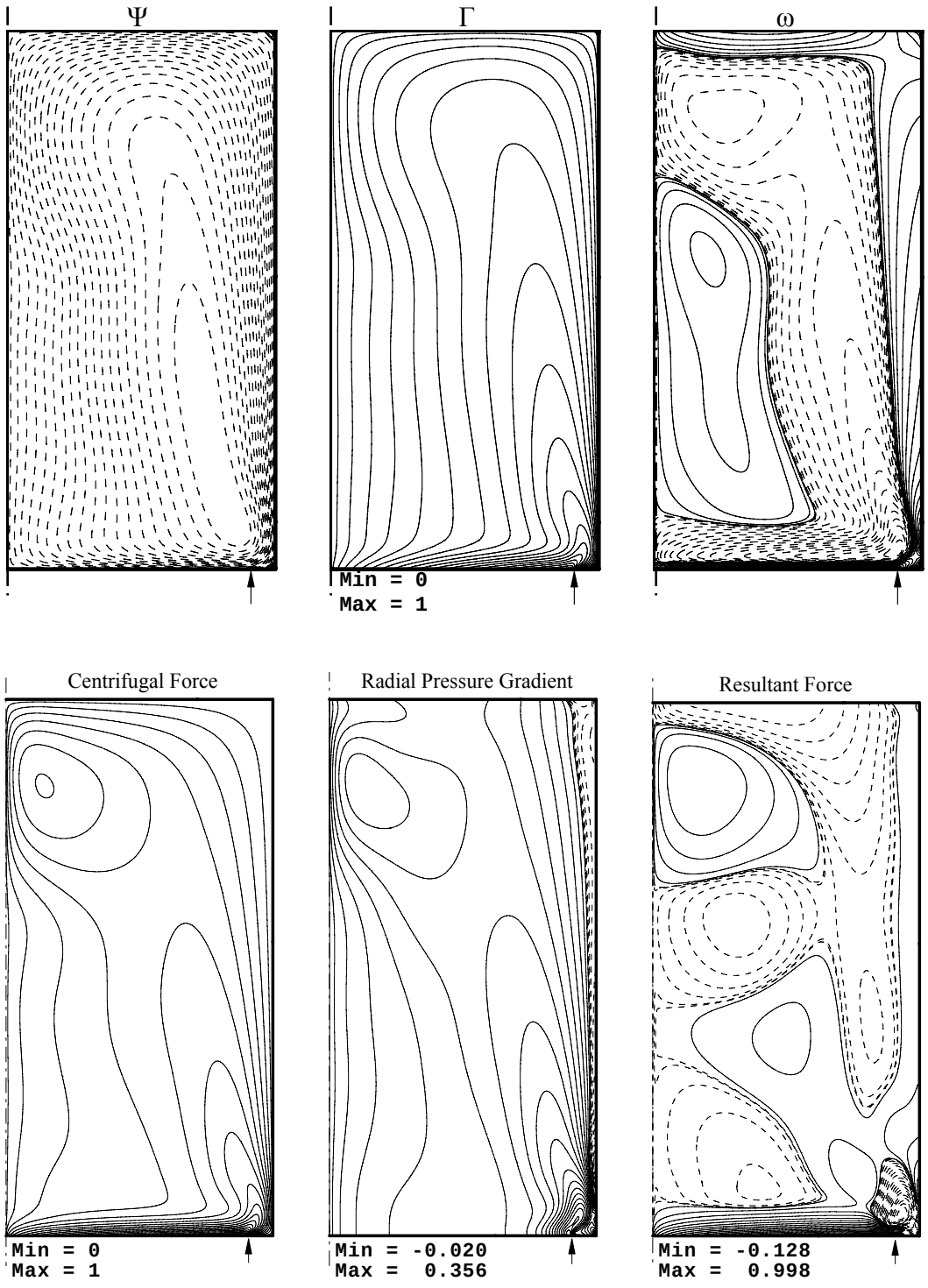

Figure 5.4 (continued).

ii) Re = 1500

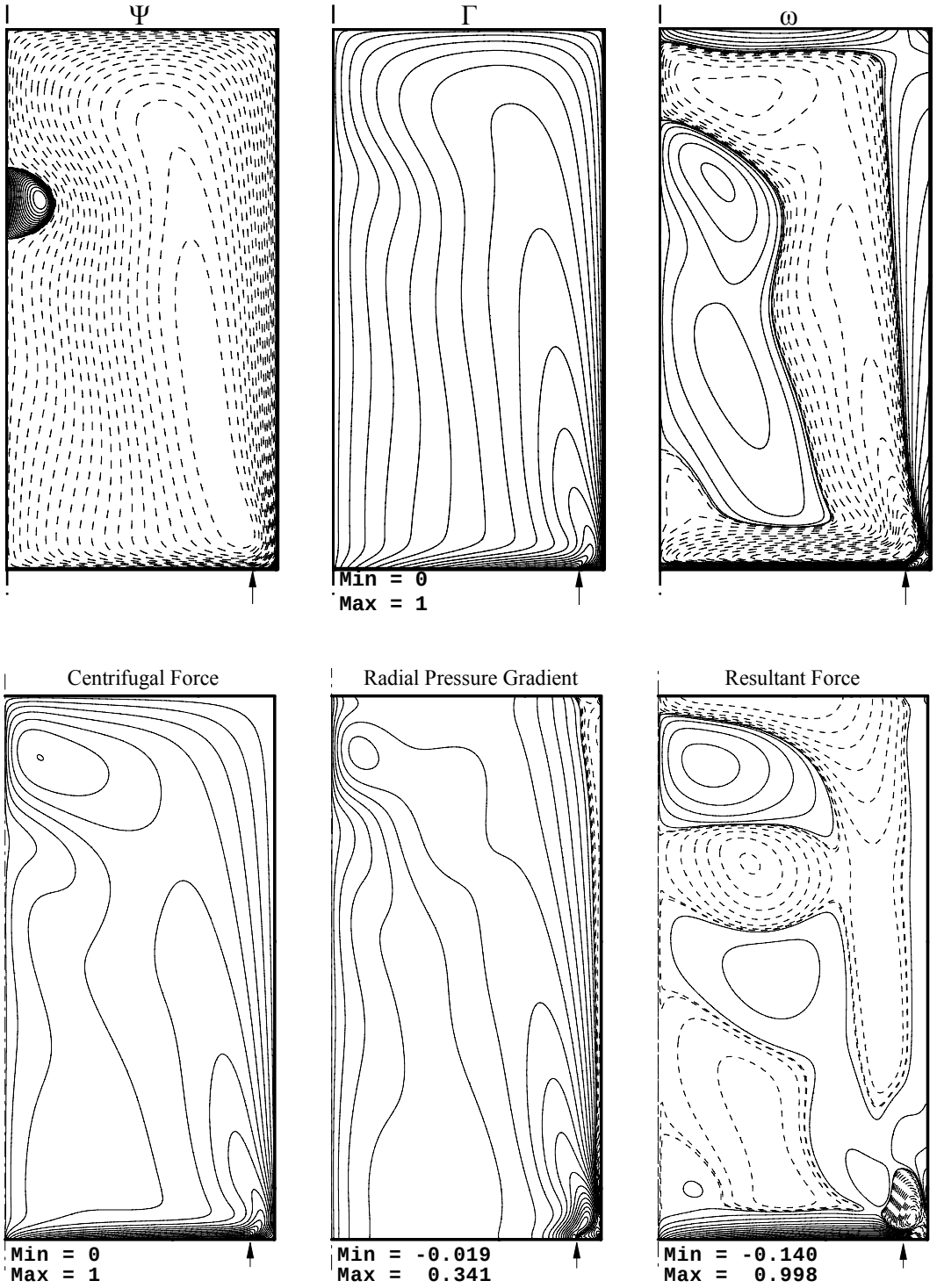

b) R/r_d = 1.1

Figure 5.4 (continued).

i) *Re*=1200

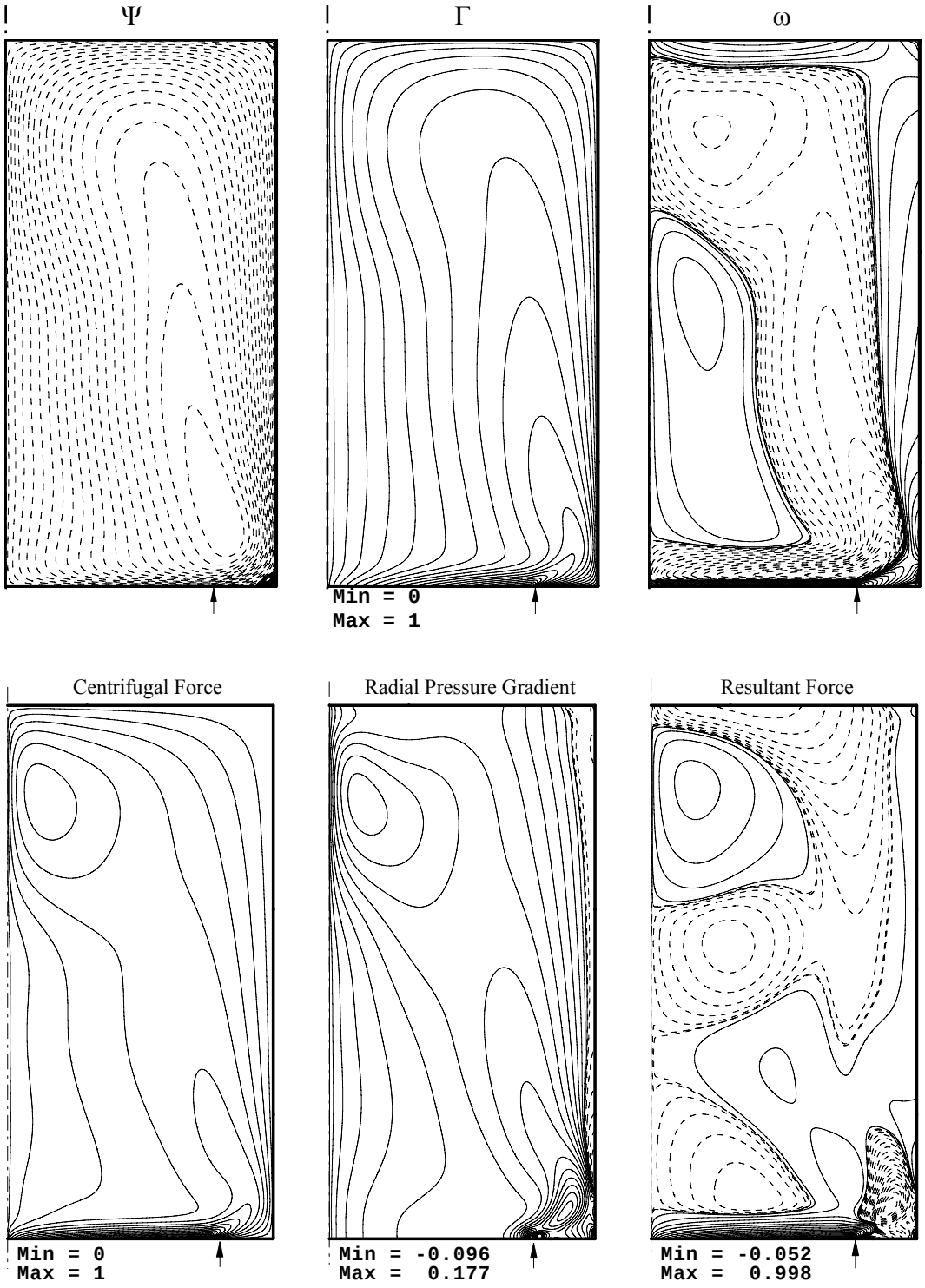

Figure 5.4 (continued).

ii) Re = 1500

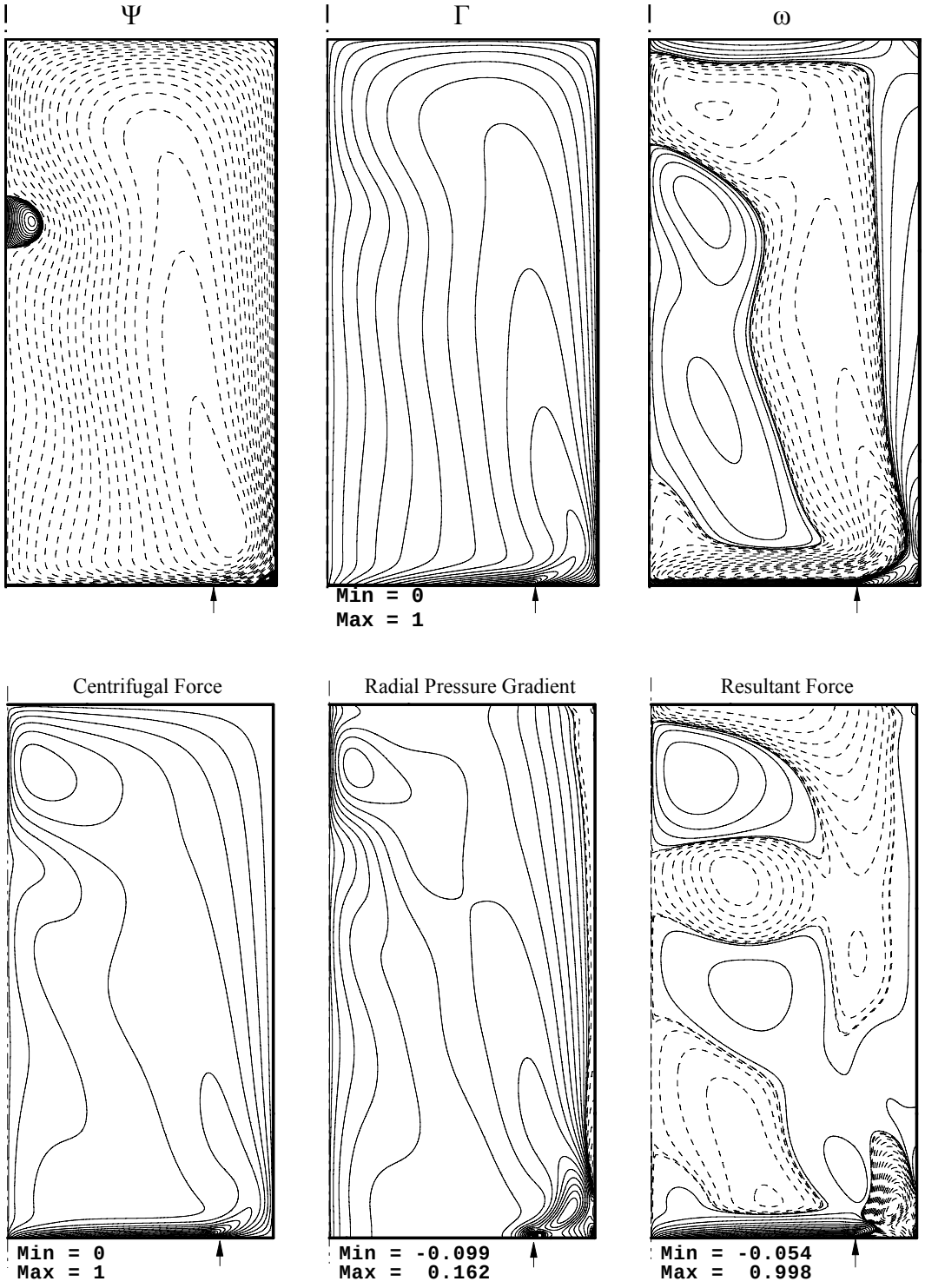

c) R/r_d = 1.3

Figure 5.4 (continued).

i) *Re*=1200

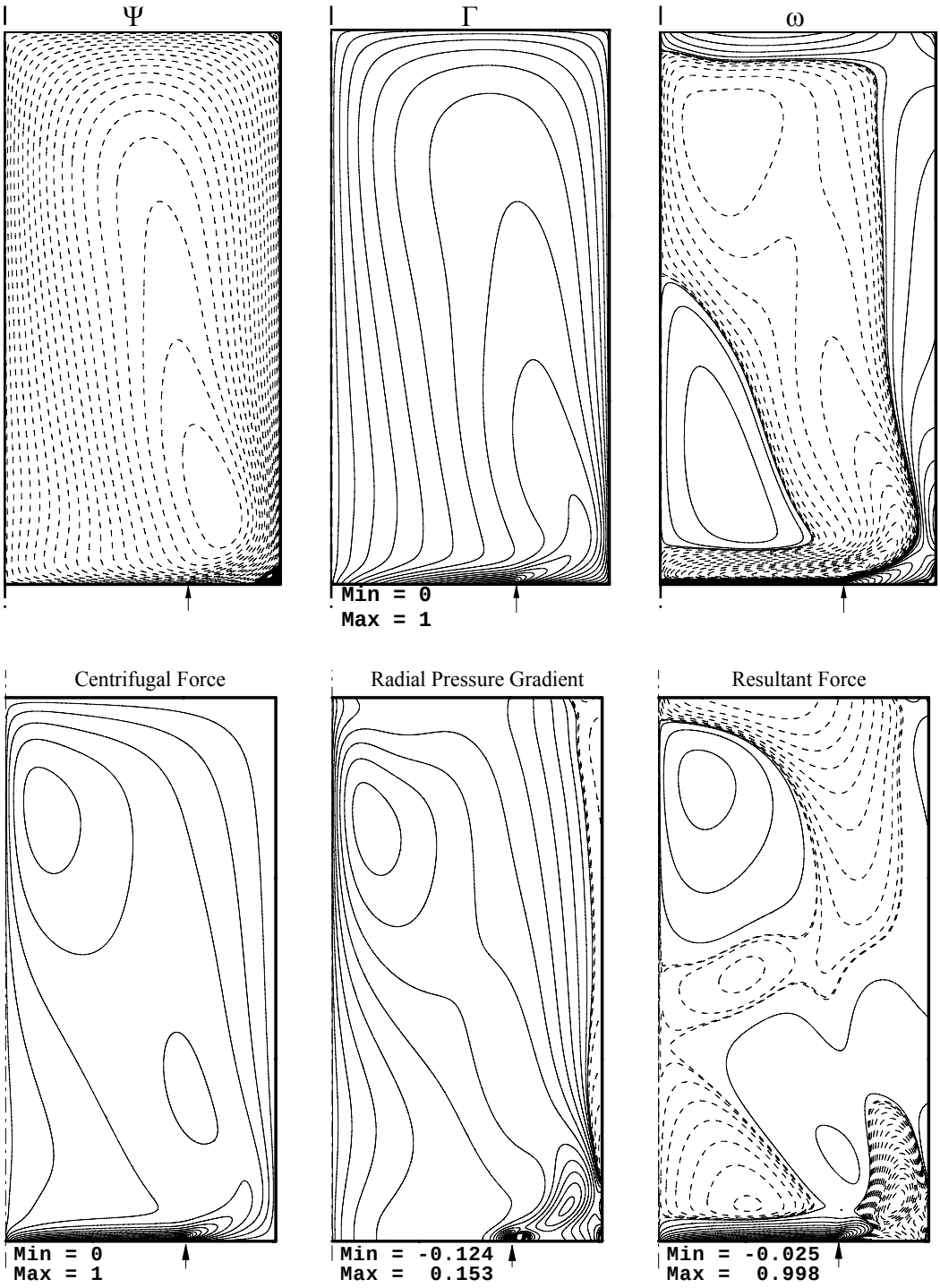

Figure 5.4 (continued).

ii) $Re = 1500$

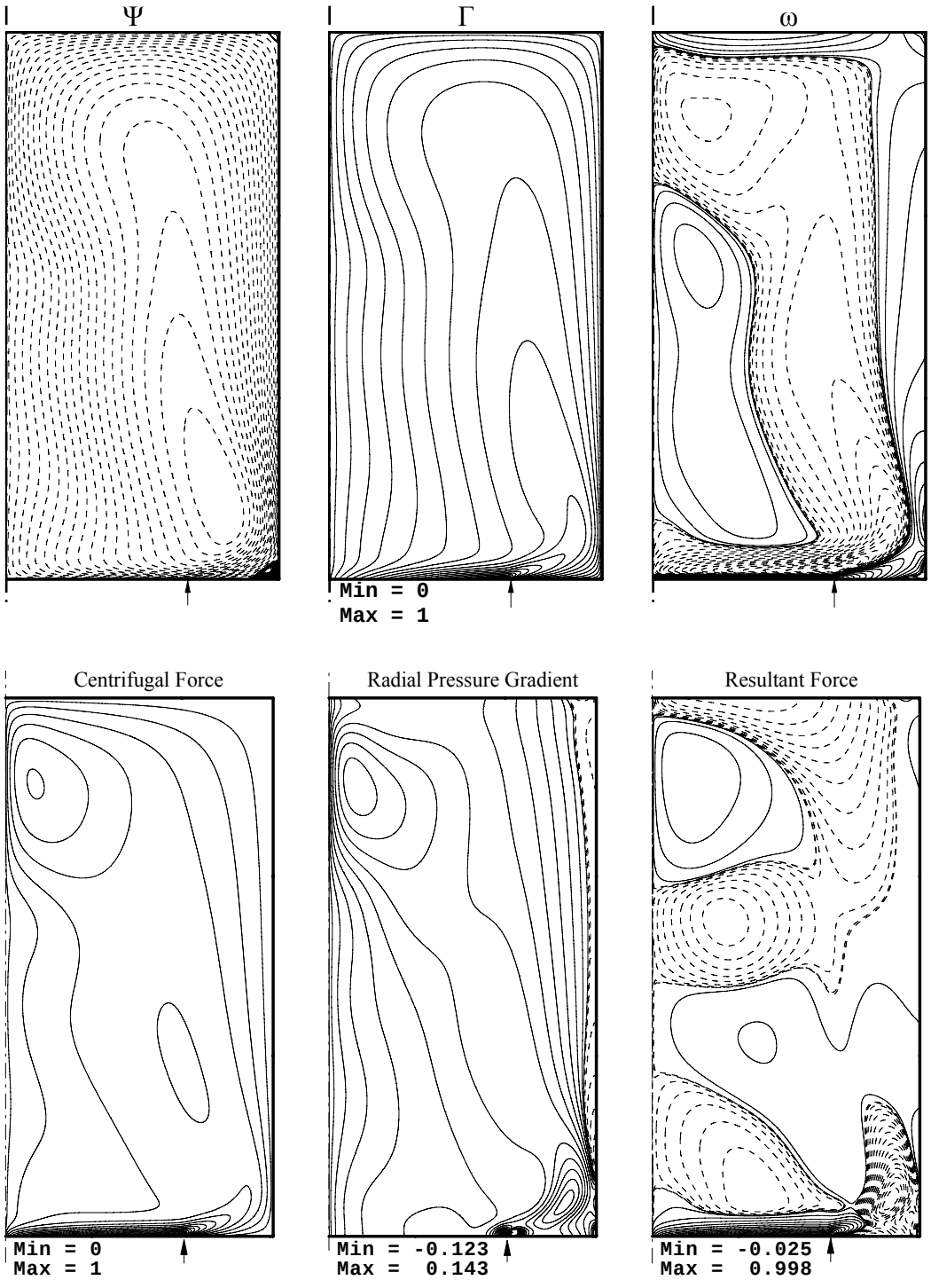

d) $R/r_d = 1.5$

Figure 5.4 (continued).

i) *Re*=1200

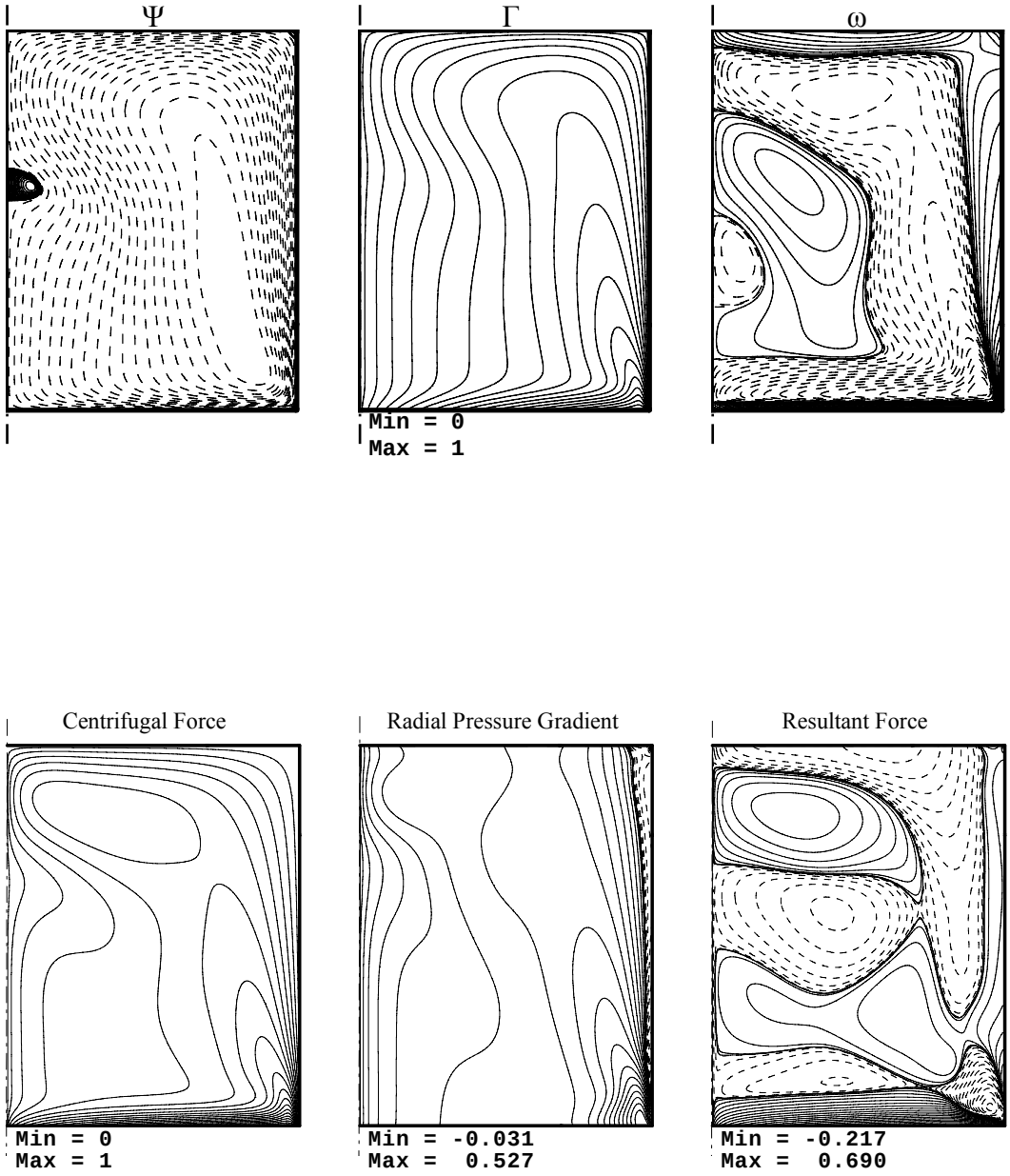

Figure 5.5 Contours of streamline Ψ, angular momentum Γ, azimuthal vorticity ω, centrifugal force v/r^2, radial pressure gradient $(1/\rho)(\partial p/\partial r)$, and resultant force $v/r^2 - (1/\rho)(\partial p/\partial r)$ in the meridional plane for the aspect ratio $H/R = 1.3$; i) $Re = 1200$ and ii) $Re = 1500$; a) $R/r_d = 1.0$, b) $R/r_d = 1.1$, c) $R/r_d = 1.3$, d) $R/r_d = 1.5$; Contour levels C_i are non-uniformly spaced, with 20 positive levels $C_i = \text{Max(variable)} \times (\text{i}/20)^3$ and 20 negative levels $C_i = \text{Min(variable)} \times (\text{i}/20)^3$.

ii) Re = 1500

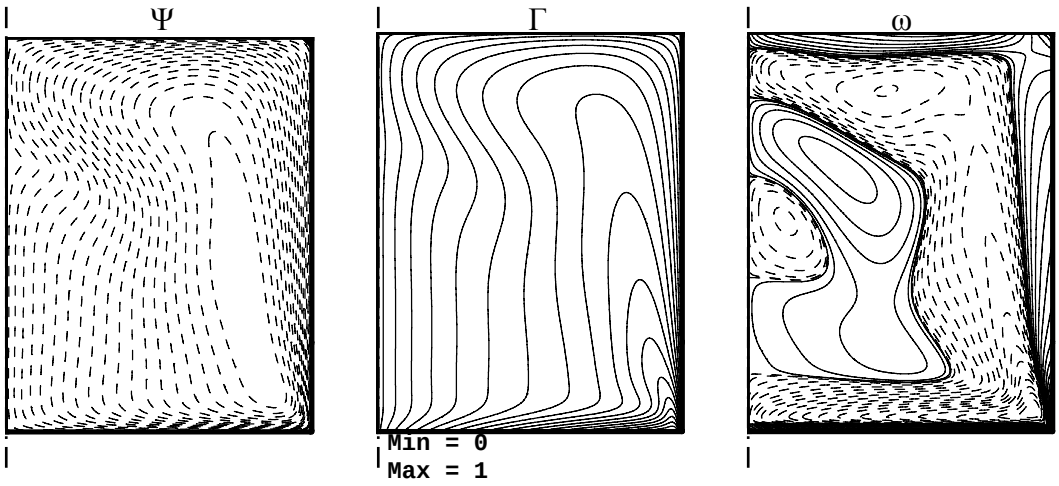

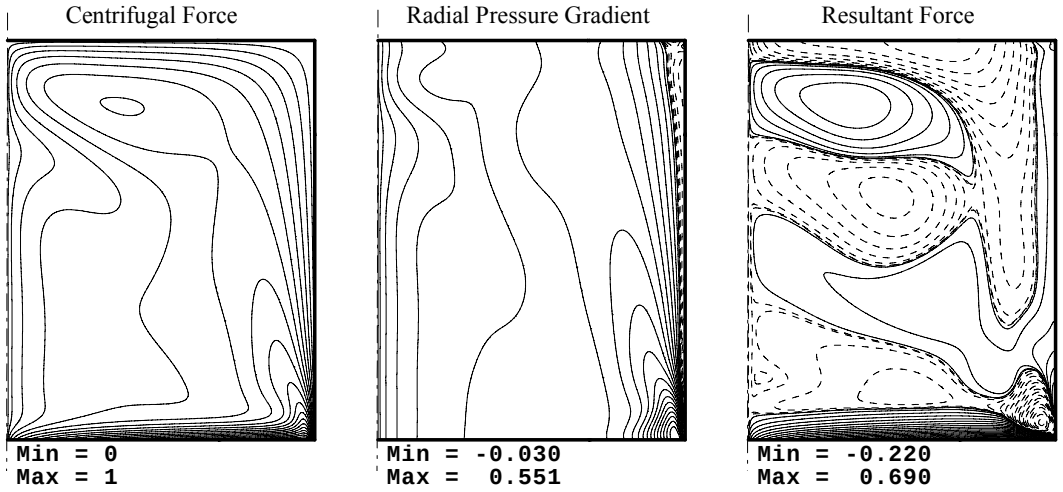

a) R/r_d = 1

Figure 5.5 (continued).

i) *Re*=1200

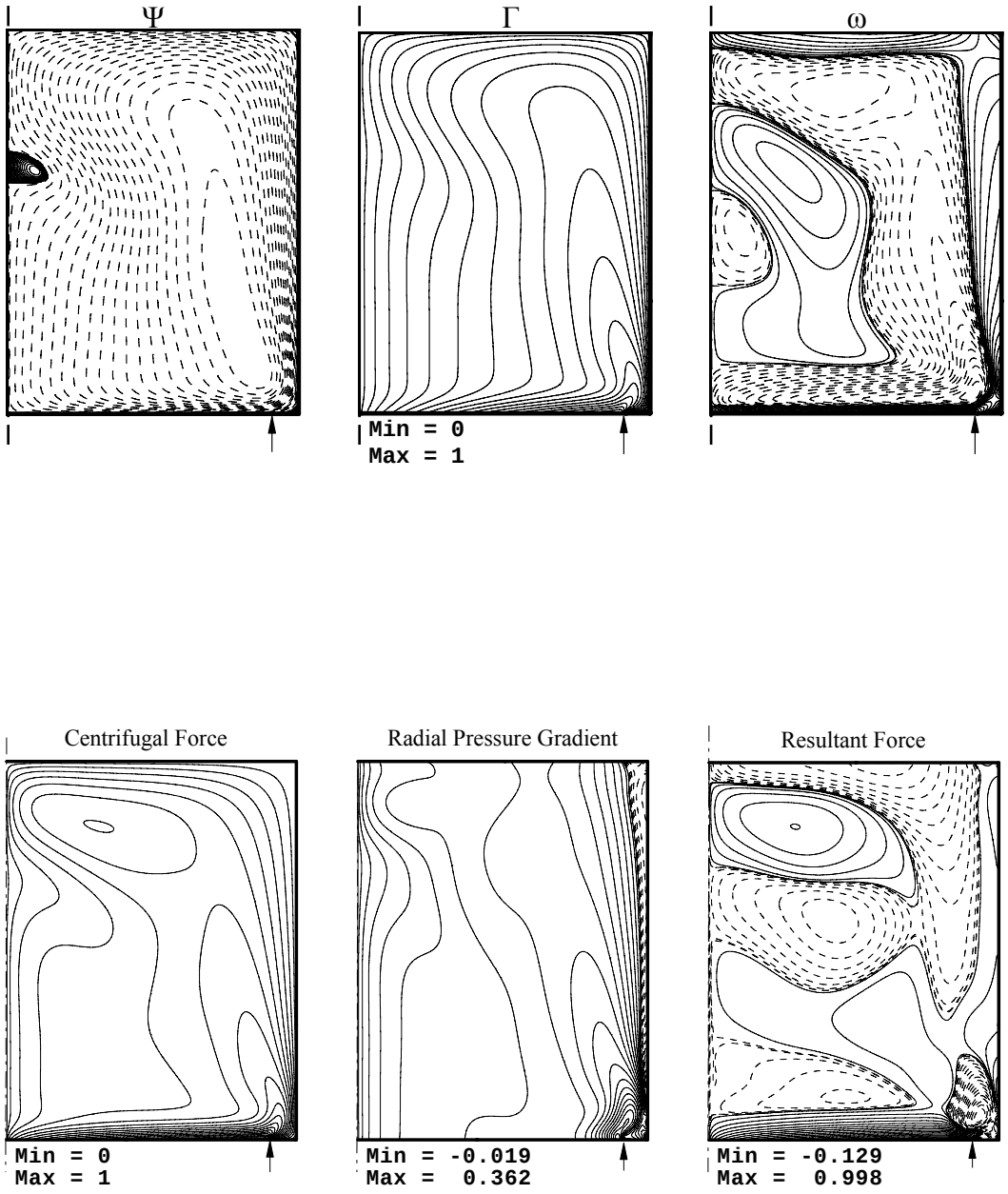

Figure 5.5 (continued).

ii) Re = 1500

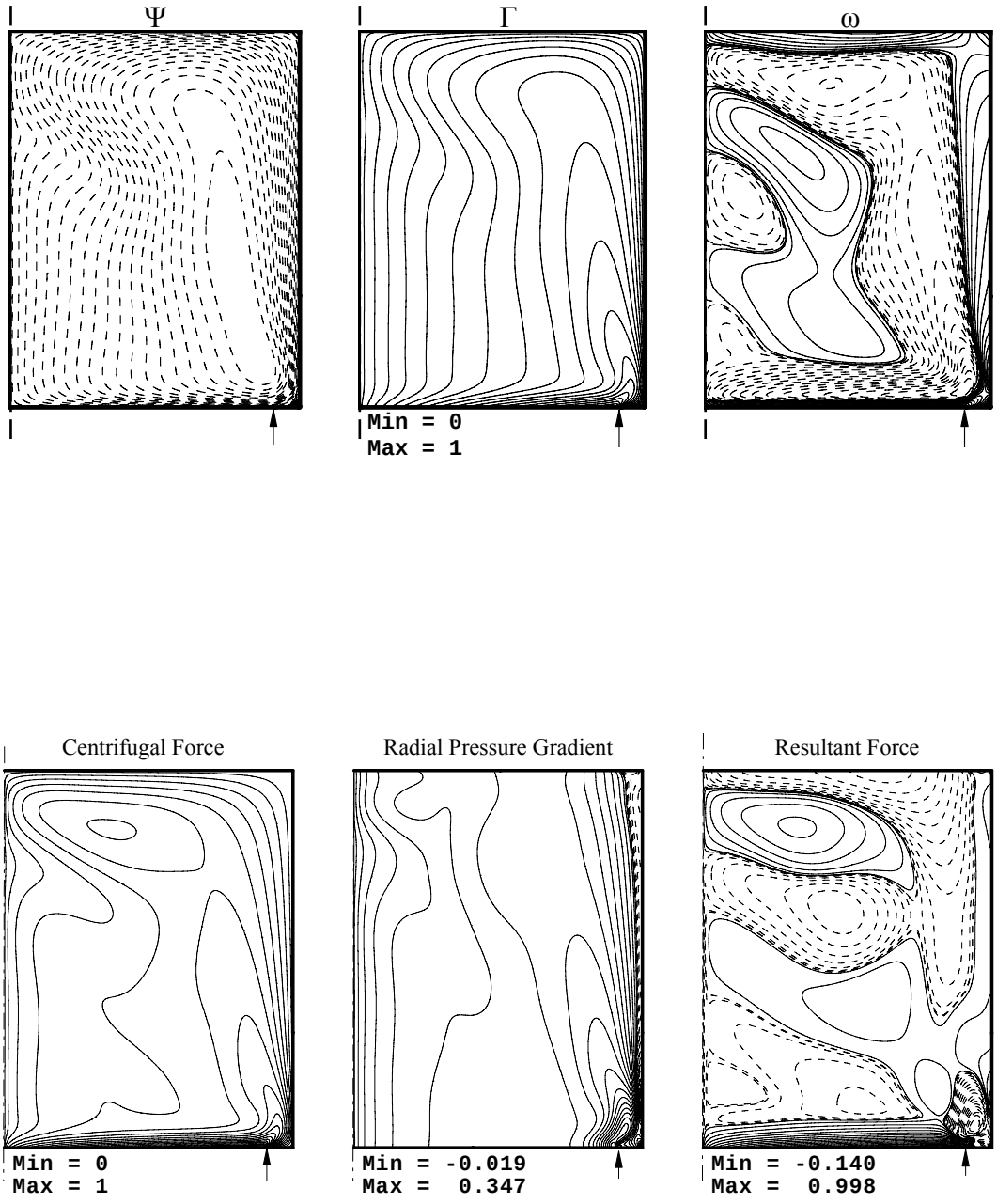

b) R/r_d = 1.1

Figure 5.5 (continued).

i) *Re*=1200

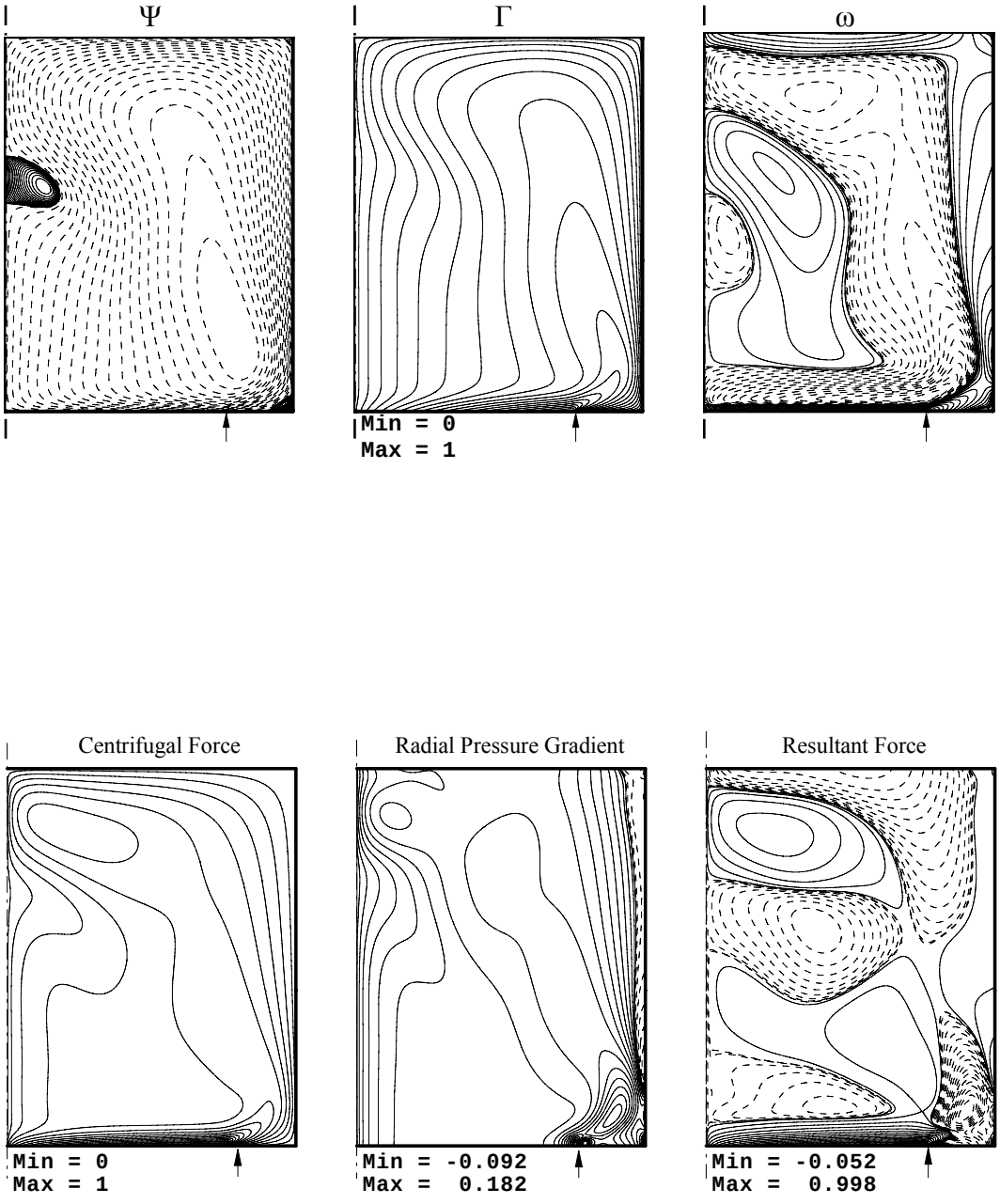

Figure 5.5 (continued).

ii) Re = 1500

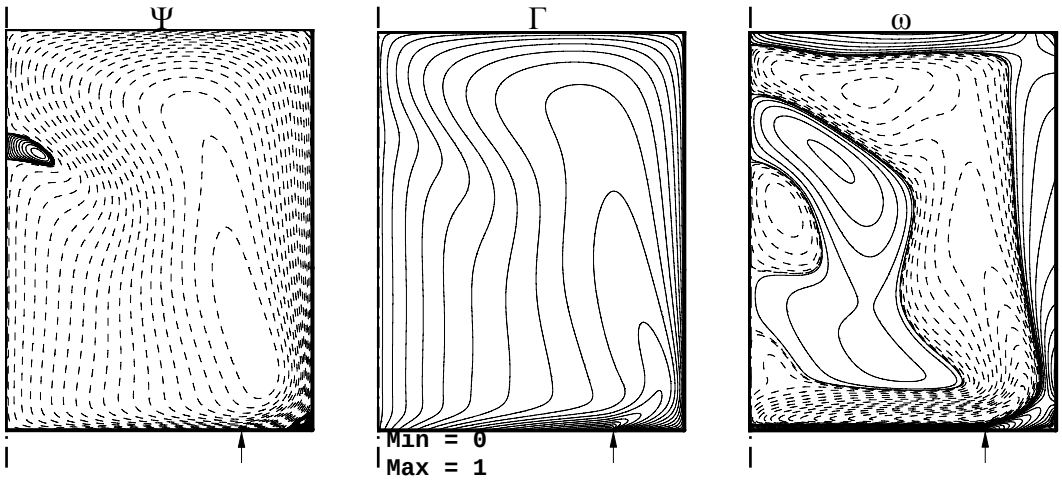

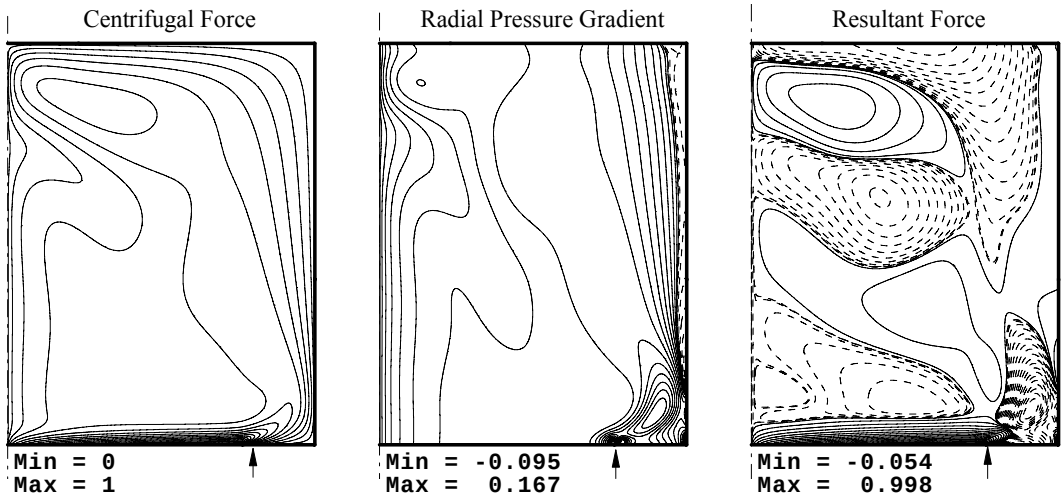

c) R/r_d = 1.3

Figure 5.5 (continued).

i) *Re*=1200

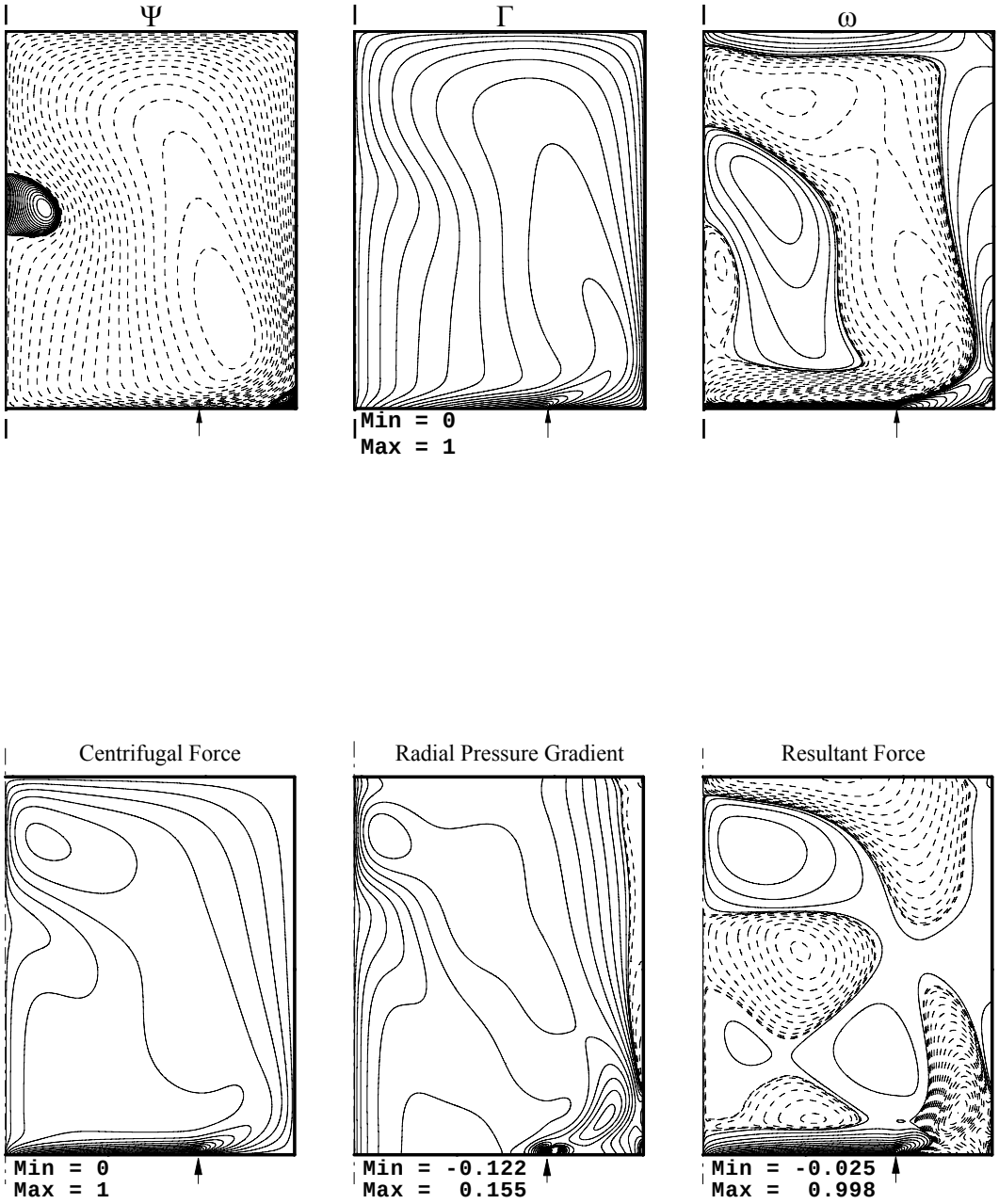

Figure 5.5 (continued).

ii) Re = 1500

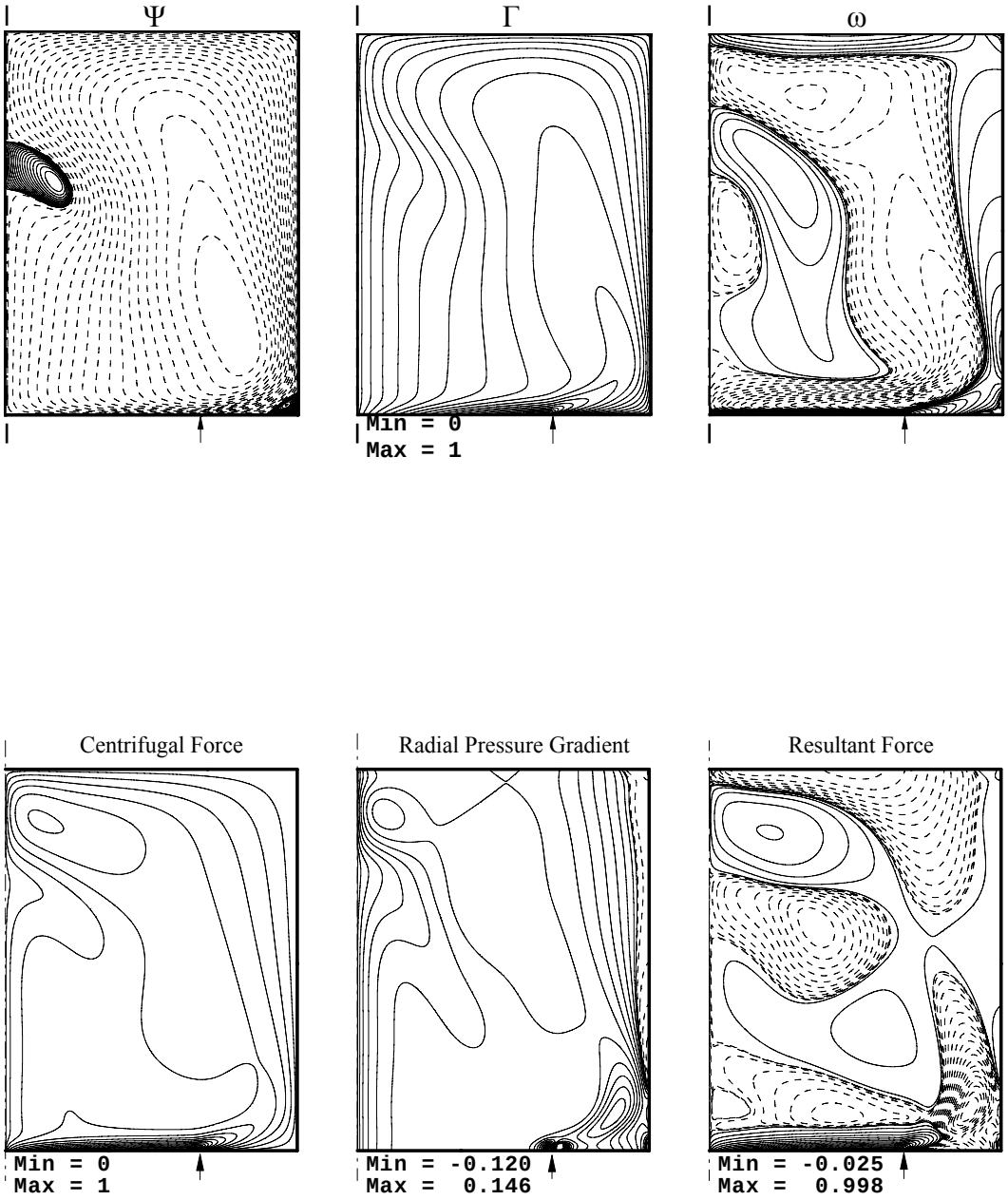

d) R/r_d = 1.5

Figure 5.5 (continued).

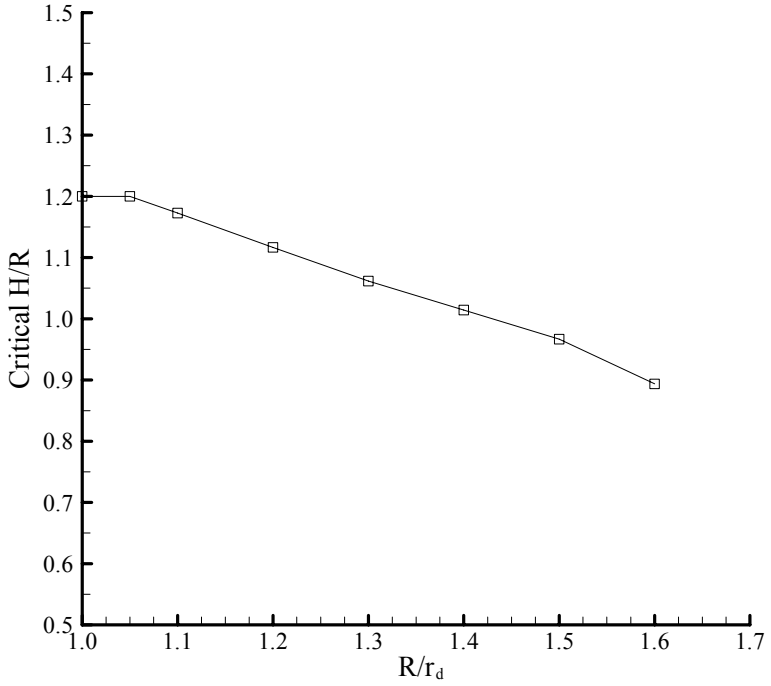

Figure 5.6 Critical aspect ratio for the onset of vortex breakdown at various R/r_d

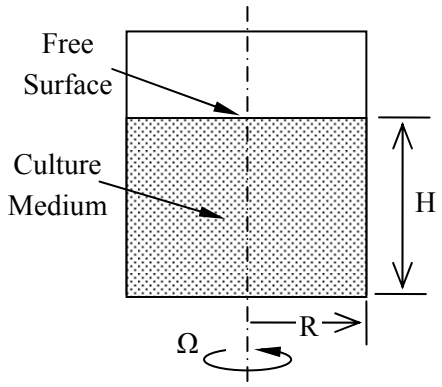

Figure 5.7 Diagram of micro-bioreactor system.

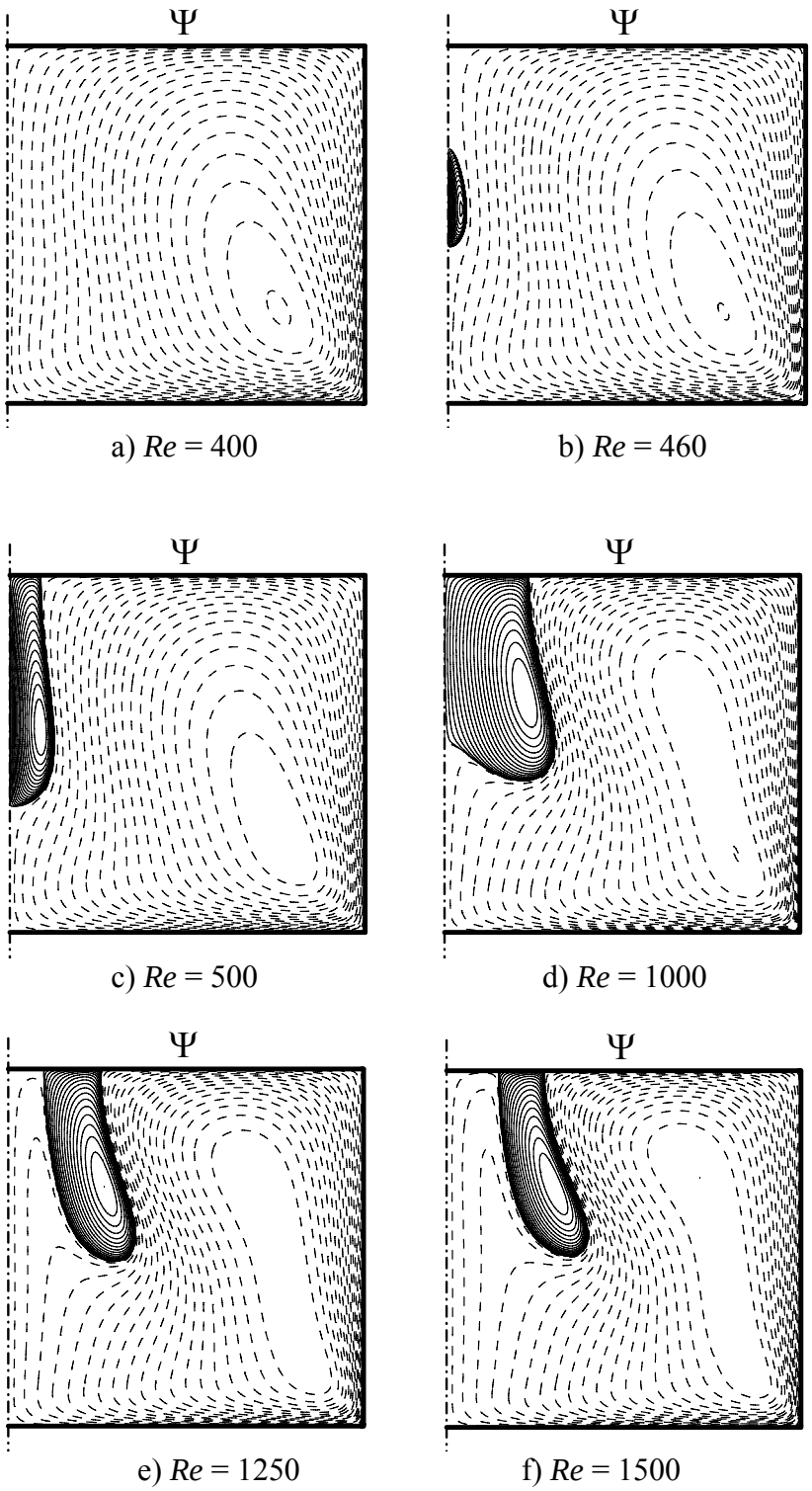

Figure 5.8 Contours of streamlines Ψ in the meridional plane for the aspect ratio H/R = 1 at different Reynolds numbers; a) Re = 400; b) Re = 460; c) Re = 500; d) Re = 1000; e) Re = 1250; f) Re = 1500; Contour levels C_i are non-uniformly spaced, with 20 positive levels C_i = Max(variable) × $(i/20)^3$ and 20 negative levels C_i = Min(variable) × $(i/20)^3$.

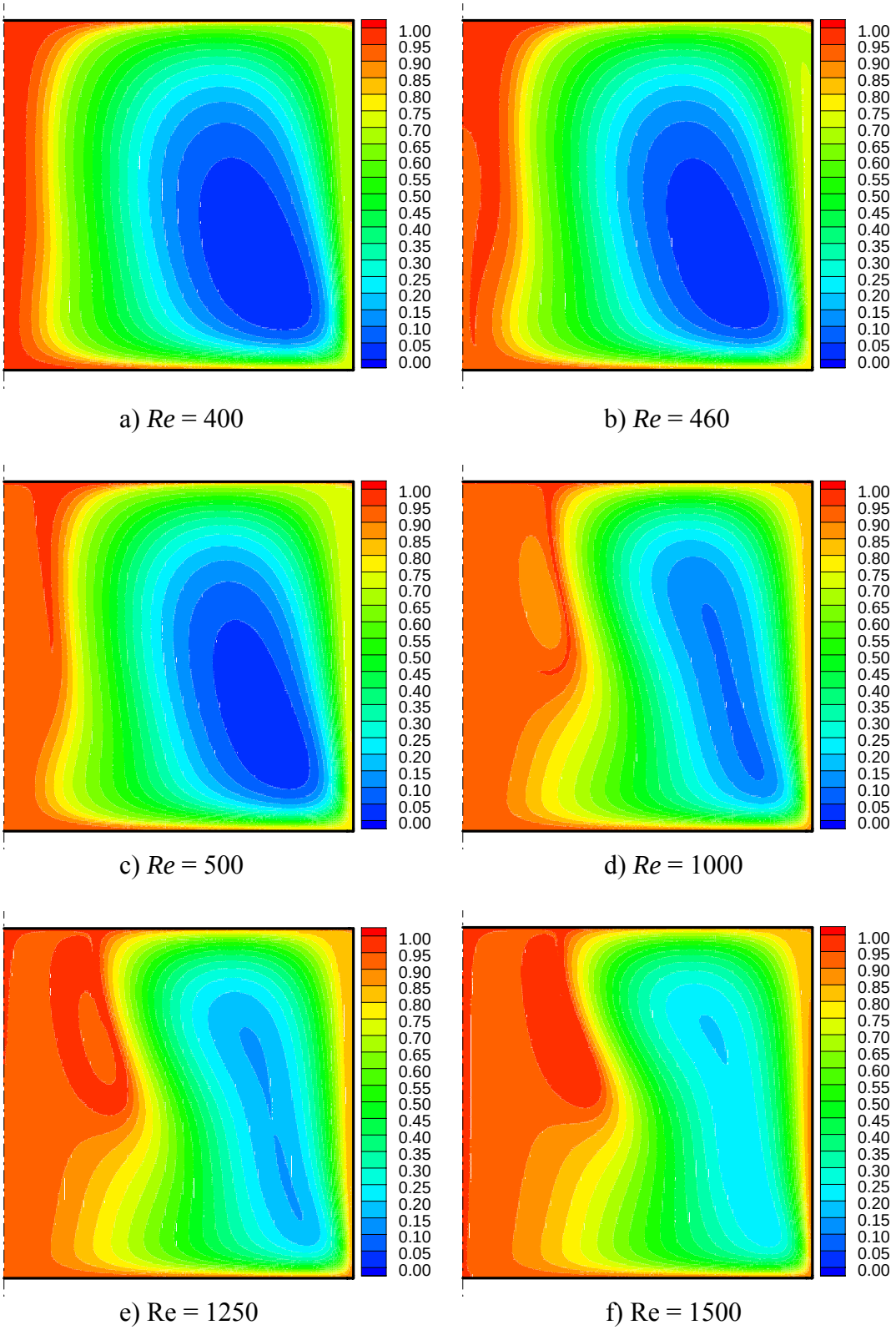

a) *Re* = 400 b) *Re* = 460

c) *Re* = 500 d) *Re* = 1000

e) Re = 1250 f) Re = 1500

Figure 5.9 Oxygen concentration distributions for the case *H/R* = 1 with different *Re*; *Da* = 40.

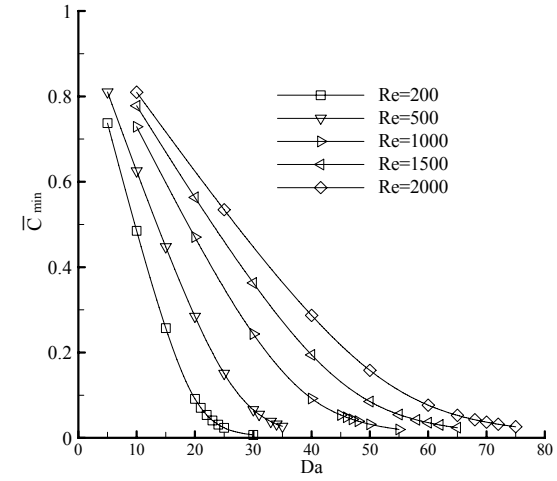

a) *H/R* = 1, recirculation center

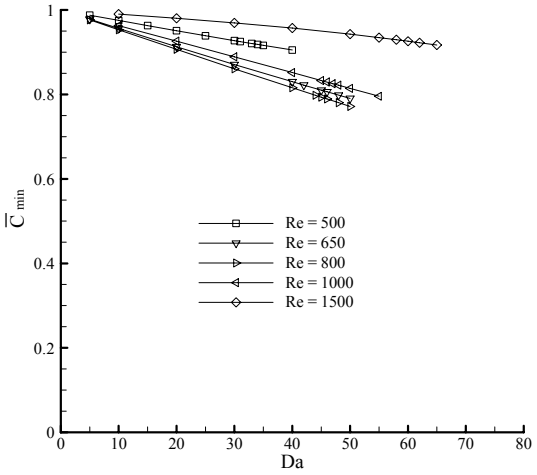

b) *H/R* = 1, vortex breakdown center

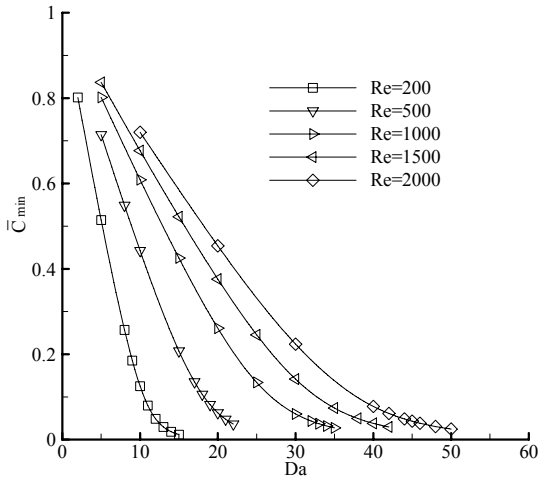

c) *H/R* = 1.5, recirculation center

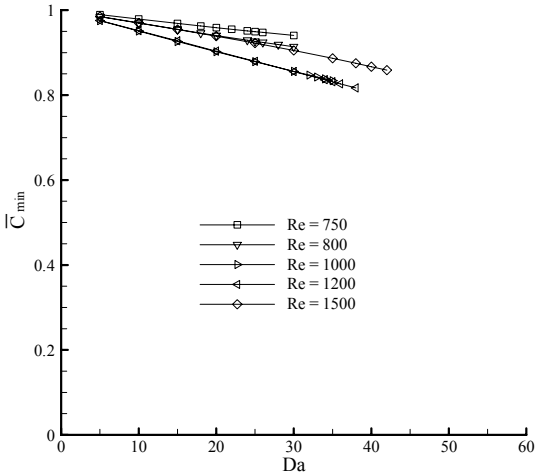

d) *H/R* = 1.5, vortex breakdown center

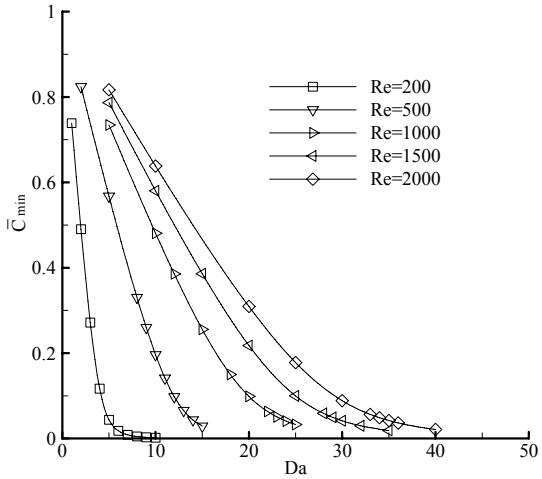

e) *H/R* = 2, recirculation center

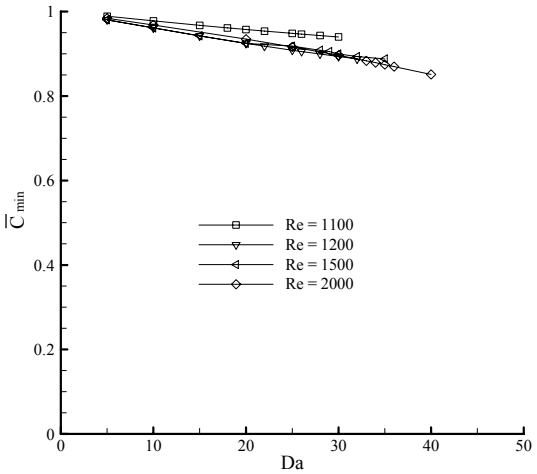

f) *H/R* = 2, vortex breakdown center

Figure 5.10 Lowest concentrations in the vortex breakdown region and the main recirculation region for different *Re*, *Da* and *H/R*.

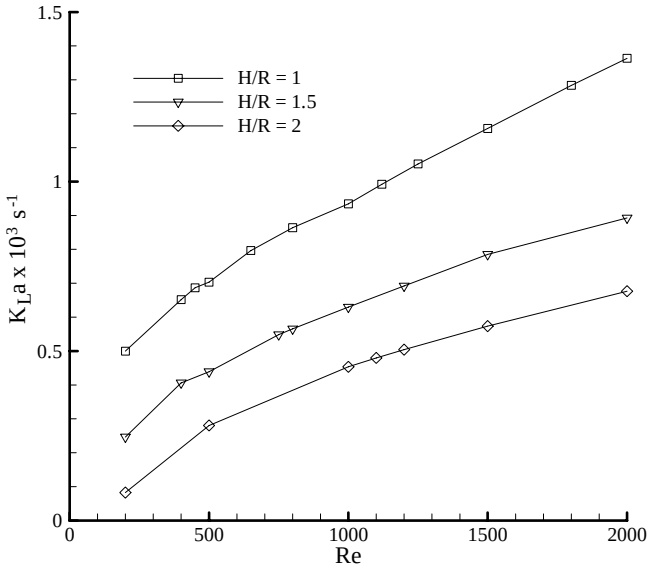

Figure 5.11 Variation of the volumetric oxygen transfer coefficients with *Re* and *H/R*.

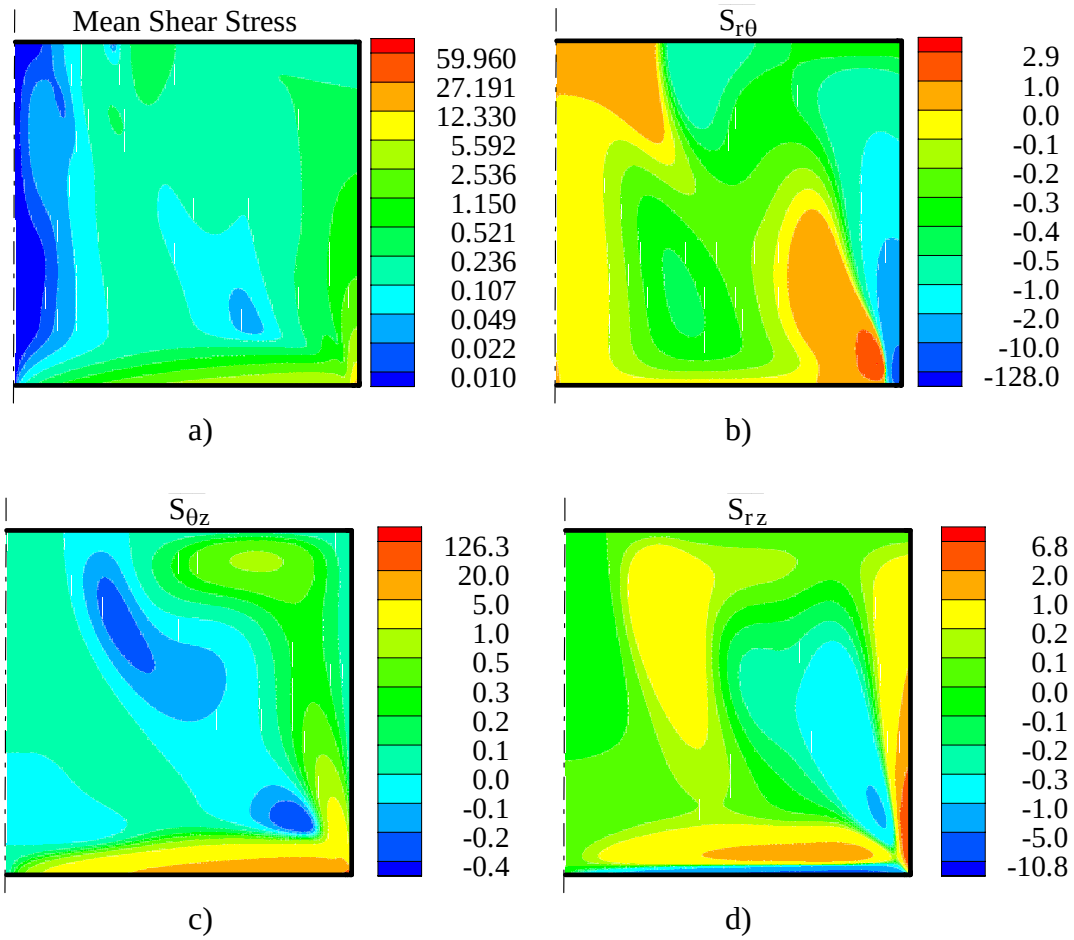

Figure 5.12 Shear stresses distributions in the meridional plane for *Re* = 1000 and *H/R* = 1; the contour levels are non-uniformly spaced.

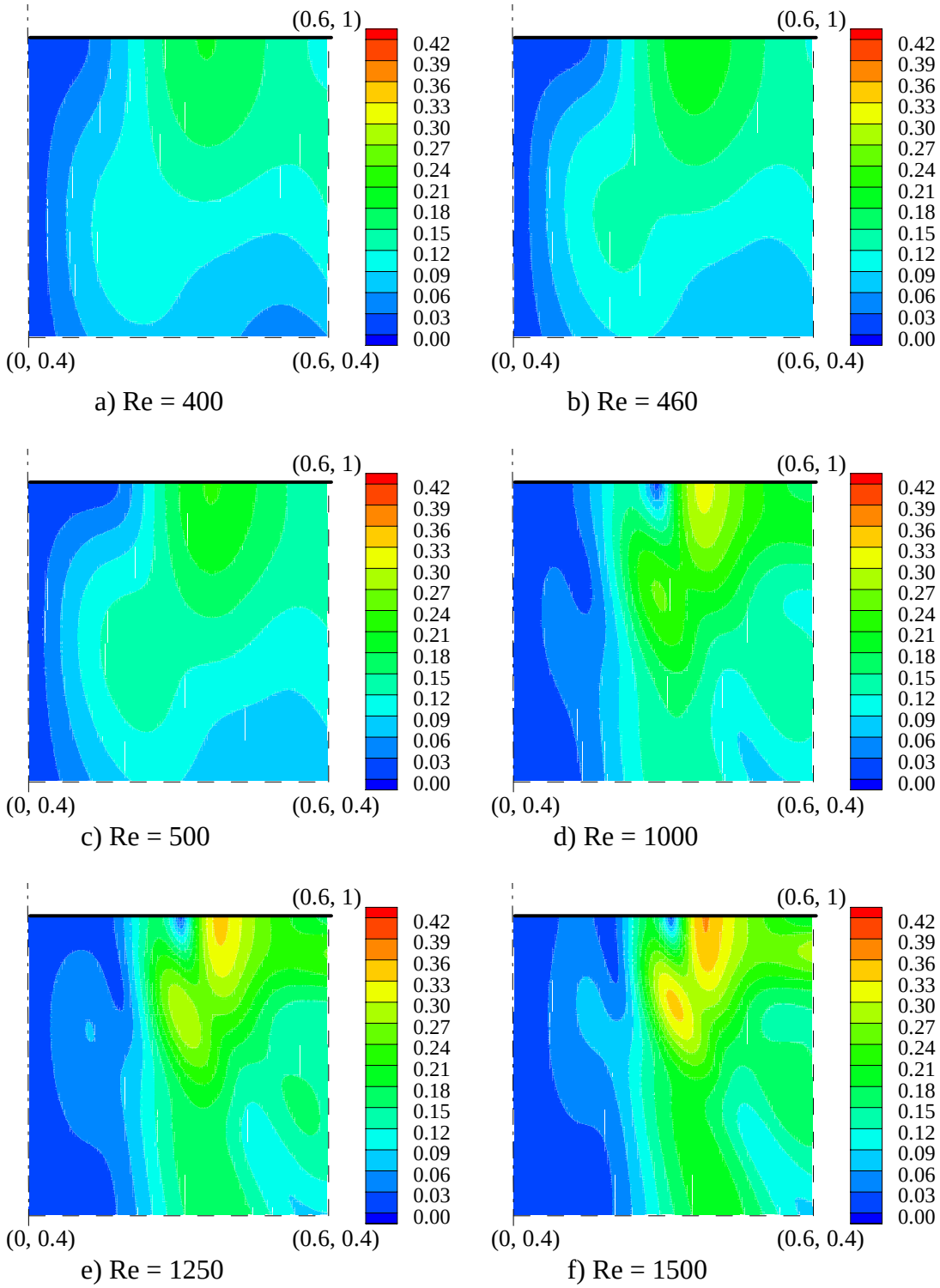

Figure 5.13 Mean shear stresses distributions in the top central region for different *Re*; the numbers at the corners indicate the border of the region.

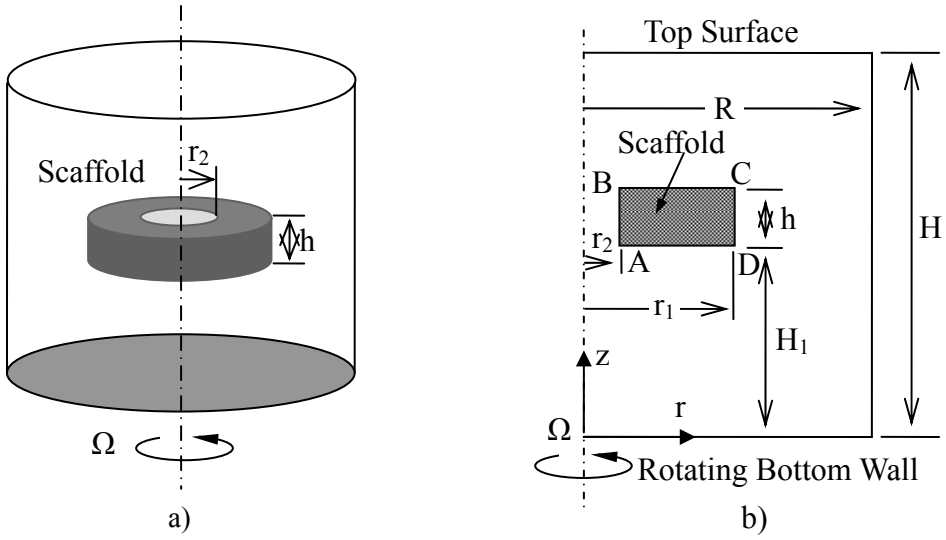

Figure 6.1 Bioreactor system with a cell scaffold; a) sketch; b) computational domain.

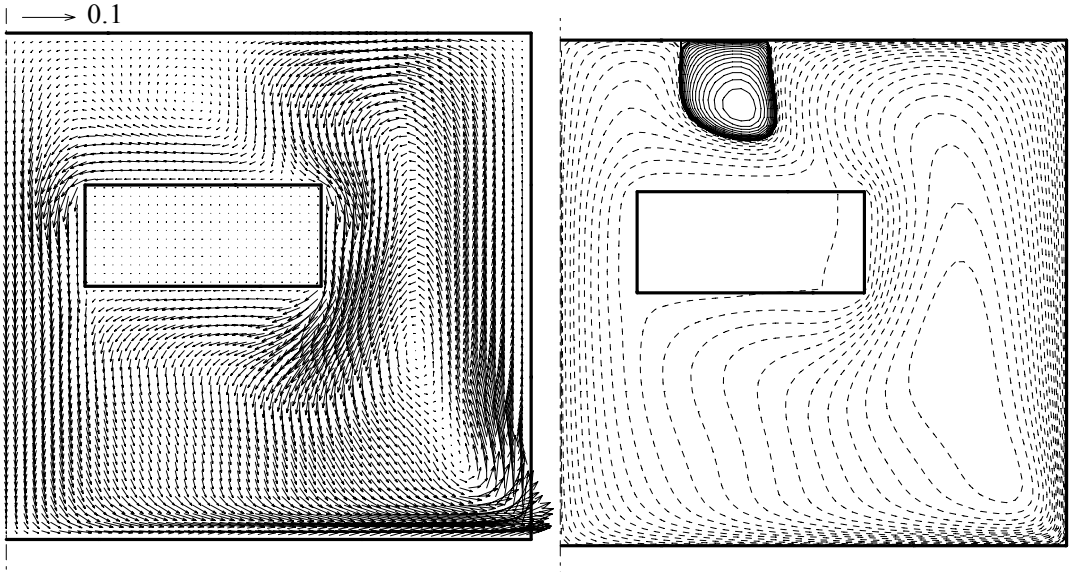

Figure 6.2 Flow field and streamlines in the bioreactor with the scaffold; H/R = 1, Re = 1500, Dar = 5 $\times 10^{-6}$, ε = 0.6. Contour levels C_i are non-uniformly spaced, with 25 positive levels C_i = Max(variable) × $(i/25)^4$ and 25 negative levels C_i = Min(variable) × $(i/25)^4$.

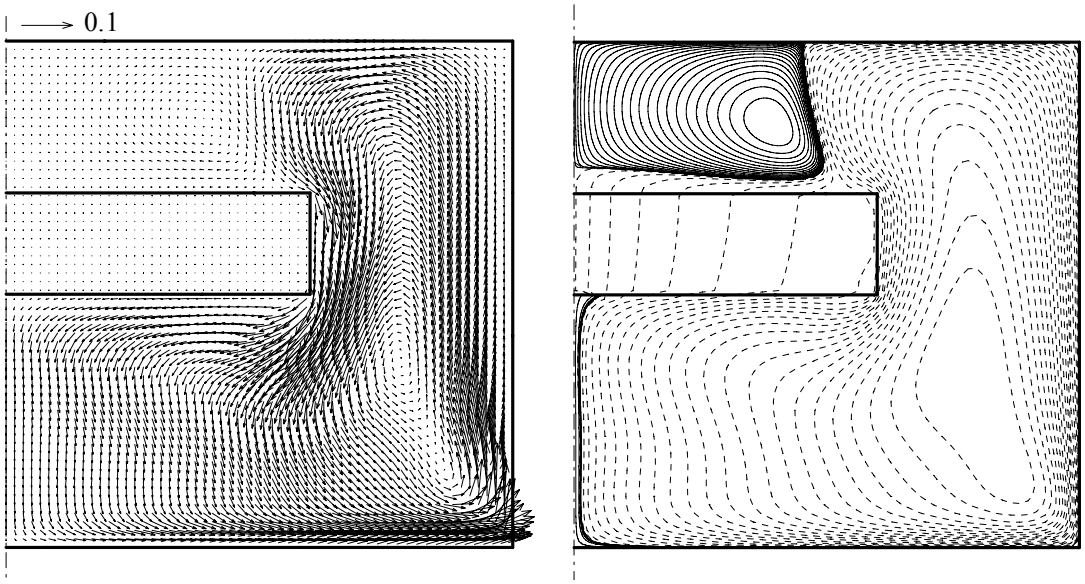

a) Flow Field b) Streamline

Figure 6.3 Flow field and streamlines in the bioreactor with the scaffold without the concentric hole; H/R = 1, Re = 1500, Dar = 5 ×10^{-6}, ε = 0.6. Contour levels C_i are non-uniformly spaced, with 25 positive levels C_i = Max(variable) × (i/25)^4 and 25 negative levels C_i = Min(variable) × (i/25)^4.

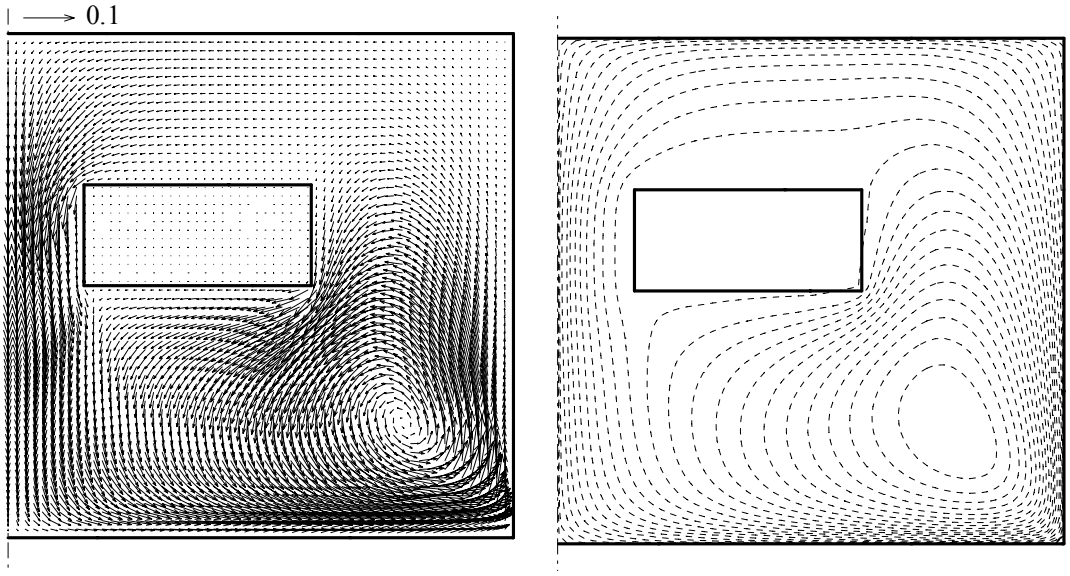

Flow Field Streamline

a) Re = 500

Figure 6.4 Flow fields and streamlines in the bioreactor at different Re; H/R = 1, Dar = 5 ×10^{-6}, ε = 0.6; a) Re = 500; b) Re = 1000. Contour levels C_i are non-uniformly spaced, with 25 positive levels C_i = Max(variable) × (i/25)^4 and 25 negative levels C_i = Min(variable) × (i/25)^4.

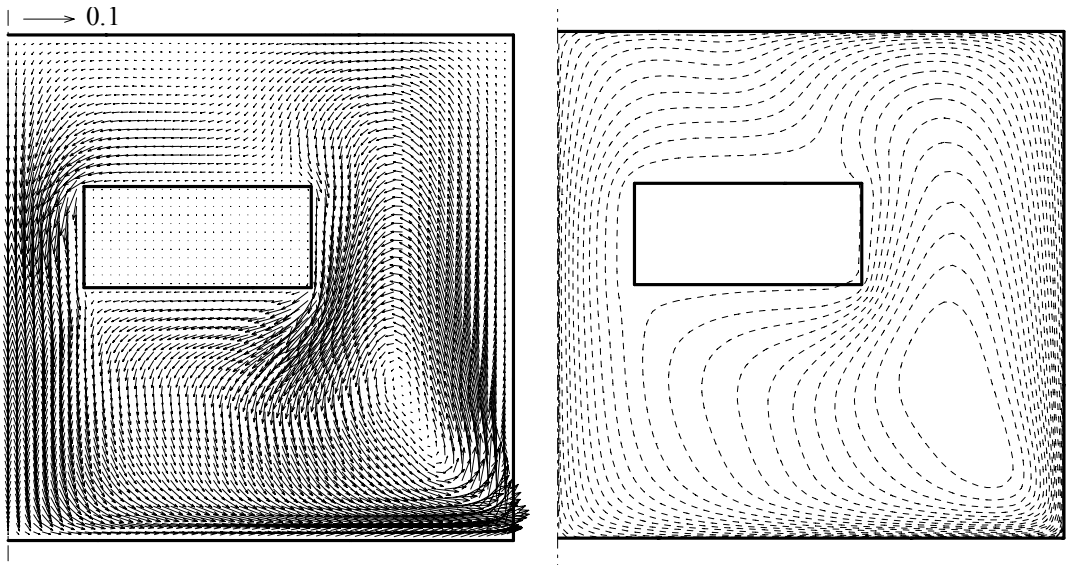

b) *Re* = 1000

Figure 6.4 (continued).

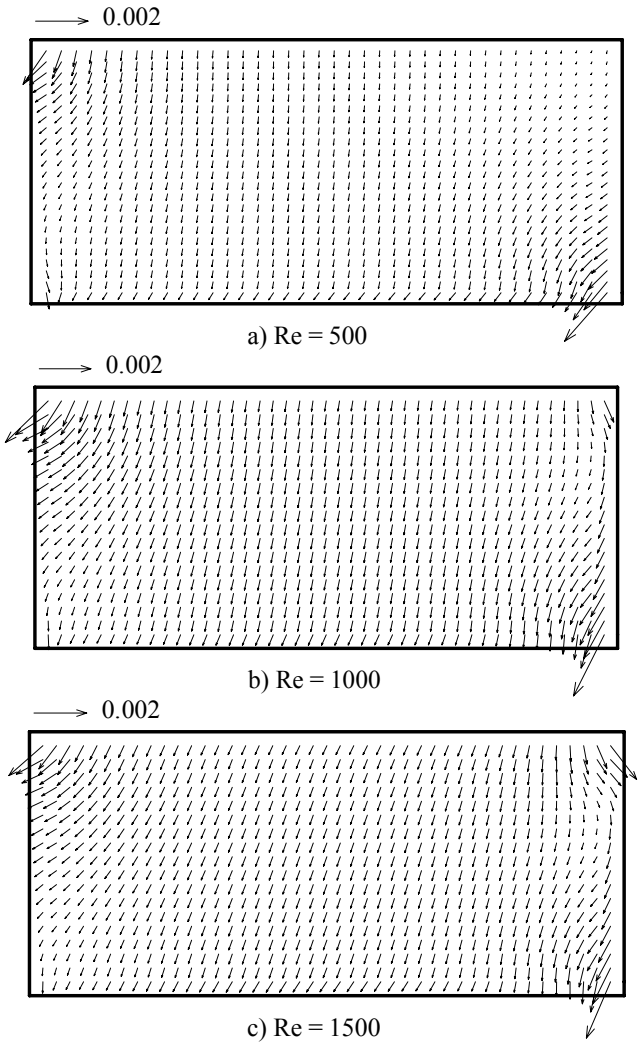

Figure 6.5 Flow fields within the scaffold in the bioreactor at different *Re*; *H/R* = 1, *Dar* = 5 ×10^{-6}, ε = 0.6; a) *Re* = 500; b) *Re* = 1000; c) *Re* = 1500.

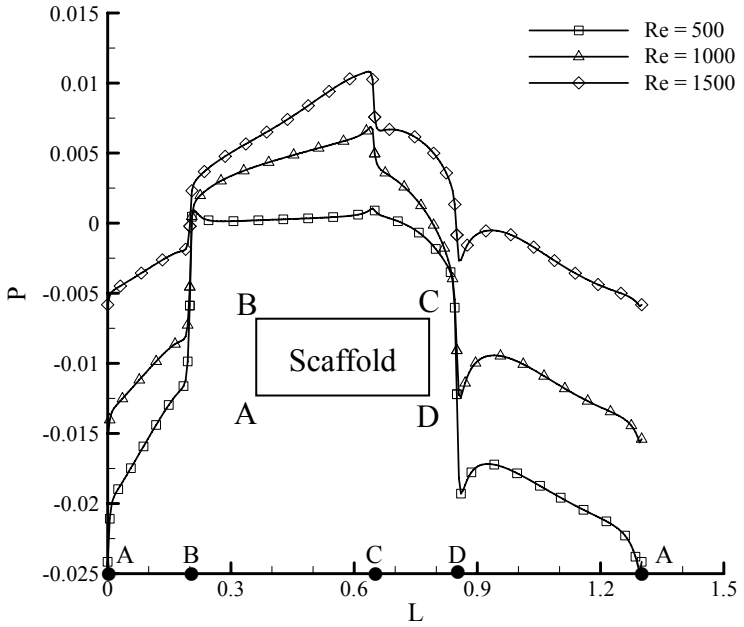

Figure 6.6 Pressure distributions along the scaffold surface for different *Re*; the reference pressure point is located at the top of the axis, where the pressure is assigned zero.

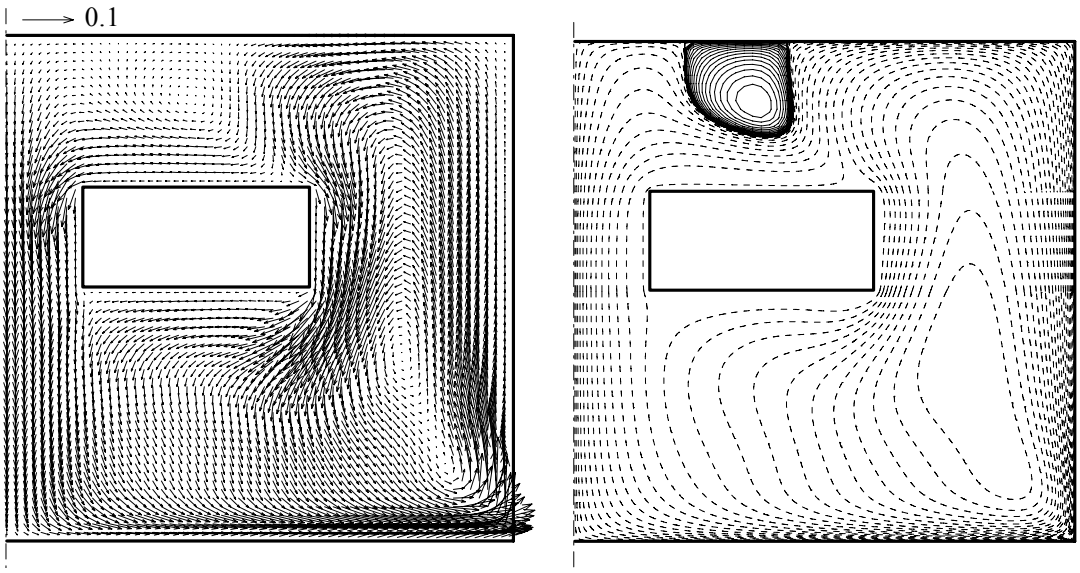

a) Solid Structure

Figure 6.7 Flow fields and streamlines in the bioreactor with the scaffold for different *Dar*; *H/R* = 1, *Re* = 1500; a) solid structure, b) $Dar = 10^{-6}$, c) $Dar = 10^{-5}$. Contour levels C_i are non-uniformly spaced, with 25 positive levels C_i = Max(variable) × $(i/25)^4$ and 25 negative levels C_i = Min(variable) × $(i/25)^4$.

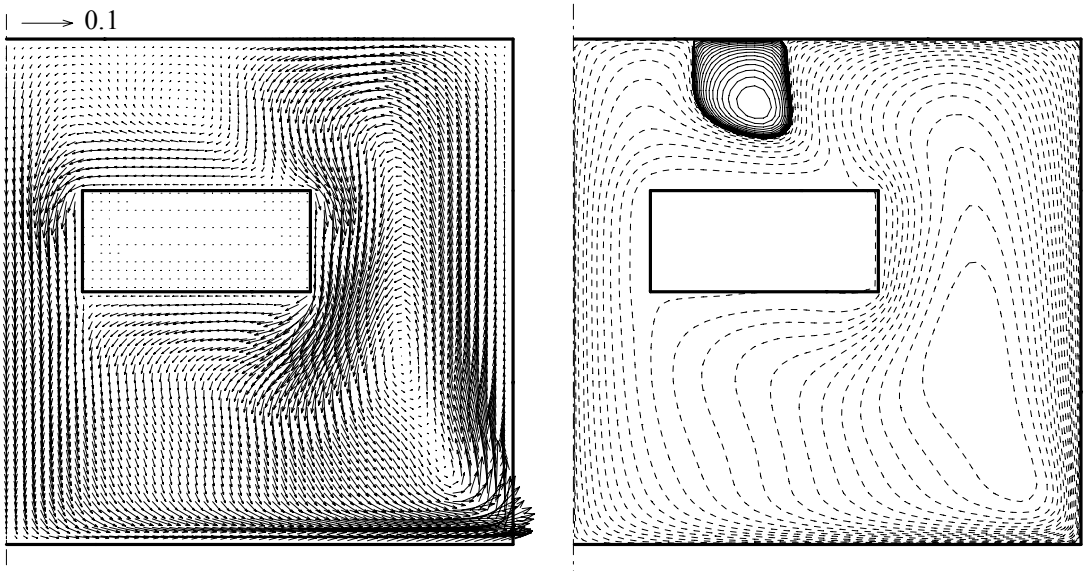

Flow Field Streamline

b) $Dar = 10^{-6}$

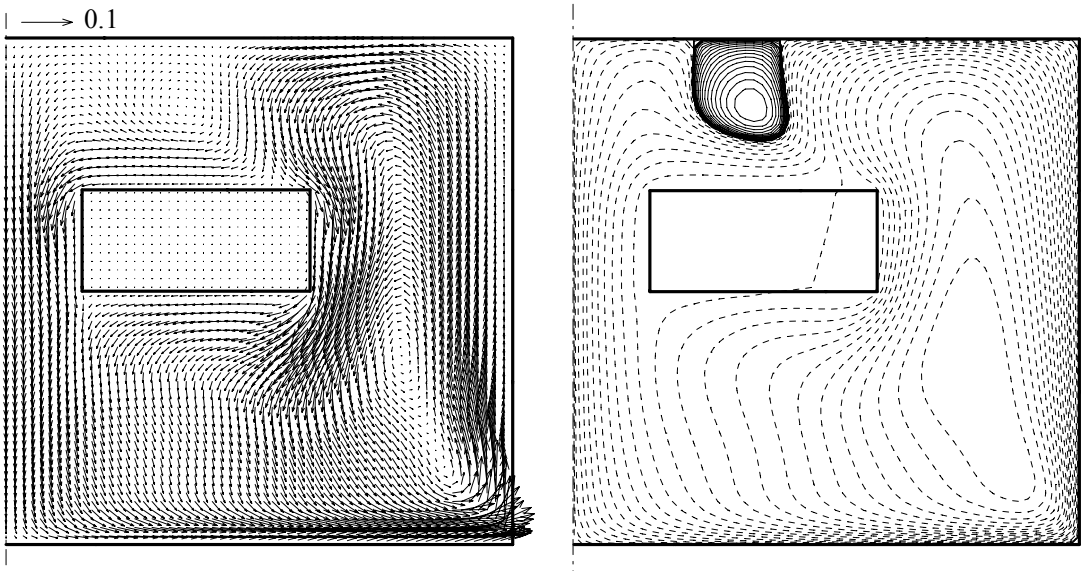

Flow Field Streamline

c) $Dar = 10^{-5}$

Figure 6.7 (continued).

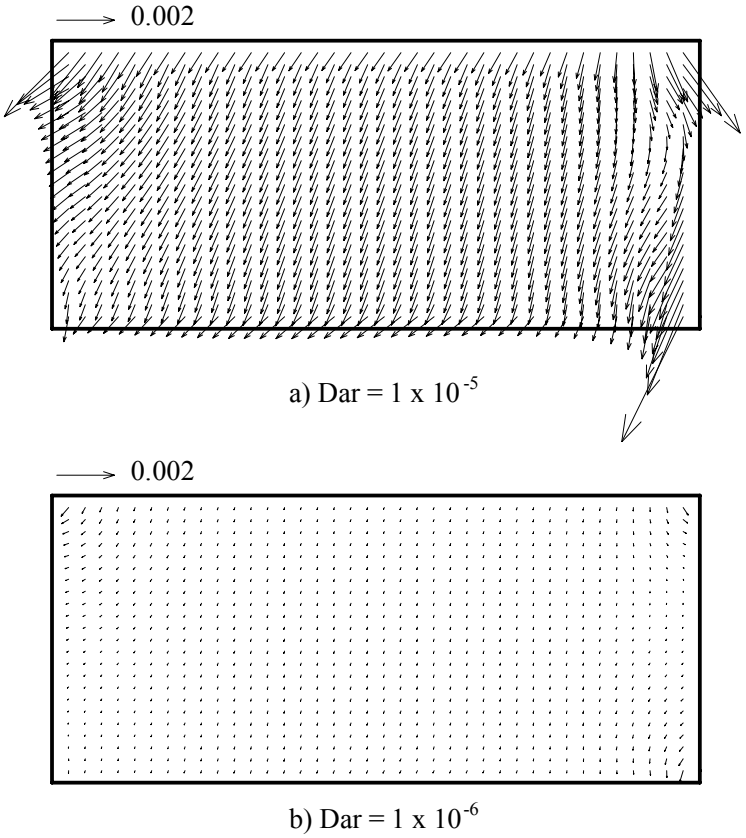

Figure 6.8 Flow fields within the scaffold for different *Dar*; *H/R* = 1, *Re* = 1500, ε = 0.6; a) *Dar* = 1 ×10^{-5}; b) *Dar* = 1 ×10^{-6}.

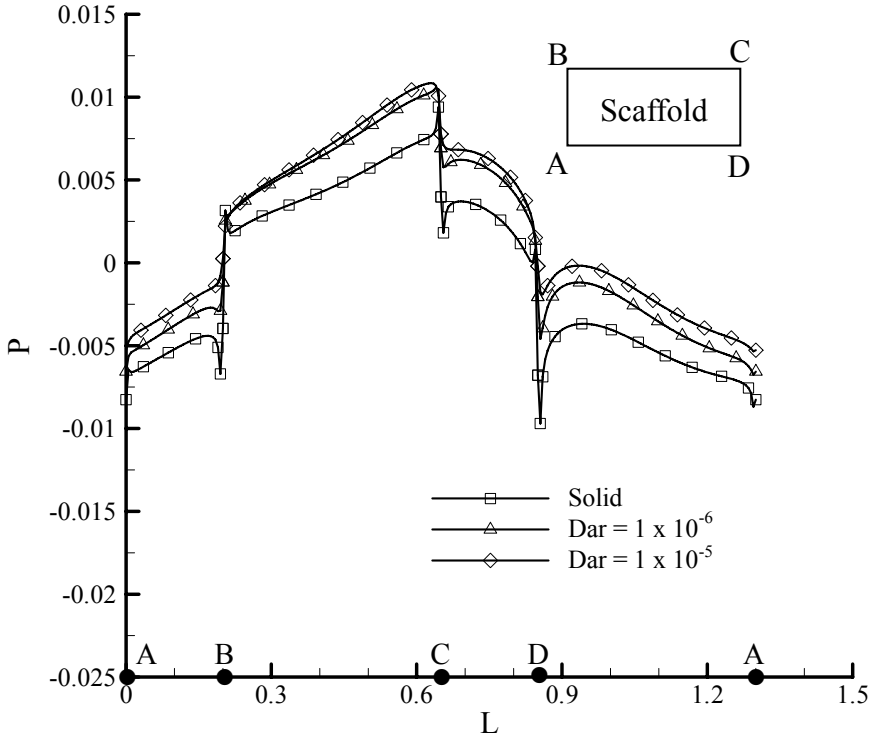

Figure 6.9 Pressure distributions along the scaffold surface for different *Dar*; the reference pressure point is located at the top of the axis, where the pressure is assigned zero.

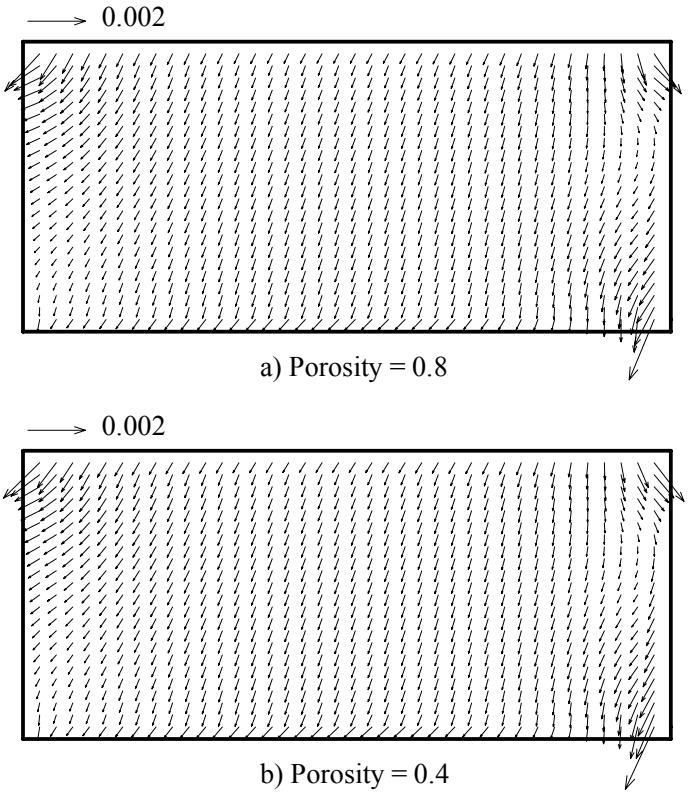

Figure 6.10 Flow fields within the scaffold for different porosities; H/R = 1, Re = 1500, $Dar = 5 \times 10^{-6}$; a) $\varepsilon = 0.8$; b) $\varepsilon = 0.4$.

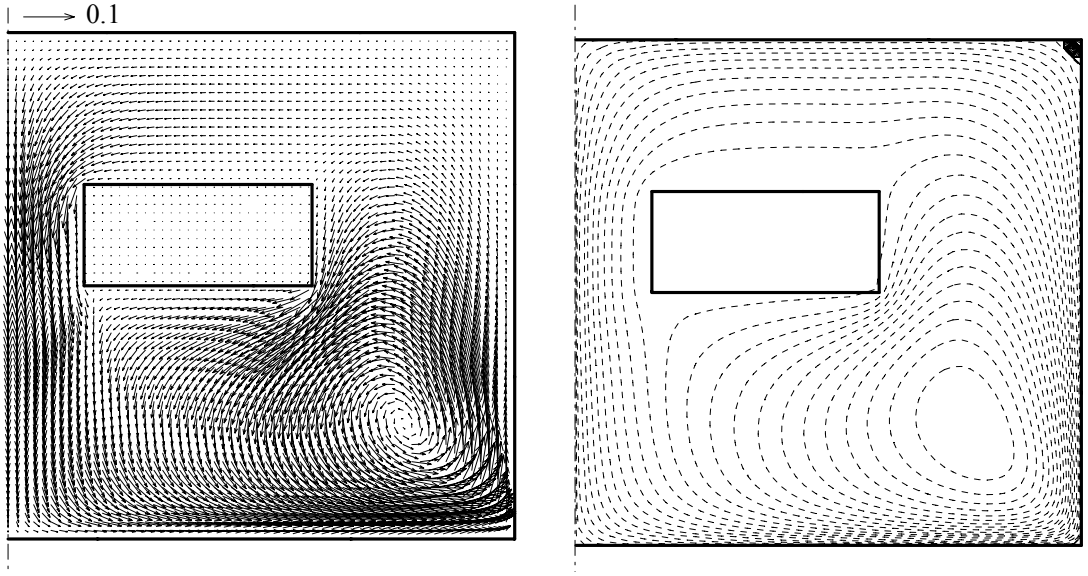

a) Re = 500

Figure 6.11 Flow fields and streamlines in the bioreactor with the rigid lid; H/R = 1, $Dar = 5 \times 10^{-6}$, $\varepsilon = 0.6$; a) Re = 500; b) Re = 1000; c) Re = 1500. Contour levels C_i are non-uniformly spaced, with 25 positive levels C_i = Max(variable) × $(i/25)^4$ and 25 negative levels C_i = Min(variable) × $(i/25)^4$.

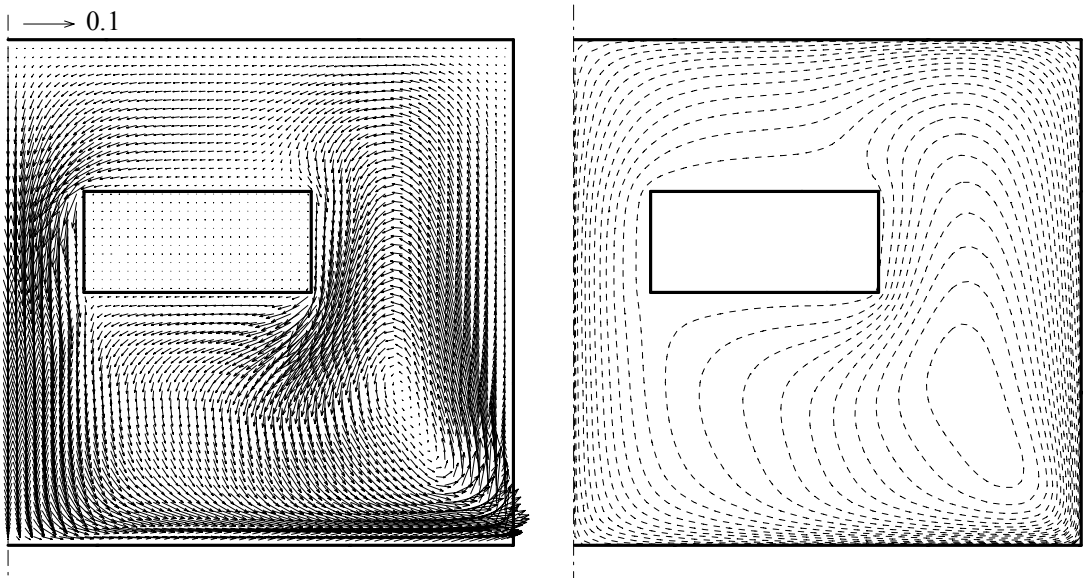

Flow Field Streamline

b) $Re = 1000$

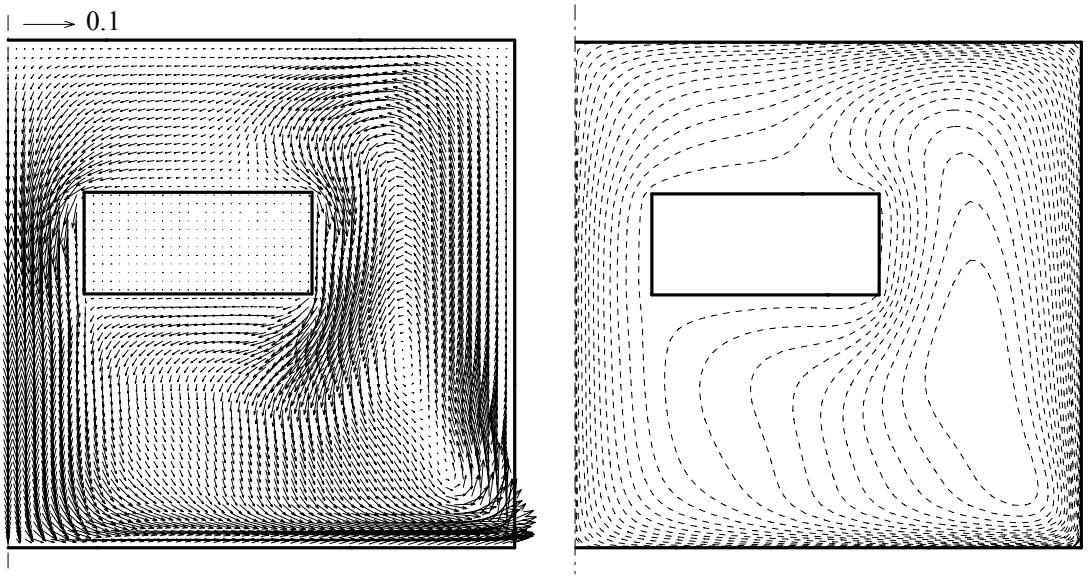

Flow Field Streamline

c) $Re = 1500$

Figure 6.11 (continued).

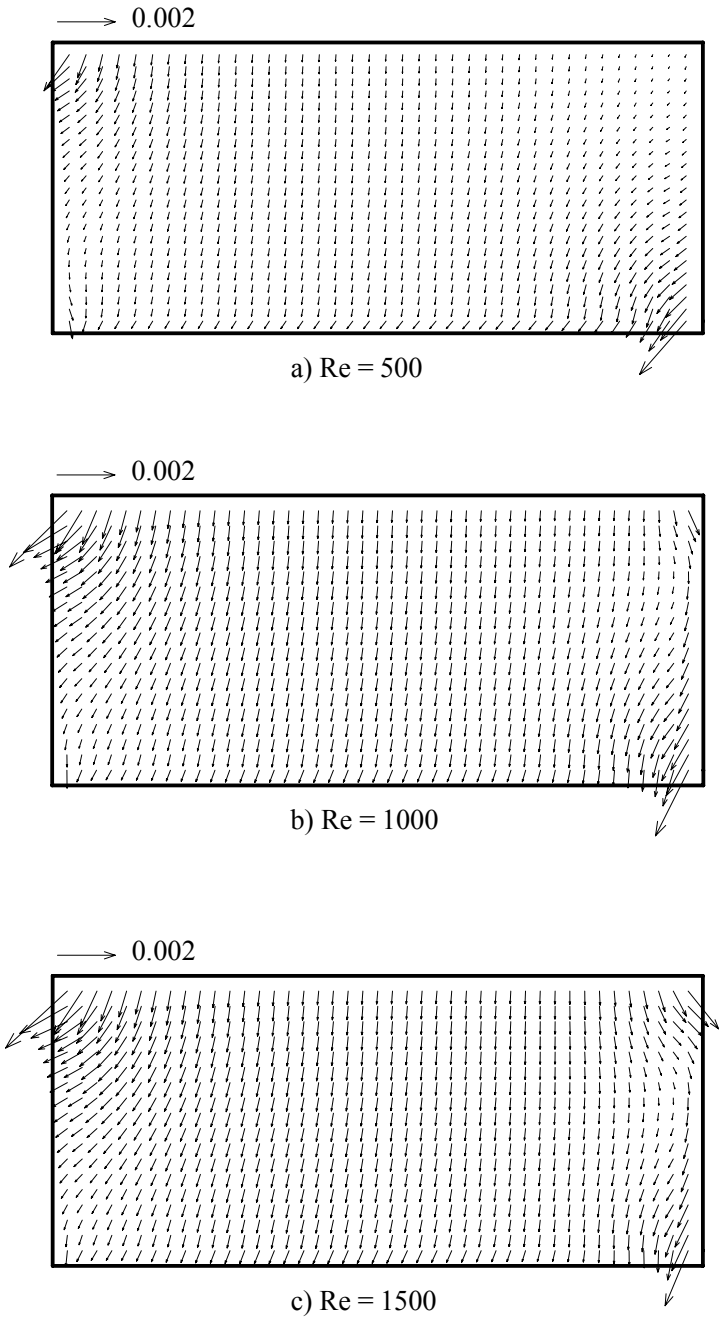

Figure 6.12 Flow fields within the scaffold in the bioreactor with the rigid lid for different *Re*; *H/R* = 1, *Dar* = 5 ×10^{-6}, ε = 0.6; a) *Re* = 500; b) *Re* = 1000; c) *Re* = 1500.

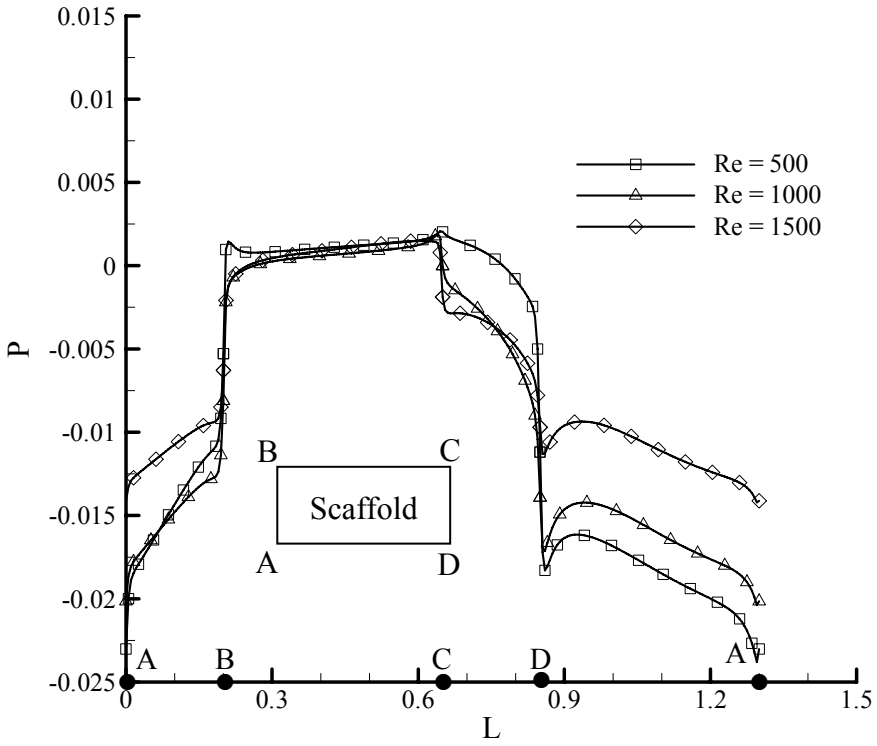

Figure 6.13 Pressure distributions along the scaffold surface for different *Re* in the bioreactor with the rigid lid; the reference pressure point is located at the top of the axis, where the pressure is assigned zero.

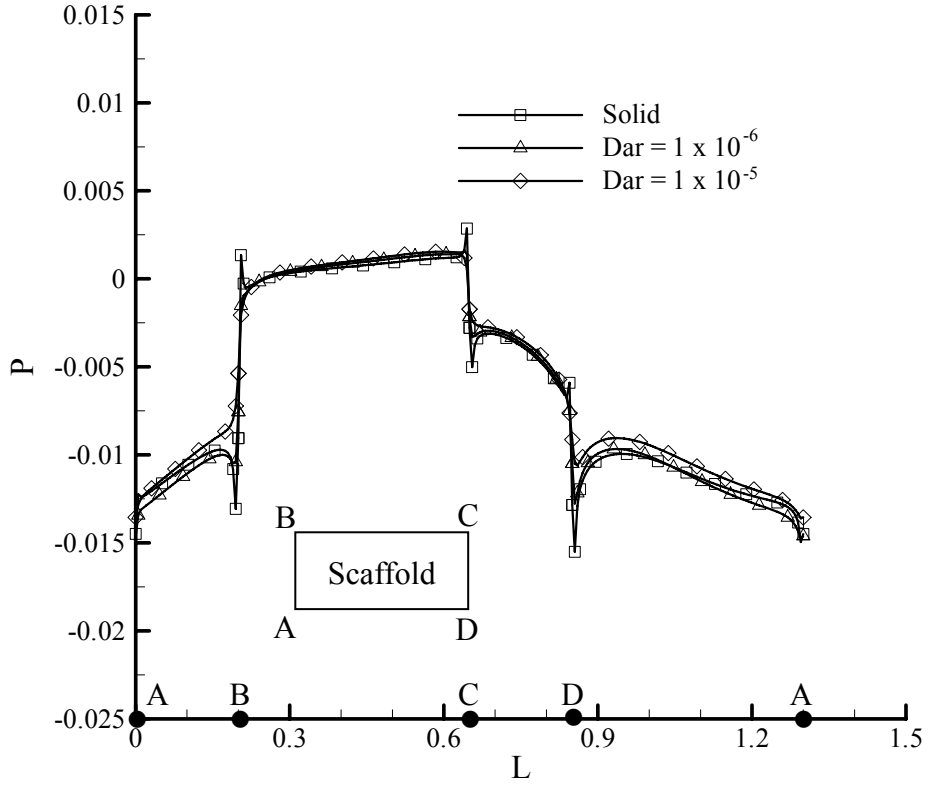

Figure 6.14 Pressure distributions along the scaffold surface for different *Dar* in the bioreactor with the rigid lid; the reference pressure point is located at the top of the axis, where the pressure is assigned zero.

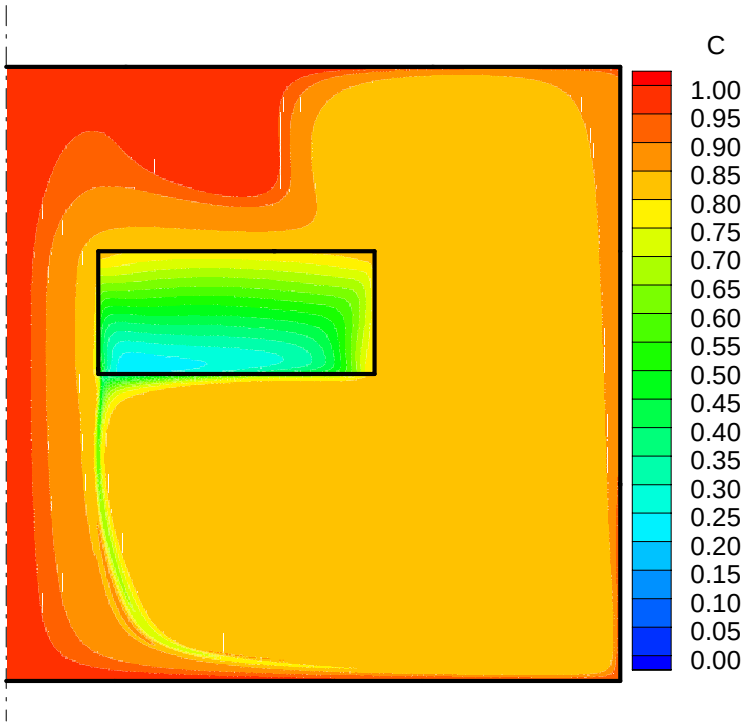

Figure 6.15 Oxygen concentration distribution in the bioreactor with the scaffold; $H/R = 1$, $Re = 1500$, $Dar = 1 \times 10^{-6}$, $\varepsilon = 0.6$, $Da = 200$.

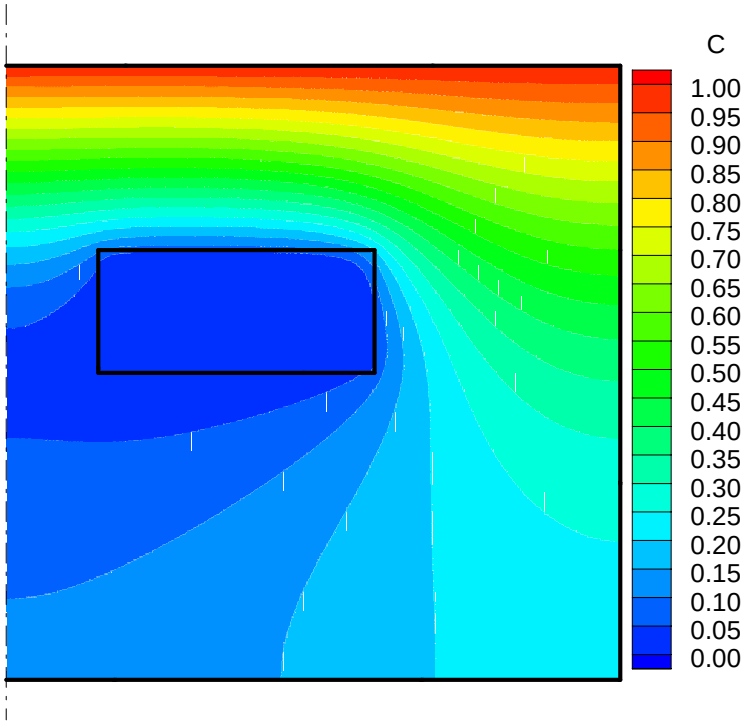

Figure 6.16 Oxygen concentration distribution in the bioreactor without the medium circulation; $H/R = 1$, $Re = 0$, $\varepsilon = 0.6$, $Da = 200$.

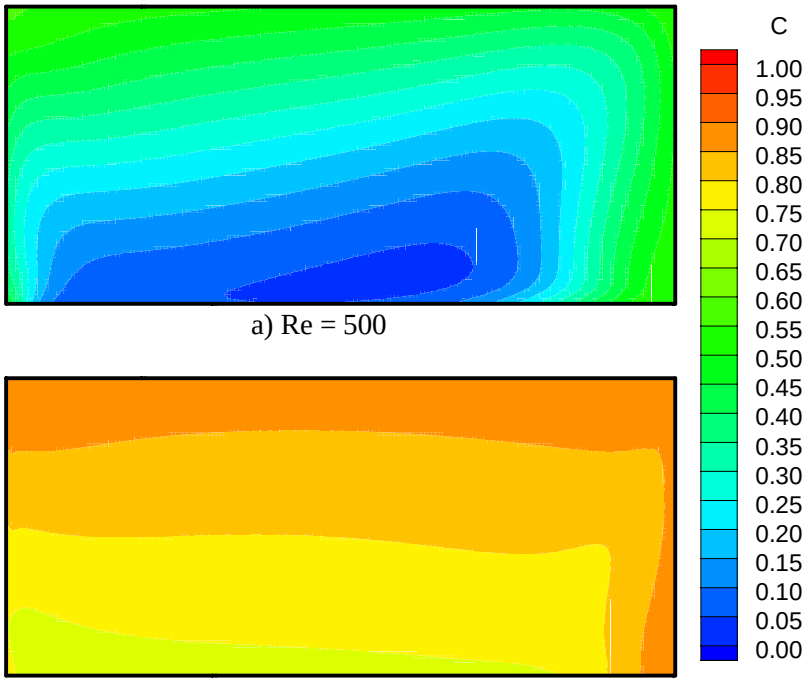

a) Re = 500

b) Re = 1500

Figure 6.17 Oxygen concentration distributions within the scaffold at different *Re*; *H/R* = 1, *Dar* = 5 × 10^{-6}, ε = 0.6, *Da* = 200; a) *Re* = 500 and b) *Re* = 1500.

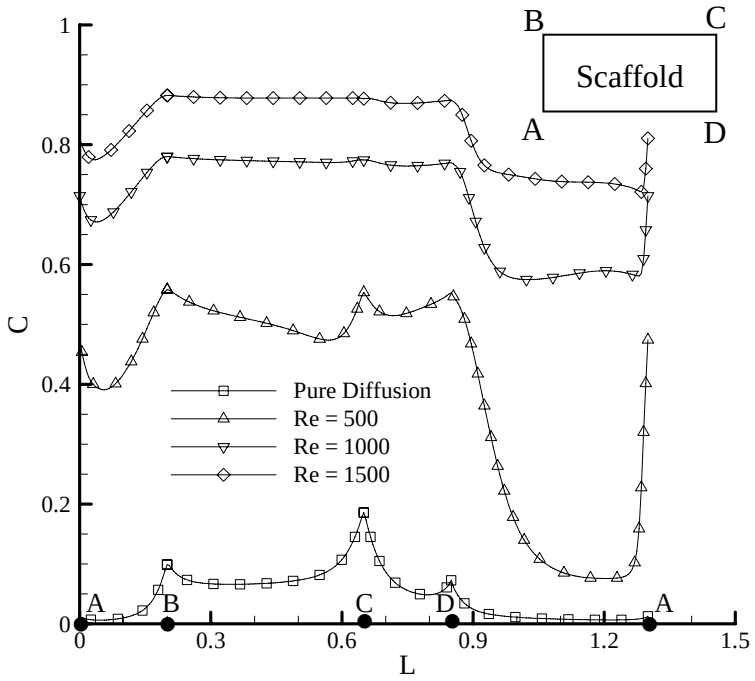

Figure 6.18 Oxygen concentration distributions along the scaffold surface at different *Re*; *H/R* =1, *Dar* = 5 ×10^{-6}, ε = 0.6, *Da* = 200.

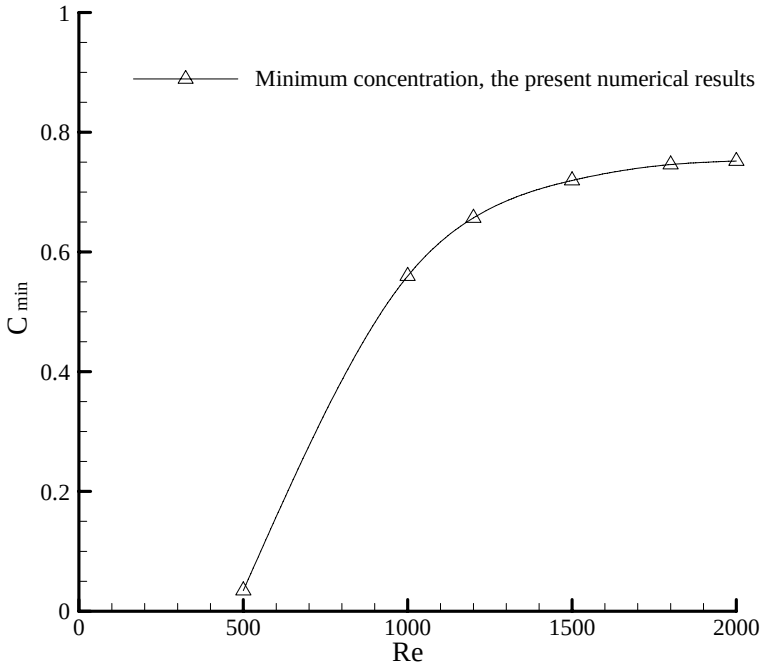

Figure 6.19 Variation of the minimum oxygen concentrations within the scaffold with *Re*; *H/R* =1, *Dar* = 5 ×10^{-6}, ε = 0.6, *Da* = 200.

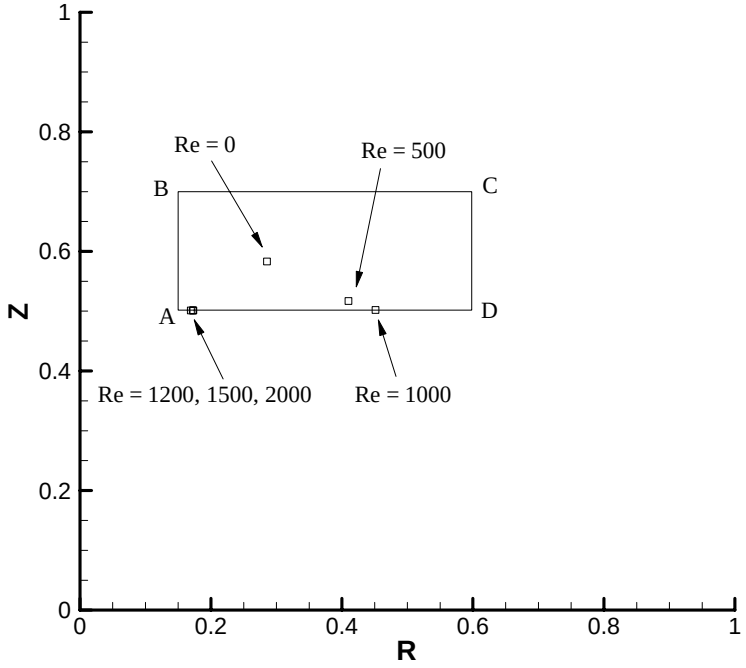

Figure 6.20 Variation of the locations of the minimum oxygen concentration in the scaffold with *Re*; *H/R* = 1, *Dar* = 5 ×10^{-6}, ε = 0.6, *Da* = 200.

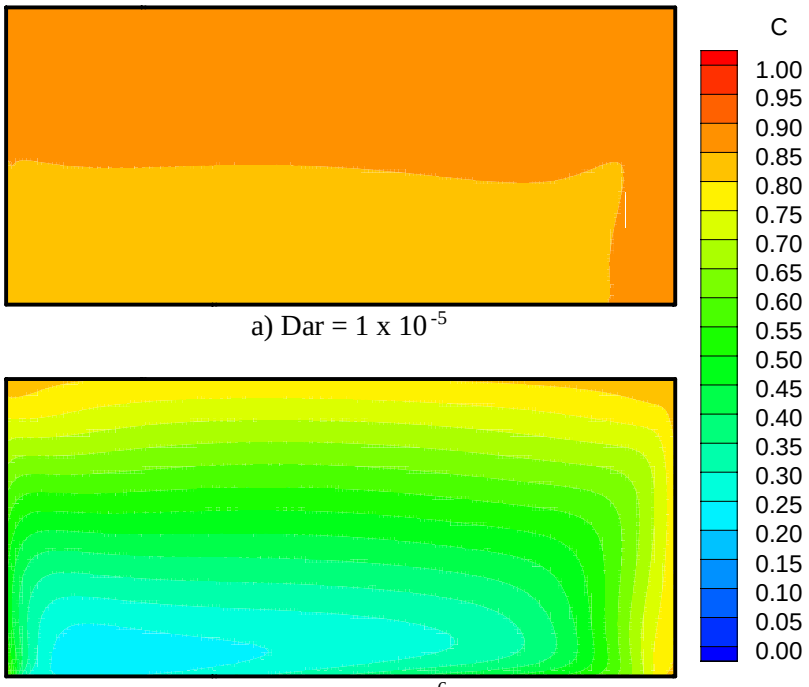

a) Dar = 1 x 10^{-5}

b) Dar = 1 x 10^{-6}

Figure 6.21 Oxygen concentration distributions within the scaffold at different *Dar*; *H/R* = 1, *Re* = 1500, ε = 0.6, *Da* = 200; a) *Dar* = 1 × 10^{-5} and b) *Dar* = 1 × 10^{-6}.

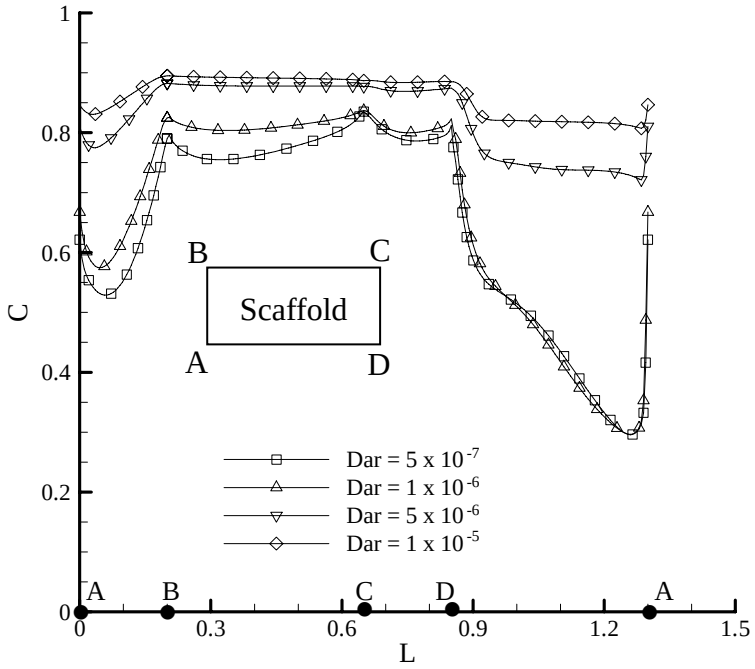

Figure 6.22 Oxygen concentration distributions along the scaffold surface at different *Dar*; *H/R* = 1, *Re* = 1500, ε = 0.6, *Da* = 200.

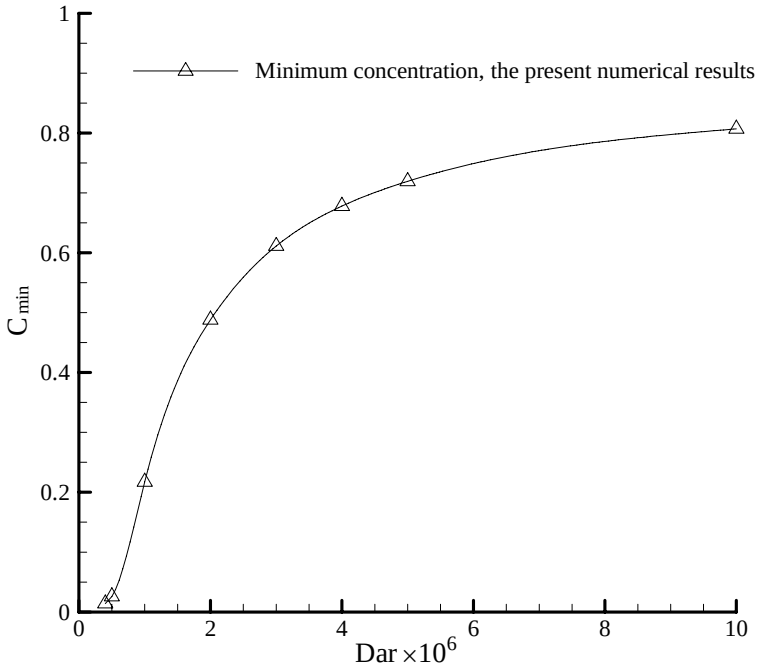

Figure 6.23 Variation of the minimum oxygen concentrations within the scaffold with *Dar*; *H/R* =1, *Re* = 1500, ε = 0.6, *Da* = 200.

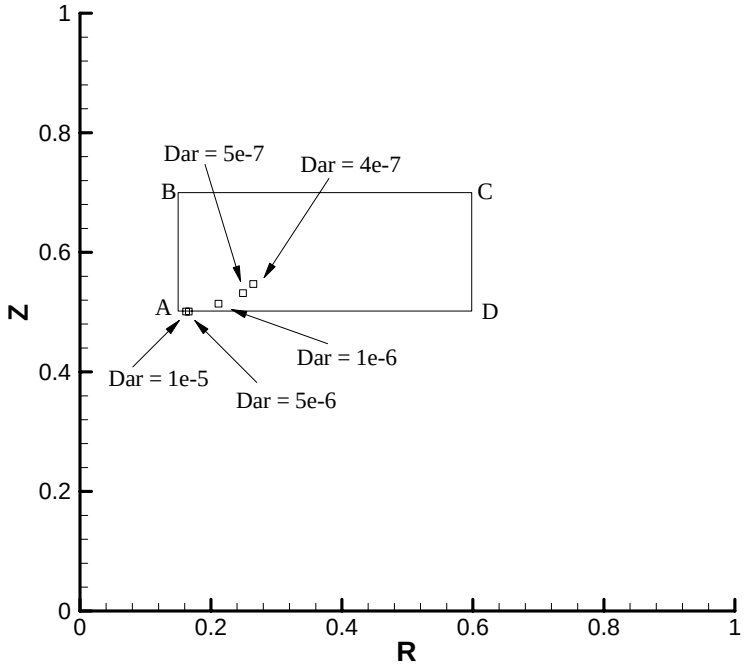

Figure 6.24 Variation of the locations of the minimum oxygen concentration in the scaffold with *Dar*; *H/R* = 1, *Re* = 1500, ε = 0.6, *Da* = 200.

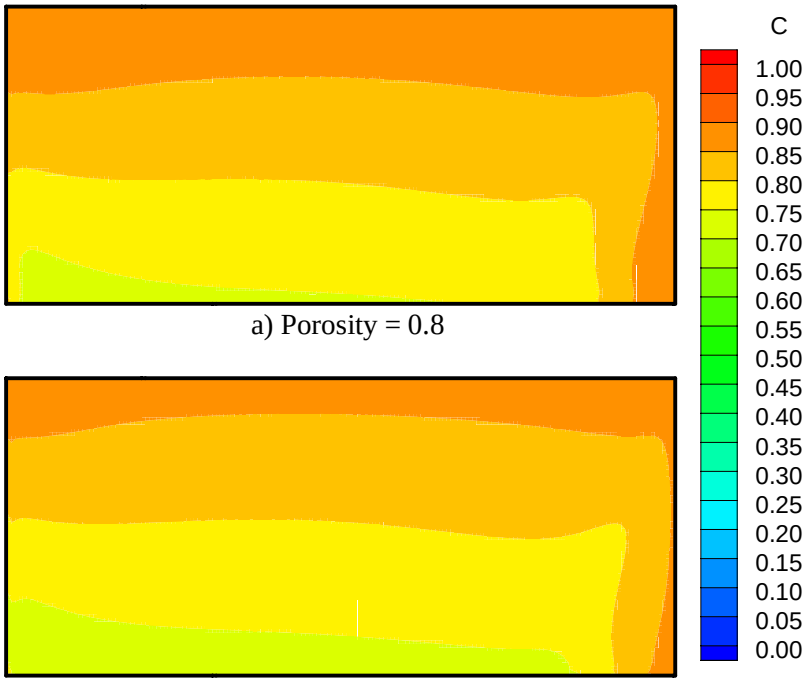

a) Porosity = 0.8

b) Porosity = 0.4

Figure 6.25 Oxygen concentration distributions within the scaffold at different porosities; H/R = 1, Re = 1500, Dar = 5 × 10^{-6}, Da = 200; a) ε = 0.8 and b) ε = 0.4.

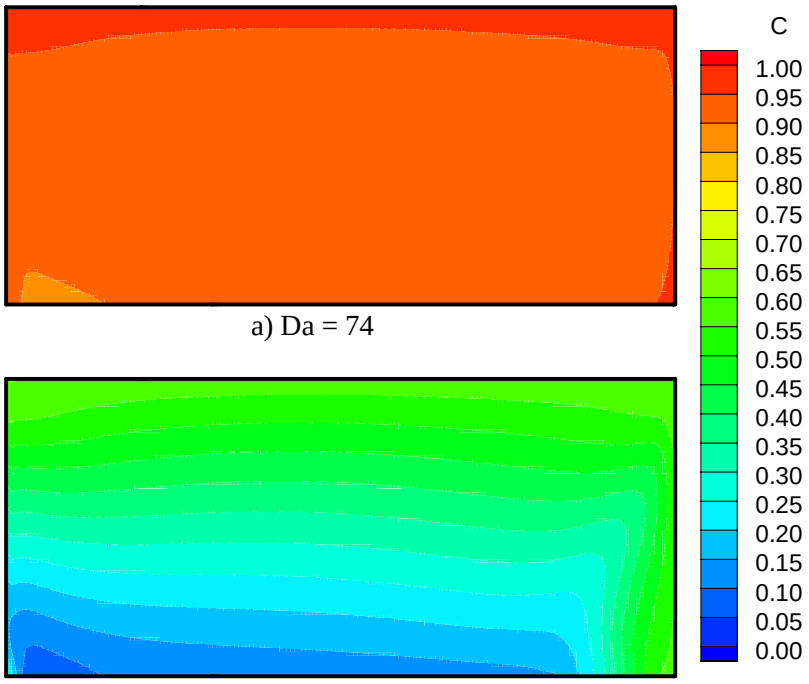

a) Da = 74

b) Da = 740

Figure 6.26 Oxygen concentration distributions within the scaffold at different Da; H/R = 1, Re = 1500, Dar = 5 × 10^{-6}, ε = 0.6; a) Da = 74 and b) Da = 740.

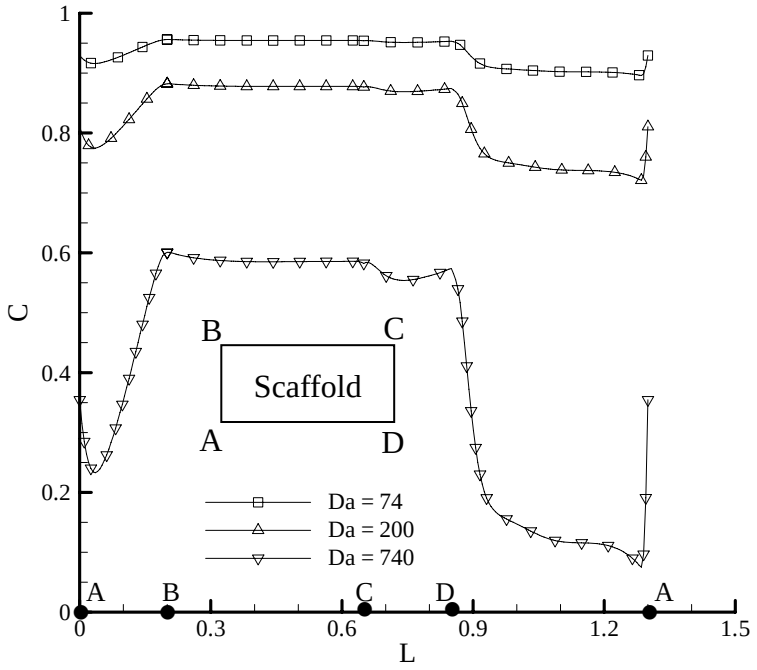

Figure 6.27 Oxygen concentration distributions along the scaffold surface at different *Da*; *H/R* = 1, *Re* = 1500, *Dar* = 5×10^{-6}, ε = 0.6.

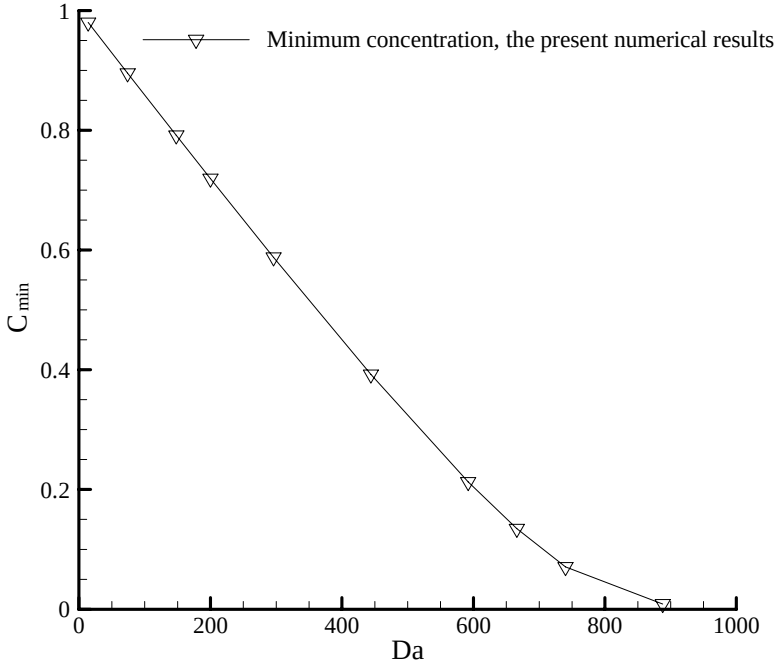

Figure 6.28 Variation of the minimum oxygen concentrations within the scaffold with *Da*; *H/R* =1, *Dar* = 5×10^{-6}, ε = 0.6, *Re* = 1500.